Limiting CP Violation Through a Search for a Permanent Electric Dipole Moment of Mercury 199 Atoms

William Clark Griffith

A dissertation submitted in partial fulfillment
of the requirements for the degree of

Doctor of Philosophy

University of Washington

2005

Program Authorized to Offer Degree: Department of Physics

University of Washington

Graduate School

This is to certify that I have examined this copy of a doctoral dissertation by

William Clark Griffith

and have found that it is complete and satisfactory in all respects,
and that any and all revisions required by the final
examining committee have been made.

Chair of Supervisory Committee:

E. Norval Fortson

Reading Committee:

E. Norval Fortson

Blayne R. Heckel

Michael V. Romalis

Date: 3/16/2005

In presenting this dissertation in partial fulfillment of the requirements for the doctoral degree at the University of Washington, I agree that the Library shall make its copies freely available for inspection. I further agree that extensive copying of this dissertation is allowable only for scholarly purposes, consistent with "fair use" as prescribed in the U.S. Copyright Law. Requests for copying or reproduction of this dissertation may be referred to Proquest Information and Learning, 300 North Zeeb Road, Ann Arbor, MI 48106-1346, to whom the author has granted "the right to reproduce and sell (a) copies of the manuscript in microform and/or (b) printed copies of the manuscript made from microform."

Signature N. Clark Kieper

Date 3/16/2005

University of Washington

Abstract

Limiting CP Violation Through a Search for a Permanent Electric Dipole Moment of Mercury 199 Atoms

William Clark Griffith

Chair of Supervisory Committee:

Professor E. Norval Fortson
Department of Physics

The measurement of a nonzero permanent electric dipole moment (EDM) on an atom or particle would reveal a new source of CP violation beyond the Standard Model. The first measurement of the ^{199}Hg EDM using a UV laser to optically pump and probe a stack of two ^{199}Hg vapor cells has been completed yielding the result, $d(^{199}\mathrm{Hg}) = -(1.06 \pm 0.49_{\mathrm{stat.}} \pm 0.40_{\mathrm{syst.}}) \times 10^{-28}\, e\,\mathrm{cm}$. This result can be interpreted as an upper bound of $|d(^{199}\mathrm{Hg})| < 2.1 \times 10^{-28}\, e\,\mathrm{cm}$ (95% confidence level), which when combined with theoretical calculations, can be used to place stringent bounds on a variety of CP violating parameters, including the EDM of the proton, $\overline{\theta}_{QCD}$, and CP-violating angles originating from supersymmetric theories. An improved version of the experiment using a stack of four ^{199}Hg vapor cells has been built where the two additional cells act as magnetometers and help to improve both the statistical and systematic uncertainties. The new apparatus has been able to improve the statistical sensitivity per unit time by a factor of three, and the magnetometer cells have helped uncover many instances of false signals.

TABLE OF CONTENTS

LIST OF FIGURES

LIST OF TABLES

GLOSSARY

AR: anti-reflection

BBO: β-barium borate nonlinear crystal

CPT: main computer system controlling experiment

DAQ: data acquisition

EDM: electric dipole moment or a permanent electric dipole moment

EMIT: HV control computer

FWHM: full width at half maximum

GP: groundplane

HG1: the first ^{199}Hg EDM measurement [Lam87]

HG2: second generation ^{199}Hg EDM measurement [Jac93, Jac95]

HG3: third generation ^{199}Hg EDM measurement using a UV laser [Rom01a]

HG4: extension of HG3 using 4 vapor cells

HV: high voltage

ID: inner diameter

MOPA: master oscillator power amplifier

OD: outer diameter

ω_L: Larmor spin precession frequency

PE: polyethylene plastic, UHWM unless otherwise indicated

PMT: photomultiplier tube

PRL: Physical Review Letters

RUN: an uninterrupted collection of "scans" between 1 and 36 hours taken with a fixed parameter configuration

SCAN: a single pump/probe cycle, the HV value is changed between successive scans

SFG: sum-frequency generation

SHG: second harmonic generation

T_1: longitudinal spin relaxation time, spins parallel to magnetic field

T_2: transverse spin relaxation time, spins perpendicular to magnetic field

UHMW: ultra-high molecular weight, a grade of polyethylene

UV: ultraviolet

UW: University of Washington, Seattle, WA

ACKNOWLEDGMENTS

I would thank my advisor, Norval Fortson, for his guidance and support throughout my graduate studies. This dissertation is especially indebted to the work and intellectual drive of Michael Romalis, who is largely responsible for the development of the apparatus and measurement technique used in this project. Much thanks to Matt Swallows, who has been as deeply involved in the work described in Chapters 6 and 7 as I was, and will hopefully be able to make it all work someday. Laura Kogler also made many contributions to this dissertation, and worked on many tedious projects that I had the pleasure of devising. Thanks to all of my labmates, past and present, who contributed much knowledge and comradeship: Justin Torgerson, Masataka Iinuma, Amar Andalkar, Roahn Wynar, Reina Maruyama, Timo Koerber, Jeff Sherman, Claire Cramer, and David Pinegar. Special thanks to officemate, bandmate, and shipmate, Tate Wilson. I am extremely grateful to the Tuesday Night Quartet (Bob Edgerton, Sandra Sinner, and Susan Stahl) and the Lake Union Civic Orchestra (LUCO) for giving me a very enjoyable reason to get out of the physics building basement on a regular basis. Finally, I'd like to acknowledge CENPA for financial support over the past several years.

Chapter 1

INTRODUCTION

This dissertation describes our experimental effort to measure the permanent electric dipole moment (EDM) of ^{199}Hg. Generally, the electric dipole moment of a charge distribution with charge density $\rho(\boldsymbol{r})$ is given by the integral

$$\boldsymbol{d} = \int \rho(\boldsymbol{r})\boldsymbol{r}\mathrm{d}^3 r, \tag{1.1}$$

but the simplest example is the case of two opposite charges ($\pm q$) separated by a distance x, giving an EDM of $\boldsymbol{d} = q\boldsymbol{x}$, where $\boldsymbol{x}$ is the vector pointing from $-q$ to $+q$.

In referring to a *permanent* EDM, we mean to specify that we are interested in an EDM of a pure eigenstate of the system when no external electric field is present. This is to differentiate from the more commonly known "electric dipole moments" of polar molecules such as water, which typically have a magnitude of about 1 debye $\simeq 2 \times 10^{-9}\ e\,\mathrm{cm}$, but only exist when an external electric field is applied that is strong enough to orient the molecule (for a full discussion see [Khr97, pg. 4]).

A permanent EDM of an atom or particle must necessarily lie along the axis of spin angular momentum $\boldsymbol{S}$. This can be seen semiclassically in that an EDM perpendicular to $\boldsymbol{S}$ automatically averages to zero. Furthermore, for an eigenstate of an isolated atom or particle, $\boldsymbol{S}$ is the only available vector, so $\boldsymbol{d}$ can only point along $\boldsymbol{S}$,

$$\boldsymbol{d} = d\frac{\boldsymbol{S}}{|\boldsymbol{S}|}. \tag{1.2}$$

Otherwise, there would have to be an additional quantum number to describe the EDM direction along with the spin direction for a given state, and this additional degeneracy would lead to many deviations from well established experimental observations (such as the structure of the periodic table).

1.1 Motivation

Searches for permanent EDMs have been carried out in many experiments over the past 50 years, starting with a measurement of the neutron EDM performed in 1951 by Smith, Purcell, and Ramsey

[Smi57], giving a null result, $|d_n| < 5 \times 10^{-20}$ e cm. Experimental sensitivity has increased by many orders of magnitude in subsequent efforts, and all experiments have so far given null results. Currently, the most precise measurement of an EDM has come from our ^{199}Hg measurement described in this work, which gives a limit of $|d(^{199}\mathrm{Hg})| < 2.1 \times 10^{-28}$ e cm. One way to visualize the extreme smallness of this limit is that if a mercury atom were as large as the earth, then the deviation of the charge distribution from a perfect sphere would be less than a 0.001 angstrom bump at the north pole. Although this is indeed a surpassingly small limit, there is still great interest in increasing the precision of this result in ^{199}Hg and other systems, due to the relation of EDMs to discrete symmetry violation, and the possibility of encountering new physics.

1.1.1 EDMs and Symmetries

Into the second half of the 20th century, it was widely assumed that the laws of physics should necessarily be invariant under time reversal (T) symmetry. In other words, if a movie is taken of some physical process, then the process shown in the movie played backward should also be physically allowed. This may seem absurd from our everyday experience, where statistics and entropy seem to indicate an obvious "arrow" of time, but at a microscopic level, particle interactions are symmetric under time reversal to an extremely high degree.

It can be seen from considering Eq. 1.2 that a nonzero EDM violates T-symmetry. Under the time reversal operation, the spin changes direction but the charge distribution does not, so if $\boldsymbol{S}$ and $\boldsymbol{d}$ of a particle are parallel, then they would be anti-parallel in the time-reversed movie, which means that the movie would show an object that does not exist in our universe. A similar argument shows that a nonzero EDM also violates parity symmetry (spatial inversion, P).

It has been found that the weak interaction is not invariant under spatial inversion (P), or particle-antiparticle inversion (charge conjugation, C), as was first observed in β decay of polarized ^{60}Co in 1957 [Wu57]. For a short time it was still hoped that the laws of physics might still be invariant under the combined C and P transformations, but then CP-violation was observed in the decays of neutral K mesons in 1964 [Chr64]. CP violation has also recently been observed in B meson decays [Bab01, Bel01].

Symmetry advocates can still hope that physics is invariant under the combined C, P, and T-transformations. CPT invariance is still subject to experimental verification, but a variety of experiments place quite stringent limits on CPT violation [Blu04], and CPT invariance is well motivated theoretically through the "CPT theorem" [Pau55], which requires that any local Lorentz

invariant field theory must be invariant under the CPT transformation. With the CPT theorem, a violation of CP implies T violation and vice versa, so if CPT is a valid symmetry of the universe then the CP violation observed in K and B mesons implies a corresponding violation of T-symmetry[1]. In the remainder of this thesis I will refer to T and CP violation interchangeably.

1.1.2 EDMs in the Standard Model and Beyond

It is now well accepted that the CP violation observed in K and B meson decays can be explained in the context of the Standard Model weak interaction, where the CP violation is caused by a single complex phase entering in interactions between quarks and W bosons from the 3×3 Cabibbo-Kobayashi-Maskawa (CKM) quark mixing matrix. CP violating particle EDMs can be calculated from this mechanism, but due to cancellations at lowest orders, the CKM phase results in negligibly small predictions compared to the experimental sensitivity of any current or proposed EDM measurement. Thus EDM searches can provide an essentially background free probe for CP violation beyond the Standard Model.

One reason to expect that new sources of CP violation will eventually be found is that Standard Model CP violation is too small to explain the matter-antimatter asymmetry of the universe [Tro99]. It is generally thought, though, that the Standard Model is not the complete story, and eventually we hope to have a theoretical model that might, for example, have fewer than 19 free parameters, or a unification of all the forces. Almost all theoretical extensions of the Standard Model contain additional particles and interactions that introduce new complex phases, leading to additional sources of CP violation that can in principle contribute to EDMs at leading order, well within reach of experiment.

Currently, the most widely touted Standard Model extension is undoubtedly supersymmetry (SUSY) [Kan98, Sch99]. Among other things, SUSY can help solve the gauge hierarchy problem, it is useful in the development of Grand Unification Theories, and SUSY is a prerequisite for superstring theories, which might hold the promise of a quantum theory of gravity. EDM predictions from the most basic SUSY models can be as much as 100 times *larger* than current experimental limits (see Section 5.4.2). In continuing to improve our experimental sensitivity, we can provide important information on the allowed SUSY model parameter space, and it is possible that a non-null result might emerge soon, perhaps giving the first experimental evidence of supersymmetry.

---

[1] Direct T violation has probably been measured in K meson experiments (see [Ger04] and the references therein).

1.2 EDM Searches

Systems that might be considered for an EDM search must have a non-zero total angular momentum $\boldsymbol{F}$ for the EDM to lie along[2]. It is also preferable to work with a neutral particle, since the measurement requires the application of a large electric field, and a charged particle would be accelerated out of the apparatus.

The general strategy used in all EDM searches is to place the particle (or atom, or molecule) of interest in an electric ($\boldsymbol{E}$) and magnetic ($\boldsymbol{B}$) field, and if there is a nonzero EDM, the usual magnetic Zeeman effect is modified by an electric field dependent term, giving the interaction:

$$H = -(\mu \boldsymbol{B} + d\boldsymbol{E}) \cdot \frac{\boldsymbol{F}}{|F|}, \tag{1.3}$$

where μ is the magnetic moment and d is the electric dipole moment of the particle. It is somewhat advantageous to study a system with $F = 1/2$, because then the only possible moments in the ground state are the magnetic and electric dipole moments shown in Equation 1.3. For a higher spin system, the presence of higher order moments would add additional interactions that would complicate the measurement and open up additional avenues for systematic effects to enter.

The EDM can then be measured by comparing the Larmor precession frequency of $\boldsymbol{F}$ about $\boldsymbol{B}$ for the conditions of having the magnetic and electric fields parallel and antiparallel. For the parallel case, $\omega_p = (\mu B + dE)/(\hbar F)$, and for the antiparallel case, $\omega_a = (\mu B - dE)/(\hbar F)$. Experimentally measuring the difference between these two cases gives a measurement of the EDM:

$$d = \frac{\hbar(\omega_p - \omega_a)F}{2E}. \tag{1.4}$$

The fundamental limitation on the sensitivity of such an experiment comes from the uncertainty in measuring ω, which goes as $\delta\omega = 1/\tau$ for a single particle, where τ is the length of time the spin precession can be measured, or the spin coherence time. The sensitivity is improved by performing the measurement on a large number of particles (N) simultaneously, and repeating the measurement a large number of times (N_m) during a total time $T = N_m\tau$, so that the uncertainty in d is

$$\delta d = \frac{\hbar F}{E\sqrt{N\tau T}}. \tag{1.5}$$

Experiments are designed to maximize the electric field strength, spin coherence time, and number of particles, in order to increase the statistical sensitivity of the measurement. The total time that the measurement takes can range from several months to many years.

---

[2]It has recently been proposed in [Bar04] that spinless atoms or molecules could be used to look for CP-odd polarizability that could arise from CP-violating electron-nucleon interactions or an EDM of the electron.

Improving the EDM statistical sensitivity of a measurement is only beneficial as long as systematic effects do not contribute at the same level as the statistical sensitivity, so understanding and controlling sources of systematic errors is an important factor in experiment design. The most dangerous systematics are magnetic field-like effects that change direction with the electric field. For example, tiny electric currents flowing between the electric field generating electrodes (leakage currents) can generate magnetic fields that reverse direction when the electric field reverses. This effect can be combated by minimizing the size of the leakage currents, and designing the apparatus so that fields generated by electric currents are mainly orthogonal to the main magnetic field; however, the true path of the currents is often not known very well. Additionally, a particle moving through an electric field experiences a motional magnetic field $\boldsymbol{B}_m = \boldsymbol{v} \times \boldsymbol{E}/c^2$ that depends on the electric field direction. Beam experiments are more subject to this effect than vapor cell type experiments where $|\boldsymbol{v}| \cong 0$, and if the main magnetic and electric fields are exactly aligned, then $\boldsymbol{B}_m$ will be orthogonal to the main magnetic field, and would not directly contribute an EDM-like signal. However, small misalignment and asymmetries in spin diffusion in a vapor cell can lead to significant systematic errors compared to the tiny EDMs one is trying to measure.

Besides the general experimental considerations discussed above, the choice of the specific species to be studied is of course important. The neutron is the most fundamental neutral particle that can be worked with practically for a precision measurement (compared to neutrinos or neutral mesons), so it is quite natural that the first EDM measurements were performed on the neutron, and it continues to be one of the main focuses of EDM research. Working with neutral atoms, though, allows for additional CP-violating interactions between the electrons and the nucleus, and between the neutrons and protons of the nucleus, which can lead to enhancements of the EDM signal. Generally, heavier atoms tend to have a higher sensitivity to possible EDM sources than light atoms. EDM searches have also been performed on polar molecules, which take advantage of their extremely high internal electric fields ($\sim 10^{10}$ V/cm) [San67] compared to the much smaller laboratory fields of $\sim 10^4$ V/cm. Customarily, experimental searches for EDMs are split into three classifications: the neutron, paramagnetic systems, and diamagnetic systems.

1.2.1 The Neutron

The first neutron EDM measurement was performed by using Ramsey's technique of separated oscillatory fields [Ram56] on a beam of neutrons at the Oak Ridge reactor, with the result of $d_n = (-0.4 \pm 2.4) \times 10^{-20}\, e$ cm [Smi57]. After the experimental discovery of CP violation in K mesons in

1964 (see Sec 1.1.2), interest in the neutron EDM was revived and the Oak Ridge measurement was repeated in 1967 with some improvements which resulted in $d_n = (2 \pm 3) \times 10^{-22}\ e\,\mathrm{cm}$ [Mil67]. The method continued to be refined, and in 1973 the apparatus was moved to the Institut Laue-Langevin (ILL) high flux reactor in Grenoble, France, where a result of $|d_n| < 3 \times 10^{-24}\ e\,\mathrm{cm}$ was obtained [Dre77]. This was the last beam-type neutron EDM measurement, as the systematic effects, the largest being due to the motional magnetic field $\boldsymbol{B}_m$, were becoming dominant over the statistical error.

Subsequent experiments have used stored ultracold neutrons (UCN), which are much less susceptible to motional magnetic field effects and also have a longer interaction time than beam experiments (10^2 compared to 10^{-2} s). The most precise published limit of the neutron EDM is $|d_n| < 6.3 \times 10^{-26}\ e\,\mathrm{cm}$, which comes from the ILL ultracold neutron measurement [Har99]. This experiment employed a ^{199}Hg comagnetometer for its most recent data, which helps discriminate magnetic systematic effects, such as fields due to leakage currents. It should be noted that Lamoreaux and Golub [Lam00] have questioned the validity of the limit quoted in [Har99], which resulted from combining a previous dataset [Smi90] that did not employ the ^{199}Hg comagnetometer. If the measurements are taken separately, then the neutron EDM limit should be relaxed by about a factor of 1.5, but for the purposes of the rest of this thesis, I will use the published [Har99] limit of $|d_n| < 6.3 \times 10^{-26}\ e\,\mathrm{cm}$. The ILL experiment is ongoing as they have worked to increase their number of stored neutrons and improve counting statistics.

Comagnetometers have become an important tool for reducing systematic errors in EDM measurements, and are used in many EDM searches, existing and planned. It must be established that the comagnetometer species has a much smaller EDM than the species whose EDM you want to measure. In this case, ^{199}Hg had been previously verified [Jac95] to have a smaller EDM than the neutron by about two orders of magnitude. The ^{199}Hg atoms occupy the same spatial region as the neutrons, and the ^{199}Hg spin precession signal is used to independently measure the magnetic field that the neutrons see while the measurement is carried out. Any systematic effect of a magnetic origin would affect both the ^{199}Hg and neutron signals, but a real EDM would likely only be observable in the neutron signal.

For a very thorough history and description of neutron EDM measurements see [Khr97], which also describes a next generation neutron experiment that would use neutrons stored in a superfluid ^{4}He bath along with a small amount of polarized ^{3}He which would act as a neutron polarizer and spin analyzer, as well as a comagnetometer.

Table 1.1: Paramagnetic electron EDM enhancement factors and limits. The reference column is for the experimental limit and the enhancement factors are from [Khr97], pg. 122.

Species	Z	Enhancement	$d_a[e\,\mathrm{cm}]$	$d_e[e\,\mathrm{cm}]$	Reference
Rb	37	24	1.2×10^{-23}	5×10^{-25}	[HH87]
Cs	55	114	1.3×10^{-23}	1×10^{-25}	[Mur89]
Tl	81	-585	9.4×10^{-25}	1.6×10^{-27}	[Reg02]
Fr	87	1150			

1.2.2 Paramagnetic Systems

Paramagnetic atoms and molecules are mainly sensitive to the EDM of the electron because of their unpaired electron spin. It was at first thought unprofitable to perform EDM searches on atoms, because when a neutral atom is placed in an external electric field, the electrons and nucleus arrange themselves in such a way that the average electric field seen by each of its constituents averages to zero, so that a measurement of the atomic EDM would be insensitive to the EDM of any of the constituents. This shielding effect, first formally described by Schiff [Sch63], is perfect in the limit of nonrelativistic point particles with only electrostatic interactions.

In spite of this shielding effect, the first atomic EDM measurement was carried out at UW in 1962 on optically pumped Rubidium in a vapor cell, which set a limit of $d(\mathrm{Rb}) < 1 \times 10^{-18}\ e\,\mathrm{cm}$ [Ens67], and an experiment on a Cesium beam was carried out in 1964 that found $d(\mathrm{Cs}) < 2 \times 10^{-19}\ e\,\mathrm{cm}$ [San64]. Just as it had a large affect on neutron experiments, the 1964 discovery of CP violation also led to increased interest in atomic EDMs, and a closer look at the shielding effect in alkali atoms by Sandars [San64] led to the realization that relativistic effects in heavy atoms enhance the effect of an electron EDM in paramagnetic atoms. The enhancement factor scales roughly as $Z^3\alpha^2$, where $\alpha \approx 1/137$ is the fine structure constant. Calculated values for the enhancement factor, and the current best limits from several atomic EDM searches are shown in Table 1.1.

The result for Rubidium in Table 1.1 was a second Rb vapor cell measurement carried out at UW, which was the PhD. thesis of Huang-Hellinger [HH87], but was not otherwise published due to concerns about some unexplained systematic effects. The result for Cesium was carried out at Amherst using Cs atoms in two vapor cells [Mur89]. Work on the Cs experiment continued after that publication using a 4-cell scheme similar to the setup being developed for an extension to the ^{199}Hg EDM measurement described in this work (see Chapter 6). Unfortunately, persistent non-

statistical fluctuations in the data eventually led to the abandonment of the experiment without another published result, although the data acquired in the experiment can be interpreted as a factor of 5 lower limit [Khr97] than the published result.

Currently, the best limit on the electron EDM comes from the Berkeley Thallium beam experiment [Reg02]. The experiment used two adjacent Tl beams traveling in a common magnetic field and oppositely directed electric fields, and also was capable of generating Tl beams in the opposite direction in the apparatus, which allows for cancellation of the $\boldsymbol{v} \times \boldsymbol{E}$ effect. The beam ovens could also produce Na beams ($Z = 11$), which served as a comagnetometer.

The Berkeley Tl experiment has been discontinued after the 2002 result, so other methods are being investigated to improve the electron EDM limit. An experiment that takes advantage of the large electric field enhancements in polarized diatomic molecules is underway using a beam of YbF at Sussex. The first result gave $d_e = (-0.2 \pm 3.2) \times 10^{-26}\ e\,\mathrm{cm}$ [Hud02] from approximately 24 hours worth of data, which is not yet competitive with the Tl limit, but the main limitation is still counting statistics, so further improvement is likely. The use of a metastable $a(1)$ state of PbO for an EDM search is being investigated at Yale [DeM00]. The experiment would be performed in a vapor cell and also has the advantage of being able to reverse the sign of the EDM signal by addressing two nearby opposite parity states, which can be used to diagnose systematic effects. The PbO group hopes to be sensitive to d_e at a level 2–4 orders of magnitude better than the Tl experiment.

1.2.3 Diamagnetic Atoms

Diamagnetic atoms used in EDM searches have zero electronic angular momentum in the ground state ($^1S_0$), and a nonzero nuclear spin I, preferably with $I = 1/2$. The nuclear spin associated with a possible diamagnetic EDM is much less sensitive to external magnetic field fluctuations than an electron spin, since the electron magnetic moment is much greater than a nuclear magnetic moment ($\mu_B/\mu_N \approx 2000$). Paramagnetic atoms are then much more sensitive to magnetic systematic effects such as leakage current and $\boldsymbol{v} \times \boldsymbol{E}$ fields. Diamagnetic atoms are also less susceptible to the spin depolarizing interactions that limit spin coherence times in paramagnetic systems to tens of milliseconds. Diamagnetic atoms with $I = 1/2$ can achieve spin coherence times over 1000 seconds in a properly prepared vapor cell.

Without a ground state electron spin, though, the enhancement of the atomic EDM due to an electron EDM present in heavy paramagnetic atoms does not help overcome the electrostatic shielding of the external field for heavy diamagnetic atoms. However, the finite size of the nucleus leads to imperfect shielding inside the nucleus, making measurements of the atomic EDM somewhat

sensitive to the EDM of the nucleus. The size of the atomic EDM relative to the nuclear EDM scales roughly as

$$d_a \approx RZ^2 \left(\frac{r_0}{a}\right)^2 d_{nuc}\,, \tag{1.6}$$

where R is a relativistic enhancement, r_0 is the nuclear radius, and $a = 0.53$ Å is the Bohr radius. For the case of ^{199}Hg, $R \sim 10$ and $r_0 \sim 7$ fm, leading to a shielding factor of about 10^{-3}. Despite the significant shielding, heavy diamagnetic atoms have resulted in limits on CP violation competitive with the neutron and paramagnetic systems, due to the much higher statistical sensitivity achievable in long coherence time vapor cell experiments, and the enhancement of CP-violating effects in the nucleus compared to the neutron.

The only stable atomic isotopes with a $^1S_0$ electronic ground state and nuclear spin of 1/2 are ^{3}He, ^{111}Cd, ^{113}Cd, ^{129}Xe, ^{171}Yb, and ^{199}Hg [Lid04]. ^{3}He is too light to be considered for an EDM measurement due to the shielding problem, and the vapor pressures of Cd and Yb are too low to be used in room temperature vapor cell measurements, which leaves ^{129}Xe and ^{199}Hg as the only diamagnetic systems that EDM searches have been carried out on. Cd and Yb would have to be heated to 120 °C and 350 °C respectively in order to achieve adequate vapor densities ($\sim 10^{12}$ cm^{-3}) for optical pumping. At room temperature, Hg has a saturated vapor density of 5×10^{13} cm^{-3}. Higher temperature can lead to longer spin relaxation times in vapor cells, due to shorter wall interaction times, but it can also lead to larger leakage currents and it simply adds another complication to the experiment. ^{171}Yb has been considered as a candidate for an EDM measurement using laser cooled and trapped atoms as is discussed in [Mar03] and [Dil01].

Interpretation of diamagnetic EDMs

A diamagnetic atomic EDM is conventionally written in terms of the "Schiff moment" (S), which quantifies the degree to which the nuclear charge distribution differs from the electric dipole moment distribution, due to the finite size of the nucleus [Sch63].

$$d_a = k \times 10^{-17} \left(\frac{S}{e\,\mathrm{fm}^3}\right) e\,\mathrm{cm}\,, \tag{1.7}$$

where k is a numerical factor from atomic calculations [Dzu02]. The Schiff moment might originate from a non-zero EDM on the protons and neutrons that make up the nucleus, but it is thought that a CP violating nucleon-nucleon interaction is more likely to be the dominant contribution. The Schiff moment can then be calculated in terms of a dimensionless parameter η that encompasses the

Table 1.2: Calculated Schiff moments for diamagnetic atoms. The k value corresponds to the factor entering in Equation 1.7 and are calculated in [Dzu02]. References are given in the table for the estimation of S.

Species	k	$S[10^{-8}\eta\, e\,\mathrm{fm}^3]$	Ref.	$d_a[10^{-25}\eta\, e\,\mathrm{cm}]$
^{129}Xe	0.38	1.75	[Fla85b]	0.7
^{199}Hg	2.8	1.4	[Fla85b]	4.0
^{225}Ra	8.5	300	[Fla03]	2500

details of the particular CP violating theory leading to the interaction. Table 1.2 shows estimates for the Schiff moments and d_a due to S for the $I = 1/2$ isotopes of Hg, Xe, and Ra.

The values in Table 1.2 indicate that ^{199}Hg is about 5 times more sensitive to CP violation than ^{129}Xe, and also that ^{225}Ra has a much larger sensitivity by a factor of 10^2–10^3.The enhancement in the calculated Schiff moment in Ra is due to octupole deformations of the nucleus not found in the smaller "spherical" nuclei of Xe and Hg [Fla03, Eng03]. ^{225}Ra is relatively stable with a half-life of 15 days, and has been proposed as a possible diamagnetic EDM measurement using cold optically trapped atoms at Argonne National Laboratory [Hol02] and the Kernfysisch Versneller Instituut (KVI) in the Netherlands [Jun03].

Diamagnetic EDM searches

A summary of the published EDM limits obtained with diamagnetic systems is shown in Table 1.3. The first diamagnetic EDM measurement was performed on ^{129}Xe at UW in 1984 using a stack of three vapor cells containing Xe and Rb [Vol84]. The Rb was optically pumped with a semiconductor laser at 795 nm, and was used to spin polarize and also detect the spin precession of the ^{129}Xe atoms.

After the ^{129}Xe measurement, the UW group turned their attention to Hg, which as shown in Table 1.2, is expected to have a higher sensitivity to CP violation than Xe, and also has the advantage that its spin can be directly optically pumped and probed using the $6^1S_0 \rightarrow 6^3P_1$ 254 nm transition, which was readily available from microwave discharge lamps. The lamp based experiment continued until the 1995 result [Jac95], at which point the statistical sensitivity was limited by shot noise on the detected photons. Additional details on the lamp based measurements will be discussed in Section 2.3. A new measurement of the ^{199}Hg EDM using a UV laser that began several years later has resulted in the most precise published EDM measurement [Rom01a], and is the subject of this dissertation.

Table 1.3: Atomic EDM limits from Xe and Hg. The values for d_a are quoted with a statistical error followed by the systematic error (if applicable). The upper bounds are quoted as a result of adding the statistical and systematic errors in quadrature and evaluating at a 95 % confidence level.

Year	Atom	Reference	d_a [e cm]	Upper bound
1984	^{129}Xe	[Vol84]	$(0.2 \pm 1.1) \times 10^{-26}$	2.2×10^{-26}
2001		[Ros01]	$(0.7 \pm 3.3 \pm 0.1) \times 10^{-27}$	6.6×10^{-27}
1987	^{199}Hg	[Lam87]	$(0.7 \pm 1.5) \times 10^{-26}$	3.2×10^{-26}
1993		[Jac93]	$(-2.7 \pm 5.8) \times 10^{-28}$	1.3×10^{-27}
1995		[Jac95]	$(-1.2 \pm 2.2 \pm 3.5) \times 10^{-28}$	8.7×10^{-28}
2001		[Rom01a]	$(-1.06 \pm 0.49 \pm 0.40) \times 10^{-28}$	2.1×10^{-28}

Measurements using ^{129}Xe have continued in other groups, despite its expected lower CP violation sensitivity, because it is possible to achieve ^{129}Xe spin coherence times an order of magnitude longer than ^{199}Hg. The best limit on the ^{129}Xe EDM now comes from a measurement performed at the University of Michigan using spin exchange pumped masers of ^{129}Xe and ^{3}He, with the ^{3}He acting as a comagnetometer [Ros01]. This measurement did not approach the sensitivity of the Hg experiment, though, and a new approach is being investigated at Princeton using polarized liquid ^{129}Xe [Rom01b, Led02]. Using liquid Xe, a much higher number of atoms can be sampled, higher electric fields can be applied, and the low temperature environment leads to lower leakage currents, so that the predicted sensitivity of the liquid ^{129}Xe EDM measurement would beat the current ^{199}Hg limit by several orders of magnitude.

Chapter 2

EXPERIMENT OVERVIEW

The experimental effort to measure the EDM of ^{199}Hg has been ongoing at the University of Washington for a little over 20 years now. There have been many changes in the details of the measurement technique over the years, but the basic concept is shown in Figure 2.1. Inside magnetic shields, two quartz vapor cells containing spin polarized ^{199}Hg are placed in a common magnetic field, and oppositely directed electric fields. The spin precession frequency about the magnetic field is measured in both cells simultaneously, and a nonzero EDM (d), from Equation 1.3, would lead to a difference in frequency between the two cells:

$$\Delta\omega \equiv \omega_1 - \omega_2 = \frac{4Ed}{\hbar}. \tag{2.1}$$

In order to cancel magnetic field drifts, the electric field direction in both cells is reversed periodically, and an EDM would lead to changes in $\Delta\omega$ correlated with the electric field reversals. Spin polarization and spin precession detection are carried out with light at the 253.7 nm resonance wavelength traveling perpendicular to $\boldsymbol{E}$ and $\boldsymbol{B}$.

In this chapter I will describe basic properties of Hg relevant to the experiment, the optical pumping methods used to achieve spin polarization, and the methods used to detect the spin precession.

2.1 Hg Properties

The only elemental metal that is liquid at room temperature, mercury has long played an important role in scientific progress (for a history of mercury and its uses see [Gol72]), from its role in alchemy, to its uses as a measurement tool of temperature and pressure. In this experiment, mercury is now used as an extremely sensitive measurement tool for CP violation.

Table 2.1 shows the abundances and nuclear spin of the seven stable isotopes of mercury. The two non-zero nuclear spin isotopes, ^{199}Hg and ^{201}Hg are capable of being optically pumped, as was first demonstrated by Cagnac and Brossel [Cag58, Cag59]. The adequate room temperature vapor pressure of Hg, and the fact that light from ^{204}Hg lamps only overlaps a single hyperfine component of ^{199}Hg ($F = 1/2 \rightarrow 1/2$) and ^{201}Hg ($F = 3/2 \rightarrow 5/2$), made Hg convenient for early optical pumping studies. Comparisons of ^{199}Hg and ^{201}Hg are also useful due to their different nuclear

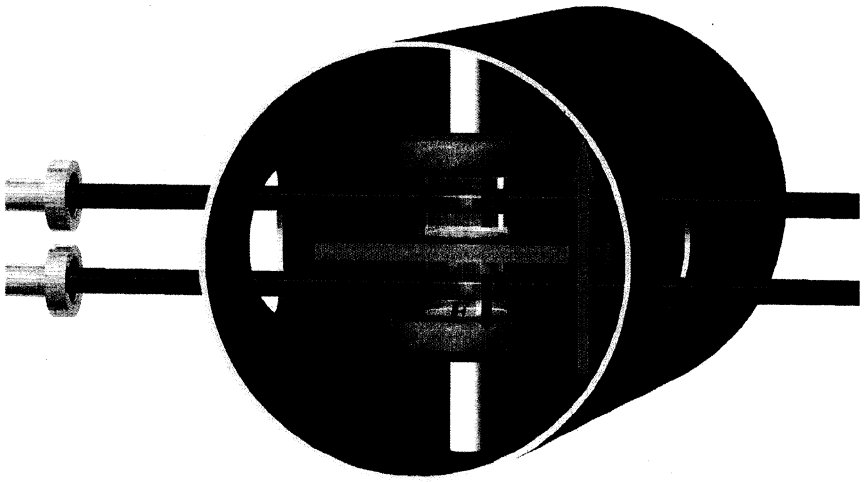

Figure 2.1: ^{199}Hg EDM measurement.

spins. For example since ^{201}Hg has $I \geq 1$, it can have an electric quadrupole moment which causes additional spin relaxation in electric field gradients at the cell walls compared to ^{199}Hg [Cag59]. A review of different precision measurements carried out with optically pumped ^{199}Hg and ^{201}Hg is given in [Lam96].

Figure 2.2 shows the lowest lying energy levels of Hg. The Hg EDM measurements have all been performed using the $6^1S_0 \rightarrow 6^3P_1$ intercombination line. This transition would be forbidden by strict electric dipole selection rules due to the change in S, but the $\boldsymbol{L} \cdot \boldsymbol{S}$ interaction causes significant mixing of the $^1P_1$ and $^3P_1$ states in heavy atoms (see [Hap72, pg. 230] or [Cor77, pg. 136]) to make the intercombination transition fairly strong in Hg with a lifetime of 119 ns.

In ^{199}Hg, the $^3P_1$ level is split into two hyperfine levels separated by 22.13 GHz [Stager1963], due to the nuclear spin of 1/2. Figure 2.3 shows a light absorption scan at 253.7 nm performed on one of the vapor cells used in this experiment. The cells contained 500 Torr of a 90% N_2 and 10% CO buffer gas mixture which broadens the lines to about 4.5 GHz (FWHM) compared to the natural width of 1.3 MHz and room temperature doppler width of 1.2 GHz. A measurement using the same laser system as this work showed that the pressure broadening of Hg in N_2 is 9 MHz/Torr and the pressure shift is -2.5 MHz/Torr [Jac03]. No recent measurements for the pressure broadening and

Table 2.1: Isotopes of Mercury. The natural abundances of the seven stable isotopes of Hg are compared to the enriched ^{199}Hg abundances [Har00] contained in the vapor cells used in this work.

Isotope:	196	198	199	200	201	202	204
Nuclear Spin:	0	0	1/2	0	3/2	0	0
Natural Abundance:	0.15%	10%	17%	23%	13%	30%	7%
Enriched ^{199}Hg	0	1.1%	92%	4%	1.1%	1.8%	0

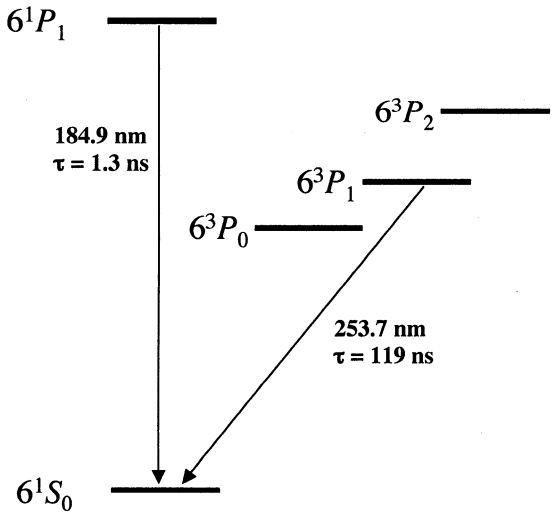

Figure 2.2: Lowest lying energy levels of Hg. Energy levels are from [Bro52b], and lifetimes are from [Cur01].

shift of Hg in CO have been performed, but earlier work [Zem30] indicates that the effects of N_2 and CO buffer gases on Hg are similar.

2.2 *Optical Pumping*

The Hg EDM measurement, along with most other atomic EDM searches, relies on optical pumping methods to prepare the atoms in a single Zeeman sublevel. More generally, optical pumping is any use of optical radiation that leads to a change in the relative populations of Zeeman or hyperfine sublevels in the ground or metastable state of atoms. Alfred Kastler received the Nobel Prize in 1966 for proposing the concept in 1950 [Kas50] and optical pumping was first demonstrated in a sodium beam in 1952 [Bro52a]. For a basic introduction to optical pumping see [Hap87], and for a thorough treatment of optical pumping theory and the first two decades of optical pumping experiments see [Hap72].

Figure 2.4 shows the setup for a basic optical pumping experiment with ^{199}Hg. ^{199}Hg atoms are contained in a vapor cell and placed in a magnetic field. Initially, the two ground state Zeeman sublevels $m_F = \pm 1/2$ have equal populations ($kT \gg \mu B$). If the cell is exposed to circularly polarized (σ^+) light directed along $\boldsymbol{B}$, and resonant with the $6^1S_0 \rightarrow 6^3P_1$, $F = 1/2$ transition, then the atoms can only make transitions out of the $m_F = -1/2$ ground state level to the $m_F = +1/2$ excited state level because Δm_F must be $+1$ for σ^+ light. From the $m_F = +1/2$ excited state, the atom will return to either of the ground state sublevels by spontaneous emission, or by collision with a buffer gas molecule. Since the spontaneously emitted photons can be absorbed by other atoms and cause $\Delta m_F = -1$ or 0 transitions, it is preferable to use a buffer gas with a high enough pressure and quenching cross section such that the excited state ^{199}Hg is collisionally quenched much faster than the 119 ns lifetime of the $^3P_1$ state.

If the atom ends up in the $m_F = +1/2$ sublevel of the ground state, then the light can no longer interact with it, so the atom can no longer be pumped out of the ground state. Eventually, barring other interactions, all of the atoms end up in the $m_F = +1/2$ ground state level, and the vapor is completely "spin polarized." There generally do exist interactions that "relax" the atoms out of the polarized Zeeman level. If Γ_r is the rate at which atoms relax out of polarized state, and Γ_p is the rate at which atoms are pumped into the $+1/2$ ground state, then the polarization can be described as

$$\frac{\mathrm{d}}{\mathrm{d}t}P_A = \Gamma_p(1 - P_A) - \Gamma_r P_A, \tag{2.2}$$

where P_A is the fraction of atoms in the $+1/2$ ground state. In the steady state limit, the polarization

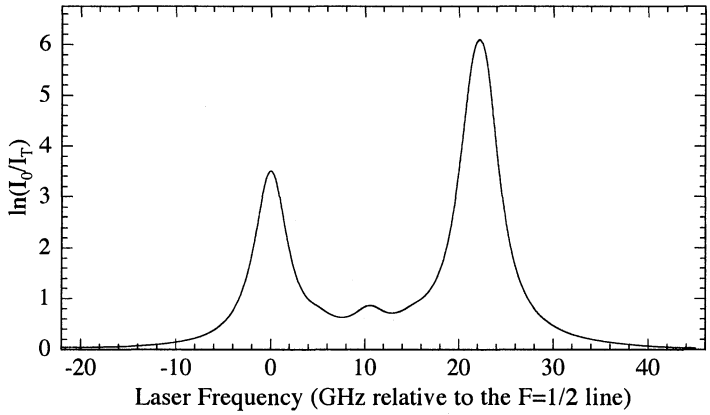

Figure 2.3: ^{199}Hg vapor cell absorption scan at 253.7 nm. The frequency is relative to the $F = 1/2$ hyperfine component and the hyperfine splitting between the $F = 1/2$ and $3/2$ lines is 22.1 GHz. The lines are broadened due to a buffer gas at 500 Torr. The small bump between the two stronger ^{199}Hg hyperfine lines is due to the presence of trace amounts of ^{200}Hg.

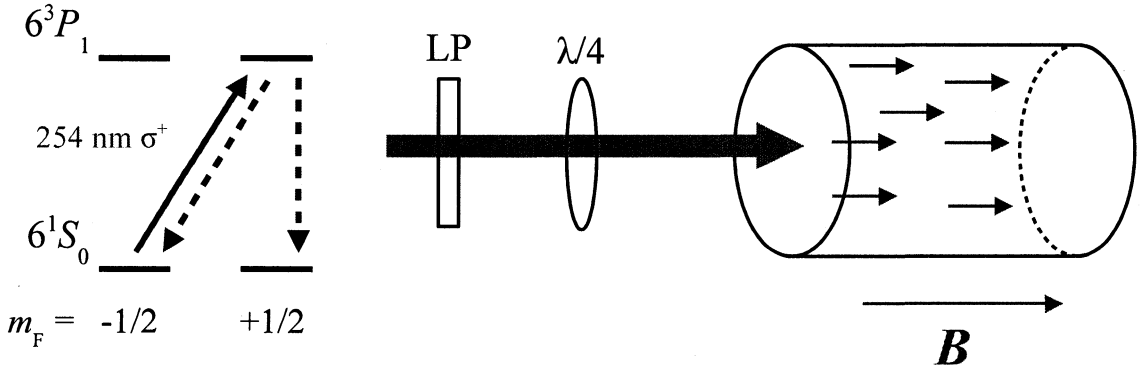

Figure 2.4: Basic optical pumping setup.

can reach a maximum value of

$$P_A = \frac{\Gamma_p}{\Gamma_r + \Gamma_p}. \tag{2.3}$$

One possible method of monitoring the degree of polarization would be to measure the amount of light transmitted through the vapor cell, since the photon absorption decreases as the polarization increases.

If the pump light is turned off, then the spin polarization will decay exponentially as e^{-t/T_1}, where $T_1 = 1/\Gamma_r$ describes the longitudinal spin relaxation time. In many optical pumping experiments, spin relaxation is dominated by interactions that occur at the cell walls. For example, ^{201}Hg is relaxed by electric quadrupole interactions with electric field gradients at the cell walls, and in our ^{199}Hg vapor cells the dominant relaxation mechanism is thought to be dipolar coupling to paramagnetic sites on the cell walls [Rom04]. Relaxation times can be increased by the presence of a buffer gas, which increases the diffusion time for a polarized atom to reach the cell walls, and a wall coating such as paraffin can reduce the time that an atom stays at the cell wall (the "sticking" time), which reduces the chance that a depolarizing interaction will occur.

Magnetic field gradients across the cell can also cause spin relaxation. If there are nonzero magnetic field components perpendicular to the main polarization direction (determined by the propagation direction of the circularly polarized pumping light), then the spins will tend to precess in a cone about the overall field direction. As the spins diffuse randomly through an inhomogeneous magnetic field, the orientation of their precession changes randomly, leading to spin decoherence [Gam65].

2.2.1 Transverse Pumping

In order to measure the Larmor precession frequency (ω_L) in the experiment shown in Figure 2.4, the magnetic field could be suddenly rotated so that it is perpendicular to the light direction. The ^{199}Hg spins would then precess about the magnetic field, which would modulate the transmitted light intensity at ω_L.

The high sensitivity of EDM measurements requires a very stable magnetic field environment, though, so large changes in the magnetic field direction are undesirable during the measurement. Spin polarization can be directly generated perpendicular to the magnetic field through transverse pumping methods, as was first demonstrated by Bell and Bloom in 1961 [Bel61]. As shown in Figure 2.5, circularly polarized light is applied along the y-direction and modulated at approximately ω_L. If we consider the atoms to initially be in equal populations of the $\pm 1/2$ sublevels in the y-direction, then the two states precess about $\boldsymbol{B}_0$ in opposite directions. By modulating the light, the atoms are

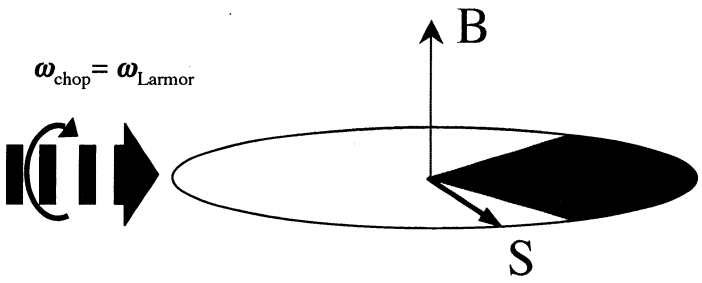

Figure 2.5: Transverse optical pumping setup.

pumped only when the two spin states return to their original orientations, and spin polarization is built up in a frame rotating about $\boldsymbol{B}_0$.

If the pump light is turned off the spin polarization decays as e^{-t/T_2} where T_2 is the transverse relaxation time. The longitudinal and transverse relaxation times, T_1 and T_2, do not necessarily have the same value, because they have a different dependence on relaxation methods due to magnetic field gradients [Cat88, McG90][1]. T_2 is shortened by gradients in the main field component (B_z) across the vapor cell, because if the atoms sample different magnetic field strengths in different parts of the cell, then they precess at different rates, leading to phase decoherence.

2.3 Lamp Based Measurements

The first three published ^{199}Hg EDM measurements [Lam87, Jac93, Jac95] were performed with light from Hg microwave discharge lamps, similar to the original Hg optical pumping experiments [Cag58]. A detailed description of the first measurement makes up the second half of Steve Lamoreaux's Ph.D. thesis [Lam86b], and I will refer to this measurement as HG1, adopting the terminology used by Jacobs in [Jac95]. The experimental apparatus was significantly altered after HG1, and I will refer to the measurements that went into [Jac93] and [Jac95] as HG2. HG2 is described in fine detail in the thesis of Jim Jacobs [Jac91] and the first half of Bill Klipstein's thesis [Kli96]. The results from the lamp based ^{199}Hg EDM measurements are summarized in Table 1.3.

---

[1] In conventional NMR terminology, T_2 includes only *homogeneous* broadening mechanisms. Relaxation due to magnetic field inhomogeneity would only be included in $1/T_2^*$, the *total* transverse relaxation rate including homogeneous and inhomogeneous broadening. For the purposes of this thesis, I use $T_2 \equiv T_2^*$.

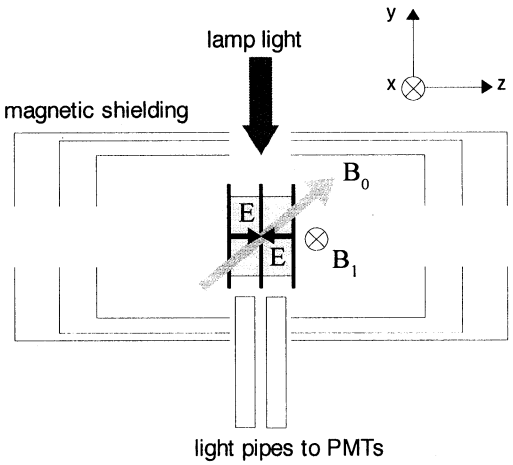

Figure 2.6: HG1 experiment diagram. $B_0 = 20$ mG and $\boldsymbol{B}_1 = B_1 \cos(\omega t)\hat{x}$ with $B_1 = 20\mu$G.

2.3.1 HG1

The first version of the experiment to measure the ^{199}Hg EDM grew out of an apparatus used to test spatial anisotropy by measuring the spin precession frequencies of ^{201}Hg and ^{199}Hg in the same vapor cell [Lam86a, Lam86b]. In that experiment, the ^{199}Hg served as a comagnetometer signal which was used to stabilize the magnetic field, while the ^{201}Hg frequency was monitored for a quadrupole interaction correlated with the apparatus's "stellar" orientation. In order to convert the experiment into an EDM measurement, the main change was to replace the single spherical vapor cell setup with two cylindrical cells with electric field plates on the ends.

HG1 used a substantially different optical pumping setup than the transverse pumping later used in HG2 and this work. Following the method of optically pumped light-absorption oscillators first proposed by Dehmelt [Deh57], the magnetic field and light geometry are shown in Figure 2.6. There is a static magnetic field $\boldsymbol{B}_0$ at an angle of 45° in the yz-plane, and an oscillating field $\boldsymbol{B}_1$ along $\hat{x}$ whose frequency (ω) is set to closely match the Larmor frequency (ω_0) of the atoms due to B_0. This geometry allows for optical pumping and spin precession detection with a single light beam. Circularly polarized light from the ^{204}Hg lamp enters the cell along $\hat{y}$, and optically pumps the atoms so that polarization builds up along $\boldsymbol{B}_0$. The oscillating field B_1 causes the polarization vector to precess at ω in a cone around $\boldsymbol{B}_0$. The projection of the precessing polarization onto $\hat{y}$ leads to a modulation at ω of the transmitted circularly polarized light through the cell. Slight deviations of ω from ω_0 cause a phase shift $\phi = T_2(\omega - \omega_0)$ between the B_1 oscillation and the resulting light modulation. Monitoring the phase difference between the light transmitted through each cell gives

a measure of the magnetic field gradient between the cells, and by looking for correlations with the electric field direction, gives the EDM sensitive signal.

The data set for HG1 consisted of 29 runs of between 1 and 15 hours each. The end result of $d(^{199}\mathrm{Hg}) = (0.7 \pm 1.5) \times 10^{-26}\, e\,\mathrm{cm}$ had no significant systematic error contribution. The main source of statistical noise was noise due to light intensity fluctuations. When circularly polarized light is projected along the spin polarization direction, unequal light shifts [Hap67] between the two m_F sublevels leads to a shift in the Zeeman splitting proportional to the light intensity. Acting as a virtual magnetic field, the light shift effectively causes a small magnetic-like perturbation along $\hat{y}$.

2.3.2 HG2

After HG1, several major improvements were implemented in the vapor cells: instead of using natural Hg with a 17% abundance of ^{199}Hg an enriched vapor with 92% ^{199}Hg was used, modifications to the buffer gas in the cells seemed to lead to improved stability of the Hg density and spin lifetimes of the cells, and a more thorough cleaning process during cell fabrication improved the leakage currents from 10–20 pA to less than 1 pA at 10 kV. Issues regarding the fabrication and performance of the Hg vapor cells will be discussed in more detail in Sections 3.1 and 6.1.

In addition to the vapor cells, the other major improvement in HG2 was to change to a transverse optical pumping method. The basic setup is as shown in Figure 2.1, with a static magnetic field perpendicular to the pump light, which significantly suppresses light shift noise from coupling to the precession frequency. Instead of modulating the intensity of circularly polarized pump light, as is done in traditional transverse optical pumping [Bel61], the polarization state of the light was modulated between σ^+ and σ^- at $\omega \approx \omega_L$, which leads to a similar buildup of polarization in the frame rotating about $\boldsymbol{B}$. Polarization modulation was achieved by passing the ^{204}Hg lamp light through a rotating linear polarizer and a fixed quarter wave plate, or a fixed linear polarizer and a rotating quarter wave plate. The intensity of the light transmitted through the polarized vapor acquires a modulation at 2ω, and becomes phase shifted from twice the drive frequency of the light polarization if ω does not exactly match ω_L. As in HG1, the vapor is simultaneously pumped and probed, and the phase difference between the signals from each cell could be monitored for electric field correlations, which gives the EDM signal.

The result in [Jac93] was based on about 236 24-hour data runs. For [Jac95] an additional 97 data runs were added, but the first 34 runs of the original data set were discarded, leaving a total of 299 × 24 hours of data. The 34 runs were removed because of a resolved frequency shift quadratic in $\boldsymbol{E}$, probably caused by an instability in the HV power supply for one polarity that was

repaired for subsequent runs. HG2's final result was $d(^{199}\mathrm{Hg}) = (-1.0 \pm 2.4 \pm 3.6) \times 10^{-28}\, e\,\mathrm{cm}$, and had comparable statistical and systematic errors. No significant systematic effects were directly measured, although there was some evidence of HV polarity dependent magnetic fields generated by solenoids in the HV power supply. Based on an external magnetometer signal, a correction of 0.6 nHz/G was applied to some of the data, giving a systematic uncertainty of $0.68 \times 10^{-28}\, e\,\mathrm{cm}$. The main contribution to the systematic error estimate was based on data taken at zero electric field between each dwell with high voltage applied. The $\boldsymbol{E} = 0$ dwells were analyzed for an EDM-like contribution by comparing dwells at zero following +HV, with dwells at zero following −HV, giving $d(E = 0) = (3.3 \pm 2.5) \times 10^{-28}\, e\,\mathrm{cm}$. Since this signal has no contribution from a real EDM, it was used to estimate a systematic error of $\pm 3.3 \times 10^{-28}\, e\,\mathrm{cm}$. Combining this in quadrature with a contribution of $\pm 1.4 \times 10^{-28}\, e\,\mathrm{cm}$ from limits on effects dependent on $|\boldsymbol{E}|$, along with the magnetometer correction gave a total systematic error of $3.6 \times 10^{-28}\ e\,\mathrm{cm}$.

Although the systematic error bar was slightly larger than the statistical error, the result was mainly limited by the statistical resolution of the measurement technique, because the dominant systematic contribution was limited by the statistical resolution of the $d(E = 0)$ data. Acquiring additional data would have improved the statistics, but an additional factor of two improvement would have required several more years (900 runs) of continuous data taking. A different optical pumping and probe method still using Hg discharge lamps was studied that could have increased the sensitivity per unit time by a factor of 2–3 [Kli96], but although the lamps used in the EDM measurement had proven themselves as reliable and stable light sources, that could operate maintenance free for weeks at a time, the ^{199}Hg EDM experiment now required a boost in photon counting statistics that the lamps could not supply.

2.4 New UV Laser Measurement

The main limitation of the Hg discharge lamp measurements was the low photon collection efficiency. Only 20% of the light entering the magnetic shields reached the vapor cells, and less than 25% of this light made it to the PMT detectors, which had a quantum efficiency of 10%. UV enhanced silicon photodiodes can have near 50% efficiencies at 254 nm[2], but the large area photodiodes necessary to collect divergent lamp light exhibited too much Johnson noise to be useful. Switching to a narrow UV laser light source can enable near perfect light collection on small area photodiodes, and the ability to tune the light frequency allows for additional optical pumping and spin precession detection options.

[2]UDT sensors, UV enhanced inversion layer photodiodes, http://www.udt.com/

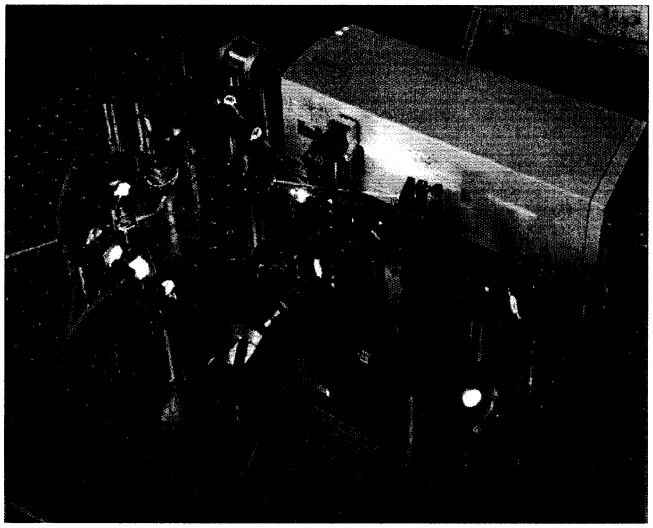

Figure 2.7: Photo of the frequency quadrupled UV laser system. The rectangular box in the upper right-hand corner is the semiconductor MOPA laser. The additional optics pictured make up the frequency doubling cavities, and the entire system fits on an 18×30" optical breadboard.

There are currently no direct laser sources at 253.7 nm, but nonlinear crystals have long been used to generate coherent UV radiation from longer wavelength lasers through sum-frequency generation (SFG) or second harmonic generation (SHG). A tunable pulsed laser at 253.5 nm, generated from mixing a ruby laser at 694.3 nm and a dye laser at 400.0 nm, was reported in 1973 [Sat73], and the first continuous-wave laser reaching 254 nm was obtained in 1980 from frequency doubling a dye laser at 508 nm [Web80].

Although UV laser technology had been established well before the start of HG1 and HG2, dye lasers are notoriously high maintenance devices, requiring frequent adjustment and messy dye changes, and the success and precision of the HG2 measurement had a lot to do with the long-term stability and trouble free operation of the discharge lamps. By 1995, though, semiconductor lasers at 4 times the Hg $6^1S_0 \rightarrow 6^3P_1$ transition frequency (1015 nm) had been developed, giving the possibility of a relatively robust frequency quadrupled laser at 253.7 nm, as was demonstrated in a semiconductor laser based system at 243 nm [Zim95].

Figure 2.7 shows a photograph of the laser system developed for the Hg EDM experiment. Light at 1015 nm is generated by a "master oscillator power amplifier" (MOPA) semiconductor laser manufactured by SDL. A potassium niobate ($KNbO_3$) crystal in a bow-tie enhancement cavity frequency doubles the infrared light to 508 nm, and a second enhancement cavity with a β-barium borate (BBO) crystal frequency doubles the light again to reach 253.7 nm. Starting with 500 mW

of infrared light, 100 mW of green, and 5 mW of UV light has been generated. Besides the Hg EDM measurement, the laser system at 253.7 nm has been used in precision spectroscopy measurements for the scalar Stark shift [Har00], and the pressure shift and broadening [Jac03] of the $6^1S_0 \rightarrow 6^3P_1$ line in Hg.

The basic setup of the measurement is again shown by Figure 2.1, with the light beams now generated by the UV laser system. Instead of the steady state "synchronous" pumping and detection used in the lamp based measurements, though, a separated pump and probe method is now used, which takes advantage of the ability to easily tune the laser anywhere in a 100 GHz range about the $F = 1/2$ and $F = 3/2$ lines (see Figure 2.3). For optical pumping, the laser is tuned on resonance with the $F = 1/2$ transition and modulated intensity transverse pumping (see Secs. 2.2.1 and A.4) is used to build up spin polarization in a frame rotating about the magnetic field. About 50 μW of circularly polarized light, modulated by a chopper wheel with about a 30% duty cycle, is incident on each cell. After 30 seconds of optical pumping, the laser light is switched to the probe configuration, where the light is linearly polarized, detuned by 10–20 GHz off resonance, and the power reduced to about 5 μW. The spin polarization then precesses about the magnetic field, and its magnitude decays as $P_A(t) = P_A(0)e^{-t/T_2}$. The spin precession is detected by monitoring for optical rotation of the probe light polarization direction induced by passing through the spin polarized vapor.

2.4.1 Detecting Spin Precession with Optical Rotation

The first use of optical rotation to monitor spin precession of a polarized Hg vapor was reported in 1963 [Man63], and optical rotation and other related magneto-optical effects in atomic vapors have been recently reviewed in [Bud02]. In this section I will briefly describe conceptually the optical rotation effect, and a more detailed calculation of the size of the effect will be given in Appendix A.

Just as the absorption probability for the two senses of circularly polarized light is dependent on the vapor spin polarization direction, so is the index of refraction. As the spin polarization precesses at ω, the difference in the indices of refraction for $\sigma_\pm$ light has a time dependence $(n_+ - n_-) \propto \sin\omega t$. The incident linearly polarized probe light can be decomposed into equal components of σ_+ and σ_- light, and after traversing a distance L through the polarized vapor, the two circular components acquire a relative phase shift

$$\varphi = \frac{\omega L}{c}(n_+ - n_-). \tag{2.4}$$

Returning to a linear polarization basis, one finds that the plane of polarization of the incoming light has rotated by an angle φ. A difference in absorption of the circular components leads to elliptical polarization, but the absorption is a relatively small effect for detuned probe light.

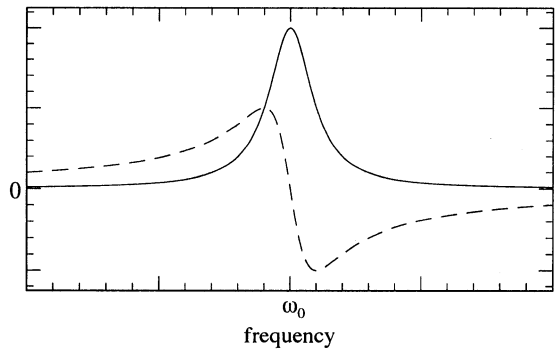

Figure 2.8: Complex index of refraction near an atomic resonance. The line is an isolated transition and assumed to be dominantly Lorentz broadened. The solid line is n_I and the dashed line is $n_R - 1$. n_I is associated with absorption while n_R gives the phase velocity of light in the vapor.

Figure 2.9 shows the detuning dependence for the optical rotation angle for the 253.7 nm ^{199}Hg transition. The contributions from the $F = 1/2$ (0 GHz) and $F = 3/2$ (22 GHz) lines are equal but have opposite signs.EDM data has been taken mainly with probe detunings of -20 and $+10$ GHz. The $+10$ GHz detuning is especially favorable due to the mutual rotation contributions from the two hyperfine components, and relatively low absorption (see Fig. 2.3). The first laser based ^{199}Hg published result [Rom01a] mainly used a -20 GHz detuning, though, which reduces light shift effects, and the larger detuning also was believed to help slow the degradation of cell lifetimes caused by UV exposure.

Figure 2.10 shows the pump and probe setup for detecting optical rotation. If the atomic polarization has a coherence time τ, and is precessing at ω, the rotation angle time dependence is given by

$$\varphi(t) = \varphi_0 e^{-t/\tau} \sin \omega t. \tag{2.5}$$

The optical rotation is detected by measuring the light intensity on a silicon photodiode after a linear polarizer, at an angle α away from the extinction point for non-rotated light ($\varphi = 0$), so that the measured intensity is

$$I = I_0 \sin^2(\alpha + \varphi(t)), \tag{2.6}$$

from which the precession frequency can be extracted. The angles were always chosen such that $|\varphi| < |\alpha| < 45°$, and in the limit of small optical rotation amplitude A, Eq. 2.6 becomes

$$I = \frac{I_0}{2}\left(1 - \cos 2\alpha + 2Ae^{-t/\tau} \sin \omega t \sin 2\alpha\right). \tag{2.7}$$

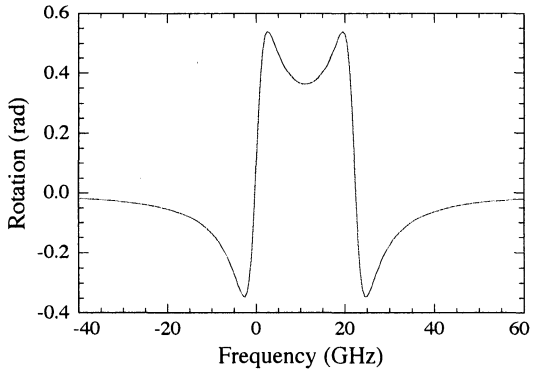

Figure 2.9: Calculated detuning dependence of the optical rotation angle. Probe laser detuning is relative to the $F = 1/2$ transition, and the angle is calculated for an HG3 vapor cell.

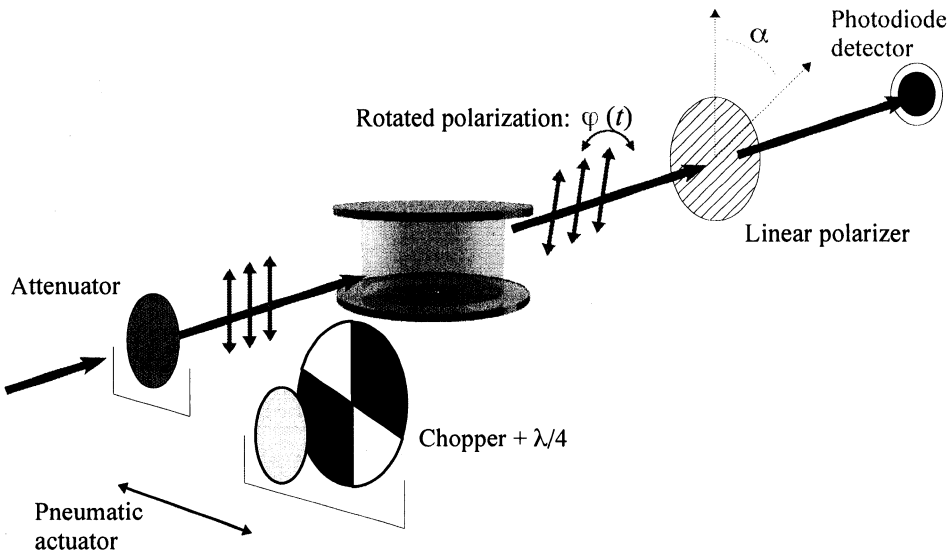

Figure 2.10: Pump and probe setup for detecting optical rotation. A pneumatic actuator moves a quarter wave plate and chopper wheel into the beam for optical pumping. For probing spin precession, the light is attenuated with a neutral density filter, and sent through an analyzing linear polarizer. The analyzing polarizer is at an angle α away from the extinction point of the incoming beam.

2.4.2 HG3

The first results of the laser based measurement of the ^{199}Hg EDM were reported in a PRL article in early 2001 [Rom01a], and this thesis contains a full description of that work. Continuing to use the shorthand of Section 2.3, I will refer to the measurement reported in [Rom01a] as HG3.

Following the completion of HG2, there was some initial development work done on the frequency doubling cavities first using a Titanium:Sapphire laser as the infrared source [Kli96], and then Jim Jacobs carried out the first efforts incorporating the SDL infrared diode system. Work really picked up again in 1997 after the arrival of Michael Romalis at UW as a post-doc. The apparatus was essentially built up again from scratch, and although many aspects are similar, the HG3 apparatus uses almost no leftover parts from HG2. Besides changes in the measurement technique related to the new laser system, the most important changes implemented in HG3 were the use of improved vapor cells (see Sec. 3.1), and the use of less metal materials near the cells (see Sec. 3.2.2).

The result, $d(^{199}\mathrm{Hg}) = (-1.06 \pm 0.49 \pm 0.40) \times 10^{-28}\ e\,\mathrm{cm}$, was based on 60 days of data (see Ch. 4). There were no measurable systematic effects, and the systematic error estimate of $\pm 0.40 \times 10^{-28}\ e\,\mathrm{cm}$ was mainly based on the contributions from uncertainties in leakage current ($\pm 0.25 \times 10^{-28}\ e\,\mathrm{cm}$) and $\boldsymbol{v} \times \boldsymbol{E}$ effects ($\pm 0.3 \times 10^{-28}\ e\,\mathrm{cm}$). Although we did not see evidence of a correlation between fluctuations of the leakage currents and the EDM signal to the level of $\pm 0.14 \times 10^{-28}\ e\,\mathrm{cm}$, we took a slightly more conservative approach by using the size of the magnetic effect if the average measured leakage current (0.6 pA) traveled in one complete loop around a vapor cell. The $\boldsymbol{v} \times \boldsymbol{E}$ estimate was limited by the statistics on a small set of data taken with $\boldsymbol{B}$ tipped off from $\boldsymbol{E}$ by 5°.

2.4.3 HG4

At the time of the [Rom01a] publication, we could have continued taking data to improve the statistics using the HG3 configuration. Systematic effects would also have to be reduced to make meaningful progress, though, since the statistical and systematic errors on that measurement were comparable. While the $\boldsymbol{v} \times \boldsymbol{E}$ contribution to the error could have been improved, the one loop leakage current error estimate would not improve with better statistics. It was decided that a modification of the measurement to address this issue was needed.

One possible approach would be to somehow lower the total leakage currents flowing between the cell electrodes. The leakage currents are believed to be significantly suppressed due to a rigorous cleaning process applied to the raw materials (see Sec. 3.1). It seems unlikely, though, that any changes in the cleaning methods would result in lowering the average leakage currents to less than 0.1 pA at 10 kV, so this avenue has not been seriously considered.

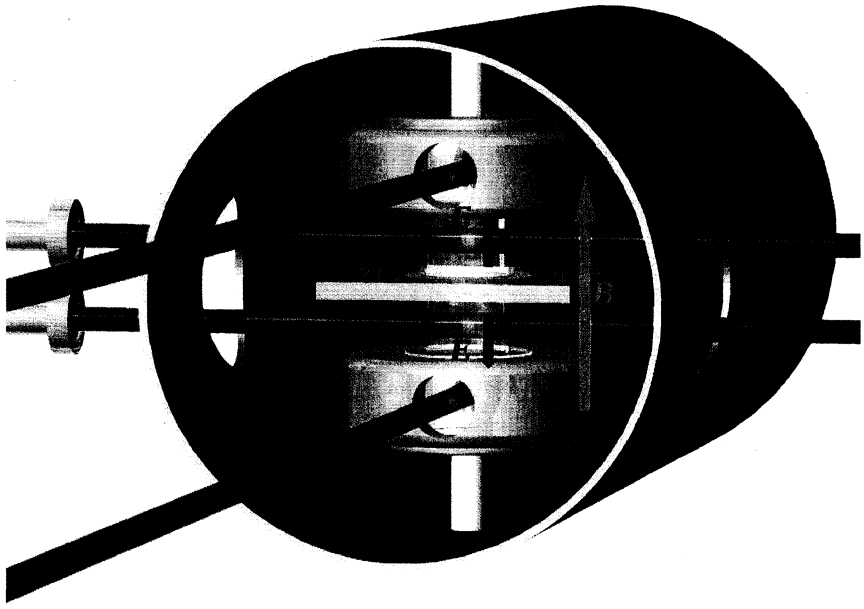

Figure 2.11: 4-cell EDM measurement. The 4-cell version includes the 2-cell measurement from Fig. 2.1, and adds two magnetometer cells inside hollow HV electrodes with light access holes. The light beams for the additional cells are directed along the axis of the magnetic shields.

The ideal solution would be to add a second spin 1/2 atomic species to the vapor cells to serve as a comagnetometer. However, as is discussed in [Jac91], it is unclear if there is a workable co-magnetometer species that can be easily optically pumped in the same cell as mercury, and if one were found, it would at minimum require an additional laser system and also likely require major changes to the vapor cell construction. If the 20 years of development for the ^{199}Hg EDM cells is any indication, making comagnetometer EDM cells that work as well as the current cells would require a large investment of time and perspiration.

Instead, it was decided that it would be better to pursue a four vapor cell EDM measurement, which could use the existing vapor cell technology and essentially the same apparatus as HG3 with only a few modifications. As shown in Figure 2.11, the additional two cells are enclosed in the HV electrode cups (see Sec. 6.2), and so are subject to zero electric field. Therefore, the middle two cells perform the EDM measurement as in Figure 2.1, and the outer cells act as magnetometers. The magnetometer cells provide sensitivity to possible magnetic systematic effects and also help improve the statistical sensitivity by allowing magnetic field gradient noise cancellation.

I will refer to the work on the four cell version of the ^{199}Hg EDM experiment as HG4. Changes implemented in the HG3 apparatus for HG4 will be described in Chapter 6. At the end of HG3, only three vapor cells were in working order, so additional cells needed to be constructed for the four cell version. Continuing the ongoing development of the ^{199}Hg EDM cells, a different buffer gas was used in the new cells that has led to improved spin coherence times (see Sec. 6.1).

Improved magnetic noise cancellation from the magnetometer cells and the longer spin coherence times have led to a factor of 2–3 improvement in the statistical sensitivity of HG4 compared to HG3. Unfortunately, problems with some persistent EDM-like false signals of as yet unknown origin have kept HG4 from yielding a new limit on $d(^{199}\mathrm{Hg})$. The data that has been taken with the HG4 setup so far will be discussed in Chapter 7.

Chapter 3

TWO CELL APPARATUS

This chapter describes the apparatus used to make the 2-cell ^{199}Hg EDM measurement which took place during the year 2000. Changes made to the apparatus after 2000 will be described in a later chapter (Ch. 6).

Figure 3.1 shows a general diagram of the apparatus. Hg atoms were contained in vapor cells placed in a 17 mG magnetic field at the center of three layers of magnetic shielding. By applying ± 10 kV across the cells, an oppositely directed electric field was created in each cell. The high voltage power supply and electronics for measuring leakage currents flowing across the cell walls were located in a separate room from the rest of the apparatus (about 50 ft away) in order to reduce the possibility of signal contamination from electronic pickup. Optical pumping and spin precession detection were achieved with laser light at the 253.7 nm $6^1S_0 \rightarrow 6^3P_1$ Hg transition, generated by frequency quadrupling the output of a MOPA semiconductor laser operating at 1015 nm. For optical pumping the light was circularly polarized and tuned to the center of the $F = 1/2$ transition. A chopper wheel modulated the light at about the Larmor precession frequency of the atoms in order to build up spin polarization in the rotating frame perpendicular to the magnetic field. After 30 seconds of optical pumping a pneumatic actuator moved the chopper and quarter wave plate out of the light beams and moved a neutral density filter into the beams, changing the intensity in each beam from 70 μW to 7μW. The light was also detuned by 20 GHz below the $F = 1/2$ resonance. Passing through the precessing spin polarization of the vapor caused the light polarization direction to be modulated, which after passing through a nearly crossed linear polarizer, gave a photodiode signal intensity modulation at the precession frequency of the Hg spins. The photodiode signal was normalized by the intensity measured immediately after the laser and recorded on a computer DAQ system. After 100 seconds of probing the spin precession, a new optical pumping cycle would begin, during which the high voltage would ramp to a new value so that the next probe cycle would observe a different electric field. The important features of the apparatus will be discussed in some detail in the following sections.

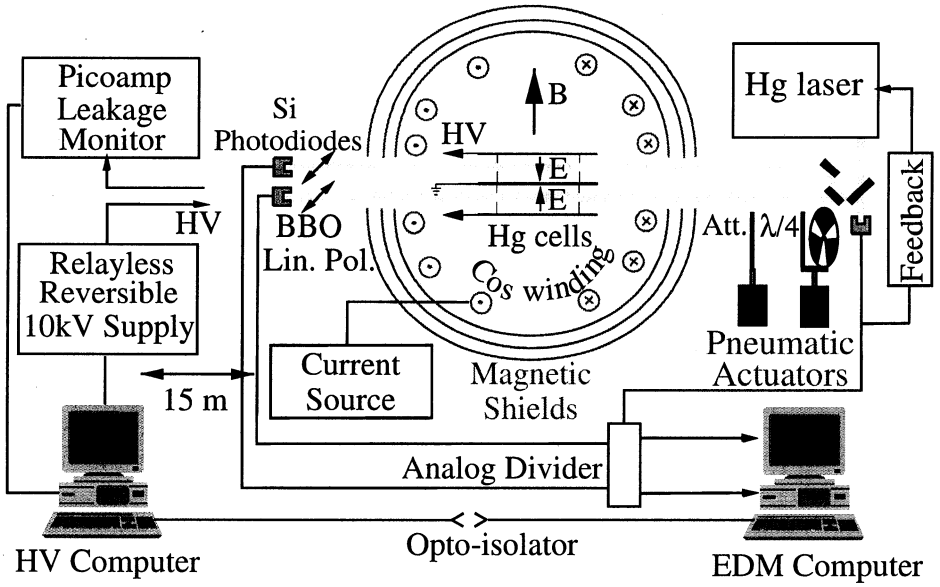

Figure 3.1: 2-cell Hg EDM experiment diagram.

3.1 Vapor Cells

The heart and center of the experiment are the vapor cells containing the ^{199}Hg atoms. The development of the cells has been ongoing throughout the 20 year history of the experiment in an effort to achieve long ($>$ 100 sec) and stable spin coherence times, stable Hg density, and low leakage currents when electric fields are applied ($<$ 1 pA). The development of the cells used in the previous measurements of the ^{199}Hg EDM is well described in a previous thesis [Jac91] and article [Jac95]. Subsequent studies of the relaxation mechanism in the cells are described in [Rom04].

The cells used for this measurement (see Fig. 3.2) were constructed out of Suprasil fused silica. A conductive tin-oxide (SnO_2) coating on the inner surfaces of the end-plates provides the electrodes for application of the electric field. If the electric field were applied externally to the cell its value would be reduced inside the cell due to charge buildup on the dielectric end-plates. A thin uniform wax (dotriacontane, $CH_3(CH_2)_{30}CH_3$) coating covers the tin-oxide electrode and the cell walls in order to increase the spin relaxation time. Coating the electrodes with wax could also lead to a reduced electric field, but it was verified with Stark shift measurements in coated and uncoated cells [Har00], that a thin wax film had no substantial effect on the electric field. The cells have two stems: one is cooled with liquid nitrogen during the filling process to collect mercury into the cell, the

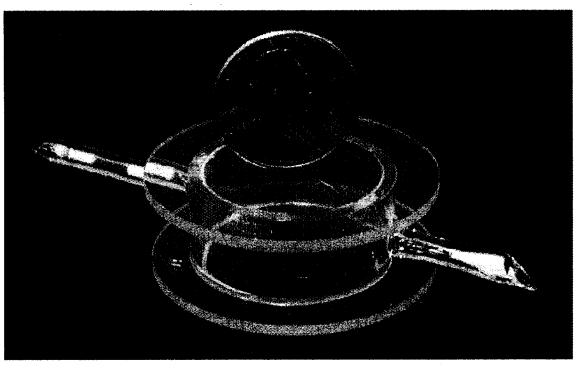

Figure 3.2: EDM vapor cell photo. The cell is constructed out of synthetic quartz and contains enriched ^{199}Hg vapor and 500 Torr of a 90% N_2 + 10% CO buffer gas. A tin oxide coating on the inner faces of the cell disks act as the electrodes and a paraffin wall coating is used to increase the spin relaxation time.

other is the pull-off stem from the vacuum system and it is used to collect excess wax. A saturated, isotopically enriched (92 %) ^{199}Hg vapor is maintained in the cell due to excess mercury collected in the stem. At room temperature this leads to 10^{14} atoms in the cell, or 3–4 absorption lengths. The cells also contained 500 Torr of a 90% N_2 + 10% CO buffer gas. The buffer gas is necessary in order to apply high electric fields inside the cell. It also increases the optical pumping efficiency by quenching excited state Hg atoms so that they do not emit photons that might depolarize other atoms, and it serves to increase the spin relaxation time by limiting diffusion of the atoms to the cell walls where depolarizing interactions are most likely to occur. The actual buffer gas composition was arrived at through a somewhat circuitous path (see Ref. [Jac91]), and will be discussed further in Section 6.1. In practice, the cells had transverse spin coherence times (T_2) between 80–150 seconds, and an average leakage current of 0.6 pA when 10 kV was applied across them.

3.1.1 Cell Construction

The cell walls and end-plates were constructed out of Suprasil I (Heraeus Optics) fused silica, a synthetic quartz with extremely high purity and homogeneity. 1" O.D. tubing with 1/16" wall thickness formed the cell walls, and the end-plates were 1.5" × 1/16" disks. The quartz parts were cleaned first in soap and water, followed by two acetone baths in an ultrasonic cleaner. They were then subjected to a hot chromic acid bath (a saturated solution of CrO_3 in sulfuric acid at 80 °C) as described in [Ros72]. After being boiled in two changes of deionized water, they were given another acetone and then methanol ultrasonic cleaning. The stems were then attached to the 1" tubing and

the tubing was cut to 11 mm lengths, after which the cell bodies were washed again using the same procedure. The cell bodies were then annealed at 1100 °C for 1-2 hours and allowed to cool slowly, followed by a third and final cleaning process.

The conductive coating was applied to the inner face of the end-plates based on the method described in [Cog66]. After heating the quartz disks to 700 °C, they were sprayed with a solution of 10 grams $SnCl_4 \times 5H_2O$ (stannic chloride) in 50 mL of ethanol from an atomizer. The temperature was then raised to 900 °C, which evaporates some of the stannic chloride solution in order to achieve a more homogeneous coating. Typically, the resulting resistance across the 1.5" disk was a few kΩ.

The end-plates were attached to the bodies with a low-outgassing UV-cured adhesive[1]. After ensuring that no dust was present on the end-plates or the inner surface of the cell body with an air-duster, adhesive was applied around the circular edge of a cell body, the cell body was carefully placed in the center of the end-plate, and then the assembly was placed under a UV lamp for 30 minutes.

The cells were then attached to the vacuum system , pumped to 10^{-7} torr, and baked at 100 °C for several days. A small amount of wax was then chased into the cells with a hand torch, during which the wax was evaporated several times in order to achieve some level of distillation. The "mercury stems" of the cells were then immersed in liquid nitrogen and the cells were exposed to the enriched ^{199}Hg vapor. After several minutes enough ^{199}Hg condensed into the cooled stems to maintain a saturated room temperature vapor, and the liquid nitrogen was removed and the valve to the ^{199}Hg ampule was closed. The cells were then filled with 450 torr of N_2 and 50 torr of CO buffer gas and were finally pulled from the vacuum system using a hand torch, leaving a 1–1.5" stem.

3.1.2 Cell Performance

Two vapor cells were needed to make EDM measurements, and a total of four vapor cells, labeled #23, 24, 25, and 26, were swapped in and out of the apparatus during the course of the data set. About halfway into the data set, one of cell 25's stems broke, while its wax coating was being remelted, and the rest of the dataset was taken with the remaining three cells.

Before they could be used, the wax inside the cells had to be carefully distributed, using a hand torch, such that there was a thin and uniform wax coating on the cell walls and electrodes. Excess wax was chased into the pull-off stem. If the coating was properly melted, which could take many tries to achieve, the cells generally could achieve a 150-200 second transverse spin relaxation time.

Only the inner faces of the cell disks had the conductive coating, but in practice, an electrical

[1]Norland Optical Adhesive 88, http://www.norlandprod.com

connection to the outer surface was required to make contact with the groundplane or HV electrodes. A conductive path was created by using silver paint[2] on the side of the disk in four spots around the edge.

As cells were exposed to resonant UV radiation, their spin relaxation times tended to decrease over time from their initial values of 150–200 seconds. After 2–3 weeks of UV exposure the spin lifetimes would typically have fallen to less than 80 seconds. Remelting the wax wall coating again could restore the longer lifetimes, which indicated that the lifetime degradation was due to damage to the wall coating caused by collisions with excited state mercury atoms (see Sec. 6.1). This behavior of the cells influenced the data taking procedure to some degree in that data would be taken with a particular pair of cells installed in the apparatus for 2–3 weeks until the relaxation times became too low, and then the cells would be remelted or new cells would be installed in a new configuration.

3.2 Cell Holding Vessel

The vapor cells were installed into a 4×4×5" box which could be slid in and out of the magnetic shields. Two versions of the vessel were used during the course of the experiment. The first was constructed mainly from Teflon with a vacuum evaporator deposited aluminum coating. About halfway through the dataset a second vessel was constructed using polyethylene, which was carbon-filled to make it slightly conductive. The design of the two vessels was essentially the same, and the choice of materials will be discussed in Section 3.2.2.

A side cutaway view of the vessel is shown in Figure 3.3. The walls of the vessel were constructed from 1/2" sheet plastic and were held together by 6-32 nylon screws. A conductive silicone based glue[3] was used in some places to fill in gaps, which unfortunately did not give an airtight seal, so it was supplemented by superglue to provide a sealant. The vessel was meant to be nominally airtight in order to accommodate a slightly overpressured SF_6 environment. SF_6 has a higher breakdown voltage than air, and also could act as a drying agent for the surfaces inside the vessel, which helps control the leakage currents upon application of high voltage. The gas was typically purged for 20 seconds on a daily basis, or slightly more frequently if the leakage currents required it. The front face of the vessel included two holes in the corners for the SF_6 to enter and exit, and for accessing the inside of the vessel, the front face was removable and interfaced with the vessel with a 1/16" thick square gasket made of conductive silicone[4].

---

[2]GC Electronics: Silver Print, 22-201

[3]silver in silicone, Effective Shielding: 41-0219, http://www.effshield.com

[4]silicone filled with silver coated aluminum particles, Effective Shielding: 58-3817-0013.

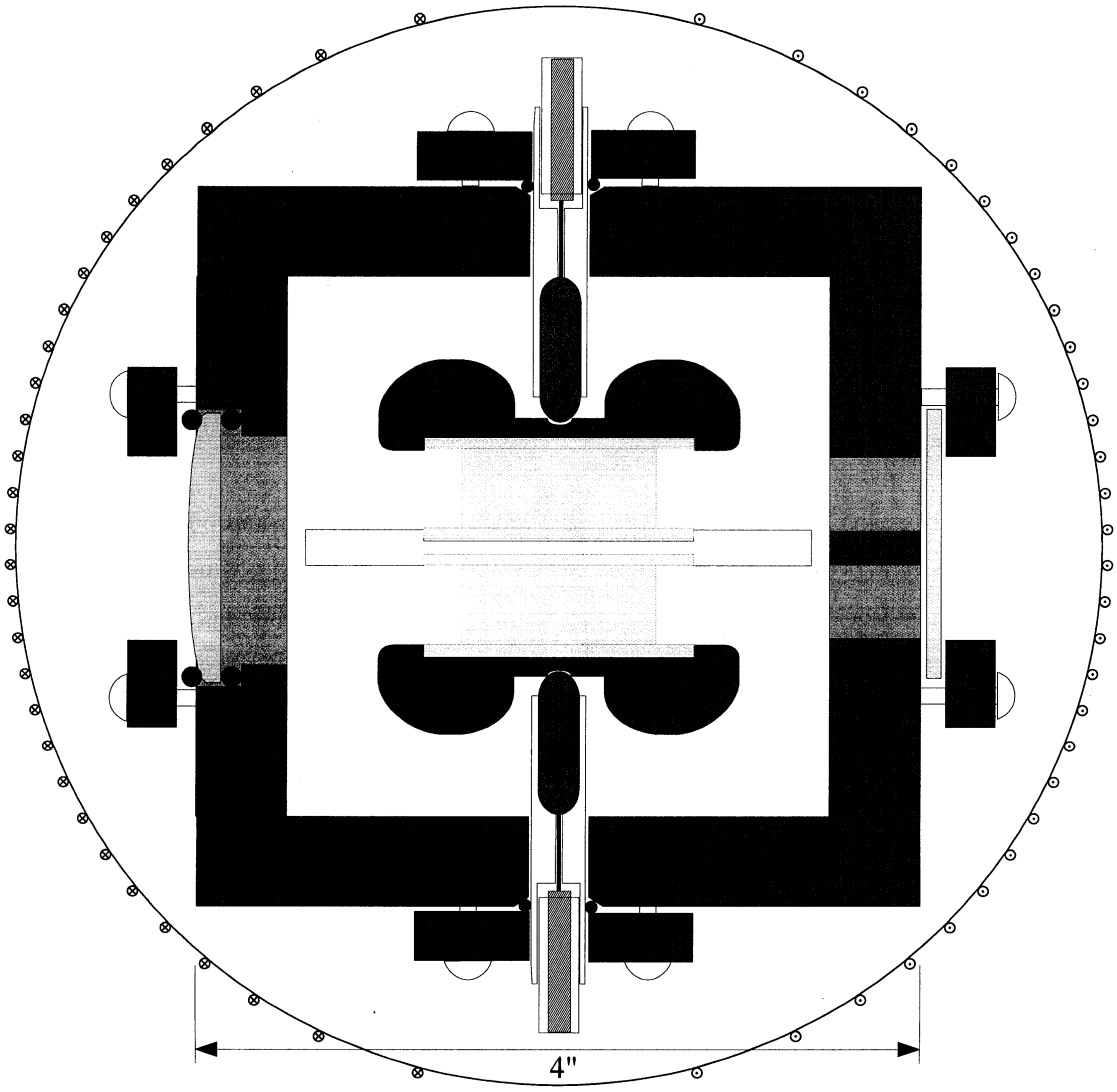

Figure 3.3: Cell holding vessel sideview. Dark grey shading indicates electrically conductive materials. The light beams enter from the right through separate holes, pass through the cells, and are refocused by a single cylindrical lens at the exit face. The locations of the current loops that generate the main vertical magnetic field are also shown.

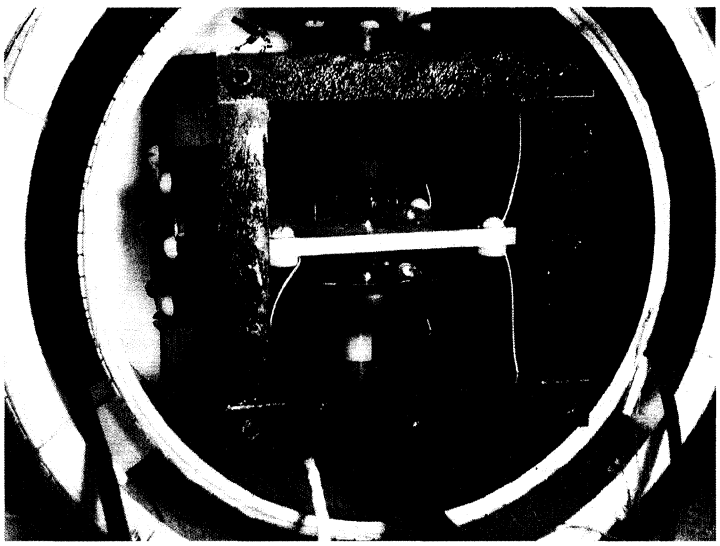

Figure 3.4: Cell holding vessel photograph. The conductive polyethylene vessel is shown inside the magnetic field coil with the front face and shape-adapter removed. The leakage current collection wires are visible connected to the corners of the groundplane.

A 0.15" thick groundplane was suspended in the middle of the vessel, supported by 4 screws entering through the side walls, so that there was a 0.1" gap between the walls and the groundplane edge. The cells sat in circular indentations such that the conductive side of the cell disk was flush with the surface of the groundplane. In both versions of the vessel the groundplane was made of nonconductive plastic with an Al coating. The coating was not applied to the edges of the groundplane, though, so that the top and bottom could be electrically isolated and the leakage currents flowing to the groundplane could be separately measured for the top and bottom halves. Leakage current collection wires were attached to the four corners of the groundplane by screws (see Fig. 3.4), and exited through small holes in the top or bottom faces, to provide a symmetric path for the currents.

The high voltage entered the vessel by way of coaxial feedthroughs with 1.5" long, 0.32" diameter, nonconductive plastic insulation (see Sec. 3.2.1). The feedthroughs pressed down on a 2" diameter electrode "cup," which interfaced with the cell end-plate. A 1/4"×2.5" diameter collar held by 4 screws pressed down on an O-ring (Buna-N) around the feedthrough on the outside of the vessel, which held the feedthrough firmly in place and also provided an airtight seal. When installing cells, it was important that the feedthrough be adjusted such that it provided enough pressure to hold the cell so that it would not move, but not so much pressure that extra birefringence would be induced in the quartz cell walls.

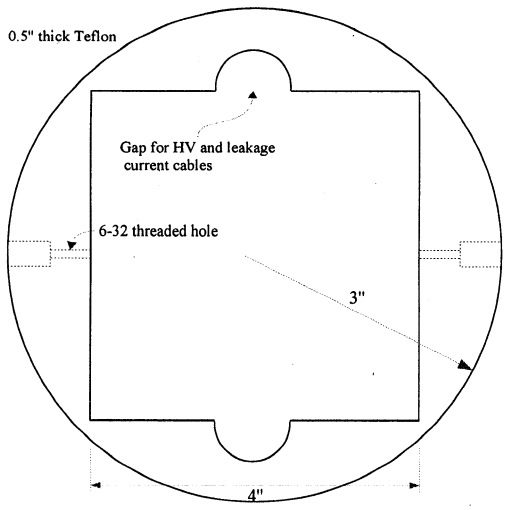

Figure 3.5: Vessel shape-adapter.

A 1/16"×1.5" diameter fused silica flat window covered two 13/32" holes in the entrance face of the vessel through which the laser light entered. The cell acts as a diverging lens in the horizontal direction, so after passing through the cell, the light must be refocused in order to reach the detector area outside the magnetic shields, which was accomplished by a 1.5" diameter, $f = 6$", cylindrical lens mounted on the exit face of the vessel. Both the entrance window and exit lens were mounted with a 2" OD collar held by 8 nylon screws, and the cylindrical lens additionally was sandwiched by 1/8" diameter O-rings (Buna-N) as shown in Figure 3.3.

In order to fit the square vessel into the round magnetic field coil, two removable shape-adapters (see Fig. 3.5) were mounted on the front and back faces of the vessel. The shape-adapters were made from 1/2" Teflon sheet and had two 6-32 tapped holes on the sides through which nylon screws were inserted such that they pressed into the sides of the vessel, which caused the shape-adapter to bulge out slightly. This was used to adjust the fit of the shape-adapter inside the coil such that it was somewhat snug but still able to be moved so that its position could be adjusted within the coil.

3.2.1 High Voltage Feedthroughs

The high voltage cables coming from the power supply terminated into coaxial feedthroughs that could be slid in and out of the vessel to aid in cell access and also to adjust the holding pressure on the cells. The overall design concept of the feedthroughs did not change during the experiment, but several details were changed.

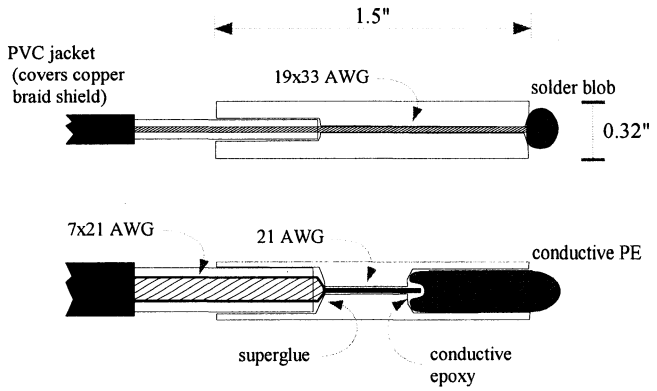

Figure 3.6: High voltage feedthroughs. The top diagram shows the feedthrough design at the beginning of the dataset, the bottom shows the feedthrough design by the end of the dataset.

The original feedthroughs were constructed with Teflon insulation, but this was changed to polyethylene before the start of the actual data set due to concerns about the piezoelectric properties of Teflon [Zoo72]. A study on the piezoelectric effect of polyethylene cable insulators [Gre74] seemed to indicate that polyethylene had a smaller piezoelectric strength, and also that the effect could be reduced by heat-treatment. This led to the replacement of the Teflon feedthroughs with polyethylene feedthroughs that, after machining, were heat annealed at 100 °C for one hour.

At the beginning of the dataset, the HV cables were made from 0.195" diameter coaxial cable[5]. About 0.5" of the inner polyethylene insulation was inserted into the end of the feedthrough, and the inner conductor (20 AWG multistranded 19×33) extended to the other end of the feedthrough through a hole just large enough to accept the wire. A smooth surfaced solder blob on the end of the conductor served to hold the feedthrough onto the cable and also provided the contact between the HV cable and the electrode cup.

The solder blob was later replaced with a 0.8" long, 0.25" diameter rounded pellet of conductive polyethylene inserted into the end of the feedthrough (see the bottom half of Fig. 3.6). This reduced the amount of metal near the vapor cells which could have been a source of magnetic noise (see Sec. 3.2.2). Conductive epoxy[6] on the inside of the feedthrough held the pellet and the cable conductor in place and also provided the electrical connection between them.

The HV cables seemed to fail occasionally, as indicated by very large currents flowing to the cable shield when high voltage was applied (see Sec. 3.3.3). This was thought to be due to failure of

[5]Belden 8262 Coax: MIL-C-17G

[6]CircuitWorks: CW2400, http://www.chemtronics.com

the polyethylene insulation, and replacing the cables with a thicker 0.405" coaxial cable[7] that had a higher maximum operating voltage rating (3700 compared to 1400 V RMS) seemed to reduce the occurrence of cable failure. However, two years later, further use of the cables that had seemed to have failed indicated that dirty surfaces on the polyethylene insulation might have led to the large cable leakage currents.

The polyethylene insulation of the new cable was 0.285" in diameter and the entrance holes in the feedthroughs were enlarged to accept the thicker cable. The new cable conductor was 13 AWG stranded (7×21) so that a single strand of the conductor was nearly the same size as the entire conductor of the thinner cable. Therefore, a single strand of the conductor was threaded through the small hole in the feedthrough to reach the conductive PE pellet. The larger cables did put more strain on the feedthroughs and they had a tendency to occasionally come apart, with either the entire cable and conductor pulling out of the feedthrough, or the conductor breaking where it was reduced from 7 strands to just 1. When this occurred, the entire feedthrough had to be disassembled so that new epoxy could be applied at the pellet and conductor interface to ensure a reliable connection. The durability of the cables was somewhat improved by applying superglue where the polyethylene cable insulation interfaced with the feedthrough.

3.2.2 Vessel Materials

Previous versions of the experiment had mainly used aluminum as the construction material for the cell holding vessel [Jac95, Lam87]. The improved frequency resolution of this measurement has led to sensitivity to magnetic noise generated by thermal currents in highly conductive materials such as metals [Var84, Lam99]. For this reason, the main construction material used in close proximity to the vapor cells has been changed to some form of plastic. Besides the effect of Johnson noise, it was believed that most metals have a higher degree of magnetic contamination than plastics. Some degree of conductivity is still required, though, in order to facilitate the required electric field application. This was achieved in two ways: the surface of nonconductive plastic (Teflon or polyethylene) was coated with an aluminum film deposited by a vacuum evaporator, or a slightly conductive form of plastic was used (carbon filled UHMW polyethylene[8]).

The evaporated aluminum coatings on plastic typically had resistances less than an ohm. The coatings were not very durable, though, and could be scraped away by a hard tool or cell disk edge if care was not taken. If too much of the coating became damaged in a particular area, silver paint was used to cover the damaged area. The conductive plastic exhibited resistances of 10^3–10^6 Ω,

[7] Belden 8237

[8] TIVAR antistatic from Poly Hi Solidur, Fort Wayne, IN 46809, http://polyhisolidur.com/

as measured by a voltmeter across two points on a surface, which was adequate for our purposes. Cleaning conductive plastic pieces in an ultrasonic cleaner was found to sometimes increase the surface resistance, which was probably due to sloughing away of carbon from the polyethylene. We did not encounter enough of a reduction in conductivity to cause us to change our cleaning procedure, but we did try not to unnecessarily subject the conductive plastic pieces to ultrasonic cleaning. The durability of the conductive plastic was certainly much better than the Al coatings, which could not be subjected to any kind of thorough cleaning process without damaging the coating.

The first portion of the data set was performed with a vessel constructed mostly from Al coated Teflon. At one point, an unreliable connection in a HV feedthrough led to occasional large current spikes in the HV cable, presumably due to arcing across the bad connection. After such a spike, spin precession measurements from the Hg vapor cell magnetometer closer to the problematic HV feedthrough always showed a relatively large ($\dot{1}0$ nG), and permanent ($>$ 1 hour), shift in the local magnetic field, and the direction of the shift depended on the polarity of the high voltage when the spark occurred. The second Hg cell typically showed a shift that was smaller than the shift in the other cell by an order of magnitude. This indicated that a ferromagnetic material was being oriented by the strong, but short lived, magnetic field generated by the current spike, leading to a smaller, but very measurable, permanent shift in the magnetic field gradient. If similar spikes occurred each time the electric field was reversed, this would lead to an EDM-like systematic effect.

The large current spikes were eliminated by repairing the feedthrough connection, but it was also desirable to locate the source of the ferromagnetic material. We attempted to simulate the high voltage sparks by discharging a 10 μF capacitor across a small coil (0.33" diameter, 5 turns) placed around the end of the HV feedthrough inside the vessel. The capacitor was charged to between 0 and 10 volts and took about 10 μsec to discharge when connected to the coil. Figure 3.7 shows a roughly quadratic magnetic field shift dependence on the capacitor voltage. We then added or removed materials (Teflon, polyethylene, and quartz) from inside the vessel and compared the size of the resulting magnetic field shifts caused by the artificial sparks. Some of the results of this study are shown in Table 3.1.

The general results were that there was evidence of ferromagnetic contaminants in almost all of the material samples we tested, although the Teflon rod exhibited the strongest effect, and we did not resolve a shift from the conductive polyethylene sample. It is possible that surface contamination or differences in the coil placement had some effect on the results, but the performance of the conductive polyethylene was enough to lead us to start construction of a new vessel and electrode cups made from the conductive polyethylene. Similar artificial spark tests were not performed on the completed conductive polyethylene parts that went into the second vessel, though.

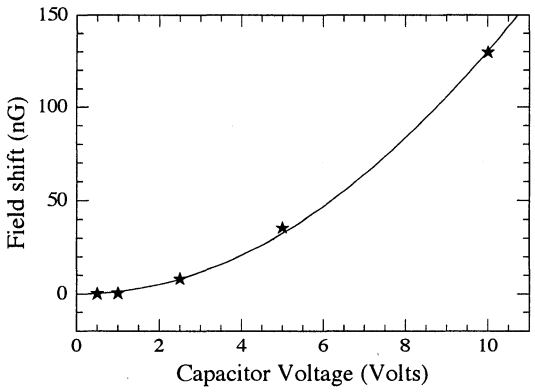

Figure 3.7: Magnetic field shift due to artificial sparks. Voltage dependence of the size of the permanent shift in the magnetic field measured by a Hg vapor cell after an artificial spark is discharged. The solid line shows a fit to $\Delta B = a\mathrm{V}^2$ with $a = 1.30$ nG/volt^2.

Table 3.1: Materials comparison for the magnetic field shift due to artificial sparks. Different materials were placed directly on top of one of the vapor cells, and an artificial spark (at 10 V) was generated, causing a permanent shift in the local magnetic field as measured by the vapor cell. A feedthrough is a 0.3" diam. rod of the material attached to a HV cable with a solder blob as described in Section 3.2.1, and a rod or tube is a bare 0.3" diam. sample of the material. The first entry is the standard configuration used to take EDM data up to this point (Run 38356).

Materials	Field Shift (nG)
PE feedthrough + Teflon electrode cup	105
quartz feedthrough + Teflon electrode cup	42
Teflon electrode	4.2
PE rod	10.5
Teflon rod	840
quartz tube	10.5
conductive PE block (1×1×0.5")	< 0.105
bare cell	< 0.13

3.3 HV Supply and Leakage Current Monitors

The high voltage supply and leakage current measuring electronics were located in a separate room from the main apparatus, about 50 feet away from the magnetic shields housing the EDM vapor cells, thus reducing the possible effects of magnetic fields generated by the HV supply and electronic pickup. Signals between the two rooms were routed through shielded coaxial cables.

3.3.1 HV Supply

High voltage for generating the electric field inside the vapor cells was provided by a relayless, all solid state commercial power supply[9]. The supply output of 0 to $\pm$10 kV (maximum current: 80 μA at 10 kV) was programmable via a 0 to 10 V input and a TTL polarity control input. We housed the 8.5×4.5×1.5" supply inside a larger 18×12×4" homebuilt box that contained a power supply to provide the 24 V DC required by the HV supply, and a feedback circuit that adjusted the control voltage sent to the supply such that the HV output divided by 1000 exactly followed the analog voltage waveform coming from the HV computer DAQ. A layer of mu-metal magnetic shielding was wrapped around the box to further protect against magnetic fields from the HV supply. The high voltage output was stable to about 0.05% at $\pm$10 kV (with the external feedback circuit).

The output of the supply was carried by a single 50 ft cable almost reaching the magnetic shields. Just outside the magnetic shields, the center conductor and shield of the long cable were connected to separate screw terminals inside a $\sim$ 6" square plexiglass enclosure, allowing the connection of two shorter ($\sim$ 5 ft) HV cables that brought the high voltage to the two sides of the cell holding vessel.

3.3.2 Leakage Current Monitors

Electric currents flowing from the HV electrodes across the cell walls were collected by four wires attached to the corners of the groundplane (top and bottom). These wires then exited through tiny holes in the top (bottom) face of the vessel where they merged into a single wire. A separate wire was affixed directly to the top (bottom) of the vessel to collect currents flowing onto the vessel. The groundplane wire and the vessel wire were then brought outside the magnetic shields by way of a two conductor shielded cable. These two cables (one from the top and bottom) then enter a small breakout box with three BNC connectors: two for the top and bottom groundplane currents, and one that merges the two wires connected to the top and bottom faces of the vessel. Three 50 foot long BNC cables then bring the leakage currents back to near the HV supply, where they were converted to a voltage readable by the HV computer DAQ.

---

[9]EMCO High Voltage Corporation: RP100, http://www.emcohighvoltage.com

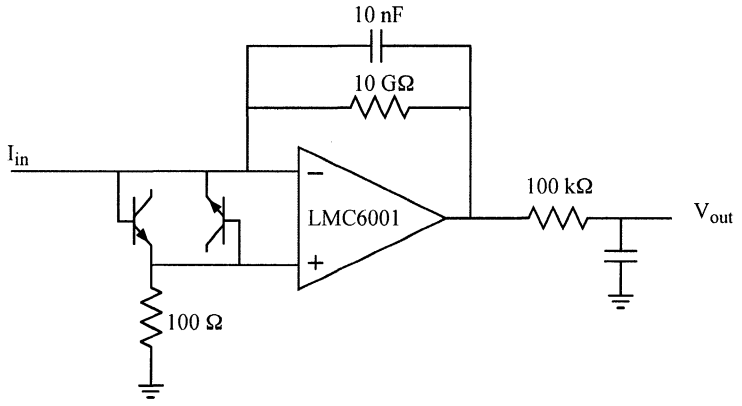

Figure 3.8: Leakage current monitor circuit.

Figure 3.8 shows the simple current to voltage converter circuit used to measure the leakage currents (0.01 V/pA). The circuit uses an electrometer amplifier[10] with an ultra-low input current rating (< 25 fA). The electrometer inputs were guarded from large fluctuations by the "diodes" across the inputs. Transistors were used in place of regular diodes for this purpose since they were found to have larger reverse biased resistance.

3.3.3 Cable Current Monitor

About one meter from the HV supply, a 150 MΩ resistor was in series with the HV cable. This allowed the current output of the HV supply to be monitored by measuring the voltage drop across this resistor. The voltage was displayed on a digital panel meter powered by a nine volt battery, and the meter and resistor were enclosed in a ~ 6" square plexiglass box. The meter was turned on only briefly (avoiding frequent battery replacement) to occasionally check the behavior of the cable current, usually when the vessel was being reinstalled into the magnetic shields. The measured cable current at 10 kV could range between 0.1 and 100 nA, and usually was dominated by the state of the exposed HV cable conductor and shield in the splitter box near the cell holding vessel. For example, higher cable currents would be seen if a strand of the braided cable shield got too close to the exposed HV terminal, or if the surface of the polyethylene cable insulation was dirty.

---

[10]National Semiconductor: LMC6001

3.4 Magnetic Field Generation and Shielding

The magnetic field coil was wound on an 18" long aluminum cylinder with a 6" ID and 1/4" thick walls. In order to generate a uniform field perpendicular to the cylinder axis, current should flow parallel to the cylinder axis such that the current density around the cylinder follows a cosine distribution. We approximate a cosine distribution with 30 discrete loops arranged as shown in Figure 3.3. The pattern is slightly altered by 1" diameter light access holes halfway down the cylinder that several loops have to go around. The wires were epoxied into shallow grooves cut into the outside surface of the cylinder. An identical distribution of wires rotated by 90° and also a solenoidal coil were wound on the cylinder to provide fields in all three directions. The horizontal field coils were generally kept grounded and were only occasionally used to provide a small field offset to tip the main magnetic field a few degrees from vertical (see Sec. 4.4.3). The vertical field coil produced a field of 1.2 mG/mA that was uniform to 0.01% in the volume that the two vapor cells occupied.

An ultra low noise current source based on Figure 2 in Ref. [Cio98] provided the current for the magnetic field coil. The current source used a 4 volt mercury battery as a voltage reference and was stable to 25 parts per billion over a 100 second time scale. The open space in the aluminum enclosure for the current source was filled with styrofoam packing peanuts to reduce the effect of air currents on the thermal stability. Additional thermal shielding was provided by placing the current source box inside a larger styrofoam box filled with more packing peanuts.

External magnetic fields were passively screened with three concentric mu-metal cylinders with diameters of 12, 18, and 24 inches. The shielding factor of the system was about 50,000. There were 2.5" diameter holes in the center of the shield end caps through which the HV cables, leakage current collection wires, and SF_6 gas lines were passed, and there were 1" diameter holes halfway down the shield cylinder for light access. Temperature changes can cause fluctuations in the magnetic domains of the shield material, so to guard against this, the surface of the outer shields was covered with a 1" layer of polyurethane foam and then Owens Corning pink fiber glass insulation was draped over the shields. These particular types of insulation have led to an accumulation of dust and fiber glass shards throughout the apparatus, so in hindsight, more durable insulating materials should have been chosen.

Any time the magnetic shields were significantly perturbed, either by opening and closing the endcaps or by changing the direction of the main magnetic field, the shields were degaussed. This was achieved by running a 60 Hz AC current through a loop that passed through the center of the shields and then back around the outside to create an alternating magnetic field inside the mu-metal

going around the shield axis. The current was increased until the shields audibly vibrated and then the current was slowly and smoothly ramped to zero with two variacs in series.

3.5 Optical Setup

Figure 3.9 gives a general overview of the HG3 optical setup. The laser light used in the experiment is initially generated by a semiconductor MOPA system[11] operating at 1015 nm, which is then converted to 253.7 nm by two stages of frequency doubling using nonlinear crystals. The design of the Hg UV laser system was based on a similar system at 236 nm developed by Warren Nagourney for an indium ion trapping experiment [Nag99]. As is shown in Fig. 3.9, the nonlinear crystals are placed in bow-tie enhancement cavities that increase the amount of light at the fundamental frequency interacting with the crystal by about a factor of 100. The mirror just after the crystal is picked to transmit the SHG light, but be highly reflective at the fundamental frequency. One of the cavity mirrors is mounted on a piezo stack that allows the length of the cavity to be electronically locked to an integer number of wavelengths. The polarization dependent Hänsch-Couillaud locking scheme [Hän80] was used based on the implementation described in the theses of Eric Burt [Bur95] and Jon Sandberg [San93]. The first cavity used a 3×3×8 mm $KNbO_3$ crystal that was bought "off the shelf" for SHG at 1064 nm and the polarization sensitivity required by the Hänsch-Couillaud scheme was provided by a tilted window in the cavity. The second cavity used a 3×3×7 mm Brewster-cut BBO crystal custom ordered for 254 nm, in which case the Brewster-cut crystal provides the polarization sensitivity. We normally operated the MOPA at about two-thirds of its maximum output of 500 mW, which generally resulted in about 30 mW of green light after the first doubling stage, and about 1 mW of UV light after the second stage.

The laser and frequency quadrupling optics were enclosed in an acrylic box meant to keep room dust away from the optics. A dust ionizer air purifier[12] was kept inside the enclosure to further reduce dust, but the mirrors of the second doubling cavity still required a daily cleaning to maintain efficient SHG. It was also found that, after several years of operation, the air purifier had led to significant oxidation on some of the optical mounts. In addition to the acrylic enclosure, a four inch thick styrofoam box was built around the laser to help reduce acoustic perturbations to the doubling cavities that might cause the locking to fail momentarily.

After exiting the second doubling cavity, a small amount of light was picked off by a fused silica window and sent to a photodiode detector. This signal was used to normalize the detected signals

[11] SDL TC40-D

[12] Sharper Image: SI626, Ionic Breeze Mini Air Purifier.

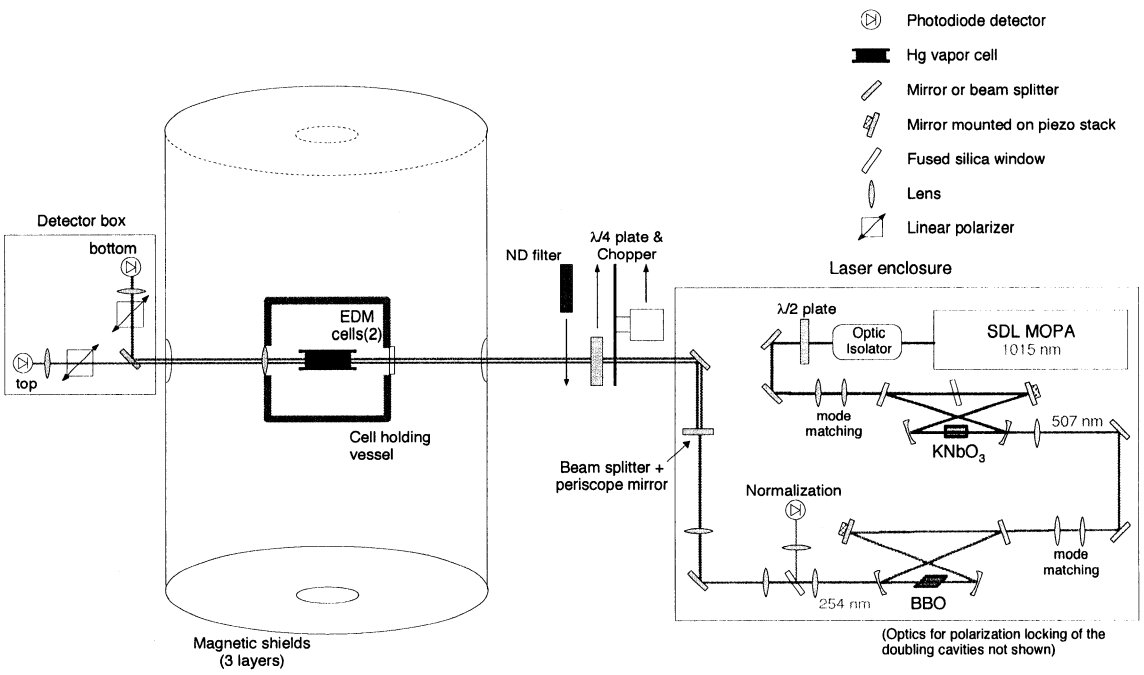

Figure 3.9: Top view of the optical setup for HG3.

after the vapor cells, and it was also used to generate a feedback signal that adjusted the MOPA tapered amplifier current to keep the intensity of the frequency quadrupled output constant. Three cylindrical lenses were used to adjust the beam profile such that it gave about a 0.5 cm^2 spot size when it reached the vapor cells. Just before leaving the laser enclosure, a beam splitter and periscope mirror created a second light beam for the top cell.

In between the laser enclosure and the magnetic shields, two pneumatically controlled actuators administered the pump and probe configurations. One arm held a 10% transmitting neutral density filter that was moved into the beam during the probe phase, and the other arm held a quarter wave plate and optical chopper wheel that were moved into the beam during the pump phase. The chopper wheel had two 45° openings and the chopper frequency was kept constant by a New Focus controller interacting with a 500 slot optical encoder[13] mounted on the back of the DC motor shaft. In order to guard against vibrations affecting the laser, the pneumatic actuators were mounted on an aluminum beam suspended over the main aluminum slab that the laser and magnetic shields sat on.

[13]Encoder: Hewlett Packard HEDS-5540-A02. Controller: New Focus 3501.

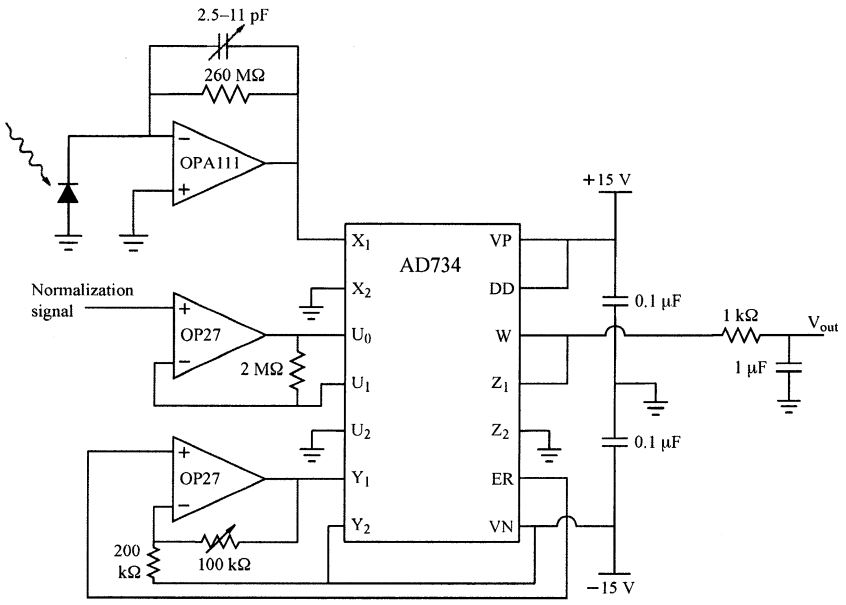

Figure 3.10: Photodiode amplifier and analog divider circuit. The photodiodes are connected to the amplifier by a ~10 ft triaxial cable (Keithley SC-22). The normalization signal is the output of an identical OPA111 photodiode amplifier stage. The divider circuit is based on Fig. 12 from the AD734 data sheet, which gives an output voltage of $W = 10\ \mathrm{V}\,(X_1 - X_2)/(U_1 - U_2)$.

After passing through the cell holding vessel, the light beams travel through a one inch diameter, divided light pipe into the detector region. The top beam went straight into its analyzing linear polarizer[14], and then was focused onto a photodiode detector[15]. The bottom beam was perpendicularly deflected by an additional mirror into its polarizer and photodiode. The photodiode signals were converted into voltages and divided by the intensity normalization signal by the circuit in Figure 3.10. Although not shown in Figure 3.9, the rejected light from the top beam analyzing polarizer was sent onto a four-quadrant segmented photodiode to look for HV correlated beam steering.

3.6 Data Acquisition

The experiment was controlled and digitally recorded by two computer systems using National Instruments (NI) DAQ hardware and software (Labwindows/CVI). The NI DAQ cards allowed the recording of analog signals, output of analog waveforms, and digital input/output. Labwindows

[14]α-BBO glan-laser polarizer from CASIX: http://www.casix.com

[15]UDT sensors: UV-005, http://www.udt.com

provides a C programming environment for setting up communication with the DAQ hardware, and building a graphical user interface for the program. The main control computer (CPT) switched the apparatus between pump and probe settings and recorded the spin precession signals and other local environmental data. A second computer (EMIT), located beside the HV power supply, controlled and recorded the HV setting, and recorded the leakage currents. Effort was made to keep the two computer systems as electrically isolated from each other as possible, in order to avoid HV-generated crosstalk or pickup contamination of the spin precession signals. All signals that were directly correlated with the HV were recorded by EMIT, and CPT was meant to have no knowledge of the actual HV status.

3.6.1 Main EDM Computer

CPT used a NI AT-MIO-16XE-50 card which was capable of 20 kS/sec sampling of analog signals at 16 bit resolution. Signals were routed through shielded BNC cables to a breakout box that interfaced with a screw terminal connector block (NI CB-68LP). Analog input channels were low pass filtered at 100 Hz between the BNC cable and the connector block. A 68 conductor shielded 2 meter cable joined the connector block to the DAQ card (NI SH68-68EP).

15 out of the 16 available analog input channels on the board were used, as outlined in Table 3.2, and all signals were sampled at 200 Hz. The two photodiode signals were monitored differentially (taking up 2 AI channels each), and saved in a binary file (suffix: .bin) at the end of each scan (one pump/probe cycle). The remaining analog inputs were single-ended configured, and were software downsampled to 2 Hz by averaging 100 data point sections of the 200 Hz waveform. These signals were recorded in a text file (monitor data file, suffix: .mon) at the end of each scan.

One of the two available 12 bit analog outputs ($\pm$10 V range, 5 mV resolution) was used to switch the laser between the pump and probe wavelength settings. In order to account for hysteresis in the piezo setting, the output waveform was set up to sweep past, and then return to, the new setpoint as shown in Figure 3.11.

Eight digital channels were available on the board, configurable as inputs or outputs. Four channels were used to open and close valves that controlled the pneumatic actuators that switched between pump and probe modes. A digital output was used to automatically open a valve that refreshed the SF_6 during the pump phase on a fixed scan number interval, typically between 50 and 150 scans. One digital output was turned on for one second at the beginning of each scan, which provided the signal to the HV computer to ramp the HV to a new value.

Table 3.2: Analog input connections on CPT.

Channels used	Description
4	Top and bottom photodiode signals (differential)
3	External flux gate magnetometer: B_x, B_y, B_z (1 V/mG)
2	Doubling cavity piezo voltages
1	Normalization photodiode laser power
1	Laser current (1 V/A)
1	Temperature monitored by a thermistor outside the mag. shields
3	4-quadrant detector: horizontal diff., vertical diff., summation

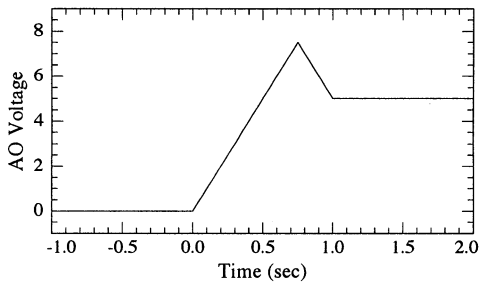

Figure 3.11: Analog output waveform used to control laser frequency. The analog output zero-point was usually set to correspond to the $F = 1/2$ resonance (the pump phase wavelength), and then the laser frequency was detuned off resonance by 4–6 volts (4.6 GHz/V) during the probe phase.

3.6.2 HV Control Computer

EMIT used a NI AT-MIO-16L-9 card which is no longer supported by National Instruments. Generally, it has the same number of analog and digital channels as the board used in CPT, but with a lower (12 bit) analog input resolution. Signals were routed to the DAQ card in a similar fashion to the CPT system, except the connector block to computer connection was made with an unshielded ribbon cable, and the connector had 50 pins instead of 68.

The analog inputs were differential configured, giving 8 channels, 7 of which were sampled at about 20 Hz. One channel monitored the HV value (1V/kV), and the three leakage current signals (top cell, bottom cell, and vessel, 0.01 V/pA) were mirrored on two input channels: a higher gain channel ($\pm$0.1 V input range), and a lower gain channel ($\pm$5 V input range). The acquisition software would record the higher gain leakage data, unless the output went out of range, in which case the lower gain channel was recorded. At the end of each scan, the three leakage currents and the HV monitor signal were saved to a text file (suffix: .dat).

In order to control the HV power supply, a digital output signal was used to set the HV polarity (on = +, off = $-$), and the HV magnitude was set by an analog output waveform (1V $\rightarrow$ 1kV). For the most common operation mode of switching the HV between $\pm$10 kV, the analog output was set to ramp the voltage from 10 to 0 linearly in 2.5–10 seconds, the polarity control would be toggled, and then the voltage would be ramped linearly back up to 10 V.

The HV control program used one digital input to watch for the digital signal from CPT, routed through an optoisolator[16], which indicated that EMIT should start a new HV ramp and start recording the leakage currents. Once EMIT finished ramping the HV, it would start monitoring the digital line from CPT again for the indication to start a new scan. EMIT's scans were set up to be several seconds longer than CPT's, and as soon as EMIT received the digital signal it would stop the current scan and begin a new one. If EMIT did not encounter a switch signal by the end of its scan, it would stop and wait until one occurred. To guard against periodic fluctuations, EMIT was programmed to occasionally not ramp the HV to a new value at the beginning of its scan. This was usually set up to occur on average every 25 scans, based on a random number generator.

---

[16] Agilent Technologies, HCPL-2231

Chapter 4

DATA COLLECTION/ANALYSIS FOR THE TWO CELL MEASUREMENT

This chapter describes the dataset for HG3, a two vapor cell, laser based measurement of the ^{199}Hg EDM. While much of the development of the apparatus occurred between 1997 and 2000, all of the data that went into the [Rom01a] result was taken between January 28 and August 31 of 2000. A few more data runs were taken for systematic checks between August and November, and data analysis was completed by the end of November, 2000.

4.1 Data Taking Procedure

4.1.1 Apparatus Preparation

While Chapter 3 described the details of the individual parts of the experiment, this section gives the general procedure followed to bring all the parts together into an EDM data taking machine.

Once the vessel was installed inside the magnetic shields, the experiment required only minor adjustments on a daily basis. The main setup work occurred when the vessel had to be removed and opened, almost always due to a need for the vapor cells to be remelted, in order to rejuvenate their spin lifetimes. Once two cells had their wax wall-coatings properly remelted, their outer cell walls would be carefully scrubbed with cotton tipped applicators soaked in solvents. The cells were scrubbed three times, first with trichloroethylene, then with acetone, and finally with methanol.

In order to install the cells in the vessel, the HV feedthroughs needed to be pulled out enough so that the cell could be maneuvered into place between the groundplane indentation and the electrode cup. Pulling the feedthroughs in and out resulted in them passing through a greasy O-ring, so care was taken to move the feedthrough out only as much as was minimally required, since dirty HV feedthroughs could lead to large leakage currents flowing onto the vessel. Occasionally the feedthrough surfaces inside of the vessel were cleaned by wrapping a rolled up, solvent soaked chemwipe around a feedthrough and "flossing" around it. The bottom electrode cup was installed first, so that it sat on top of the tip of the feedthrough, and then a cell would be placed on top of the electrode cup. The feedthrough would then be carefully pushed up to hold the cell against the

groundplane so that the vessel could be inverted. Once inverted, the cell position in the groundplane was adjusted and the feedthrough would be fixed in place by tightening the screws on the collar pressing down on the O-ring. The other cell was installed with the same procedure, and then the front face of the vessel was closed and the shape adapters were attached to the front and back vessel faces.

Before installing the vessel inside the magnetic field coil, the alignment of the two laser beams through the shields was checked on two alignment jigs, one before the shields, and one after the shields in the detector area. Then the vessel was slid into the coil while monitoring the two photodiode signals. The axial position of the vessel along the coil was adjusted such that the photodiode signals were maximized, and then the orientation was checked with a bubble level against the top or bottom edge of the vessel front face. After rechecking the laser alignment after the vessel, the three magnetic shield front endcaps were closed (the back endcaps could also be removed, but this was never done in normal operation), with the HV cables, leakage current collection wires, SF_6 gas lines, and degaussing wires threaded through the center holes. These cables and wires were strapped to an aluminum bar outside the shields, which was meant to keep them from resting on the magnetic shield endcaps. The shields were then degaussed, and allowed to settle for at least an hour before data taking began.

The alignment of the laser beams in the detector area was then rechecked to make sure that the position of the vessel had not shifted significantly during the process of closing the magnetic shields. Also, the angles of the analyzing linear polarizers usually had to be adjusted to optimize the photodiode signals. First the polarizers were rotated to the maximum extinction point, which typically gave a residual signal between 0.05 and 0.5 Volts. The DAQ analog inputs had a unipolar range of 0 to 10 V, so the polarizers were rotated such that the unmodulated signal was in the middle of this range at 5 V, which typically was given by an angle of $\alpha \approx 20°$. Because it was more convenient for directing the rejected light beam onto the four-quadrant detector, the analyzing polarizer for the top beam was always rotated clockwise (looking in the light propagation direction) away from the extinction point. Usually the bottom beam polarizer was rotated in the corresponding direction such that the top and bottom signals started out in phase after optical pumping, although since the transverse pumping chopper wheel intersected the top beam first, the phase of the top signal was initially always a few tenths of a radian ahead of the bottom signal.

The magnetic field environment inside the shields was always slightly different after opening and closing the shields, which required rematching of the transverse pumping chopper frequency to the new Larmor frequencies. The chopper frequency could only be adjusted in discrete steps of about

40 mHz, so instead of adjusting the chopper, the current for the magnetic field coil was tuned so that the Larmor frequency matched the chopper. This was done by observing the light transmission through the cells during the optical pumping phase. If the chopper and Larmor frequencies were properly matched, then the spin precession and light modulation would be perfectly in phase, and the transmission would be symmetrically peaked at the center of the period when the light was unblocked, because the atoms absorb the least light when the spins are along the light direction. Mismatched frequencies lead to a phase difference that causes the transmission peak to be ahead or behind the center of the light-on period.

The adjustments described above were only performed when the vessel had to be removed from the shields, which occurred every 2–3 weeks. On a daily basis, the laser usually needed adjustment to maintain the output efficiency of the doubling cavities. This normally only required a quick cleaning of the second doubling cavity mirrors, and an adjustment of the beam steering into this cavity. No active stabilization of the laser wavelength was performed, and the laser frequency would typically drift by a few hundred megahertz in 24 hours. Due to the 4.5 GHz wide pressure broadened transitions, this would lead to only a small loss in optical pumping efficiency. Before starting a data run, the laser wavelength was retuned to the center of the $F = 1/2$ resonance by minimizing the transverse pumping light transmission while the atoms were still mostly unpolarized.

4.1.2 Data Runs

The main units of data collection were "scans" and "runs." A "scan" consists of an individual pump/probe cycle resulting in a measurement of the difference in spin precession frequencies between the two cells. The timing sequence of the HV and laser parameters during two consecutive scans is shown in Figure 4.1. The total duration of a scan was typically 133 seconds, with a 30 second pump phase, 100 second probe phase, and 3 seconds to allow for switching between the two configurations. At the start of the pump phase, the HV was ramped to its new value. HV ramp times of 5, 10, 15, or 20 seconds were used, and the HV was typically alternated between ± 10 kV. Occasionally, a HV sequence of $(+10, 0, -10, 0, +10, 0, \ldots)$ was used, and the ± 10 kV scans were compared with the zero electric field scans to look for signals dependent on $|\boldsymbol{E}|$.

All scans taken with the data acquisition program were numbered sequentially, and for each scan number three data files were saved: the photodiode signals (.bin), the lower scan rate environmental conditions (.mon), and the HV data file (.dat). The initial data analysis results in the creation of three additional files (see Sec. 4.2) for each scan number. In 24 hours, 650 scans of 133 sec. duration could be taken, which would result in 560 MB of data.

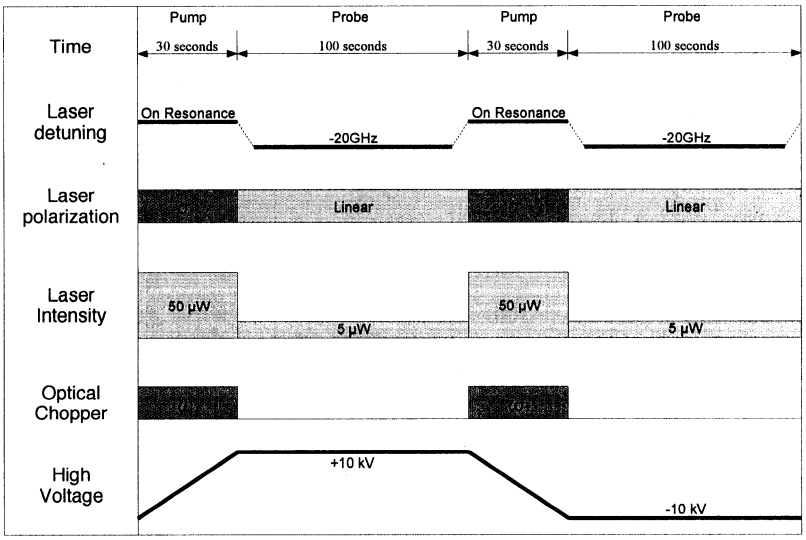

Figure 4.1: Measurement sequence for two consecutive pump/probe cycles.

A "run" is a collection of consecutive scans taken with a particular set of experimental parameters and is designated by the initial scan number. The average run duration was 17 hours, but ranged from as short as 2 hours, to as long as 38 hours. The main limitation on the length of data runs was usually the laser, whose performance typically started to degrade after $\sim$ 15–20 hours, at which point the run would have to be stopped to make adjustments to the laser.

A summary of the experimental parameters for all the runs in the HG3 data set is given in Table 4.1. The table column headings are as follows: RUN is the number of the first scan; L is the length of the run in scans; C is the type of HV sequence used (D $= + - +-$, Q $= +0 - 0+$); B gives the direction of the magnetic field ('+' corresponds to down, '$-$' is up); Ch describes the order in which the two photodiode signals connected into the DAQ system (for '+,' the top cell signal is channel 1 and the bottom signal is channel 2, for '$-$' the top signal is on channel 2 and the bottom is on channel 1); t_{pump} and t_{probe} give the pump and probe time lengths in seconds; det. is the probe laser detuning relative to the $F = 1/2$ resonance given in units of the DAQ analog output voltage (4.6 GHz/Volt); HV is the high voltage setting in kV; t_{HVS} is the High Voltage Switch time (the time it takes for the supply to ramp from +HV to $-$HV); cells gives the vapor cells used in the run (the first number is the cell in the top position, and the second is the bottom); misc indicates miscellaneous nonstandard conditions applied in some runs as defined in Table 4.2.

Table 4.1: HG3 data run summary.

RUN	L	C	B	Ch	t_{pump}	t_{probe}	det.	HV	t_{HVS}	cells	misc
21011	267	D	+	+	30	108	−5.5	10.0	20	25,24	
21283	1022	D	+	+	30	100	−5.5	10.0	20	25,24	
22308	152	D	+	+	30	100	−5.5	10.0	10	25,26	FS
22478	68	D	+	+	30	100	−5.5	10.0	20	25,26	
22547	169	D	+	+	30	100	−5.5	10.0	10	25,26	
22717	225	D	+	+	30	100	−5.5	10.0	5	25,26	
22943	126	D	+	+	30	100	−5.5	10.0	12	25,26	
23085	105	D	+	+	30	100	−5.5	10.0	11	25,26	
23191	502	D	+	+	30	100	−5.5	10.0	9	25,26	
23697	313	D	+	+	30	100	−5.5	10.0	10	25,26	
24016	549	Q	+	+	30	100	−5.5	10.0	10	25,26	
24583	364	D	+	+	30	100	−6	10.0	15	23,26	
24952	404	D	+	+	30	100	−5.5	10.0	15	23,26	
25357	599	Q	+	+	30	100	−5.5	10.0	15	23,26	
25958	660	D	+	+	30	100	−6	10.0	15	23,26	
26621	577	D	+	+	30	100	+9.5	10.0	15	23,26	
27199	368	D	+	+	30	100	+9.5	10.0	15	23,26	
27622	734	Q	+	+	30	100	+9.5	10.0	15	23,26	
28357	414	D	+	+	30	100	+9.5	10.0	5	23,26	
28773	420	D	+	+	30	100	+9.5	10.0	5	23,26	
29195	138	D	+	+	30	100	+9.5	10.0	5	23,26	
29335	421	D	+	+	30	100	−10	10.0	5	23,26	NOF
29757	184	D	+	+	30	100	−4	10.0	5	23,26	H
29942	246	D	+	+	30	100	−4	10.0	5	23,26	H
30191	217	D	+	+	30	100	−4	10.0	5	23,26	XA
30471	863	D	+	+	30	100	−4	10.0	5	23,26	XA
31342	570	D	−	+	30	100	−7	10.0	5	23,26	
31913	525	D	−	+	30	100	−4.5	10.0	5	23,26	XA
32441	470	D	−	+	20	60	−4.5	10.0	5	23,26	

Table 4.1 continued.

RUN	L	C	B	Ch	t_{pump}	t_{probe}	det.	HV	t_{HVS}	cells	misc
32913	221	D	−	+	20	60	−4.5	10.0	5	23,26	OB
33483	463	D	−	+	30	100	−5	7.0	10	24,25	
34158	295	D	+	+	30	100	−5	7.0	20	24,25	
34455	209	D	+	+	30	100	−5	7.0	20	24,25	
34665	624	D	−	+	30	100	−5	7.0	20	24,25	
35304	588	D	−	+	30	100	−5	7.0	20	24,25	
35893	53	D	−	+	30	100	−5	10.0	20	26,23	
35990	810	D	−	+	30	100	−5	10.0	20	26,23	
36803	761	D	−	+	30	100	−5	10.0	20	26,23	
37565	349	D	−	−	30	100	−5	10.0	20	26,23	
37917	438	D	+	−	30	100	−5	10.0	20	26,23	
38356	408	Q	+	−	30	100	−4.5	10.0	20	26,23	
40938	300	D	−	−	30	100	−5	10.0	10	25,26	HVT
41239	124	D	−	+	30	100	−5	10.0	10	25,26	HVT
41364	164	D	−	+	30	100	−4.5	10.0	10	25,26	HVT
41529	313	D	−	+	30	100	−4.5	10.0	10	25,26	HVT
41843	544	D	−	+	20	60	−4.5	10.0	5	25,26	HVT
42388	466	Q	−	+	20	60	−4.5	10.0	5	25,26	HVT
42890	525	Q	−	+	20	60	−4.5	10.0	5	25,26	HVT
43416	297	D	−	+	30	100	−5	10.0	10	23,24	
43715	586	D	−	+	30	100	−5	10.0	10	23,24	
44303	640	D	−	+	30	100	−5	10.0	10	23,24	
45006	368	Q	−	+	30	100	−5	10.0	5	23,24	
45376	236	Q	−	+	30	100	−5	10.0	5	23,24	
46607	586	Q	−	+	30	100	−4.5	10.0	20	23,24	
47251	709	Q	−	+	20	60	−4.5	10.0	10	23,24	
47961	735	D	−	+	20	60	−4.5	10.0	10	23,24	
48705	999	D	−	+	20	42	−4.5	10.0	10	23,24	
49705	917	D	−	+	20	60	−4	10.0	10	23,24	

Table 4.1 continued.

RUN	L	C	B	Ch	t_{pump}	t_{probe}	det.	HV	t_{HVS}	cells	misc
50623	703	D	−	+	30	70	−4	10.0	10	23,24	
51332	620	D	−	+	30	70	+8.5	10.0	15	23,24	
51953	511	D	−	+	30	70	+8.5	10.0	15	23,24	
52468	235	D	+	+	30	100	+8.5	8.0	10	26,25	
52704	495	D	+	+	30	70	+8.0	10.0	10	26,25	
53203	575	Q	+	−	30	100	+8.0	10.0	5	26,24	HVT
53779	213	Q	+	−	20	60	+8.0	10.0	5	26,24	HVT
53996	382	Q	+	−	30	100	−4.5	10.0	5	26,24	HVT
54379	802	Q	+	−	30	70	−4.5	10.0	10	26,24	HVT
55182	434	D	+	−	30	100	−5	10.0	10	23,26	
55617	503	D	−	−	30	100	−5	10.0	15	23,26	OB
56121	444	D	−	−	30	100	−5	10.0	10	23,26	OB
56569	510	Q	−	−	30	100	−5	10.0	10	23,26	OB
57080	540	D	−	−	30	100	−4.5	10.0	10	23,26	OB
57621	524	D	−	−	30	100	−4.5	10.0	10	23,26	OB
58199	535	Q	−	−	30	100	−4.5	10.0	10	23,26	OB;HVB
58735	978	D	−	−	30	70	−4.5	10.0	15	23,26	
59717	876	D	−	+	30	100	−5	10.0	10	24,23	
60594	388	D	−	+	30	100	−5	10.0	8	24,23	
60983	212	D	−	+	30	100	−5	10.0	5	24,23	
61196	454	D	−	+	30	100	−5	10.0	10	24,23	
61651	706	D	−	+	30	100	−5	10.0	7	24,23	
62358	333	Q	−	+	30	100	−5	10.0	10	24,23	HVT
62692	678	Q	−	+	30	100	−5	10.0	15	24,23	HVT
63372	213	D	−	+	30	100	−5	10.0	15	24,23	
63586	999	D	−	+	30	100	−5	10.0	15	24,23	
64594	532	D	−	+	30	100	−5	10.0	10	24,23	MS
65127	574	D	−	+	30	100	−5	10.0	10	24,23	HVB;MS
65702	500	Q	+	+	30	100	−4.5	10.0	10	24,23	HVB

Table 4.1 continued.

RUN	L	C	B	Ch	t_{pump}	t_{probe}	det.	HV	t_{HVS}	cells	misc
66208	523	Q	+	+	30	100	−4.5	10.0	15	24,23	HVB
66733	172	D	+	+	30	70	−4.5	10.0	20	24,23	
66906	552	D	+	−	30	100	−4.5	10.0	10	24,23	
67459	631	D	+	−	30	70	−4.5	10.0	10	24,23	
68091	264	D	+	−	30	70	−4.5	10.0	10	24,23	
68469	398	D	+	−	30	100	−5	10.0	10	23,24	HVB;FS
68869	56	D	+	−	30	100	−5	5.0	10	24,26	HVB;FS
68926	81	D	+	−	30	100	−5	1.0	10	24,26	HVB
69008	51	D	+	−	30	100	−5	10.0	10	24,26	HVB;MS
69060	44	D	+	−	30	100	−5	10.0	10	24,26	HVB;FS
69105	163	Q	+	−	30	100	−5	10.0	10	24,26	HVB
69271	70	D	−	−	30	100	−5	10.0	10	24,26	HVB;FS
69342	526	D	+	−	30	100	−5	10.0	10	24,26	HVT
69869	964	D	−	−	30	100	−5	10.0	10	24,26	
70834	819	D	−	−	30	100	−5	10.0	10	24,26	
71654	920	D	−	−	30	100	−4.5	10.0	20	24,26	
72576	937	Q	−	−	30	100	−4.5	10.0	10	24,26	HVT
73514	977	Q	−	−	30	100	−4.5	10.0	20	24,26	HVB
74492	901	D	+	−	30	70	−4.5	10.0	20	24,26	
75394	844	D	+	+	30	70	−4.5	10.0	5	24,26	
76239	521	D	+	+	30	70	−4.5	10.0	5	24,26	
76761	580	D	+	+	30	70	−4.5	10.0	15	24,26	
77352	680	D	+	+	30	100	−5	10.0	20	26,23	
78048	490	D	+	+	30	100	−5	10.0	5	26,23	
78539	428	D	+	+	30	100	−5	0.0	10	26,23	
78968	606	D	+	+	30	100	−5	10.0	15	26,23	
79575	518	D	+	+	30	100	−4.5	10.0	15	26,23	
80098	352	D	+	+	30	100	−5	10.0	10	26,23	OB
80451	235	D	+	+	30	100	−5	10.0	5	26,23	OB

Table 4.1 continued.

RUN	L	C	B	Ch	t_{pump}	t_{probe}	det.	HV	t_{HVS}	cells	misc
80688	367	D	+	+	30	100	−4.5	10.0	10	26,23	OB
81058	527	D	+	+	30	100	−4.5	10.0	10	26,23	OB
81666	443	D	+	+	30	100	−4.5	10.0	10	26,23	OB
82112	712	D	+	+	30	70	−4.5	10.0	10	26,23	OB
82895	637	D	+	+	30	100	−4.5	10.0	15	26,23	OB
83533	581	D	+	+	30	100	−4.5	10.0	5	26,23	OB
84115	573	D	−	+	30	100	−4.5	10.0	20	26,23	OB
84689	708	D	−	+	30	100	−4.5	10.0	5	26,23	OB
85398	432	D	−	+	30	100	−4.5	10.0	10	26,23	OB
85834	560	D	−	+	30	100	−4.5	10.0	15	26,23	OB

Table 4.2: Code descriptions for "misc" parameters used in Table 4.1.

Code	Description
FS	A frequency parameter showed an anomalously large HV correlation
H	Probe light had horizontal polarization (normally is vertical)
HVB	HV connected to bottom cell only, top was grounded
HVT	HV connected to top cell only, bottom was grounded
MS	HV ramped midway through the probe phase
NOF	No ND filter used in probe beam (increases light intensity by 10×)
OB	Horizontal offset magnetic field applied (tips $\boldsymbol{B}$ by 5° from vertical)
XA	Extra attenuation in probe beam (33% of normal)

Important apparatus changes discussed in Chapter 3 that occurred during the dataset corresponded to the following run numbers: the magnetization effect of artificially generated sparks (Sec. 3.2.2) was studied from scan 38765–40935. Vapor cell number 25 died (broke and became unusable) at Run 53203. The Teflon vessel was replaced with the conductive PE vessel at Run 59717. The solder blob contact at the end of the HV feedthroughs (Sec. 3.2.1) was changed to a conductive PE pellet at Run 68537, and shortly after that the thinner HV cables were replaced with thicker cables at Run 69869.

4.1.3 Parameter Reversals

An ideal experimental program would include a regular schedule of frequent reversals of conditions in order to reveal possible sources of systematic effects, and evenly apply all possible combinations of parameters. This was eventually the case in the HG2 data-taking procedure [Jac95], but was never satisfactorily implemented in HG3. It was not until Run 31342, over a month into the dataset, that the magnetic field direction was switched, and the Channel direction was first switched several weeks later in Run 37565. After this point, some effort was made to make sure that parameters were changed more regularly, and by the end of HG3, there was a fairly equal application of conditions. However, a large amount of exclusive 'OB' data had to be taken at the end of the dataset (Runs 80098–85834) in order to gain decent statistics on data of this type (see Sec. 4.4.3). It is planned that in future EDM data (HG4), the data taking procedure will follow a more premeditated reversal schedule (see Sec. 7.2.2).

Of the parameters changed throughout the dataset, the magnetic field direction (B) and data acquisition channel direction (Ch) have a direct effect on the sign of a measured EDM signal relative to the raw frequency difference ($\omega_1 - \omega_2$). The HV value affects the magnitude of an EDM inversely relative to the frequency difference, and applying HV to one side (HVT or HVB) gives the same EDM sensitivity as applying half of the HV magnitude to both cells. Runs taken with HV$<$ 10 kV or with HV applied only to one cell were not generally performed as a planned parameter change, but were more often used as an occasional stopgap measure when the vessel or vapor cells were not holding high voltage well enough to apply the full field strength. HVT and HVB runs often were associated with the "Quadrupole" HV sequence $(+, 0, -, 0)$, because the frequency difference between the two cells is not sensitive to $|\boldsymbol{E}|$ dependent effects if both cells are subject to an equal $|\boldsymbol{E}|$ strength.

The probe light detuning was usually set between 18 and 28 GHz to the red of the $F = 1/2$ transition (-4 to -6 Volts). A small number of runs were taken with the probe detuning on the

other side of the transition at 15 to 22 GHz to the blue of the $F = 3/2$ line (+8 to +9.5 Volts). These two regions have similar optical rotation strengths (see Fig. 2.9), but the blue detuning has slightly higher absorption due to the proximity of the stronger $F = 3/2$ line (see Fig. 2.3).

Varying the t_{HVS} setting effectively changes the size of the charging currents that flow while the HV is being ramped. Setting the HVS time was simply a matter of changing one control on the HV acquisition program, which led it to be the most frequently changed parameter.

The other miscellaneous conditions in Table 4.2, besides OB, HVT, and HVB, were applied only in a few evaluation runs and were not applied as regular reversals. In principal, the initial probe light polarization direction could have been periodically changed which might lead to different sensitivity to light shift type effects, but changing the polarization direction requires the addition of a half-waveplate after the laser. The waveplate used in Runs 29757 and 29942 was of somewhat low quality, and seemed to add some circularity to the probe beam in addition to attenuating it somewhat, which led to its not being used again in a data run. At around the same time, several runs were taken with substantially larger (NOF) and smaller (XA) probe beam intensities, but it did not seem useful to pursue this any further. Three runs (64594, 65127, 69008) were taken where the HV was ramped with $t_{HVS} = 10$ halfway through the 100 second probe phase in every scan, instead of at the start of the pump phase, giving a 10 second surge current several thousand times larger than the typical steady state currents. No resolved frequency shit was seen in these MS runs, though, which indicated that the current paths for the charging currents had been well symmetrized.

4.2 Data Analysis

Initial data analysis was carried out by two computer programs written in the same Labwindows CVI environment that the data acquisition programs used. The first analysis program (Sec. 4.2.1) ran on the main acquisition computer, CPT, and its purpose was to read in the photodiode signal data files saved after every scan and process them to extract the spin precession frequency for each cell by fitting an exponentially decaying sine function to the precession signal.

The second analysis program (Sec. 4.2.2) ran on a separate computer from CPT and EMIT. It collected the fit results and monitor data from CPT, and the HV data files from EMIT, over the local ethernet network, and calculated the degree to which any of the fit results and monitored signals correlated with the HV polarity over the course of a run, which, in the case of the spin precession frequency difference, gives the EDM signal.

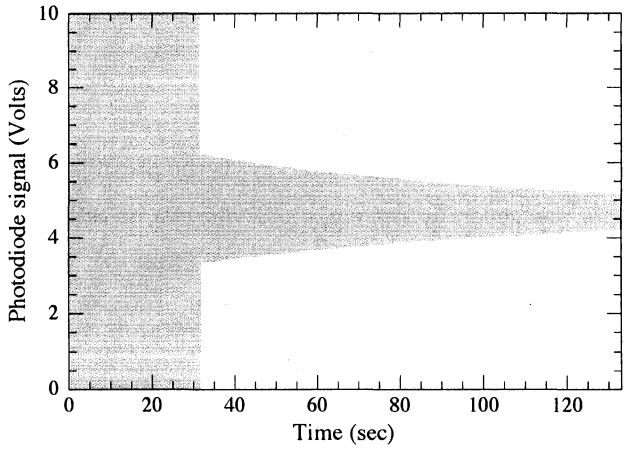

Figure 4.2: Photodiode signal from the top cell for Scan 44023. The total scan time is 133 seconds. During the pump phase the photodiode signal saturates. The configuration switches from pump to probe between 30 and 33 seconds into the scan.

4.2.1 Fitting Procedure

A typical photodiode signal for a single scan as saved by the acquisition program and then read in by the fitting program is shown in Figure 4.2. The initial 33 seconds of the scan is discarded, which is during optical pumping and the switchover from pump to probe configuration. A few runs had $t_{pump} = 20$ sec, in which case the first 23 seconds were discarded. The spin precession signal is extracted from the photodiode intensity with a linearization procedure based on Equations 2.5 and 2.6 from Section 2.4.1. Next, a digital filter is applied with a cutoff at 1.5 times the precession frequency to remove higher order harmonics in the signal, and a low frequency ($f < 1$ Hz) background is subtracted off. Finally, the filtered signal is fit to an exponentially decaying sine wave and the fit information is saved to file.

Linearization procedure

Solving Equation 2.6 for the optical rotation signal $\varphi(t)$ in terms of the photodiode signal gives

$$\varphi(t) = \arcsin\left(\sqrt{I(t)/I_0}\right) - \alpha, \tag{4.1}$$

where, for non-rotated light ($\varphi = 0$), I_0 is the light intensity incident on the linear polarizer, and α is the polarizer angle that completely extinguishes the incident linearly polarized light. In practice, the extinction by the polarizer is not perfect, partially due to slight birefringence induced in the

light beams from passing through the walls of the vapor cells. To account for this, and any other backgrounds on the detected light, an offset is added to the signal:

$$I(t) \rightarrow V(t) + V_{off},$$

where $V(t)$ is the detected photodiode voltage, and V_{off} is the photodiode signal background that is measured when $\alpha = 0$. I_0 was generally not measured, but can be estimated by taking the average of the signal over the entire scan, which from Equation 2.6 gives

$$I_0 = \frac{\overline{I(t)}}{\sin^2 \alpha} \rightarrow \frac{\overline{V(t)} - V_{off}}{\sin^2 \alpha},$$

where we have assumed that $\overline{\varphi(t)} = 0$. We can then rewrite Equation 4.1 as

$$\varphi(t) = \arcsin\left(\sqrt{\sin^2 \alpha \frac{V(t) - V_{off}}{\overline{V} - V_{off}}}\right) - \alpha'. \tag{4.2}$$

The last term in Eq. 4.2 is denoted with a prime because instead of using a measured polarizer angle α, which could at best be known to $\pm 0.5°$, the arcsine term is averaged over the entire probe phase and subtracted as α' so that the result for $\varphi(t)$ ends up centered about zero. Equivalently, α' could be treated as a fit parameter for a constant background.

So, given V_{off} and α, which can be measured each time the analyzing polarizers are aligned (see Sec. 4.1.1), Equation 4.2 can transform the photodiode signal $V(t)$ into the optical rotation angle $\varphi(t)$. However, having said all this, V_{off} and α for the two signals were not generally kept track of, and the linearization for all of the HG3 data was performed using $V_{off} = 0$ and $\alpha = 0.10$ rad (5.73°) in Eq. 4.2. The only effect of this shortcut is that when $\varphi(t)$ is fit to the exponentially decaying sine wave given in Equation 2.5, the fit value for the amplitude does not end up corresponding to the actual optical rotation angle amplitude φ_0. This can easily be seen in the small φ limit given in Equation 2.7, where the photodiode signal has an essentially linear dependence on $\varphi(t)$:

$$V(t) = C_0 + C_1\varphi(t), \quad \text{with} \quad C_0 = \frac{I_0}{2}(1 - \cos 2\alpha)$$
$$\text{and} \quad C_1 = I_0 \sin 2\alpha.$$

So misinterpretation of the C_0 term is removed by subtracting the averaged value α', and uncertainty in the C_1 value can be absorbed into the amplitude of $\varphi(t)$. For the -20 GHz probe detuning used in most of HG3, $\varphi_0 \approx 0.05$ rad., so this is a fairly good approximation. The loss of knowledge of the actual optical rotation amplitude makes it somewhat more difficult to judge the overall system performance throughout the dataset, but the fitted amplitude can still be analyzed for fluctuations correlated with the electric field. Also, the main goal of the initial analysis is to find the frequency of the optical rotation angle modulation, which ends up being insensitive to the values of V_{off} and α actually used in Eq. 4.2.

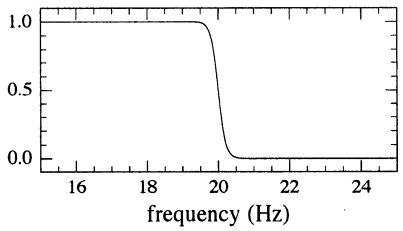

Figure 4.3: Digital filter function (Eq. 4.3) near the cutoff frequency. $f_c = 20$ Hz and $f_w = 0.1$ Hz.

Digital filtering

After applying Equation 4.2, the "linearized" data is digitally filtered in frequency space. To accomplish this, the data is transformed into frequency space with the fast Fourier transform (FFT) function provided in the CVI Advanced Analysis library, which is based on a split-radix algorithm [Duh84]. The result of the Fourier transform is then multiplied by a filter function based on the Fermi distribution:

$$F(f) = \frac{1}{e^{(f-f_c)/f_w} + 1} \tag{4.3}$$

so that $F(f) \cong 1$ for $f \ll f_c$, $F(f) \cong 0$ for $f \gg f_c$, and the transition from 1 to 0 occurs mainly in a width f_w about the cutoff f_c (see Fig. 4.3). The width of the filter was set at $f_w = 0.1$ Hz and the cutoff was at 20 Hz, which was chosen to be about halfway between the typical Larmor frequency of 13 Hz and the second harmonic at 26 Hz. After applying the filter function, an inverse Fourier transform was applied to the result to return to the time domain.

The filtering process would then be repeated with a cutoff of $f_c = 1$ Hz, which leaves only the longer-term "background" drifts in the linearized signal. After again inverse Fourier transforming back, this low-frequency background was directly subtracted from the result of the first ($f_c = 20$ Hz) filter to give the signal that would be fit to find the precession frequency. Figure 4.4 shows the Fourier power spectrum of a typical scan, where the top panel is the spectrum of the raw photodiode signal, the middle is after the linearization procedure is applied, and the bottom panel shows the end result after the digital filtering.

Edge effects from applying Fourier filtering to a non-infinite function can lead to transient behavior at the beginning and end of the filtered result. We deal with this by cutting the first 10 seconds and final 5 seconds of the filtered data, leaving a total of 85 seconds out of a typical 133 second pump/probe cycle that is actually fit to determine the spin precession frequency.

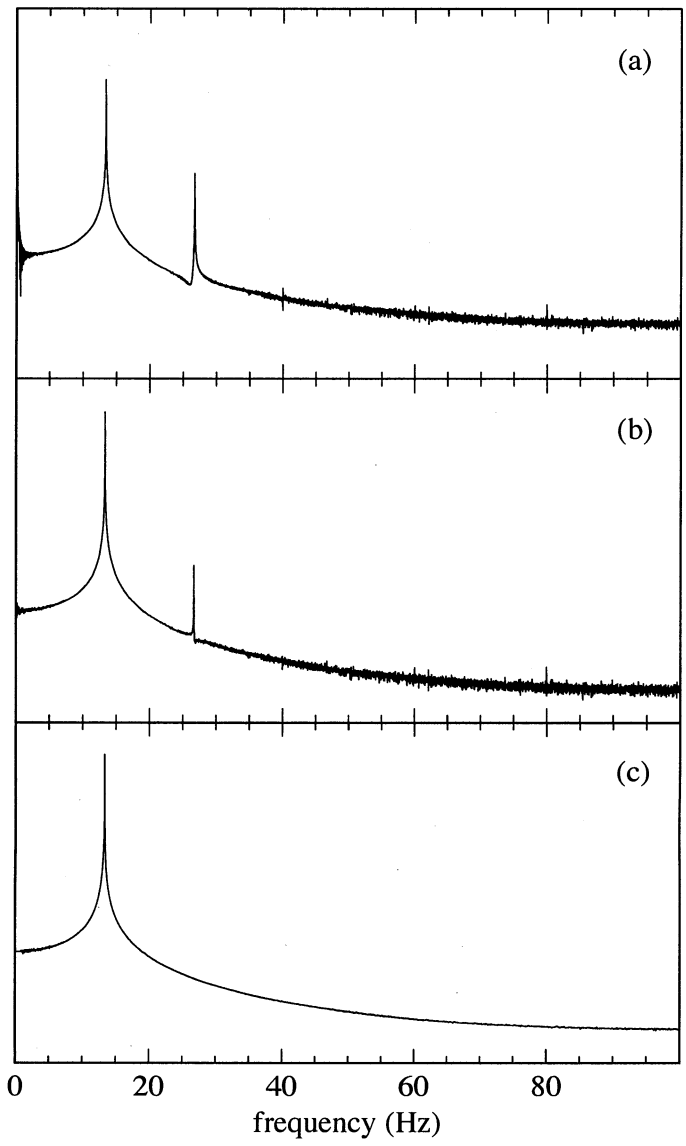

Figure 4.4: Spin precession signal frequency power spectrum. The signal is from the top cell in Scan 44023. (a) is the raw photodiode signal shown in Figure 4.2, (b) is the linearized signal, and (c) is after the digital filtering process. The spectrum is peaked at $f = 13.3$ Hz.

Nonlinear fitting

The linearized and filtered data is then fit to the function

$$y(t) = Ae^{-t/\tau} \sin(\omega t + \phi), \tag{4.4}$$

which is essentially the same as Equation 2.5 with the addition of a phase ϕ in the sine function, and replacing the optical rotation amplitude φ_0 with a more generic amplitude A, to reflect the uncertainty in the polarizer angle α. A Levenberg-Marquardt nonlinear least-squares routine, based on the *Numerical Recipes in C* (see [Pre92, Sec. 15.5]) implementation, is used to fit Equation 4.4 to the data, with ω, τ, A and ϕ as free parameters.

Before the fit is performed, guesses for the initial values for the four fit coefficients need to be made. The frequency is estimated by counting the number of zero crossings (N_z) in the data curve and dividing by twice the time length (T) of the data, so that

$$\omega_g = 2\pi \frac{N_z}{2T} . \tag{4.5}$$

To estimate the spin relaxation time (τ), the amplitude of the precession signal is sampled at the beginning and end of the scan by finding the maximum valued data point within 2.5 precession periods from the start of the data (t_1, y_1), and within 2.5 precession periods from the end of the data (t_2, y_2). Then τ_g can be found by solving $y_2 = y_1 \exp[-(t_2 - t_1)/\tau_g]$, which gives

$$\tau_g = \frac{t_2 - t_1}{\ln(y_1/y_2)} , \tag{4.6}$$

and the amplitude is then given by

$$A_g = y_1 e^{+t_1/\tau_g} . \tag{4.7}$$

The phase is estimated by finding the time of the first zero crossing (t_z) and taking

$$\phi_g = -(\omega_g t_z \bmod 2\pi) . \tag{4.8}$$

If the derivative of the signal at time t_z is negative, then ϕ_g given by Eq. 4.8 is off by a half period. This is checked for by finding the sign of the signal a quarter period after the first zero crossing, and if it is negative, then $\phi_g \rightarrow \phi_g + \pi$.

The *Numerical Recipes* Levenberg-Marquardt χ^2 minimization routine (`mrqmin`) can fit the N data points (t_j, y_j) to Eq. 4.4 with unequal weighting of the data points described by their individual standard deviations σ_j. In our case all the data points are assumed to have an equal standard deviation so the σ_j array is set to 1.0. Starting at the initial coefficient guesses (Eqs. 4.5–4.8), the `mrqmin` routine is iterated until the χ^2 changes by less than 1% compared to the previous value, and

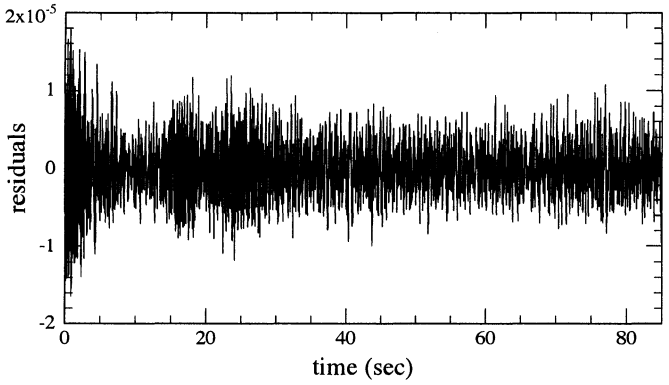

Figure 4.5: Residuals after fitting to Eq. 4.4. The difference between the data points (Scan 44023, top cell) and the fit to Equation 4.4 is plotted. The amplitude of the linearized precession signal for this scan is 0.014, about 700 times larger than the maximum residual size.

if this condition holds true after two more iterations, the fit is assumed to have converged. Typically, convergence was achieved within 4–5 iterations, and the maximum allowed iterations was set at 20, but this was only reached if the particular scan had serious problems, such as a loss of laser light due to a doubling cavity failing to properly lock. The final `mrqmin` call returns the fitted coefficients a_i, and error estimates in the coefficients can be estimated by taking (see [Pre92, Sec. 15.6])

$$\delta a_i = \sqrt{\frac{\chi^2 C_{ii}}{N}} \tag{4.9}$$

where C is the covariance matrix returned by `mrqmin`, and the factor of $\sqrt{\chi^2/N}$ accounts for setting the weights σ_j to 1. The residuals for the fit from our typical scan are shown in Figure 4.5.

After fitting the data over the entire fit range (10–85 sec. of a 100 sec. probe phase), the scan was divided into 100 separate sections ($n = 1 \ldots 100$) of equal length. The shorter sections were individually refit to Eq. 4.4, but with ω and τ fixed at the values from the overall fit, and the amplitude and phase as the free parameters. Taking the ratio of the amplitudes of the individual fits and the overall amplitude (A_n/A) gives the degree of "amplitude deviation" over the course of the scan. The amplitude deviations mainly give a measure of how well the post-linearization and digital filtering signal envelope matches a true exponential decay. The amplitude deviation for a typical scan is shown in Figure 4.6(a).

Taking the difference between the phases of the shorter segments and the overall phase ($\phi_n - \phi$) gives the "phase deviation" over the course of the scan. Drifts in the phase deviation give a measure

of how stable the frequency is during the probe phase, and the time derivative of the phase can be thought of as a time dependent correction to the frequency:

$$\omega(t) = \omega_0 + \frac{\mathrm{d}\phi(t)}{\mathrm{d}t} ,$$

where ω_0 is the frequency obtained from the fit over the entire scan. Since drifts in the frequency measured in the vapor cell are most likely directly related to magnetic field drifts ($\omega = 2\mu B/\hbar$), the phase deviation can be interpreted as the integral of the magnetic field inside the cell. For example, a linear drift in the magnetic field would lead to a quadratic drift in the phase deviation. A linear drift in the phase deviation, on the other hand, indicates that the overall fitted frequency does not give the true average frequency over the probe phase, which can happen because the fitting procedure is more heavily influenced by the first portion of the scan, where the rotation amplitude is largest. Figure 4.6.b shows the phase deviation from a typical scan.

Data files

The last step for the precession signal fitting program is to save the fit information. For each scan, a summary file (suffix: .sum) is saved which contains the fit information for the top and bottom precession signals including: the fit parameters and their error estimates, the top and bottom χ^2 values for the overall fit, the transmission averages of the raw signals, the amplitude and phase deviation values and errors, and other miscellaneous settings such as the linearization settings and the time ranges used. The low frequency background found from the digital filtering process is saved to a separate file (suffix: .bak).

The fitting program was set up to analyze data runs by sequentially processing scans with consecutive scan numbers. Given a specific starting scan number, a cumulative data file would be created named, for example, "Series1_21011-.cum", where "Series1" was the designation given to all of the HG3 data, and 21011 was the starting scan number. Then, a line would be appended to this file for each scan in the run giving the scan number, the time in minutes relative to the initial scan that the precession signal file was created, the fit values (ω, τ, A, and ϕ) for the two signals, the estimated fit error for the frequency parameter, and the averaged transmission values. The frequency values were recorded relative to the average of the top and bottom cell frequencies from the initial scan.

On a Pentium III 666 MHz processor running Windows 98 and no other programs, the entire time to process the two precession signals in a single data file was about 2 seconds. Of that time, 0.3 sec. was spent reading in the data file, 0.7 sec. for the linearization and digital filtering, 0.6 sec. to fit over the entire probe time, and 0.4 sec. to fit the 100 shorter segments for the amplitude and

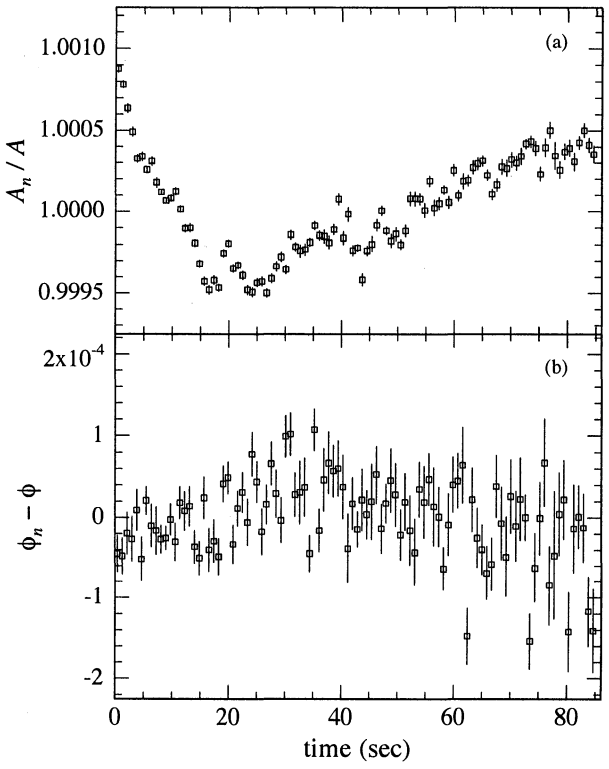

Figure 4.6: Amplitude and phase deviations plot. The fit results are from the top cell signal in Scan 44023. (a) shows the ratio of the 100 segment amplitudes (A_n) to the amplitude fit for the entire scan. (b) shows the difference between the segment phases (ϕ_n) and the phase fit for the entire scan. The error bars are found from the variance returned by `mrqmin`.

phase deviations. If the acquisition program was also running on the same computer, the processing time per file increased by about a factor of 3.

4.2.2 HV Correlation Analysis

The second analysis program was set up to track the 36 parameters listed in Table 4.3 for possible correlation with the high voltage. For each scan in a data run, a single value was recorded for each of the 36 parameters. In the case of the ".cum" parameters, the data were already stored in this format, so these values were copied directly from the cumulative file. The other files contained data sampled between 1 and 20 Hz for each scan, so these parameters were averaged over the probe phase to give a single value for each scan. Before the averaging was carried out, though, 20% of the probe phase data were discarded by dropping the minimum 10% and the maximum 10% data values, which lessens the impact of any spikes or transient behavior on the calculated average. An error bar was assigned to the averaged values by calculating their variance σ ($\sigma^2 = (\sum x - \bar{x})/N$) over the probe phase. By definition, the amplitude deviations and phase deviations should always average to one and zero respectively, so instead of recording their average values, the variance was recorded and no error bar was assigned. The final two parameters, the phase and frequency differences, were found by simply taking the difference of the single cell values from the cumulative file.

The ".cum" parameters were not assigned error bars, except for the fitted frequencies Omega 1 and Omega 2. As was mentioned in the description of the nonlinear fitting procedure, the phase deviations give a measure of the frequency stability during the measurement, and a misestimation of the average frequency over the probe time results in a linear drift in the phase deviation. Therefore, the error in the fitted frequency from phase noise was estimated as the error on the slope from a linear fit performed on the phase deviation points. Similarly, for the frequency difference (Omega1 − Omega2), the error was estimated by taking the error on the slope from a linear fit of the difference between the two phase deviations. The linear slope of the phase deviation difference was added to the frequency difference as a correction.

String analysis

The top part of Figure 4.7 shows several hours of typical frequency difference data from an HG3 run. We are generally only interested in the portion of the frequency difference signal that is correlated with the HV polarity. The HV correlation is extracted by performing a string analysis[1] on all of the data parameters to remove background drifts. For example, if $p_j = \pm 1$ gives the HV polarity for

[1] "String analysis" was first used in the 1977 neutron EDM experiment, and is discussed in the appendix of [Dre77].

Table 4.3: Parameters tracked for HV correlations.

File	Parameter name	Description
.cum	Time	.bin file creation time (minutes)
	Omega 1	fitted frequency from 1st DAQ channel
	Omega 1 Err	error from `mrqmin`
	Omega 2	fitted frequency from 2nd DAQ channel
	Omega 2 Err	error from `mrqmin`
	Rel Time 1	fitted spin relaxation time
	Rel Time 2	
	Phase 1	fitted phase
	Phase 2	
	Amplitude 1	fitted amplitude
	Amplitude 2	
	Transmission 1	raw signal average
	Transmission 2	
.mon	Field Bx	external magnetometer-EW (1 V/mG)
	Field By	external magnetometer-NS (1 V/mG)
	Field Bz	external magnetometer-vertical (1 V/mG)
	Piezo 1	1st doubling cavity piezo voltage
	Piezo 2	2nd doubling cavity piezo voltage
	Laser Power	normalization photodiode signal
	Laser Current	MOPA amplifier current (1 V/A)
	Temperature	thermistor voltage
	Beam Horizontal	4-quadrant detector (hor. difference)
	Beam Vertical	4-quadrant detector (vert. difference)
	Beam Transmission	4-quadrant detector (summation)
.hvs	Leak Cell 1	top cell leakage current (0.01 V/pA)
	Leak Cell 2	bottom cell leakage current (0.01 V/pA)
	Leak Vessel	current flowing onto vessel (0.01 V/pA)
	High Voltage	HV monitor (1 V/kV)

Table 4.3 continued.

File	Parameter name	Description
.bak	Background 1	subtracted background from digital filtering
	Background 2	
.sum	Amplitude Dev 1	amplitude deviation
	Amplitude Dev 2	
	Phase Dev 1	phase deviation
	Phase Dev 2	
.cum	Omega1 − Omega2	main EDM sensitive signal
	Phase1 − Phase2	phase difference between top and bottom cells

data point j, and the polarity for subsequent points is given by $p_{j+k} = (-1)^k p_j$, then we assume that the signal in a series of 3 consecutive points is given by

$$\begin{aligned} y_j &= y_0 + p_j \delta_j \\ y_{j+1} &= y_0 - p_j \delta_j + \theta \\ y_{j+2} &= y_0 + p_j \delta_j + 2\theta, \end{aligned} \tag{4.10}$$

where δ_j describes an HV polarity dependent effect, and θ describes a linear drift of the signal in time. Solving Eq. 4.10 for δ_j gives

$$\delta_j = \frac{p_j}{4}(y_j - 2y_{j+1} + y_{j+2}). \tag{4.11}$$

Higher order time dependencies in the background drift can be removed if a longer string is used. Generally, a string of length $m+1$ points cancels up to an $m-1$ order background, and the HV correlation is found from

$$\delta_j = \frac{p_j}{2^m} \sum_{n=0}^{m} (-1)^n \, {}_mC_n \, y_{j+n}, \tag{4.12}$$

where ${}_mC_n \equiv \frac{m!}{(m-n)!n!}$ is the binomial coefficient. For data points with individual uncertainties σ_{y_j}, we estimate the uncertainty in the string point to be

$$\sigma_{\delta_j} = \frac{1}{2^m} \sqrt{\sum_{n=0}^{m} ({}_mC_n)^2 \, (\sigma_{y_{j+n}})^2}. \tag{4.13}$$

We analyzed our data with 3, 4, 5, and 6 point strings. We also analyzed the data with both overlapping strings, where a new string starts at each data point, and with independent strings,

where the next string starts after the last data point in the previous string. Our final analysis used 3-point overlapping strings, which gave a slightly better statistical sensitivity over the other methods (see Table 4.4).

After calculating the string points δ_j over an entire run for a particular parameter, the HV correlation of the run is estimated by taking the weighted average of its string points:

$$\overline{\delta} = \frac{\sum \left(\delta_j/(\sigma_{\delta_j})^2\right)}{\sum \left(1/(\sigma_{\delta_j})^2\right)}. \tag{4.14}$$

The uncertainty in $\overline{\delta}$ is estimated to be

$$\sigma_{\overline{\delta}} = f_o \sqrt{\sum \left(1/(\sigma_{\delta_j})^2\right)} \sqrt{\chi^2}, \tag{4.15}$$

where f_o is a correction factor to account for the fact that adjacent string points are not independent if overlapping strings are used. For independent strings, $f_o = 1$, but for overlapping strings of length $m+1$,

$$f_o = \frac{2^m}{\sqrt{\sum_{n=0}^{m} ({}_mC_n)^2}}. \tag{4.16}$$

For example, 3-point overlapping strings require $f_o = 4/\sqrt{6}$. $\sigma_{\overline{\delta}}$ is also corrected by the square root of the chi-square, as given by

$$\chi^2 = \frac{1}{N} \sum \frac{(\delta_j - \overline{\delta})^2}{(\sigma_{\delta_j})^2}. \tag{4.17}$$

Multiplying the error estimate of the weighted average by $\sqrt{\chi^2}$ effectively scales the error to match the scatter in the string points, rather than relying only on the uncertainty estimates of the individual data points σ_{y_j}. For the frequency difference parameter, the χ^2 value was typically between 1 and 3, indicating that the phase noise as estimated from the phase deviation curves did not account for all of the scatter in the measured frequencies. This is partially due to magnetic field drift that occurs during the 45 seconds between successive precession signal fit ranges.

Data point removal

Before applying the string analysis, the data points are filtered to avoid unnecessary scatter in the string points. As is shown in Figure 4.8, there are occasional outlying data points that fall well outside the general character of the surrounding data. There are many possible causes for these outliers depending on the parameter being monitored, but the most common source for outliers in the frequency difference data points was probably misfits of the precession signal due to momentary laser light fluctuations. The outliers are excluded from the string analysis such that no strings span over the cut point. If excluded points occur close together, such that there are not enough data points in between to fill a string, then no string points are recorded for that region.

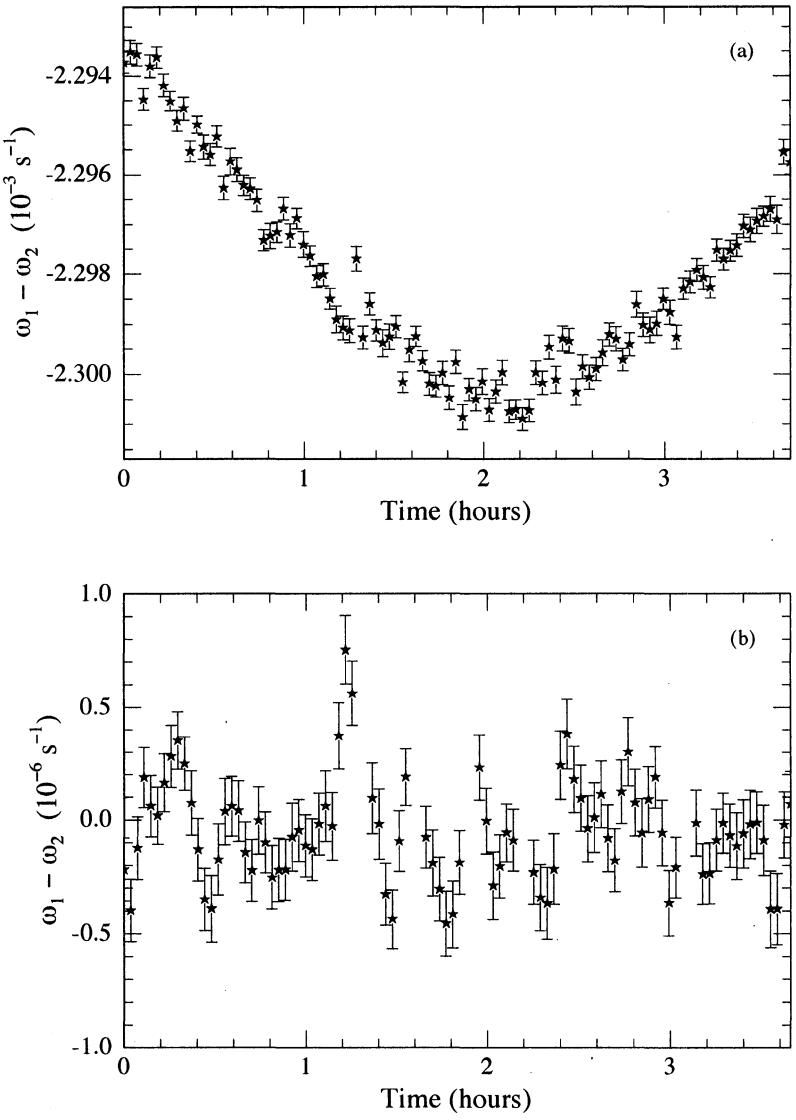

Figure 4.7: Frequency difference data excerpted from HG3 Run 43715 (Scans 44000–44100). Each point represents the frequency difference fit for a single 100 second HV dwell. Plot (a) shows the raw frequency difference and plot (b) shows the string points found from Eq. 4.11 for 3-point overlapping strings.

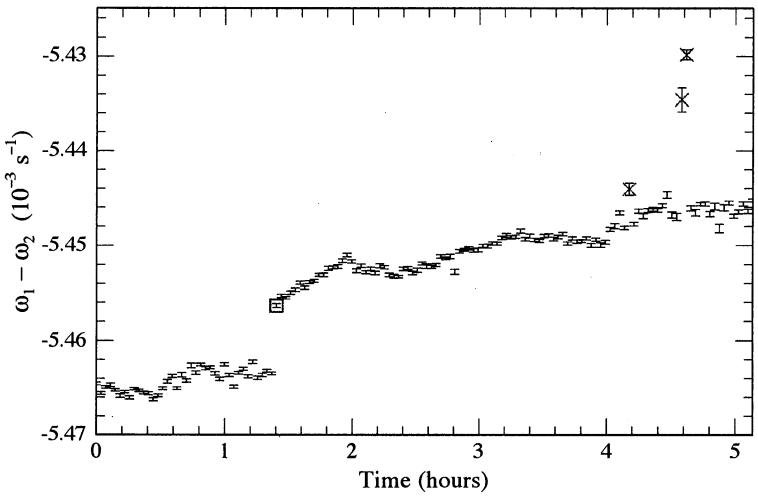

Figure 4.8: Frequency difference data excerpted from HG3 Run 21011 (Scans 21011–21150). The boxed data point at around 1.5 hours marks a sudden shift in the background magnetic field gradient where a "force stop" would be applied so that data strings do not span over the shift. The three data points marked by X's are excluded from the string analysis.

In other cases, the background might shift to a new value, as is shown at the boxed point in Figure 4.8. Once again, we would like to avoid having data strings span over this shift, but there is no need to exclude a data point: the previous string ends with the last point before the shift, and the next data point begins the next string. These instances are referred to as a "force stop." Force stops are also applied to all parameters when the HV does not change sign between successive scans.

An automatic algorithm was used to initially decide if a data point should be excluded or designated a force stop. The aim of the algorithm is to identify semi-permanent shifts in the background that require a force stop, and to remove individual or short sections of points where the scatter is much larger than the surrounding behavior. First, the algorithm looks backward at up to 15 previous points (excluding previously cut points) and fits a straight line to the backward data. If the distance from the current point to the backward fit is greater than a cutoff of 5 times the mean scatter of the backward data, then the point is flagged for possible removal. Next, up to 10 data points in the forward direction are examined as follows:

1. If any of the forward points fall within the cutoff region (5 times the backward scatter) when compared to the backward fit, then it is assumed that the intervening points are outliers and they are cut, otherwise, step 2 is taken.

2. A linear fit is made to the forward data (maximum of 10 points). If the mean scatter of the first three points about the forward line is less than 2.0 times the scatter of the backward data about the backward line, then it is assumed that a shift in the background has occurred and a force stop is inserted, otherwise step 3 is taken.

3. If any 3 point sequence in the forward region (maximum of 10 points) has a scatter within the step 2 cutoff (2.0 times the backward scatter), then the data points are cut between the current point and the first section that meets the cutoff criterion, otherwise step 4 is taken.

4. Step 3 is repeated, except that the cutoff is changed to 2.0 times the minimum scatter of any 3 point segment in the forward region.

This particular algorithm was cobbled together at the start of the HG3 dataset, and the particular cutoff values and forward and backward ranges were picked such that they seemed to work well on a couple of early runs. Generally, though, we found that the automatic algorithm did not always give what we judged to be sensible results, depending on the behavior of the data. It might have been possible to tailor the algorithm parameters to work better in certain situations, or to develop a "smarter" algorithm, but instead we manually checked the results of the automatic filter in each run, paying the most careful attention to the precession frequency channels. The manual adjustments are affected to some degree by the human operator subjectivity. However, by applying the cuts to the data points y_j before the string points are calculated, the HV correlation result should not be consciously influenced in a particular direction. We also compared the end results with those obtained by three completely automatic point removal systems which I will denote as:

Auto-c The algorithm described above is applied to the data with no manual check afterwards.

Auto-s The weighted average of the string points from an uncut data run is calculated. Each string point is compared to the weighted average for the run and if a string point is more than 3 times its error bar away from the average then it is cut. After removing these points, the weighted average is recalculated.

Auto-j After computing χ^2 for a run without removing any points, successive data points are checked, and if

$$|y_j - y_{j+1}| > 3\sqrt{\chi^2}\sqrt{(\sigma_{y_j})^2 + (\sigma_{y_{j+1}})^2},$$

a force stop is inserted at y_j. This method is similar to the method used in the HG2 measurement [Jac91], except that in HG2 the cutoff was not weighted by a χ^2 estimate.

The results from all of these methods are shown in Table 4.5.

4.3 Raw Results

The sign of the EDM signal is affected by the magnetic field direction ($B = \pm 1$), and whether ω_1 originates from the top or bottom cell (Ch $= \pm 1$). For $B = +1$, our convention is that the magnetic field is directed downward, which is the same direction as the electric field in the top cell for positive HV. The magnetic moment of ^{199}Hg is positive, so for positive HV, a positive EDM would cause the top cell frequency to increase, and the bottom cell frequency to decrease, leading to a correlation value $\delta(\omega_T - \omega_B) > 0$. The HV correlation of the frequency difference channel $(\omega_1 - \omega_2)$ for each run was converted into EDM units by taking

$$d = \frac{\hbar\bar{\delta}(\omega_1 - \omega_2)}{4\,\mathrm{HV}/(1.1\ \mathrm{cm})}\,(B)\,(\mathrm{Ch}), \tag{4.18}$$

where HV, B, and Ch are the values from Table 4.1, and HV/(1.1 cm) gives the electric field magnitude in units of kV/cm. Runs where HV was applied to only one of the cells were accounted for by entering half of the applied HV value into Eq. 4.18. For the standard operating voltage of 10 kV, a frequency difference correlation of $\delta(\omega_1 - \omega_2) = 10^{-8}$ s^{-1} would correspond to an EDM of $d = 1.81 \times 10^{-28}\ e\,\mathrm{cm}$.

The EDM value for each dipole $(+-+-)$ HV sequence data run was found from Eq. 4.18, and then the weighted average of all the runs gives the EDM value of the entire dataset. We excluded the offset magnetic field runs (OB) from the EDM dataset because they are used in a systematic error evaluation (see Sec. 4.4.3). The couple of runs where the HV was switched in the middle of the probe phase (MS) were also excluded. Figure 4.9 shows the EDM signal from all the non-OB or MS dipole data runs in Table 4.1. From this dataset we excluded three runs that had significantly larger error bars than the rest of the dataset: Run 32441 had many misfits because the acquisition program often changed the configuration from pump to probe much later than it should have, Run 35893 was much shorter than most of the other runs and had additional noise due to bad steering of the probe light beam, and Run 63372 had extra noise because the pneumatic switch often failed to move the chopper into the pump beam.

We also excluded several runs where there were anomalously large HV correlated shifts in the frequency difference channel (FS). Run 22308 gave an EDM signal of $(51 \pm 7) \times 10^{-28}\ e\,\mathrm{cm}$, but the large signal was not present in any of the adjacent runs. It is possible that this signal was related to a periodic fluctuation since random HV reversal skips (see Sec. 3.6.2) to guard against this had not been implemented yet (implemented after Run 23697). A large correlation again appeared in Run 68469 that gave a signal of $(-38 \pm 3) \times 10^{-28}\ e\,\mathrm{cm}$. This time the behavior persisted through several runs until the vessel was opened and modifications were made to the HV cables, after which the EDM signal seemed to disappear. The HV cable leakage current was probably saturating during

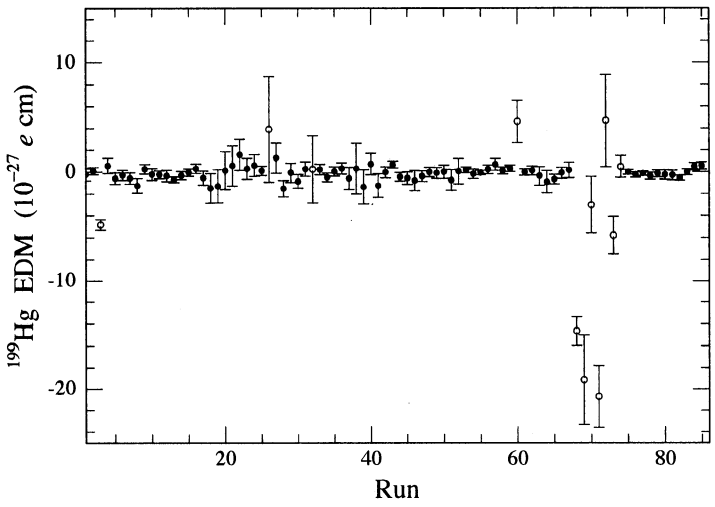

Figure 4.9: EDM signal from all HG3 dipole runs. OB and MS runs are not displayed. Open points mark runs that are excluded from the final analysis, either due to excessive noise or anomalously large HV correlations. The x-axis in this plot (and in Figures 4.10 and 4.12) simply labels the runs sequentially, and so does not match the run numbers given in Table 4.1.

these runs, and it was also found that the electrical resistance between the vessel and the HV ground was somewhat low, but it is not clear if the large signals were related to these issues (see App. C for more details). Unfortunately, we are not sure what caused these large HV correlated frequency shifts, but they are possibly related to the large number of unexplained false signals we have now seen in the 4-cell dataset (see Sections 7.4.1 and 7.5). Since the EDM signals for these particular runs are so much larger than the rest of the dataset, we feel that it is safe to assume that the particular systematic effects that caused the HV correlated shifts were not present in the other data runs. Therefore, we excluded the data runs where the large systematic effect seems to be present: Run 22308, and Runs 68469–69342 (8 runs).

After these exclusions, there are 74 data runs which contribute to the EDM measurement. The EDM value obtained from a weighted average of these runs is shown in Table 4.4 for overlapping and independent strings of length 3–6 points. Initially, only independent string points were calculated, and it was only at the very end of the HG3 dataset that we decided to also examine overlapping string points. The overlapping strings give very consistent central values for the different string lengths, and the statistical uncertainty increases slightly as the strings get longer. The difference in uncertainty can be accounted for by the lower number of total string points available when a longer string is used. There are less string points for longer strings because, for a string of length n,

Table 4.4: HG3 EDM value obtained with different types of strings. The EDM value is given in units of 10^{-28} e cm.

string type	length	$d(^{199}\mathrm{Hg})$	χ^2	total string points
overlapping	3	$-1.073(.490)$	0.83	31045
	4	$-1.067(.503)$	0.79	29010
	5	$-1.075(.517)$	0.75	27162
	6	$-1.065(.533)$	0.74	25421
independent	3	$-1.049(.503)$	0.89	10967
	4	$-1.232(.535)$	1.00	7981
	5	$-1.344(.563)$	0.85	6159
	6	$-0.204(.608)$	0.91	4907

every time the overlapping string must be terminated due to a force stop or excluded point, $n-1$ overlapping string points are lost. The results for independent strings show much more variation in the central value estimate, especially for $n = 6$. This is probably because the longer independent strings end up sampling a somewhat different set of data points than the shorter strings. For the case of overlapping strings, the length 6 strings sample almost all the same points as the length 3 strings, unless force stops or cut points occur 6 points apart or less, in which case a 6 point string is not calculated for that interval. For independent strings, though, any instances of force stops or cut points will likely lead to several data points that would be sampled by a 3-point string but not by a longer string.

Since it has the best statistical sensitivity in Table 4.4, we chose to use 3-point overlapping strings for our final analysis, and all the results discussed in the rest of this thesis are based on 3-point overlapping string analysis. Figure 4.10 shows the EDM signal obtained from the 74 HG3 data runs included in the final analysis. The weighted average of these runs gives an EDM value of

$$d(^{199}\mathrm{Hg}) = (-1.07 \pm 0.49) \times 10^{-28}\ e\,\mathrm{cm},\ \chi^2 = 0.83. \tag{4.19}$$

If we kept all runs shown in Figure 4.9, then the result would be $-0.94 \pm 0.48 \times 10^{-28}$ e cm with a χ^2 of 3.9.

Having obtained the Eq. 4.19 result, it seemed that the χ^2 value might be a little low. For 73 degrees of freedom, there is an 85% probability that the χ^2 will be greater than 0.83. There was a wide variation in the number of scans included in each run (from 68 to 1022 scans), and we thought that slowly changing experimental conditions during the longer runs might have led to a low χ^2. For example, a systematic drift in the HV correlation during a run would cause the scatter of the string

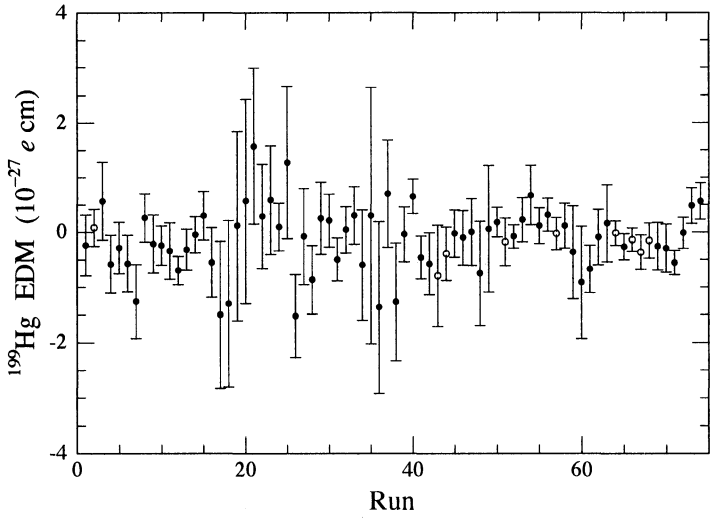

Figure 4.10: EDM signal from HG3 dipole runs included in the final analysis. Open points denote runs that would be split into two sections if the binning method described in this section with $N_b = 500$ was applied.

points about the weighted average of the entire run to be larger than if smaller portions of the run were examined. We tested for this possibility by breaking up the longer runs into smaller sections. For a given bin size of N_b, a run with total string points N_s was divided into

$$n = \text{nint}(N_s/N_b)$$

bins of equal length[2]. This meant that a run with less than $1.5N_b$ string points was left alone, a run with $1.5N_b \leq N_s < 2.5N_b$ was split into two sections, etc. After sectioning the data in this manner, the normal averaging would proceed as if each bin were a separate run. In looking at bin sizes from 100 to 650 points, we found that the central value and uncertainty did not change by more than 5%, but as is shown in Figure 4.11, there is a sudden drop in the χ^2 when the binsize is larger than 550.

The drop in χ^2 was found to be mainly due to Run 69869, which seems to exhibit a shift in the HV correlation value about halfway through the run. Averaging the entire run gives an EDM value of $(-0.18 \pm 2.25) \times 10^{-28}$ e cm, but when the run is split into two bins, the first half averages to $(6.85 \pm 3.03) \times 10^{-28}$ e cm, and the second half gives $(-8.47 \pm 3.22) \times 10^{-28}$ e cm. Adding the uncertainties for the first and second halves in quadrature gives a difference between the two central values of about 3.5 standard deviations. This is perhaps an indication that a systematic effect is present during this run that shifts in character partway through. It is somewhat suggestive that

[2] nint(x) denotes the nearest integer or round function.

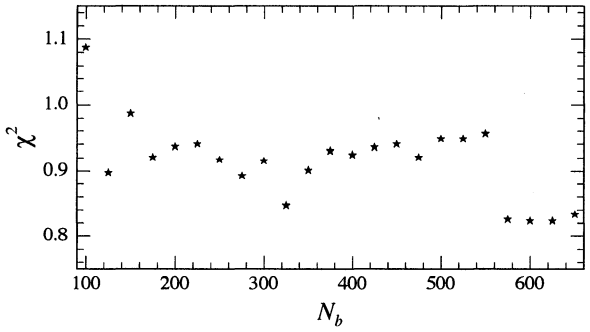

Figure 4.11: χ^2 of the EDM result versus bin size.

this run happens to occur right after the vessel was opened to investigate a much larger systematic effect (Runs 68469–69342). However, neither section gives a result that is particularly significant in itself, and there is no evidence of similar behavior in subsequent runs. We do not have a significant reason to drop this run from the dataset, but it also does not seem appropriate to include it as a single data point. We therefore decided to split this run and other long runs by using a bin size of $N_b = 500$ in our final analysis.

Figure 4.12 shows the final dataset used for the HG3 EDM result, using 3-point overlapping strings and the data binning method described above with $N_b = 500$. The weighted average of this dataset gives

$$d(^{199}\mathrm{Hg}) = (-1.06 \pm 0.49) \times 10^{-28}\ e\,\mathrm{cm},\ \chi^2 = 0.95. \tag{4.20}$$

The data binning increases the number of points from 74 to 83, and the probability of having a χ^2 larger than 0.95 with 82 degrees of freedom is 61%. The result in Eq. 4.20 does not represent the final result of HG3, as it does not include an estimate of the systematic error, as will be discussed in the next sections. The statistical error of $0.49 \times 10^{-28}\ e\,\mathrm{cm}$ represents about a factor of 5 improvement over the statistical error of the final HG2 result.

The results given in this section are all obtained after the frequency difference data is filtered by the Auto-c algorithm described in the previous section, followed by a manual check of the automatic results. In order to make sure that the human element in the filtering process was not significantly biasing the result, several other point removal systems (also described in the previous section) that did not involve a manual checking of the results were applied to the dataset, as is shown in Table 4.5. The results are all fairly consistent with each other. One of the automated methods gives a slightly better uncertainty estimate in the EDM result, however we did not feel significantly compelled to change our main analysis method.

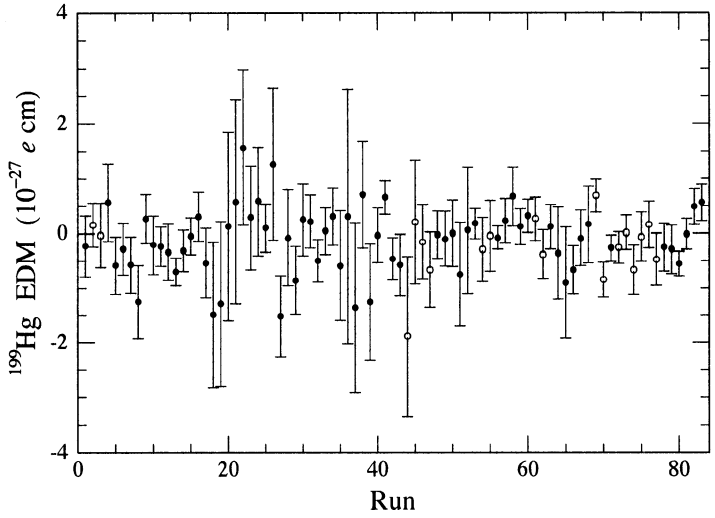

Figure 4.12: Final dataset for the HG3 EDM result. The open points denote runs that have been split into two sections by the $N_b = 500$ binning process.

Table 4.5: HG3 EDM value obtained with different point removal algorithms. The EDM value is given in units of 10^{-28} e cm.

point removal method	$d(^{199}\mathrm{Hg})$	χ^2	total string points
Auto-c + manual check	−1.064(.490)	0.95	31045
none	−1.044(.564)	0.69	34154
Auto-c	−0.709(.512)	0.81	32671
Auto-s	−0.819(.518)	0.68	30490
Auto-j	−0.905(.477)	0.84	32790

4.4 Analysis of Systematic Effects

Understanding and limiting the size of systematic effects is an extremely important part of performing a precision EDM measurement. To generate an effect that has the signature of an EDM, a systematic effect would have to cause a shift in the measured ^{199}Hg spin precession frequency that is asymmetric between the two vapor cell positions and is correlated with the applied HV polarity. While a systematic effect could generate a false EDM signature that would not actually be due to T violation, it is also possible that a systematic effect could act in such a way to cancel the signal of a real EDM, thus giving a false null measurement.

We made many modifications to the apparatus over the course of the HG3 measurement, and regularly changed the experimental parameters. We found no significant dependence of the measured EDM value on any of these changes. About one third of the entire dataset was devoted to systematic checks looking for E^2 dependent frequency shifts and effects that would be enhanced for $\boldsymbol{B}$ tilted away from $\boldsymbol{E}$.

4.4.1 Leakage Currents

Any electrical currents that flow due to the application of HV generate magnetic fields that can possibly cause HV correlated frequency shifts. Under normal operating conditions, about 1 pA of steady state current flows across the vapor cell walls when 10 kV is applied across them. The average cell leakage currents during the HG3 dataset were about 0.60 pA. The size and direction of the magnetic field generated by this leakage current depends on the (unknown) details of the current path, but to first order, only a helical current path around the cell cylinder will generate an EDM-like signal.

It seems likely that the leakage current path would be different for different vapor cells, and though the orientations of the cells were varied each time they were inserted into the vessel, a cell with a fixed helical current path would always produce the same sign of false EDM regardless of its orientation. It is possible, though, that redistributing the wax wall coating affects the leakage current paths. The leakage current paths might also be affected by the groundplane and electrode cup surfaces, and the specific details of their interface with the cell disks. Figure 4.13 shows the EDM signal obtained when only runs that had a particular cell in the vessel are averaged. There does not appear to be a significant difference between the results for different cells.

Figure 4.14 shows a scatter plot of the EDM signal and top cell leakage current string points from the HG3 dataset. A linear fit to this data gives a correlation slope of $-0.04 \pm 0.20 \times 10^{-28}$ e cm/pA. Similarly, a scatter plot of the EDM signal and bottom cell leakage current leads to a correlation

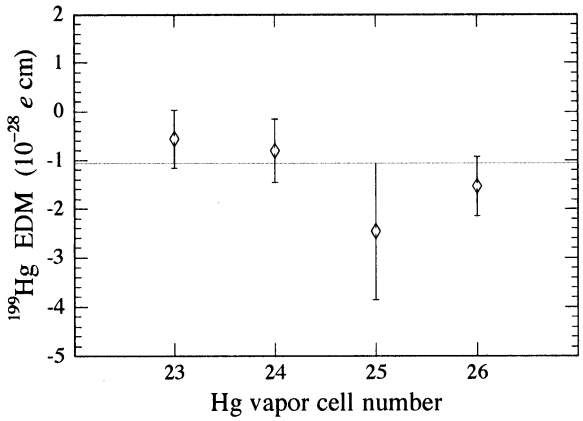

Figure 4.13: EDM signal obtained with different vapor cells. Each point gives the average signal for all runs where the numbered cell was present in either the top or bottom vessel positions. The solid line is the average of the entire dataset. Cell 25 gives a comparably larger error bar because there were fewer runs using it because it broke partway through the dataset.

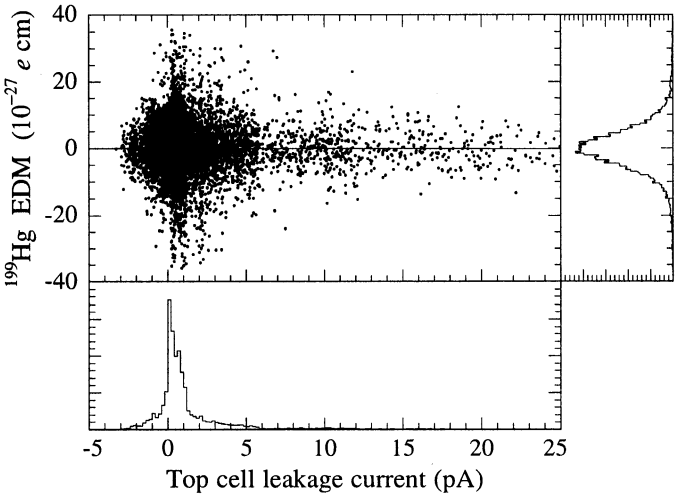

Figure 4.14: Correlation between the top cell leakage current and the EDM signal. Histograms of the leakage current and EDM data are shown below and to the right of the scatter plot. The solid line shows a linear fit giving the correlation between the EDM signal and leakage current of $(-0.04 \pm 0.20) \times 10^{-28}$ e cm/pA.

slope of $-0.02 \pm 0.18 \times 10^{-28}$ e cm/pA, and the vessel current correlation slope is $-0.03 \pm 0.05 \times 10^{-28}$ e cm/pA. Taking the average cell leakage current of 0.6 pA, we can use the correlation slope to place a limit on the average leakage current contribution to the EDM signal,

$$d_{leak}(\text{correlation}) < 0.14 \times 10^{-28}\ e\,\text{cm}. \tag{4.21}$$

It should be noted, though, that the evaluation of the leakage current contribution given by Eq. 4.21 assumes that all of the measured cell leakage current contributes linearly to a false EDM systematic. However, it might be the case that for large measured currents, a smaller proportion of the current follows a path that generates a false EDM systematic, and the increase in current is mainly due to charge flowing in a different path that does not contribute to an EDM signal.

A slightly more conservative estimate of the leakage current systematic is obtained by assuming that the leakage currents flow in a path that makes no more than one complete loop around the vapor cell. The magnetic field generated in the center of the cell is then about $B = \mu_0 I/2R = 0.5$ pG/pA. For an average leakage current of 0.6 pA, this then sets a limit on the leakage current systematic of

$$d_{leak}(\text{oneloop}) < 0.25 \times 10^{-28}\ e\,\text{cm}. \tag{4.22}$$

4.4.2 Effects Proportional to E^2

There are a variety of possible effects proportional to E^2 that might affect the ^{199}Hg spin precession frequency, and these effects can then generate an EDM-like systematic if the electric field magnitude is not perfectly symmetric for both HV polarities. Some examples of quadratic effects are motion of the vapor cells in the background magnetic field gradient due to electrostatic forces or electrostriction, the Kerr effect could modify the light polarization, which coupled to the vector light shift could cause a spin precession frequency shift, and changes in absorption due to the quadratic Stark effect could also lead to frequency shifts if coupled to other effects.

We checked for quadratic electric field effects by taking runs with the HV sequence +0−0+0− (quadrupole). These runs were analyzed in a similar manner as the dipole runs, except that instead of comparing +10 to −10, the ±10 scans were compared to the 0's. Prior to Run 42388, four quadrupole runs were taken where the HV was connected to both sides of the vessel, which gives zero signal in the frequency difference channel for a quadratic effect. After this, 13 quadrupole runs were taken only with the HV attached to one side (9 HVT runs, and 4 HVB runs). From these runs, the shift in the precession frequency at ±10 kV compared to zero field was less than 2 nHz.

The reversibility of the electric field in the EDM vapor cells was checked during a measurement of the scalar Stark shift of the ^{199}Hg $6^1S_0 \rightarrow 6^3P_1$ transition made shortly before the start of the

HG3 dataset [Har00]. It was found that measurements of the Stark shift changed with the polarity of the HV by less than 3%, indicating that the electric field is reversible inside the cell to within 1.5%. If a possible quadratic frequency shift is less than 2 nHz at ±10 kV, then a 1.5% change in the electric field magnitude upon HV reversal would cause an apparent EDM shift of

$$d_{quad} < 0.07 \times 10^{-28}\ e\,\mathrm{cm}. \tag{4.23}$$

4.4.3 Motional Magnetic Field

Particles moving at velocity $\boldsymbol{v}$ relative to a static electric field will experience a magnetic field in the moving frame that to first order in v/c is given by

$$\boldsymbol{B}_m = -\frac{1}{c^2}(\boldsymbol{v} \times \boldsymbol{E}).$$

If the static magnetic field ($\boldsymbol{B}_0$) and electric field are nearly parallel, then the magnetic field seen by the moving particles is

$$\boldsymbol{B} = \boldsymbol{B}_0 + \theta_{EB}\boldsymbol{B}_m + \frac{1}{2}\frac{\boldsymbol{B}^2}{\boldsymbol{B}_0},$$

where it is assumed that $\boldsymbol{B}_m \ll \boldsymbol{B}_0$, and θ_{EB} is the angle between $\boldsymbol{E}$ and $\boldsymbol{B}_0$ in the plane perpendicular to $\boldsymbol{v}$. If $\langle \boldsymbol{v} \rangle \neq 0$ and $\theta_{EB} \neq 0$, then the motional magnetic field contributes a linear electric field dependent magnetic field that mimics an EDM. This presents a very important systematic challenge for beam type experiments, but in vapor cell experiments it is generally assumed that the average velocity of the particles making up the vapor should be zero. Even so, a small asymmetry in the diffusion of polarized ^{199}Hg atoms in the cell, perhaps due to a spot on the cell walls that preferentially relaxes spins compared to the rest of the cell, could lead to a small but potentially dangerous nonzero velocity component. In order to set a limit on this possibility, we enhanced the potential systematic contribution of $\boldsymbol{B}_m$ by taking data runs with the magnetic field tilted about 5° from the electric field. Under normal conditions, we believe that the magnetic field was aligned to within 1° relative to the electric field.

The magnetic field was tilted in the offset $\boldsymbol{B}$ (OB) runs by applying a 1 mA current on either of the normally unused horizontal field generating coils that were wound on the same coil form as the main vertical field generating coil. 7 data runs were taken with the field tilted along the light propagation direction giving a HV correlation in the frequency difference channel of $\Delta\omega = (-0.08 \pm 0.96) \times 10^{-8}$ s^{-1}, and 10 data runs were taken with the field tilted along the magnetic shield axis which gave $\Delta\omega = (0.07 \pm 0.64) \times 10^{-8}$ s^{-1}. The uncertainty in these results would correspond to an EDM signal of less than $1.5 \times 10^{-28}\ e\,\mathrm{cm}$ at a 5° misalignment of the magnetic

field. Assuming a better than 1° alignment for the non-OB data runs, this sets a limit on the possible motional magnetic field contribution to our EDM signal:

$$d_{v\times E} < 0.3 \times 10^{-28}\ e\,\mathrm{cm}. \tag{4.24}$$

It turned out that all of the OB data runs happened to be taken with cells 23 and 26 in the vessel, so cells 24 and 25 were not tested for this effect. It can also be noted that remelting the wax cell wall coating would most likely change the location of enhanced relaxation points on the cell walls, and changing the orientation of cells throughout the dataset would likely change the direction of the motional magnetic field, unlike a fixed helical leakage current systematic.

4.4.4 Parameter Correlations

As was mentioned in Section 4.2.2, we looked for possible HV correlations in all of the 36 fit parameters and monitored signals listed in Table 4.3. If fluctuations in a particular parameter are well correlated with fluctuations in the precession frequency difference, then a HV correlation of that parameter might lead to an EDM-like systematic shift.

We estimated the correlation between each parameter and the frequency difference channel by making a scatter plot of their string points in the same manner as in Figure 4.14. Assuming that the random scan to scan fluctuations in each channel might be linearly related to the fluctuations in the frequency difference, we fit a straight line to the scatter plot and take the slope of this line to be the size of the correlation. The fitted correlation slopes are listed in the second column of Table 4.6. These slope estimates give a fair number of significant ($> 3\sigma$) correlations, including the external magnetometer, the beam position, the doubling cavity piezo voltages, the signal amplitude and transmission level, the backgrounds, and the phase deviation channels. It is certainly not surprising that the frequency difference fluctuations are affected by external magnetic fluctuations. We have generally found that shifts in the doubling cavity piezo voltages cause changes in the beam position, so the correlations seen in both these monitors likely have the same source, perhaps directly related to the beam steering or possibly a probe light wavelength effect. The various fit parameters are all interrelated, so their correlation is probably due to a single source, which might be due to a light shift effect, or might indicate a small systematic shift in the fitted frequency related to the shape of the precession signal envelope.

Regardless, these linear correlations do not constitute an EDM systematic unless the parameter fluctuations are correlated with the electric field direction. The overall HV correlation during the dataset for each parameter was calculated in the same manner as the frequency difference channel and these values are listed in the third column of Table 4.6. In this case we see no especially

Table 4.6: Possible systematic contributions from parameter correlations. Parameter descriptions are given in Table 4.3. The second column gives the linear slope fit to a scatter plot of the frequency difference channel vs. that parameter's string points (s^{-1}/that parameter's standard units). The third column is the average HV correlation for each parameter and column four gives the product of columns two and three in EDM units.

Parameter Name	Linear correlation slope	HV correlation	d_{Hg} (10^{-30} e cm)
Time	$-3.0 \pm 2.3 \times 10^{-7}$	$-3.2 \pm 6.8 \times 10^{-5}$	0.37
Omega 1 Err	$1.5 \pm 0.8 \times 10^{-1}$	$-0.8 \pm 1.5 \times 10^{-10}$	0.41
Omega 2 Err	$1.7 \pm 1.3 \times 10^{-1}$	$-3.5 \pm 1.8 \times 10^{-10}$	1.08
Rel Time 1	$-1.6 \pm 3.8 \times 10^{-8}$	$-7.4 \pm 3.0 \times 10^{-4}$	0.51
Rel Time 2	$-1.8 \pm 3.1 \times 10^{-8}$	$-3.3 \pm 2.8 \times 10^{-4}$	0.19
Phase 1	$-3.0 \pm 1.6 \times 10^{-9}$	$2.3 \pm 9.8 \times 10^{-3}$	0.53
Phase 2	$-2.3 \pm 1.6 \times 10^{-9}$	$8.7 \pm 9.8 \times 10^{-3}$	0.41
Amplitude 1	$-1.5 \pm 0.3 \times 10^{-5}$	$-0.1 \pm 1.9 \times 10^{-7}$	0.05
Amplitude 2	$-9.2 \pm 2.4 \times 10^{-5}$	$-1.5 \pm 2.0 \times 10^{-7}$	0.33
Transmission 1	$-3.5 \pm 0.4 \times 10^{-6}$	$-9.7 \pm 9.0 \times 10^{-6}$	0.61
Transmission 2	$-1.9 \pm 0.4 \times 10^{-6}$	$2.0 \pm 9.0 \times 10^{-6}$	0.31
Field Bx	$7.0 \pm 1.7 \times 10^{-7}$	$6.5 \pm 2.9 \times 10^{-5}$	0.82
Field By	$-5.0 \pm 1.2 \times 10^{-6}$	$5.1 \pm 4.1 \times 10^{-7}$	0.05
Field Bz	$-2.1 \pm 0.2 \times 10^{-6}$	$-2.0 \pm 1.8 \times 10^{-5}$	0.76
Piezo 1	$-3.1 \pm 1.0 \times 10^{-8}$	$-0.8 \pm 2.7 \times 10^{-5}$	0.02
Piezo 2	$-4.3 \pm 0.9 \times 10^{-8}$	$-7.3 \pm 3.0 \times 10^{-5}$	0.06
Laser Power	$-6.6 \pm 5.0 \times 10^{-5}$	$-0.6 \pm 2.5 \times 10^{-7}$	0.30
Laser Current	$-7.2 \pm 3.5 \times 10^{-6}$	$-1.3 \pm 1.1 \times 10^{-6}$	0.17
Temperature	$5.6 \pm 2.8 \times 10^{-5}$	$0.1 \pm 1.8 \times 10^{-7}$	0.18
Beam Horizontal	$-5.1 \pm 0.8 \times 10^{-6}$	$-0.4 \pm 2.7 \times 10^{-6}$	0.25
Beam Vertical	$3.9 \pm 1.0 \times 10^{-6}$	$5.5 \pm 9.1 \times 10^{-7}$	0.06
Beam Transmission	$-1.8 \pm 1.2 \times 10^{-6}$	$-3.4 \pm 2.7 \times 10^{-6}$	0.11

Table 4.6 continued.

Parameter Name	Linear correlation slope	HV correlation	d_{Hg} (10^{-30} e cm)
Background 1	$-4.0 \pm 1.0 \times 10^{-3}$	$2.1 \pm 8.3 \times 10^{-9}$	0.60
Background 2	$-5.4 \pm 1.3 \times 10^{-3}$	$-1.0 \pm 0.9 \times 10^{-8}$	0.99
Amplitude Dev 1	$5.0 \pm 2.6 \times 10^{-5}$	$-5.3 \pm 6.1 \times 10^{-7}$	0.55
Amplitude Dev 2	$2.5 \pm 2.8 \times 10^{-5}$	$-1.2 \pm 6.3 \times 10^{-7}$	0.32
Phase Dev 1	$1.6 \pm 0.3 \times 10^{-3}$	$1.4 \pm 5.8 \times 10^{-8}$	1.68
Phase Dev 2	$1.8 \pm 0.3 \times 10^{-3}$	$-7.5 \pm 5.4 \times 10^{-8}$	2.44
Phase1 - Phase2	$3.9 \pm 1.6 \times 10^{-6}$	$5.4 \pm 8.1 \times 10^{-6}$	0.57

significant HV correlations, although there are three parameters with an HV correlation greater than 2σ: relaxation time 1, the Bx magnetometer channel, and the second doubling cavity piezo voltage.

The contribution of these correlations to the EDM signal is found from multiplying the HV correlation value by the slope of the linear correlation with the frequency difference. For the purposes of this estimate, we pick the larger of either the central value or uncertainty from columns two and three in Table 4.6 and multiply them together, giving the EDM contribution in column four. The largest value is 0.024×10^{-28} e cm from the Phase Deviation 2 channel, a factor of 20 smaller than our statistical error. We estimate the limit on possible EDM contributions from these types of correlations by adding together all of column four of Table 4.6 in quadrature, which gives

$$d_{corr} < 0.04 \times 10^{-28}\ e\,\mathrm{cm}. \tag{4.25}$$

4.4.5 Light Effects

Interactions with the off-resonant probe light can shift the ^{199}Hg energy levels, but in order to directly generate an EDM systematic, a light induced effect would have to differentially shift the ground or excited state Zeeman sublevels to effect the Larmor frequency, and the shift would also have to be dependent on the electric field direction. The only probe light effect we are aware of that meets both of these requirements is caused by electric field induced interference of magnetic dipole ($M1$) and electric quadrupole ($E2$) amplitudes into the $6^1S_0 \rightarrow 6^3P_1$ ^{199}Hg intercombination

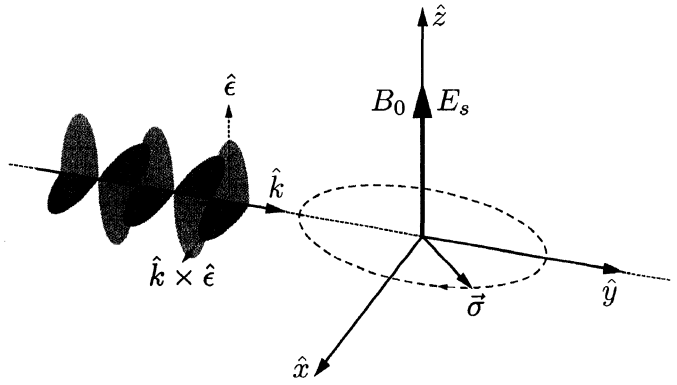

Figure 4.15: Coordinate system for the EDM measurement. Incident linearly polarized light propagating in the $\hat{y}$ direction interacts with ^{199}Hg spins precessing in the xy-plane.

transition. This Stark interference effect leads to a small fractional change in the absorptivity α of the ^{199}Hg vapor:

$$\frac{\delta\alpha}{\alpha} = (a_{E2} + a_{M1})(\hat{\boldsymbol{\epsilon}} \cdot \boldsymbol{E}_S)(\hat{\boldsymbol{k}} \times \hat{\boldsymbol{\epsilon}}) \cdot \boldsymbol{\sigma}, \tag{4.26}$$

where $\hat{\boldsymbol{\epsilon}}$ is the electric field direction of the probe light, $\boldsymbol{E}_S$ is the applied static electric field, $\hat{\boldsymbol{k}}$ is the propagation direction of the probe light, and $\boldsymbol{\sigma}$ is the spin polarization of the ^{199}Hg atoms. A derivation of the vector structure of Eq. 4.26 is given in [Hod91] and the a_{E2} and a_{M1} amplitudes have been calculated for ^{199}Hg in [Lam92] giving

$$a_{E2} + a_{M1} = -6.6 \times 10^{-8}\ (\mathrm{kV/cm})^{-1}. \tag{4.27}$$

With minimal modifications to the ^{199}Hg EDM apparatus, we have recently been working on measuring this effect [Swa05]. Our preliminary result is that $(a_{E2} + a_{M1}) \simeq -6 \times 10^{-8}\ (\mathrm{kV/cm})^{-1}$ with an uncertainty of about 20%, which is in good agreement with Eq. 4.27.

The change in absorptivity due to this effect leads to a change in the transition pump rate, $\delta\alpha/\alpha = \delta\Gamma_S/\Gamma$, and a corresponding energy shift, which for a Lorentzian line with a width of γ is

$$\delta\omega_S = \frac{\omega - \omega_0}{\gamma}\,\delta\Gamma_S = \frac{\omega - \omega_0}{\gamma}\,\frac{\delta\alpha}{\alpha}\,\Gamma(\omega).$$

The spin dependence of this energy shift, $(\hat{\boldsymbol{k}} \times \hat{\boldsymbol{\epsilon}}) \cdot \boldsymbol{\sigma}$ is equivalent to a Zeeman shift from an effective magnetic field in the $\hat{\boldsymbol{k}} \times \hat{\boldsymbol{\epsilon}}$ direction.

Figure 4.15 shows the general vector alignment used during the EDM measurement. For perfect alignment the effective magnetic field is in the $\hat{\boldsymbol{x}}$ direction, so even though Eq. 4.26 is linear in the

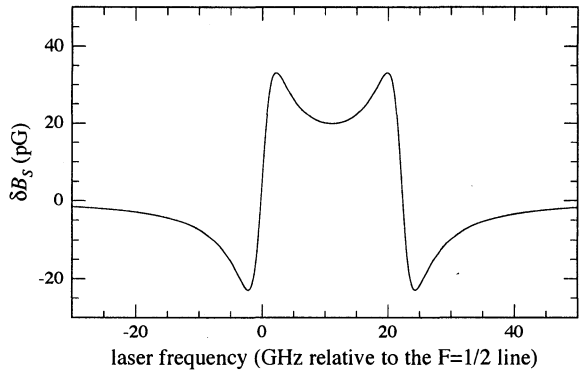

Figure 4.16: Effective magnetic field due to Stark interference versus the probe light detuning. The size of the effect is calculated using the results of [Lam92] with $(\hat{\boldsymbol{\epsilon}} \cdot \boldsymbol{E}_S)(\hat{\boldsymbol{k}} \times \hat{\boldsymbol{\epsilon}}) \cdot \boldsymbol{\sigma} = 10$ kV/cm, and an incident light intensity of 10 μW/cm^2.

electric field, the Stark interference would not cause an EDM-like shift to first order. A direct EDM systematic arises only if there is a misalignment such that $\hat{\boldsymbol{k}} \times \hat{\boldsymbol{\epsilon}}$ has a projection along the main magnetic field direction. Since this effect is enhanced when the magnetic field is tilted away from $\hat{\boldsymbol{\epsilon}}$, the limit on a possible motional magnetic field systematic effect (Eq. 4.24) obtained from the tilted magnetic field runs can also be interpreted as an upper bound on the Stark interference systematic contribution.

However, the calculated size of the Stark interference effect is substantially smaller than the limit given in Eq. 4.24. Figure 4.16 shows the size and frequency dependence of the effective magnetic field due to the Stark interference effect evaluated for the ideal vector orientation at an electric field of 10 kV/cm and an incident intensity of 10 μW/cm^2. For a probe detuning of -20 GHz, the effective magnetic field is about 3 pG, corresponding to a shift in the Larmor frequency of 2 nHz. If we assume that the experimental alignment is good to the 1° level, then the upper bound on a Stark interference systematic contribution is

$$d_S < 0.04 \times 10^{-28}\ e\,\mathrm{cm}. \tag{4.28}$$

Additionally, if the probe light is not perfectly linearly polarized, then the two ground state Zeeman sublevels experience different energy shifts from the slightly circularly polarized light field, leading to an effective magnetic field along $\hat{\boldsymbol{k}}$. At -20 GHz, a 10 μW/cm^2 fully circularly polarized probe beam would cause a 5 μG effective magnetic field (see Sec. A.2). The effect of this light shift field on the precession frequency is suppressed as long as $\hat{\boldsymbol{k}}$ is perpendicular to $\boldsymbol{B}_0$. If we assume a

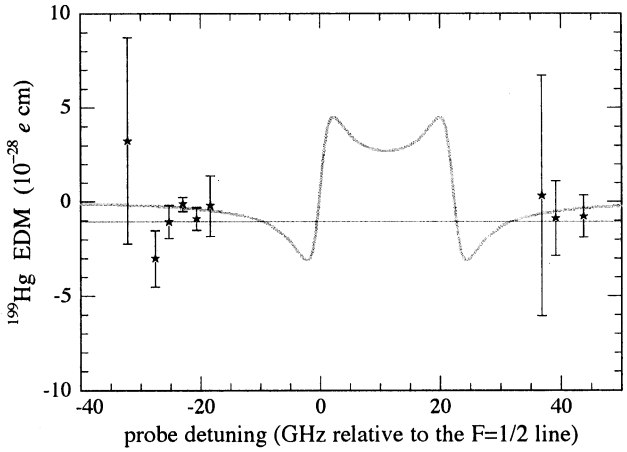

Figure 4.17: EDM signal dependence on probe light detuning. The horizontal line denotes the average EDM value from the entire dataset and the grey curve denotes the expected frequency dependence of a light shift effect but is of arbitrary magnitude. The size of the error bars mainly reflects the amount of data taken at each detuning.

1° tilt of the magnetic field and a probe beam circularity of 1%, then this effective magnetic field would still cause a relatively substantial shift in the precession frequency of 0.7 μHz. However, this effect is not directly related to the applied electric field and would only lead to a systematic effect if probe light intensity, steering, or circularity were correlated with the electric field direction. Due to the magnetic field alignment dependence, any effect of this type can also be considered to fall within the constraint of Eq. 4.24.

Figure 4.17 shows the EDM results when binned versus the probe light detuning. These results show no significant dependence of the EDM signal on the detuning. The majority of the dataset was taken around -20 GHz (65 runs) and a small set of runs was taken at $+40$ GHz (9 runs). The average EDM signal at the -20 GHz detuning was $-1.04 \pm 0.51 \times 10^{-28}$ e cm, and at -40 GHz the signal was $-1.36 \pm 1.74 \times 10^{-28}$ e cm. However, the Stark interference effect and the vector light shift both have the same detuning dependence behavior, and as is shown in Figure 4.16, the shift at -20 GHz due to these types of effects has the same sign and magnitude as the shift at $+40$ GHz.

4.4.6 Other Systematic Checks

Of all the changes made to the apparatus during the dataset, the most substantial change was switching from the Al coated Teflon vessel to the conductive polyethylene vessel at Run 59717. The

Table 4.7: HG3 EDM value obtained from subsets of the final HG3 dataset. The EDM value is given in units of 10^{-28} e cm.

subset		$d(^{199}\mathrm{Hg})$	χ^2	number of runs
vessel	Teflon	−1.49(.72)	0.79	51
	PE	−0.71(.65)	1.35	23
B direction	up	−0.36(.69)	0.94	34
	down	−1.78(.70)	0.93	40
Ch direction	+	1.01(.57)	0.90	62
	−	−1.21(.95)	1.24	12

EDM result obtained for data taken with each vessel is shown in Table 4.7, and the two values are within 0.8σ of each other. Each vessel gave one instance of large HV correlated frequency shifts, as was discussed in Section 4.3, although the false signal that occurred with the Teflon vessel disappeared after only one run, and the false signal occurrence with the PE vessel persisted for eight runs. Beyond the HG3 dataset, the conductive PE 2-cell vessel was brought back into operation in 2004 to help investigate the origin of false signals seen in the 4-cell apparatus, at which point the 2-cell PE vessel participated in producing additional instances of HV correlated false signals (see Sec. 7.4.1). The Teflon vessel, on the other hand, has not been used since being retired before HG3 Run 59717.

The magnetic field direction gives the largest deviation of EDM value out of the data subsets considered in Table 4.7, giving a 1.4σ difference between the EDM results for the magnetic field up and down. A resolved difference between the magnetic field direction results would be evidence for a systematic effect that would not reverse with the magnetic field, but such an effect would cancel in the end result as long as equal amounts of data were taken with both field directions. The DAQ channel direction (Ch) results are quite consistent with each other. A resolved difference for this reversal might be evidence for an electronic crosstalk systematic issue in the data acquisition system.

Figure 4.19 shows the dependence of the EDM signal on the HV reversal time (t_{HVS}). A shorter HV reversal time leads to larger charging currents flowing during the pump phase, although since the HV ramp always started at the beginning of the 30 second pump phase, a shorter HV reversal time also gives more "settling" time between the end of the HV ramp and the start of the probe phase. By eye, Figure 4.19 appears to show a slight negative trend in the EDM result for longer HV reversal times, but the data is consistent with a single average ($\chi^2 = 0.72$).

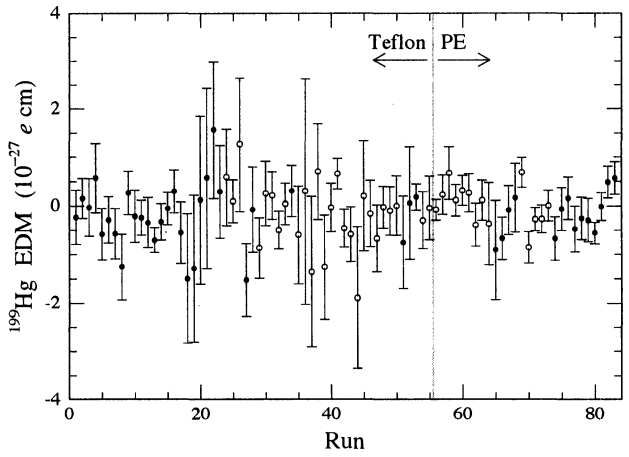

Figure 4.18: EDM signal from HG3 data runs. Runs where the magnetic field was in the $B+$ direction (down) are solid points, and the open points show when the magnetic field was in the $B-$ direction (up). The vertical line denotes the transition point from the Teflon vessel to the polyethylene vessel.

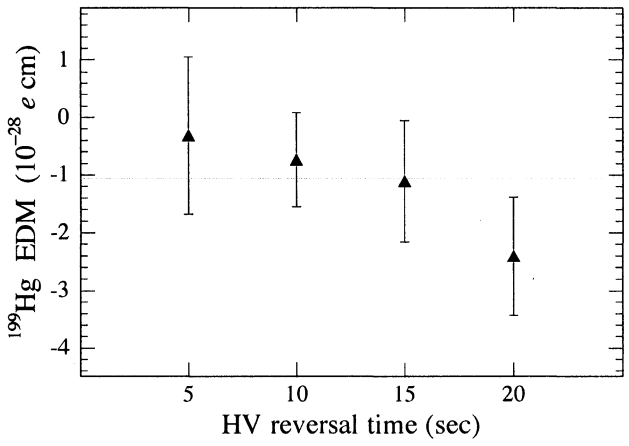

Figure 4.19: Dependence of the EDM result on the HV reversal time. The horizontal line denotes the average EDM value from the entire dataset.

Table 4.8: Systematic error budget for the HG3 measurement.

	Limit (10^{-28} e cm)
$\boldsymbol{B}$ misalignment ($\boldsymbol{v} \times \boldsymbol{E}$ and light shifts)	0.30
leakage currents (one loop estimate)	0.25
E^2 effects	0.07
parameter correlations	0.04

4.5 Final Results

We estimate our total systematic error by combining in quadrature the limits on EDM contributions from leakage currents, $\boldsymbol{B}$ misalignment, E^2 effects, and parameter correlations (Eqs. 4.22, 4.24, 4.23, and 4.25). This gives a total systematic error of 0.40×10^{-28} e cm, with the dominant contributions overwhelmingly coming from the leakage current and $\boldsymbol{B}$ misalignment estimates. Our final ^{199}Hg EDM result for the HG3 dataset is then

$$d(^{199}\mathrm{Hg}) = (-1.06 \pm 0.49_{\mathrm{stat.}} \pm 0.40_{\mathrm{syst.}}) \times 10^{-28}\ e\,\mathrm{cm}. \tag{4.29}$$

If we combine the statistical and systematic uncertainties in quadrature, then our total uncertainty is 0.63×10^{-28} e cm, which places our EDM central value 1.68σ away from zero. There is a 10% probability that a Gaussian distribution would give a greater than 1.68σ measurement, and we interpret our result as being consistent with zero. Again assuming a Gaussian distribution, our result of $d = -1.06 \pm 0.63 \times 10^{-28}$ e cm sets a 95% confidence level upper bound on the magnitude of the ^{199}Hg EDM:

$$\left|d(^{199}\mathrm{Hg})\right| < 2.1 \times 10^{-28} e\,\mathrm{cm} \quad (95\%\ \mathrm{C.L.}). \tag{4.30}$$

Chapter 5

THEORETICAL INTERPRETATION OF THE ^{199}Hg EDM

The final result quoted in Section 4.5 is the most precise (null) energy shift measurement ever performed. However, a null atomic EDM measurement by itself is not all that interesting unless it can be interpreted in terms of the EDMs of more fundamental particles, or compared to the predictions of theoretical models. Fortunately, the problem of interpreting atomic EDMs has attracted a number of excellent theorists over the years, and with their help we are able to use the ^{199}Hg measurement to set limits on physics beyond the standard model such as supersymmetry. A thorough examination of the theory behind atomic EDMs is given in Khriplovich and Lamoreaux's book [Khr97], and in a review article by Ginges and Flambaum [Gin04].

In this chapter I will sketch out some of the theoretical steps involved in relating the ^{199}Hg EDM to more fundamental quantities. The EDM of a ^{199}Hg atom could arise from three general types of CP violating interactions: leptonic (the EDM of the electron), semileptonic (an interaction between an electron and nucleon), or hadronic (the EDM of a nucleon or an interaction between nucleons).

5.1 Electron EDM

Since Hg has no ground state electronic spin, its sensitivity to the electron EDM is small compared to paramagnetic systems (see Sec. 1.2.2). However, the electron EDM can generate an EDM in ^{199}Hg through higher order perturbations, and the extremely high precision obtained in our ^{199}Hg result can be used to set a competitive limit on the electron EDM.

In atoms with a $^1S_0$ ground state, the interaction between an electron EDM and the magnetic field due to the nuclear magnetic moment can generate an EDM of the atom. Flambaum and Khriplovich in [Fla85a] show that this effect roughly scales as

$$d_{atom} \sim (R-1)Z^2\alpha^2(m_e/m_p)d_e. \tag{5.1}$$

R is a relativistic factor that also appears in Eq. 1.6, and it is given by

$$R = \left(\frac{a}{2Zr_0}\right)^{2-2\gamma} \frac{4}{[\Gamma(2\gamma+1)]^2}, \quad \gamma = (1-Z\alpha^2)^{1/2}, \tag{5.2}$$

where a is the Bohr radius and r_0 is the nuclear radius ($r_0(\mathrm{H}g) = 7$ fm). In the case of mercury, $R = 8$, so that $d_{atom} \sim 10^{-3}d_e$. It is also shown in [Fla85a] that there is a somewhat larger effect

due to the hyperfine interaction coupling to the electron EDM as a third order perturbation. The combination of these effects was calculated to give $d(^{199}\mathrm{Hg}) = -0.014\, d_e$.

A Hartree-Fock calculation of these effects has also been performed [MP86], which obtained the result $d(^{199}\mathrm{Hg}) = 0.0116\, d_e$. The magnitude is essentially the same, but it has the opposite sign from the [Fla85a] estimate, possibly indicating that a higher order calculation might change the result significantly. If we use the result in [MP86], then our ^{199}Hg EDM limit can be used to set a limit on the magnitude of d_e:

$$|d_e| < 1.8 \times 10^{-26}\ e\,\mathrm{cm}. \tag{5.3}$$

This limit is an order of magnitude larger than the limit set from Thallium ($|d_e| < 1.6 \times 10^{-27}\ e\,\mathrm{cm}$) [Reg02].

5.2 *Semileptonic*

The ^{199}Hg limit can also be used to set tight bounds on CP violating electron-nucleon interactions. The general form of for these interactions can be written as [Gin04, Khr97]:

$$H = \frac{G_F}{\sqrt{2}} \sum_{j=p,n} \left[C_j^{SP} (\overline{N}_j N_j)(\overline{e} i\gamma_5 e) + C_j^{PS} (\overline{N}_j i\gamma_5 N_j)(\overline{e} e) + C_j^{T} (\overline{N_j} i\gamma_5 \sigma_{\mu\nu} N_j)(\overline{e}\sigma_{\mu\nu} e) \right], \tag{5.4}$$

where G_F is the Fermi coupling constant of the weak interaction, the summation runs over all protons and neutrons, and N and e represent the nucleon and electron wave functions. The dimensionless constants[1] C_j^{SP}, C_j^{PS}, and C_j^T set the strength of the scalar-pseudoscalar, pseudoscalar-scalar, and tensor electron-nucleon interactions for nucleon j.

The dependence of the atomic EDM on the constants C^{SP}, C^{PS}, and C^T has been calculated for ^{199}Hg and other relevant atomic systems, assuming that the EDM is due only to one of the electron-nucleon interactions, and the results are summarized in [Gin04], Table 14. For ^{199}Hg, the dependence is:

$$d(\mathrm{Hg})/(e\,\mathrm{cm}) = \begin{cases} -5.9 \times 10^{-22} (0.40\, C_p^{SP} + 0.60\, C_n^{SP}) \\ 2.0 \times 10^{-20}\, C_n^T \\ 6.0 \times 10^{-23}\, C_n^{PS} \end{cases} \tag{5.5}$$

[1] In [Khr97], $k_1 = C^{SP}$, $k_2 = C^T$, and $k_3 = C^{PS}$.

Using Eqs. 4.30 and 5.5, we can set upper bounds on semileptonic CP violation. The best limit on C^{SP} comes from the Tl experiment, which gives $(0.40\,C_p^{SP} + 0.60\,C_n^{SP}) < 1.3 \times 10^{-7}$. Since the C^{SP} term in Eq. 5.4 mainly depends on the electronic spin, $\vec{J}$, the ^{199}Hg EDM has a relatively small dependence on C^{SP}, but due to the same effect discussed in the previous section (5.1), the ^{199}Hg limit can be used to set a bound:

$$(0.40\,C_p^{SP} + 0.60\,C_n^{SP}) < 3.4 \times 10^{-7} \tag{5.6}$$

that is only slightly larger than the Tl limit.

The ^{199}Hg EDM limit currently sets the tightest constraints on the tensor and pseudoscalar-scalar components of Eq. 5.4. The bound on the tensor component from ^{199}Hg is

$$C_n^T < 1.1 \times 10^{-8}. \tag{5.7}$$

The next best limit on C^T comes from the TlF EDM experiment [Cho89, Khr97], which gives $(0.75\,C_p^T + 0.25\,C_n^T) < 4.5 \times 10^{-7}$. The bound on the pseudoscalar-scalar component from ^{199}Hg is

$$C_n^{PS} < 3.5 \times 10^{-6}, \tag{5.8}$$

and the next best limit is again set by TlF, which gives $(0.75\,C_p^{PS} + 0.25\,C_n^{PS}) < 3 \times 10^{-4}$.

5.3 Hadronic

5.3.1 The Schiff Moment

An EDM of a nucleon or a CP violating nucleon-nucleon interaction can lead to a CP odd nuclear moment (electric dipole, magnetic quadrupole, electric octupole, etc.). Since ^{199}Hg has a nuclear spin $I = 1/2$, the only possible CP odd nuclear moment is an electric dipole moment. As was discussed in Sec. 1.2.3, when the EDM of a neutral atom is measured by applying an external electric field, the electron cloud conspires to cancel the electric field at the nucleus, and a nuclear EDM would not produce an energy shift due to the external electric field. This shielding is perfect in the limit of purely electrostatic forces and point particles, but breaks down for heavy atoms such as Hg, where the finite size of the nucleus can cause the dipole moment and charge distributions to be different. For example, if the nuclear EDM is generated by a valence nucleon, there can be a net electric field on this valence nucleon, while the electric field averaged over the entire nuclear charge density is zero.

The degree to which the nuclear EDM is unshielded is traditionally parameterized in terms of the Schiff moment, $\boldsymbol{S} = S\boldsymbol{I}/I$, where the size of S depends on the details of the CP violation occurring in the nucleus. The electric dipole moment and the Schiff moment of the nucleus with a charge density $\rho(\boldsymbol{r})$ is given by [Gin04, Eq. 160]:

$$\boldsymbol{d} = \int e\boldsymbol{r}\rho(\boldsymbol{r})\mathrm{d}^3r, \tag{5.9}$$

$$\boldsymbol{S} = \frac{1}{10}\left[\int e\rho(\boldsymbol{r})\boldsymbol{r}r^2\mathrm{d}^3r - \frac{5}{3}\boldsymbol{d}\frac{1}{Z}\int \rho(\boldsymbol{r})r^2\mathrm{d}^3r\right]. \tag{5.10}$$

The effect of the Schiff moment can be thought of as generating an electrostatic potential which corresponds to a constant electric field ($\boldsymbol{E}_S = -\nabla V_S$) inside the nucleus pointing along the nuclear spin [Fla02]:

$$V_S(\boldsymbol{r}) = -\frac{15\,\boldsymbol{S}\cdot\boldsymbol{r}}{r_0}n(r), \tag{5.11}$$

where r_0 is the nuclear radius and $n(r)$ is a smooth function approximating the nuclear density with $n(r) = 1$ for $r < r_0 - \delta$ and $n(r) = 0$ for $r > r_0 + \delta$. The interaction of this field with the atomic electrons leads to an EDM of an atom (in the ground state) [Dmi03b]:

$$d_{atom} = \sum_n \frac{\langle 0|-e\sum_i^Z V_S(\boldsymbol{r}_i)|n\rangle\langle n|-e\sum_i^Z \boldsymbol{r}\cdot(\boldsymbol{I}/I)|0\rangle}{E_n - E_0} + \text{H.C.}, \tag{5.12}$$

where the summation is over all atomic states, but since V_S is nonzero only inside the nucleus, mainly s and p electron orbitals contribute.

The atomic calculation (Eq. 5.12) has been carried out for ^{199}Hg recently by Dzuba et al. [Dzu02], and it was found that,

$$d(^{199}\mathrm{Hg}) = -2.8\times10^{-17}\left(\frac{S}{e\,\mathrm{fm}^3}\right)\ e\,\mathrm{cm}, \tag{5.13}$$

which we can use to set a limit on the magnitude of the ^{199}Hg Schiff moment, $S < 7.5\times10^{-12}\ e\,\mathrm{fm}^3$. Dzuba et al. estimate the maximum error in this calculation to be 20%.

Prior to the [Dzu02] calculation, the ^{199}Hg EDM was interpreted using a somewhat larger relation, $d(^{199}\mathrm{Hg}) = -4\times10^{-17}S(e\,\mathrm{fm}^3)^{-1}\ e\,\mathrm{cm}$ [Fla85b]. This relation was not based on a direct calculation, but was interpolated by combining a calculation of the ^{129}Xe EDM due to its Schiff moment, and direct calculations of the dependences of the ^{199}Hg and ^{129}Xe EDMs on the semileptonic tensor interaction strength (C_N^T) [Khr97, pg. 172]. The smaller dependence of the ^{199}Hg EDM on the Schiff moment given by Eq. 5.13 relaxes by 30% the bounds quoted in Table 1 of our last publication [Rom01a].

5.3.2 Nucleon EDMs

A Schiff moment of ^{199}Hg could be generated by the EDM of a nucleon. In the simple nuclear shell model a nuclear spin of 1/2 is associated with a single valence nucleon, and for ^{199}Hg the valence nucleon is a neutron, so the main nucleon EDM contribution to the ^{199}Hg Schiff moment is from the neutron EDM. Interactions between the valence neutron and protons in the core can lead to a proton EDM contribution to the ^{199}Hg Schiff moment. The dependence of the ^{199}Hg Schiff moment on the proton and neutron EDMs has been recently calculated by Dmitriev and Sen'kov to be [Dmi03b]

$$S(^{199}\text{Hg}) = (0.2d_p + 1.9d_n)\ \text{fm}^2. \tag{5.14}$$

By combining equations 5.13 and 5.14 the dependence of the ^{199}Hg EDM on the proton and neutron EDMs is

$$d(^{199}\text{Hg}) = -(0.56d_p + 5.3d_n) \times 10^{-4}. \tag{5.15}$$

Our result (Eq. 4.30) can then be used to estimate a limit on the neutron EDM, $|d_n| < 4.0 \times 10^{-25}\ e\,\text{cm}$, which is within an order of magnitude of the direct neutron limit. The limit on the proton EDM is $|d_p| < 3.8 \times 10^{-24}\ e\,\text{cm}$, which is significantly lower than the previous best limit of $d_p = -4 \pm 6 \times 10^{-23}\ e\,\text{cm}$, derived from the TlF EDM measurement [Cho89].

Dmitriev and Sen'kov claim a maximum error of 30% in the numerical factors in Eq. 5.14, and including this uncertainty they estimate the upper bound from ^{199}Hg on the proton EDM to be $|d_p| < 5.4 \times 10^{-24}\ e\,\text{cm}$, which is the currently accepted limit by the Particle Data Group [Eid04].

5.3.3 Nucleon-Nucleon Interactions

From the previous sections, it may be noticed that the ^{199}Hg EDM is actually 20 times less sensitive to a nucleon EDM than to an electron EDM ($d(^{199}\text{Hg}) \sim 0.01d_e - 0.0005d_n$). It is true that Standard Model predictions for the electron EDM are at least 5 orders of magnitude smaller than the neutron EDM, but this is not necessarily the case in other theoretical models of CP violation. However, it has been estimated that for a given source of CP violation, the contribution to the nuclear Schiff moment due to nucleon-nucleon interactions is likely two orders of magnitude larger than the contribution due to nucleon EDMs (see [Gin04, Sec. 9.3.3] and [Sus84]). So it is expected that the dominant contribution to an EDM of ^{199}Hg would be through nucleon-nucleon interactions.

The largest contribution to a CP odd nucleon-nucleon interaction is expected to arise from the exchange of π-mesons. This is because pions are the lightest mesons, so they lead to the longest

range interactions, and the strong force pion-nucleon coupling is relatively large. The Lagrangian of the interaction can be separated into isospin components [Her88]:

$$L_{I=0} = \overline{g}_0 \overline{N} \vec{\tau} N \cdot \vec{\pi}, \tag{5.16}$$

$$L_{I=1} = \overline{g}_1 \overline{N} N \pi^0, \tag{5.17}$$

$$L_{I=2} = \overline{g}_2 \overline{N} (3\tau_z \pi^0 - \vec{\tau} \cdot \vec{\pi}) N, \tag{5.18}$$

where $\vec{\tau}$ contains the Pauli spin matrices, $N = \{p, n\}$, $\vec{\pi} = \{\pi^+, \pi^0, \pi^-\}$, and the dimensionless constants $\overline{g}_I \equiv \overline{g}^I_{\pi NN}$ give the strength of the isoscalar, isovector, and isotensor interactions. The isovector contribution to the mean nuclear potential seen by a nucleon scales roughly as $N + Z = A$ in heavy nuclei, but the isoscalar and isotensor components scale as $N - Z$ [Dmi04a], so the ^{199}Hg EDM is expected to be most sensitive to $\overline{g}_1$, and its sensitivity to $\overline{g}_0$ and $\overline{g}_2$ somewhat smaller.

The couplings in Eqs. 5.16–5.18 lead to a finite range CP violating interaction between two nucleons of the form [Dmi03a]

$$\begin{aligned} V = -\frac{g}{8\pi m_N} \Big[&\left(\overline{g}_0 \vec{\tau}_1 \cdot \vec{\tau}_2 + \overline{g}_2 (\vec{\tau}_1 \cdot \vec{\tau}_2 - 3\tau_{1z}\tau_{2z})\right)(\boldsymbol{\sigma}_1 - \boldsymbol{\sigma}_2) \\ &+ \overline{g}_1 (\tau_{1z}\boldsymbol{\sigma}_1 - \tau_{2z}\boldsymbol{\sigma}_2) \Big] \cdot \boldsymbol{\nabla}_1 \frac{\exp(-m_\pi |\boldsymbol{r}_1 - \boldsymbol{r}_2|)}{|\boldsymbol{r}_1 - \boldsymbol{r}_2|}, \end{aligned} \tag{5.19}$$

where $g \simeq 13.5$ [Mac01] represents the (CP conserving) strong force pion-nucleon coupling and the $\boldsymbol{\sigma}_k$ are the spin of the nucleons.

Simple shell model calculation

A full calculation of the nuclear Schiff moment due to the potential given in Eq. 5.19 is an extremely complex many body nuclear calculation in a large nucleus such as ^{199}Hg. The interpretation of the nucleon-nucleon contribution to atomic EDMs has generally used what could be called lowest order, crude estimates based on the simple nuclear shell model, that do not take into account any many-body effects. For a nucleus with an odd number of protons and an even number of neutrons it is expected that the main contribution to the Schiff moment comes from the valence proton. In the case of a CP violating nucleon-nucleon interaction, the valence proton wave function becomes polarized due to the potential in Eq. 5.19, which then generates a nonzero Schiff moment. However if the valence nucleon is a neutron, as is the case for ^{199}Hg, the polarization of the neutron wave function does not generate a Schiff moment because it carries no net charge, and the Schiff moment is calculated from the nuclear charge density. The lowest order contribution to the ^{199}Hg Schiff moment then comes from single proton excitations out of the closed shell core ground state [Dmi04b]:

$$\boldsymbol{S} = \sum_{1p1h} \frac{\langle \nu, 0 | \hat{\boldsymbol{S}} | 1p1h, \nu \rangle \langle \nu, 1p1h | V | 0, \nu \rangle + \langle \nu, 0 | V | 1p1h, \nu \rangle \langle \nu, 1p1h | \hat{\boldsymbol{S}} | 0, \nu \rangle}{E_0 - E_{1p1h}}, \tag{5.20}$$

where $\langle \nu, 0|$ denotes the nuclear ground state of a closed core and one valence nucleon, $\langle \nu, 1p1h|$ is the single proton (1 particle, 1 hole) core excitation, and V is the CP violating interaction.

The nucleon-nucleon interaction contribution to the ^{199}Hg EDM has traditionally been interpreted with a calculation of Eq. 5.20 performed in 1985 by Flambaum, Khriplovich, and Sushkov [Fla85b, Fla86] using nuclear wave functions from a Woods-Saxon potential with spin-orbit correction. The calculation used a contact interaction potential to describe the interaction between nucleons a and b:

$$\begin{aligned} V_{ab} =& \frac{G_F}{\sqrt{2}} \frac{1}{2m_N} \big((\eta_{ab} \boldsymbol{\sigma}_a - \eta_{ba} \boldsymbol{\sigma}_b) \cdot \boldsymbol{\nabla}_a \delta(\boldsymbol{r}_a - \boldsymbol{r}_b) \\ &+ \eta'_{ab} [\boldsymbol{\sigma}_a \times \boldsymbol{\sigma}_b] \cdot \{ (\boldsymbol{p}_a - \boldsymbol{p}_b), \delta(\boldsymbol{r}_a - \boldsymbol{r}_b) \} \big), \end{aligned} \tag{5.21}$$

where the constants η_{NN} set the strength of the interaction. In the lowest order approximations used, the ^{199}Hg Schiff moment is dependent on a single constant, η_{np}.

We can compare the coupling constants for the finite range interaction (Eq. 5.19) and the contact interaction (Eq. 5.21) by taking the zero-range limit of Eq. 5.19 ($m_\pi \to \infty$), which then reduces to Eq. 5.21. In this limit the correspondence for η_{np} is [Dmi04b]

$$\eta_{np} = \frac{\sqrt{2}}{G_F \, m_\pi^2} g(\overline{g}_0 + \overline{g}_1 - 2\overline{g}_2) \simeq 6.7 \times 10^6 g(\overline{g}_0 + \overline{g}_1 - 2\overline{g}_2). \tag{5.22}$$

The result of the calculation was

$$S(^{199}\mathrm{Hg}) = -\, 1.4 \times 10^{-8} \, \eta_{np} \, e\,\mathrm{fm}^3 \tag{5.23}$$

$$\simeq -\, 0.09 g(\overline{g}_0 + \overline{g}_1 - 2\overline{g}_2) \, e\,\mathrm{fm}^3. \tag{5.24}$$

Flambaum et al. estimate that the many body corrections to this estimate might be as large as 100% [Fla86].

Finite range many body calculation

In order to incorporate many-body effects into the Schiff moment calculation, a mean field approximation method must be used. At present, there has been one published calculation of the ^{199}Hg Schiff moment that has considered many-body effects. The calculation was performed by Dmitriev and Sen'kov [Dmi03a], and they used the random phase approximation (RPA) method with effective residual forces and a finite range potential (Eq. 5.19). The result of their calculation gave

$$S(^{199}\mathrm{Hg}) = g(-0.0004\,\overline{g}_0 - 0.055\,\overline{g}_1 + 0.009\,\overline{g}_2) \; e\,\mathrm{fm}^3. \tag{5.25}$$

So compared to the simpler estimate (Eq. 5.24), the newer calculation finds a large (one or two orders of magnitude) cancellation of the isoscalar and isotensor components, and about a factor of

two reduction in the isovector component. Dmitriev and Sen'kov find that the difference in the calculated size is mainly due to the many-body effect of the core polarization, and the finite range potential has only a small effect.

At least one other many-body calculation has been performed, although it was not published except for being mentioned in a conference proceedings [Hax94]. The calculation was the thesis project of Kar Lee [Lee94] advised by Wick Haxton, and it used the Nilsson rotational model to approximate the nuclear wave functions. The Nilsson model can describe the slight deformation of the ^{199}Hg nucleus ($\delta \simeq -0.1$) and allows for a full calculation of the core polarizability. The result of this calculation gave

$$S(^{199}\mathrm{Hg}) = g(0.044\,\overline{g}_0 - 0.23\,\overline{g}_1 - 0.0011\,\overline{g}_2)\ e\,\mathrm{fm}^3. \tag{5.26}$$

Lee and Haxton planned to vary the deformation parameter δ to check that their calculation did not happen to be subject to a chance cancellation region, but unfortunately this work was not completed and the result was not published [Hax04]. Compared to Dmitriev and Sen'kov's result (Eq. 5.25), Lee's calculation gives a comparable, although a few times larger, value for the isovector coupling, but the isoscalar and isotensor results are of opposite sign and a substantially different magnitude. The discrepancy in the $\overline{g}_0$ and $\overline{g}_2$ terms is likely a result of the $N-Z$ cancellation in these channels, which leads to a larger fractional uncertainty compared to the $\overline{g}_1$ term. There is still a factor of four difference between the isovector estimates of Eqs. 5.25 and 5.26, and additional nuclear calculations would be very welcome at this point.

Limits from ^{199}Hg

Ignoring for now the (large) nuclear theory uncertainties, we can combine the nuclear calculations (Eqs. 5.23, 5.25, and 5.26) with the atomic calculation (Eq. 5.13) to set limits on the CP violating nucleon-nucleon coupling constants. Our upper bound on the ^{199}Hg EDM sets a limit on the contact interaction coupling strength η_{np}:

$$\begin{aligned} d(^{199}\mathrm{Hg}) &= 3.9 \times 10^{-25}\eta_{np}\ e\,\mathrm{cm}, \\ |\eta_{np}| &< 5 \times 10^{-4}. \end{aligned} \tag{5.27}$$

The best other limit on η_{np} comes from the ^{129}Xe EDM measurement [Ros01], which gives $|\eta_{np}| < 9 \times 10^{-2}$.

From Dmitriev and Sen'kov's calculation we can set limits on the CP violating pion-nucleon couplings:

$$\begin{aligned} d(^{199}\mathrm{Hg}) &= (0.015\,\overline{g}_0 + 2.1\,\overline{g}_1 - 0.34\,\overline{g}_2) \times 10^{-17}\ e\,\mathrm{cm}, \\ \rightarrow \quad |\overline{g}_0| &< 1.4 \times 10^{-9}, \quad |\overline{g}_1| < 1.0 \times 10^{-11}, \quad \text{and} \quad |\overline{g}_2| < 6.2 \times 10^{-11}, \end{aligned} \tag{5.28}$$

where in the individual limits we have assumed that only one of the coupling constants is nonzero. Similarly, Lee and Haxton's calculation gives:

$$\begin{aligned} d(^{199}\mathrm{Hg}) &= (-1.7\,\overline{g}_0 + 8.7\,\overline{g}_1 + 0.04\,\overline{g}_2) \times 10^{-17}\ e\,\mathrm{cm}, \\ \rightarrow \quad |\overline{g}_0| &< 1.3 \times 10^{-11}, \quad |\overline{g}_1| < 2.4 \times 10^{-12}, \quad \text{and} \quad |\overline{g}_2| < 5.0 \times 10^{-10}. \end{aligned} \tag{5.29}$$

The best other limits on the $\overline{g}_I$ coupling constants are derived from the neutron EDM limit. The neutron EDM is mainly sensitive to the isoscalar and isotensor components, and has a relative suppression of the isovector component. Herczeg estimates that the neutron EDM arising from $\overline{g}_I$ is given by [Her95]

$$d(n) \simeq 9 \times 10^{-15}(\overline{g}_0 + 0.1\overline{g}_1 - \overline{g}_2), \tag{5.30}$$

where there is a somewhat larger uncertainty in the $\overline{g}_1$ numerical coefficient, than in the other two terms. The neutron EDM limit [Har99] then sets limits on $\overline{g}_I$:

$$|\overline{g}_0| < 7 \times 10^{-12}, \quad |\overline{g}_1| < 7 \times 10^{-11}, \quad \text{and} \quad |\overline{g}_2| < 7 \times 10^{-12}, \tag{5.31}$$

which gives comparatively tighter bounds on $\overline{g}_0$ and $\overline{g}_2$, and a somewhat larger bound on $\overline{g}_1$. In the chiral limit ($m_\pi \rightarrow 0$) the neutron EDM dependence on $\overline{g}_I$ reduces to two calculable one loop diagrams, the result of which is [Cre79]

$$\begin{aligned} d(n) = \frac{e}{4\pi^2\, m_N} g(\overline{g}_0 - \overline{g}_2) \ln(m_N/m_\pi) \ &\simeq 1.4 \times 10^{-14}(\overline{g}_0 - \overline{g}_2)\ e\,\mathrm{cm} \\ \rightarrow \quad |\overline{g}_I| &< 4.5 \times 10^{-12} \quad (I = 0, 2). \end{aligned} \tag{5.32}$$

In this case there is a slightly smaller bound on $\overline{g}_0$ and $\overline{g}_2$, but no dependence on $\overline{g}_1$, and Eq. 5.32 is only strictly valid when $m_\pi \rightarrow 0$.

There are a large number of other model-independent phenomenological hadronic coupling constants that the ^{199}Hg EDM limit can constrain, but I will not describe them here. The interested reader can refer to the summary table in Ref. [Gin04, Table 20] and the references therein.

5.4 Model Dependent Limits

So far, I have discussed limits on CP violating parameters that are valid for any model of CP violation. The wide variety of possible CP violating theories that could lead to EDMs are far too

numerous to fully discuss, so I will limit this section to the Standard Model, supersymmetry, and a couple of other theoretical models discussed in a review article by Stephen Barr [Bar93].

5.4.1 The Standard Model and the Strong CP Problem

As has been mentioned previously, the CP violation in the Standard Model from the CKM quark mixing matrix responsible for the observed CP violation in K and B meson decays is far too small to generate a measurable EDM. The CKM contribution to the CP violating pion-nucleon couplings is of order $\overline{g}_1 \sim 10^{-17}$ [Dmi04a], which would generate a ^{199}Hg EDM of about 10^{-33} e cm (from Eq. 5.29).

However, there is another possible source of CP violation in the Standard Model. The most general form of the quantum chromodynamics (QCD) Lagrangian includes a CP violating term

$$L_{\not CP} = \theta \frac{\alpha_s}{8\pi} G^a_{\mu\nu} \tilde{G}^a_{\mu\nu}, \tag{5.33}$$

where G are gluon fields, a is the color index, α_s is the strong force coupling constant, and θ is an angle that could be anywhere between 0 and 2π. When the weak interaction is included, θ is shifted to its observable value $\overline{\theta}$.

The QCD θ-term is an isoscalar, and it can contribute to the CP violating isoscalar pion-nucleon coupling, $\overline{g}_0$. The calculated $\overline{\theta}$ contribution to $\overline{g}_0$ is [Cre79]

$$\overline{g}_0 = 0.027\,\overline{\theta}, \tag{5.34}$$

which can then be related to the EDM of the neutron or ^{199}Hg with the relations in Section 5.3.3. A more direct calculation using QCD sum rules of the neutron EDM due to $\overline{\theta}$ found that with about 50% accuracy, $d(n) = 1.2 \times 10^{-16}\,\overline{\theta}\ e$ cm[Pos99], which can be used to convert the experimental limit on $d(n)$ [Har99] into a limit on $\overline{\theta}$

$$|\overline{\theta}|_n < 6 \times 10^{-10}. \tag{5.35}$$

The extreme smallness of $\overline{\theta}$ implied by the neutron EDM limit is referred to as the strong CP problem. Theorists are very uncomfortable with the extreme degree of "fine tuning" involved in having to set a parameter, that *a priori* is of order unity, to $\sim 10^{-10}$, unless there is some fundamental reason that $\overline{\theta}$ should be zero. One possible reason that allows $\overline{\theta}$ to be zero was postulated by Peccei and Quinn [Pec77], where a spontaneously broken symmetry leads to a nearly massless Goldstone boson called the axion. The axion is a possible dark matter candidate, but there is currently no experimental evidence for its existence.

Using our ^{199}Hg EDM limit, we can set a bound on $\overline{\theta}$ comparable to the neutron limit. In our last publication [Rom01a], a limit of $|\overline{\theta}| < 1.5 \times 10^{-10}$ was given, based on the simple nuclear estimate in Eq. 5.24. With the result of the newer atomic calculation [Dzu02], this limit is slightly relaxed to

$$|\overline{\theta}|_{\mathrm{Hg}} < 2.3 \times 10^{-10} \quad [\mathrm{Fla85a,\ Fla86}], \tag{5.36}$$

where the reference denotes the nuclear calculation used. This limit is still a few times better than the neutron limit, but it does not reflect the decreased sensitivity of the ^{199}Hg Schiff moment to $\overline{g}_0$ expected in more realistic nuclear calculations. If Dmitriev and Sen'kov's calculation is used (Eq. 5.25), the extreme cancellation of the $\overline{g}_0$ component leads to a limit that is two orders of magnitude worse than the neutron limit:

$$|\overline{\theta}|_{\mathrm{Hg}} < 5.2 \times 10^{-8} \quad [\mathrm{Dmi03a}], \tag{5.37}$$

but from Lee and Haxton's calculation (Eq. 5.29), the limit is still slightly better than the neutron limit:

$$|\overline{\theta}|_{\mathrm{Hg}} < 4.8 \times 10^{-10} \quad [\mathrm{Lee94}]. \tag{5.38}$$

However, it is difficult to trust the limit on $\overline{\theta}$ from ^{199}Hg at this point, due to the large theoretical uncertainty in the dependence of $d(^{199}\mathrm{Hg})$ on $\overline{g}_0$, compared to the 50% uncertainty for the neutron.

5.4.2 Limits on Supersymmetry

Although many particle and string theorists seem fairly certain that supersymmetry (SUSY) is such a beautiful theory that it must be true, there is currently no experimental evidence of SUSY. Superpartner masses might be in the range of the next generation of accelerator experiments, but it is also quite possible that a non-zero EDM measurement might be the first experimental signature of SUSY, given that the natural sizes of EDMs generated by SUSY can be about 1000 times larger than present experimental limits. There are a wide range of possible SUSY models which might describe nature, and the specific details of the model can have a strong effect on the size of SUSY-generated EDMs. Typically, EDMs are calculated in the simplest SUSY formulation, the minimal supersymmetric standard model (MSSM), which has two independent CP violating phases that can generate EDMs.

In the MSSM the largest contribution to the Hg EDM is expected to arise from chromoelectric dipole moments of the light quarks ($\tilde{d}_q$) [Fal99]. A quark chromo-EDM arises from the same diagrams that would generate a quark electric dipole moment (d_q), except the external photon line is replaced with a gluon. The quark chromo-EDMs generate a CP violating pion-nucleon coupling parameterized

by $\overline{g}_1$, which in turn leads to a Schiff moment and EDM of ^{199}Hg. A calculation of $\overline{g}_1$ due to $\tilde{d}_q$ using QCD sum rules has been performed by Pospelov [Pos02] giving

$$\overline{g}_1 = 2^{+4}_{-1} \times 10^{16}(\tilde{d}_u - \tilde{d}_d)\ \mathrm{m}^{-1}. \tag{5.39}$$

Combined with Eqs. 5.13 and 5.24, our experimental limit places a bound on this combination of chromo-EDMs:

$$\left|\tilde{d}_u - \tilde{d}_d\right| < 3 \times 10^{-26}\ \mathrm{cm}. \tag{5.40}$$

Using the more recent nuclear calculations (Eqs. 5.28 and 5.29) does not change the limit substantially, since their estimates of the $\overline{g}_1$ contribution to the Schiff moment differ by only a factor of two from the simple shell model estimate (Eq. 5.24). For comparison, the neutron EDM is generated in the MSSM by a different combination of quark EDMs and chromo-EDMs [Pos01]:

$$d_n = (1 \pm 0.5)\left\{0.55e(\tilde{d}_d + 0.5\tilde{d}_u) + 0.7(d_d - 0.25d_u)\right\}. \tag{5.41}$$

While the neutron EDM is expected to be directly sensitive to both quark EDMs and chromo-EDMs, the ^{199}Hg Schiff moment is generated mainly by quark chromo-EDMs, and the quark EDMs contribute to the ^{199}Hg EDM only through its sensitivity to d_n and d_p.

The MSSM contributions to d_e, d_q, and $\tilde{d}_q$ can be calculated (see Ref. [Fal99]), and then can be compared to the experimental bounds on the thallium, neutron, and mercury EDMs. Figure 5.1 shows the bounds placed on the two CP violating phase angles θ_A and θ_μ when the MSSM superpartner masses are set to be $M = 500$ GeV. The combined constraints from the three experiments limit both phases to be very near zero, a result that is sometimes referred to as the SUSY CP problem. Just as is the case for $\overline{\theta}$ in the strong CP problem, phases that are *a priori* assumed to be of order unity are constrained by EDM limits to be close to zero, indicating a need for fine tuning of these parameters. The size of EDMs generated by the MSSM scale as $1/M^2$, so one way to restore order unity phases is to assume that the superpartner masses are greater than 1 TeV. However, in this limit SUSY becomes less able to help with the gauge hierarchy problem, one of SUSY's main attractive qualities.

Some theorists have attempted to get around the SUSY CP problem by constructing SUSY models where fortuitous cancellations allow for both small EDMs and natural values for phases and masses, but this is difficult to accomplish when all three classes of EDM limits are considered, due to their different dependencies on the CP violating phases. For example, in a particular string-theory motivated model involving D-branes [Brh99], considering only the neutron and electron EDM limits can allow large CP violating phases, but as is shown in Figure 5.2, adding the ^{199}Hg limit leads

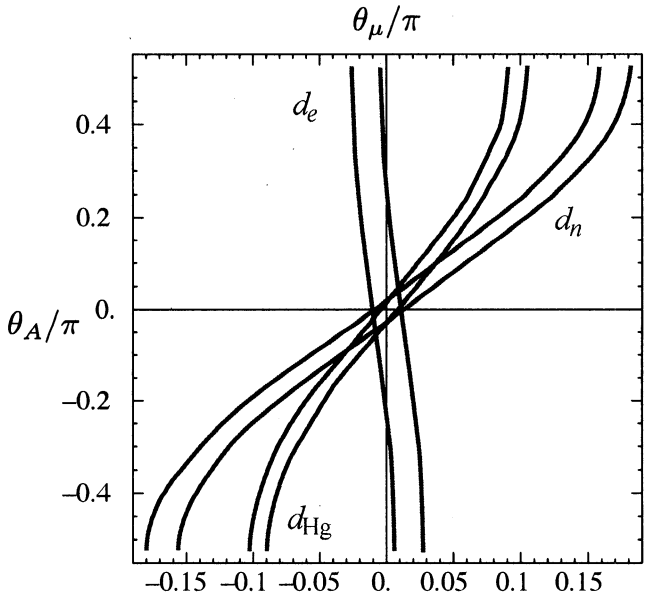

Figure 5.1: EDM based constraints on CP violating phases in the MSSM. The figure is adapted from Ref. [Fal99], updated by M. Pospelov in 2003 to include the more recent experimental and theoretical results.

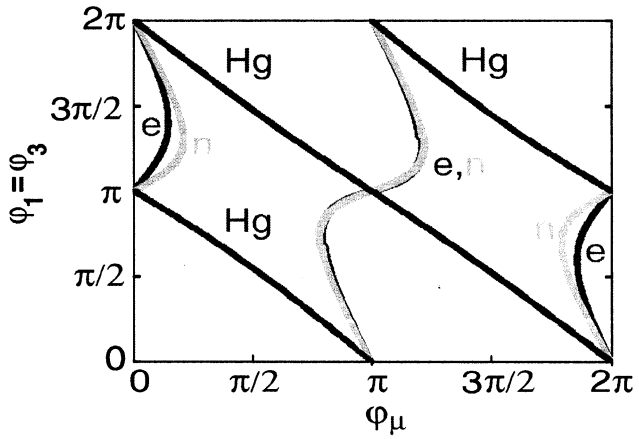

Figure 5.2: EDM constraints on CP violating phases in a D-brane model [Brh99]. The figure is adapted from Ref. [Abe01].

again to very tight bounds on the phases [Abe01]. This highlights the importance of continuing to pursue EDM measurements in a wide variety of systems.

Explaining the smallness of current EDM limits is a fairly serious problem in the MSSM, but SUSY encompasses a wide variety of possible theories, many of which can reasonably suppress EDMs below current limits (see references 21–24 of [Dem04], for example). Most of these models will be strenuously tested, though, when improved limits from the next generation of EDM experiments arrive.

5.4.3 Naturalness Parameters

A review article by Stephen Barr [Bar93] gives estimates for EDMs in several extensions of the Standard Model. The estimates are rather crudely derived through "naive dimensional analysis" [Man84], and should probably only be trusted as order of magnitude estimates, but this approach allows for the easy comparison of the sensitivity to new physics of a wide variety of experimental EDM searches. Barr gives EDM predictions for supersymmetry, multi-Higgs models, and left-right symmetric models. The predictions are expressed in terms of "naturalness parameters" (ε^{Model}), which should be of order unity if the most natural values for the model parameters are used. If the experimental EDM limits imply a very small ε^{Model}, then this indicates that the theoretical model requires a correspondingly large degree of fine tuning in order to explain the smallness of EDMs. The naturalness parameters are calculated in terms of d_e, d_n, and the nucleon-nucleon contact interaction coupling strength η. Current limits on the naturalness parameters are summarized in Table 5.1.

Supersymmetry

To make a prediction for EDMs generated in supersymmetric theories, Barr estimates the contribution of one loop SUSY diagrams. For the electron EDM, there is a contribution from a diagram involving the photino and scalar electron (selectron):

$$d_e(\tilde{\gamma}) = -e\frac{\alpha}{24\pi} m_e |A_e/m_{\tilde{\gamma}}^3| \sin(\phi_{A_e} - \phi_{\tilde{\gamma}}) f(m_{\tilde{e}}^2/m_{\tilde{\gamma}}^2), \tag{5.42}$$

where $f(x)$ is a function of order unity, A_e and ϕ_{A_e} come from the soft-SUSY-breaking mass term of the selectron, $\tilde{e}_L^*(m_e A_e \exp(i\phi_{A_e}))\tilde{e}_R + \text{hc}$, and $m_{\tilde{\gamma}} \exp(i\phi_{\tilde{\gamma}})$ is the photino mass. Barr takes the natural scale for A_e and $m_{\tilde{\gamma}}$ to be about 100 GeV, and the angles ϕ_{A_e} and $\phi_{\tilde{\gamma}}$ about unity, so the naturalness parameter is defined to be,

$$\varepsilon_e^{\text{SUSY}} \equiv |A_e/m_{\tilde{\gamma}}^3| \sin(\phi_{A_e} - \phi_{\tilde{\gamma}}) f(m_{\tilde{e}}^2/m_{\tilde{\gamma}}^2)(100\text{ GeV})^2, \tag{5.43}$$

so that $|d_e| \approx [(e\alpha m_e/(24\pi))/(100\text{ GeV})^2]\varepsilon_e^{SUSY}$.

The SUSY one loop contribution to the neutron EDM and η are estimated from an expression analogous to the electron, but involving the gluino and scalar quarks (squarks). The relevant naturalness parameter is then

$$\varepsilon_q^{\mathrm{SUSY}} \equiv |A_q/m_{\tilde{g}}^3| \sin(\phi_{A_q} - \phi_{\tilde{g}}) f(m_{\tilde{q}}^2/m_{\tilde{g}}^2)(100\ \mathrm{GeV})^2. \tag{5.44}$$

Numerically, the SUSY naturalness parameters are related to d_e, d_n, and η by

$$d_e \sim (1.1 \times 10^{-25}\, e\,\mathrm{cm})\, \varepsilon_e^{\mathrm{SUSY}}, \tag{5.45}$$

$$d_n \sim (4.3 \times 10^{-24}\, e\,\mathrm{cm})\, \varepsilon_q^{\mathrm{SUSY}}, \tag{5.46}$$

$$\eta \sim (1.8 \times 10^{-1})\, \varepsilon_q^{\mathrm{SUSY}}. \tag{5.47}$$

It is apparent from the limits in Table 5.1 that SUSY currently requires a fair amount of fine tuning. A small value of ε^{SUSY} could arise for larger superpartner masses, small phase angles, or a fortuitous cancellation of the phase angles.

Multi-Higgs

The existence of multiple Higgs doublets is a common prediction of extensions of the standard model. One such theory is, of course, supersymmetry, but many grand unification theories also require two or more Higgs doublets, as do some axion models. Any of these models can lead to CP violation through Higgs exchange that can generate EDMs. Barr estimates that the natural scale of CP violation from Higgs exchange is

$$d_e \sim \tan\beta(1-k)(5.2 \times 10^{-27}\, e\,\mathrm{cm})\, \varepsilon^{\mathrm{Higgs}}, \tag{5.48}$$

$$d_n \sim \tan\beta(1.25 \times 10^{-26}\, e\,\mathrm{cm})\, \varepsilon^{\mathrm{Higgs}}, \tag{5.49}$$

$$\eta \sim \tan\beta(9.2 \times 10^{-4})\, \varepsilon^{\mathrm{Higgs}}, \tag{5.50}$$

where k is a positive number less than one accounting for cancellation due to other diagrams, and $\tan\beta$ is the ratio of the vacuum expectation values for the two Higgs doublets. There are good reasons to believe that $\tan\beta$ should be large (~ 50), and from current experimental constraints it is expected that $\tan\beta \gtrsim 5$ [Dem04].

Left-Right Symmetric

In left-right symmetric theories parity is assumed to be a fundamental symmetry of nature. This is generally accomplished in the charged weak interactions by introducing two kinds of charged bosons, W_L and W_R, that correspondingly couple to left and right handed fermions. Mixing of the W_L and

W_R bosons can lead to EDMs at the one-loop level. Barr's estimate for the natural scale of CP violation in these theories is

$$d_e \sim (3.3 \times 10^{-26}\, e\,\mathrm{cm})\, x_e^{\mathrm{LR}}, \tag{5.51}$$

$$d_n \sim (3.7 \times 10^{-24}\, e\,\mathrm{cm})\, x_q^{\mathrm{LR}}, \tag{5.52}$$

$$\eta \sim (2.7 \times 10^{-1})\, x_q^{\mathrm{LR}}, \tag{5.53}$$

where the subscripts in x_e^{LR} and x_q^{LR} reflect the different origins of the dominant contributions. In the case of d_e, the main contribution is from the one loop W_L and W_R mixing, while for d_n and η the main contribution arises from CP violating four-quark operators in $W_{L,R}$ exchange.

5.5 Summary of Limits

Table 5.1 displays the limits on CP violating parameters discussed in this chapter, based on the theoretical interpretation of the three most important experimental EDM limits: mercury, thallium [Reg02], and the neutron [Har99]. It can be noted that ^{199}Hg can set limits on the widest variety of CP violating parameters, and in many cases it sets the most stringent bound. However, the limits in Table 5.1 generally include only experimental error estimates, and not uncertainties in the theoretical calculations. The electron EDM limit as derived from thallium gives the most theoretically sound limits on CP violation, as it only requires an atomic calculation, and the ^{199}Hg EDM is the most difficult to interpret theoretically, involving several levels of calculations in QCD, nuclear, and atomic theory.

Table 5.1: Summary of limits on CP violation from $d_{\rm Hg}$, d_n, and $d_{\rm Tl}$. The experimental limits are from references [Rom01a], [Har99], and [Reg02]. The last column gives references for the theoretical interpretation.

Parameter	Hg	neutron	Tl	Ref.
d_e	$1.8 \times 10^{-26} e\,\text{cm}$	—	$1.6 \times 10^{-27} e\,\text{cm}$	a,b
d_n	$4.0 \times 10^{-25} e\,\text{cm}$	$6.3 \times 10^{-26} e\,\text{cm}$	—	c
d_p	$3.8 \times 10^{-24} e\,\text{cm}$	—	—	c
Semileptonic				
C^{SP}	3.4×10^{-7}	—	1.3×10^{-7}	d
C^{T}	1.1×10^{-8}	—	1.4×10^{-4}	d
C^{PS}	3.5×10^{-6}	—	—	d
Hadronic				
η	5×10^{-4}	—	—	e
$\overline{g}_{\pi NN}$	$\lvert\overline{g}_1\rvert < 1 \times 10^{-11}$	$\lvert\overline{g}_0\rvert < 7.0 \times 10^{-12}$	—	f,h
	$\lvert\overline{g}_1\rvert < 2.4 \times 10^{-12}$			g
$\overline{\theta}_{\rm QCD}$	5×10^{-8}, 4×10^{-10}	6×10^{-10}	—	f,g,i
$\tilde{d}_q$	3×10^{-26} cm	1.1×10^{-25} cm	—	j,k
Naturalness parameters				
$\varepsilon^{\rm SUSY}$	3×10^{-3}	1.5×10^{-2}	1.5×10^{-2}	l
$\varepsilon^{\rm Higgs}$	$0.5/\tan\beta$	$5.0/\tan\beta$	$0.3/(1-k)/\tan\beta$	l
$x^{\rm LR}$	2×10^{-3}	1.7×10^{-2}	5×10^{-2}	l

[a][MP86], [b][Liu92], [c][Dmi03b], [d][Khr97], [e][Fla86], [f][Dmi03a], [g][Lee94], [h][Her95], [i][Pos99], [j][Pos02], [k][Pos01], [l][Bar93].

Chapter 6

DEVELOPMENT OF THE FOUR CELL APPARATUS

This chapter describes the changes made to the ^{199}Hg EDM apparatus in order to embark on a 4-cell EDM measurement (HG4) after the completion of the HG3 measurement published as [Rom01a]. Design and construction began in late 2000, and a working 4-cell system was in place in April 2001. Additional modifications made in the subsequent months and years will also be described here and are referenced by the Run number (see App. B) closest to when the change was implemented.

6.1 New Vapor Cells (CO)

After starting the HG3 measurement with four reliable vapor cells, three were remaining at the end of the measurement. In order to move to a 4-cell measurement at least one new cell was needed, and at least eight working cells was preferable, so that all four positions could possibly be replaced with one interchange.

The buffer gas used in the HG3 cells, a mixture of 90% N_2 and 10% CO, was arrived upon through about 10 years of tinkering with various aspects of the EDM cell making process for HG1 and HG2. A buffer gas of some sort is required in vapor cells used under high voltage conditions [Khr97, pg. 33], and nitrogen is a good candidate, being an inert gas with a relatively high dielectric strength and a long history of usage as an optical pumping cell buffer gas. Cells made with pure N_2 gas were found to have very unstable spin lifetimes that would decay after only a few hours of UV exposure, and it was found that adding a small amount of carbon monoxide stabilized the spin lifetime at a reasonable level for long term usage. It was believed that the reduction in spin lifetime under UV exposure was due to extra relaxation caused by atomic hydrogen liberated from the wax wall coating through an interaction with the UV light or collisions of excited state Hg atoms. The CO was supposed to act as a getter for the liberated hydrogen by forming formaldehyde [Jac95].

An extensive study of the magnetic field and temperature dependence of surface spin relaxation of ^{199}Hg in wax coated cells was performed by Mike Romalis (Ref. [Rom04]) prior to the HG3 dataset. The magnetic field dependence gives information about the correlation time τ_c of the spin relaxation mechanism, because the relaxation will be suppressed if the Larmor frequency $\omega_L = \gamma B$ is greater than $1/\tau_c$. The temperature dependence gives information about the amount of time the

^{199}Hg spins spend at the cell wall surface, or the sticking time τ_s. The study indicated that the relaxation mechanism was consistent with a dipolar-dipolar interaction (with $\tau_c \sim 2$ ns) between the ^{199}Hg spins "stuck" to the surface ($\tau_s \sim 5$ ns) and paramagnetic sites about 7–10 Å away. The paramagnetic sites are possibly free radicals on the wax surface, and since it has been our experience that our cells' spin relaxation times tend to degrade when they are exposed to resonant UV radiation, a likely model is that the collisions of excited state ^{199}Hg atoms with the wax surface create additional paramagnetic sites. Remelting the wax coating apparently "repairs" the damage to the coating.

In order to avoid damaging the wax coating, efficient quenching of excited state Hg atoms ($^3P_1 \rightarrow {}^1S_0$) is required. The effect of a pure N_2 buffer gas is to mainly quench the $^3P_1$ state to the metastable $^3P_0$ state, and there is no measurable quenching of either the $^3P_1$ or $^3P_0$ states to the ground state [Pit72]. CO also dominantly quenches the $^3P_1$ state to $^3P_0$ [Vik72], but unlike N_2, fairly efficiently quenches the $^3P_0$ state to the $^1S_0$ ground state [Phi77]. At 300 Torr buffer gas pressure, the effective quenching rate for $^3P_1 \rightarrow {}^1S_0$ is 4×10^3 s^{-1} with pure N_2, and 8×10^7 s^{-1} with pure CO [Rom04].

We now believe that the addition of the small amount of CO buffer gas was helping to stabilize the spin lifetimes by providing improved ground state quenching, and the quenching could be improved further by increasing the CO percentage. A new batch of six cells (#32–37) was made in late 2000 using the same procedure as was used for the HG3 cells (see Sec. 3.1.1), except that the new cells were filled with a different buffer gas (100% CO). The cells were filled to a pressure of about 475 Torr, which was set "automatically" because the fill line was run through a liquid nitrogen cold trap, and the CO would condense in the cold trap above this pressure.

The CO cells have generally tended to perform much better than the N_2+CO cells. As shown in Figure 6.1, the relaxation times for the cells used in HG3 usually dropped to less than 100 seconds after less than two days of UV exposure, and would then stabilize somewhere between 50 and 80 seconds. The CO cell relaxation times also tended to decay under UV exposure, but the falloff is much slower than the HG3 cells. Just as with the HG3 cells, the spin lifetimes of the CO cells can be rejuvenated by remelting the wax wall coating. We plan to switch vapor cells out of the 4-cell apparatus with about the same period as was used for the HG3 data, about every two weeks, so on average the spin coherence times will be significantly longer.

Two more batches of CO EDM cells were constructed and filled about a year later (#38–43 and #44–49). Most of these cells have been used in taking EDM data successfully. A few cells from the original batch (#32, 34 and 37), when under UV exposure, have exhibited a gradual drop in their ^{199}Hg density for an unknown reason. The density can be rejuvenated by heating the cell with

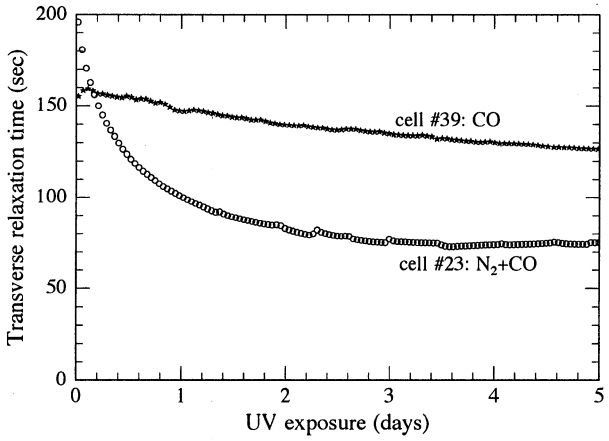

Figure 6.1: Effect of UV exposure on transverse spin relaxation time. The relaxation time for the cell containing 90% N_2 and 10% CO quickly drops below 100 seconds, while in the cell containing pure CO the relaxation time decays much more slowly.

a hand torch, but then drops to minuscule levels in several days to a week. A similar behavior in older cells was attributed to the presence of impurities such as oxygen in the cell [Jac95]. All of the cells from the second batch have performed well, although cell #42 cracked while being cleaned in an ultrasonic cleaner (after Run 89310). The third batch has not been as successful, as we have not been able to achieve decent spin precession signals from #44, 45 or 46, and cell #49 was damaged while being pulled from the vacuum system. This currently (as of March 2005) leaves ten working EDM cells for use in HG4.

6.2 Four Cell Vessel

In order to accommodate the two additional cells, a larger cell holding vessel was required. A cutaway sideview of the 4-cell vessel is shown in Figure 6.2 (compare to Fig. 3.3). The larger vessel has outer dimensions 5×5×6", which is too large to fit in the magnetic field coil cylinder (ID = 6") used in HG3, but as is visible in the photo in Figure 3.4, the HG3 field coil was nested inside a slightly larger coil with ID = 7.5". The larger coil had an essentially identical winding as the smaller coil, and its original purpose was to provide a compensation field to help cancel image current effects of the magnetic shields, but the second coil was not used at all during the HG3 dataset. The larger

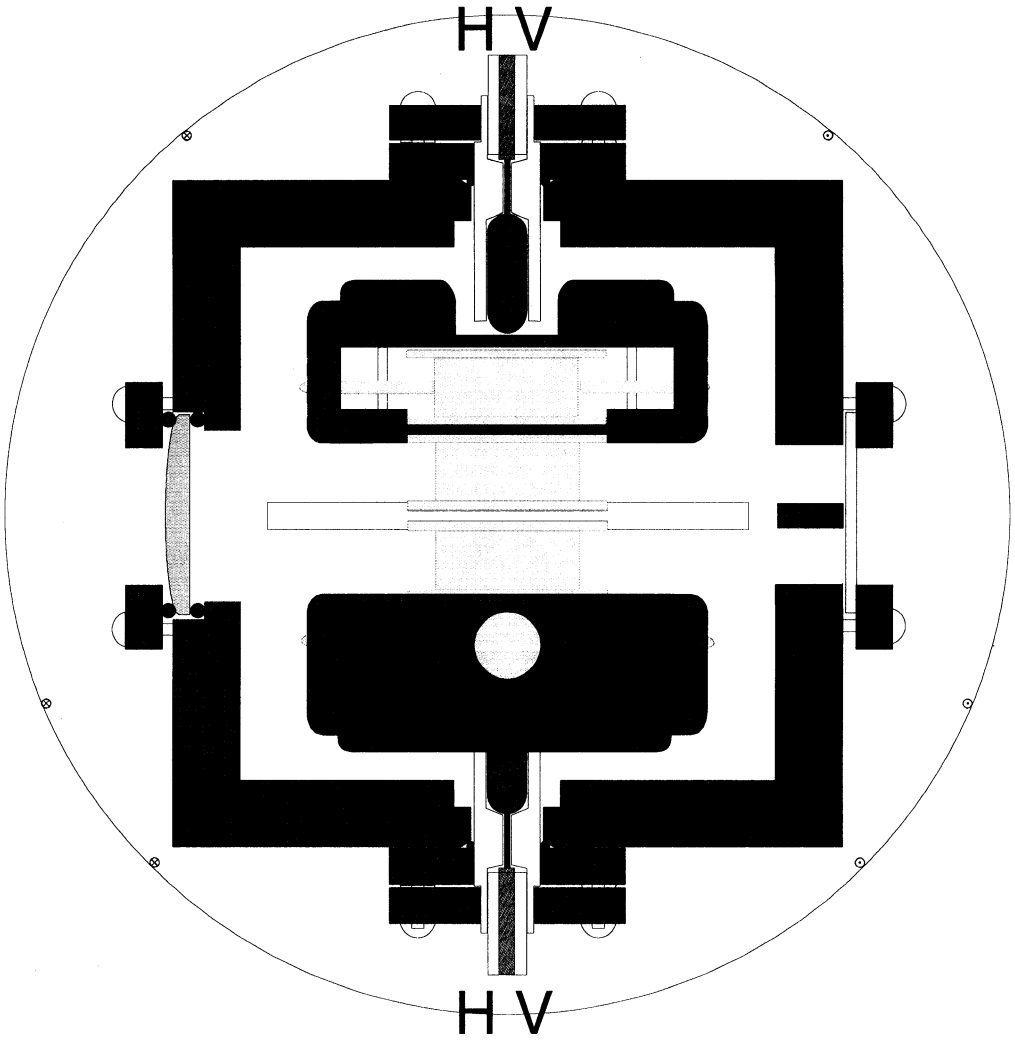

Figure 6.2: 4-cell vessel sideview. Dark grey shading indicates electrically conductive materials. The outer cells are enclosed inside the HV electrodes with holes for light access (shown for the bottom electrode). The locations of the three current loops used to equalize the Larmor frequencies in all four cells are shown (see Sec. 6.5.1).

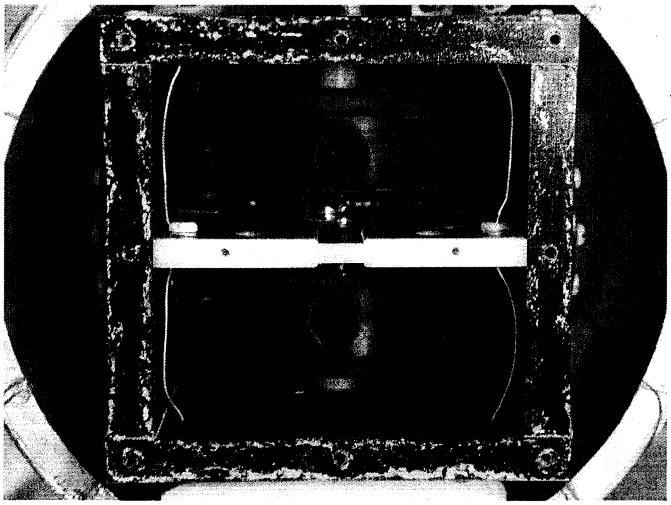

Figure 6.3: 4-cell vessel photograph. The front face, gasket, and shape adapter have been removed.

vessel was accommodated by simply removing the smaller coil, and the larger coil was hooked up to the current source.

Aside from being slightly larger, most aspects of the 4-cell vessel design and materials were very similar to the conductive polyethylene 2-cell vessel, and are described in Section 3.2. The main outward difference is the additional light access needed for the outer cells, whose light beams ran parallel to the magnetic shield axis, perpendicular to the existing middle cell beams (the reasons for this are discussed in Sec. 6.4.1). Light access was provided by two 13/32" holes in the front vessel-face, covered by 3/4" fused silica flat windows, and a 3×1" rectangular, f = 200 mm, cylindrical lens was mounted on the back face to focus the light into the detector region. The other main differences in the larger vessel were the groundplane design, the larger hollow electrodes, and aspects of the HV feedthroughs.

6.2.1 Groundplane

The main concern in designing the 4-cell vessel groundplane was that with the larger inner dimensions of the vessel, the groundplane would need to have a larger area, and we did not want this to lead to a loss of rigidity in the middle of the groundplane. In the HG3 vessel, the groundplane was a 0.2" thick, 2.8×2.8" square that did not quite extend all the way to the inner surface of the vessel walls, and was suspended from the sides by screws. As shown in Figure 6.4, the HG4 groundplane was designed to interface directly with the cell walls, and is thicker at the edges (0.3"). The middle

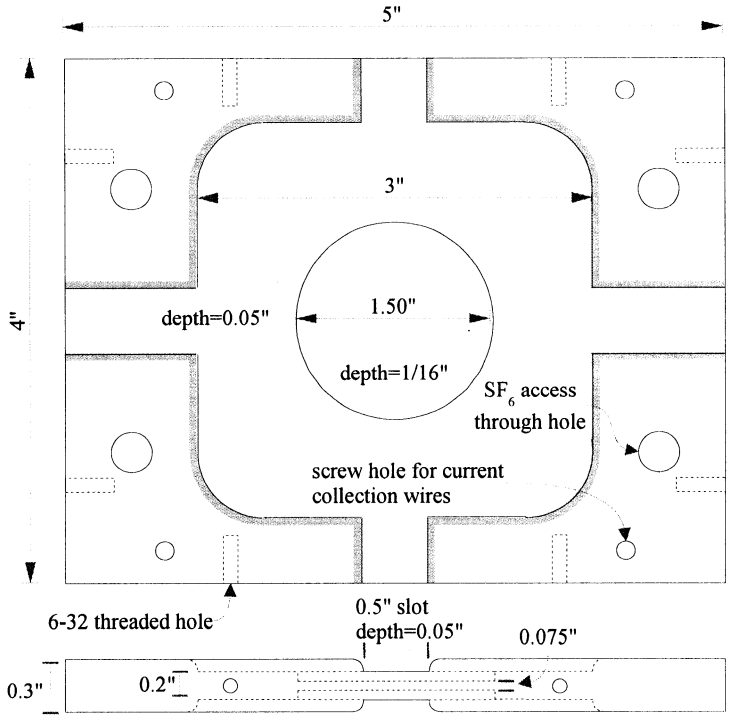

Figure 6.4: Top and sideview of the 4-cell vessel groundplane. The grayed lines in the top view denote rounded (radius = 0.05") edges.

section of the groundplane is the same thickness as the HG3 version, and the area of the thinner region is about the same area as the HG3 groundplane. The 0.3" thickness does not extend all the way around the outer edge, but has four gaps to allow for full light access to the middle cells. In principle only two gaps are needed (if the middle cell light beams are perpendicular to the shield axis, then the gaps are needed on the longer edges), but the extra gaps allow more flexibility in case it is ever deemed necessary to run the middle cell light beams down the magnetic shield axis.

The groundplane is constructed from nonconductive UHMW polyethylene, and a metal coating is evaporated onto the top and bottom surfaces, leaving a $\sim$ 0.1" gap at the edges so that there is electrical isolation between the groundplane and the vessel walls. The initial HG4 groundplane was coated with aluminum, as were the HG3 groundplanes, but this coating suffered from oxidation problems, leading to very low conductivity between some regions of the surface. Subsequent groundplanes (there have been four) were coated with gold instead of aluminum to avoid the oxidation problem.

Soon after the first gold coated groundplane was installed (Run 21208), the vessel began having trouble holding 10 kV. This was thought to be due to the cell disk indentations being slightly too large, leading to sharp edges at the cell-groundplane interface that could more easily lead to electrical discharge. The vessel was able to hold 10 kV after the cell disks were enlarged with layers of silver paint to fit the groundplane indentations. This groundplane was later replaced (Run 37192) with another gold groundplane with smaller cell indentations. The indentations were perhaps a little too small, and after a half of year of use, much of the gold around the cell indentation had scraped off, leading to the installation of the third gold groundplane (Run 68818), which had cell indentations of intermediate size between the first and second gold groundplanes. This groundplane was used for about a year until one side of the groundplane would not hold high voltage. The problem may have been due to the groundplane becoming slightly bowed in the middle after being used for an extended period of time with cells installed in only one half of the vessel. However, pressure was applied to try to re-flatten the groundplane, and this did not solve the problem. Enlarging the cell disks with silver paint also did not work. Once again, a new groundplane was installed (Run 105989), this time with a gold coating on top of an aluminum coating, as it has been found that the aluminum adheres slightly better to the polyethylene than gold does. So far, there have not been any problems with the latest groundplane, although there has been some loss of coating around the cell interface.

6.2.2 Electrodes

As shown in Figure 6.2, the electrodes that enclose the outer cells are constructed in two pieces that are held together with four nylon screws. There are four symmetrically placed 7/16" holes in the side walls, two of which provide light access, and the other two are needed to accommodate the cell stems. For most cells the stems poke about 1–3 mm outside the electrode. The electrode "lid" (the piece closer to the HV feedthrough) is sized to easily slide into the bottom half, and electrical contact is made between the two pieces by a conductive silicone gasket around the bottom edge of the electrode lid. The gasket enlarges the lid diameter slightly, and is squeezed against the inner wall of the electrode bottom to provide electrical contact all around the interface.

Two electrodes were machined originally, denoted as 'C' and 'P.' After taking a large amount of data with these electrodes, a series of false EDM signals seemed to be correlated with the location of electrode P (see App. C). The reason for this could have been that the electrode had somehow picked up a larger degree of ferromagnetic contamination, making it capable of generating HV correlated magnetic fields. A new electrode was constructed (T) to replace electrode P (Run 65338). The false signal problem did not seem to be solved by this, though, and in order to make sure that the other

original electrode was not the source of the problem, electrode C was replaced with a new electrode, E (Run 68222). It is not entirely clear at this point if any particular electrode has caused more or less false signals, but we at least now have the option of taking data with different sets of electrodes, although all data since Run 68222 has been taken with electrodes T and E.

6.2.3 HV Feedthroughs

Compared to the HV feedthroughs used in HG3 (see Sec. 3.2.1), the HG4 feedthroughs are slightly thicker (0.5" OD instead of 0.32"). The HG3 feedthroughs had been barely wide enough to accommodate the 0.285" diameter PE insulation of the thicker HV cable that was used in the second half of the HG3 dataset. As shown in Figure 6.2, the feedthrough diameter is slightly thinner (0.4") near the end where the HV cable is inserted. A system of two 1/4"×2.5" diameter collars, each independently attached to the top (or bottom) vessel face with 4 nylon screws, is used to hold the feedthrough in place. The inner collar serves the same purpose as the single collar used in the HG3 vessel, and presses down on an O-ring on the outside of the vessel, providing an air-tight seal and some amount of horizontal holding pressure on the feedthrough. The outer collar presses down on the lip of the feedthrough where the diameter increases, which fixes the vertical position of the feedthrough. The amount of pressure the feedthrough exerts on the electrode and cells can be set by adjusting the 4 outer collar screws.

Aside from the diameter changes, the initial feedthroughs used in HG4 were the same as the feedthroughs that were in use at the end of HG3 (thick Belden 8237 HV cables, and conductive PE pellet at the end). After we started monitoring the charging currents while the HV ramped (see Sec. 6.3.1), we noticed that spikes in the charging currents were occurring fairly regularly, always after the HV polarity switched during the ramp. Figure 6.5 shows charging current data with these spikes. A 20 turn, 5 cm radius, loop was mounted on the outside of the vessel front plate and hooked to an oscilloscope, and when the current spikes occurred, magnetic pickup evens were seen on the coil in the form of a 0.5 V signal with a < 50 ns rise time, followed by a ringing decay. A simple analysis,

$$B_{\max} \approx \frac{V\Delta t}{NA}, \tag{6.1}$$

where N is the number of turns and A is the area of the coil, indicates a field of ~ 1 mG outside the vessel due to these current spikes. The magnetic fields from these spikes did not seem to have a dependence on the direction of the HV ramp, and there did not seem to be false EDM signals associated with the spikes, but whatever sparking behavior was leading to the current spikes could potentially lead to ferromagnetic orientation, so we sought to fix this behavior.

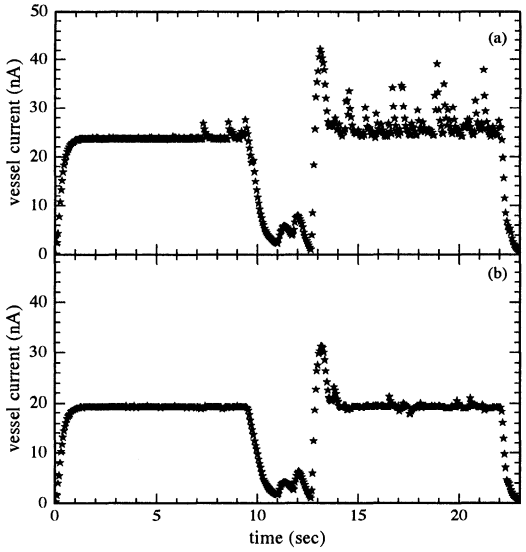

Figure 6.5: Current spikes observed during HV ramp. Plot (a) shows the current flowing onto the vessel for a scan using HV feedthroughs with the thick HV cable (Scan 42350), and plot (b) is from a scan after switching to the thinner HV cable (Scan 57100). In both scans the HV ramps from -10 to 10 kV in 20 sec. with a two second delay in the middle while the polarity is switched.

It was found that feedthroughs that used the thick (13 AWG) HV cable all exhibited the sparking behavior, while feedthroughs that used the thinner (20 AWG) cable did not show any charging current spikes or pickup events on the coil. The sparking may have to do with the cable/feedthrough interface, where for the thicker cable, six of seven 21 AWG conductors are snipped off, giving somewhat sharp edges. The entire conductor of the thinner cable is passed through the feedthrough, which then avoids this issue. The thicker cable was switched to during HG3 because it seemed that the thinner cables sometimes had large cable leakage currents, possibly due to failure of the insulation. At this point, some of the same cables that had seemed to suffer from large leakage currents before no longer had this problem. It has been our experience that when large cable leakage currents occur they can usually be fixed by cleaning the exposed surfaces of the PE insulation, so it was probably the case that the cable insulation did not fail, but just needed to be cleaned.

Since using the thinner cable seems to fix the sparking behavior, we switched back to feedthroughs using the thin HV cable (Run 57005). The feedthrough/electrode interface was also switched from a conductive PE pellet back to a solder blob. It was felt that the solder blob added an insignificant amount of metal near the cells, and also gives a much more robust connection between the cable and

feedthrough. Feedthroughs using the PE pellet had been pulling apart somewhat frequently around this time. So currently the HV feedthroughs are very similar to the feedthroughs used at the start of the HG3 dataset (Belden 8262 cables, and solder blob at the end).

6.3 Current Monitors

6.3.1 Charging Currents

Depending on the HV ramp rate, charging currents of up to 100 nA flow into the vessel. The leakage current monitors were set up to measure $\sim$ 1 pA currents and saturated at about 200 pA, so the leakage monitors gave no useful information during the HV ramp. In order to verify that the currents were behaving normally during the charging phase, a ramp rate of less than 10 V/s was required, which is very different from the ramp rates of 1–4 kV/s normally used. The charging currents could be monitored during normal operation if the amplifier gain could be switched to a lower setting by computer control. Such a system was installed (Run 12590) using a digitally controlled reed relay[1] with an insulation resistance rated to be $> 10^{12}$ Ω, that when enabled, switches a 20 MΩ resistor in parallel with the normal 10 GΩ gain resistor. The HV control computer enables the relay right before starting a HV ramp, and disables it one second after the HV reaches its final value. This way, during the ramp the current monitor gain is 50 nA/V, compared to 100 pA/V during the rest of the scan.

6.3.2 Cable Current Monitor

As was described in Sec. 3.3.3, a voltage meter across a resistor in series with the HV cable was used to occasionally check the current flowing in the HV cable, but there was no way to continuously record this voltage drop with the computer DAQ system. In order to do this, the voltage drop referenced to the HV value would need to be transferred out of the high voltage environment to a safe range for the DAQ input. This was accomplished by converting[2] the analog voltage (-5 to $+5$ V) to a frequency (0–40 kHz) that then drives a LED fiber optic transmitter[3]. A 0.5 m fiber takes the signal to a low voltage environment where the frequency is converted back to an analog voltage readable by a DAQ analog input.

---

[1] COTO technology, 8002-05-10.

[2] Analog Devices AD650 is used for both voltage-to-frequency and frequency-to-voltage conversion.

[3] Agilent Technologies: HFBR-1527 transmitter and HFBR-2526 receiver.

The voltage to frequency conversion circuit and the fiber optic transmitter require a DC power source floating at high voltage. It was decided that the power source should be able to run continuously for time scales of at least a month, which ruled out reasonably sized rechargeable battery options. Solar power and a well insulated AC transformer were also considered as power sources, but in the end we settled on using an AC motor that drives a plastic shaft, which in turn drives the shaft of a motor in the high voltage environment that is used as a generator from which the ± 15 V DC is obtained to power the electronics at high voltage. This system was installed around Run 34658, and although this mechanical system is somewhat noisy and has suffered from occasional breakdowns when one or the other motors has seized up, it is capable of running continuously for several months at a time.

6.4 Optical Setup

6.4.1 Additional Light Beams

The additional two cells added to the experiment effectively doubled the amount of 254 nm light required to make measurements in the same manner as in HG3. This light was acquired by upgrading much of the optics after the second doubling cavity. For HG3, none of the lenses or windows had anti-reflection (AR) coatings, so there was about 10% loss at every surface. For HG4, all of the lenses and windows in the UV beam have been AR coated to provide $< 0.5\%$ reflectivity at every surface. The two main beam steering mirrors used in HG3 after the second doubling cavity were broadband metallic mirrors with about 90% reflectivity at 254 nm (at 45° incidence). These and all other mirrors in the UV beam are now dielectric coated laser line mirrors (designed for the 248 nm KrF laser line) that have reflectivity $> 98\%$ at 254 nm. With these upgrades we were able to gain the overall factor of two increase in light intensity without needing to increase the power output of the laser system.

The light beams for the middle two cells need to be about 0.3" above and below the magnetic shield axis, and they reach the vessel by passing through a 1" hole in the side of the magnetic shields. The outer cell light beams need to be about 1" above and below the magnetic shield axis. If the outer cell beams were to follow the same general path as the middle beams, then new holes would need to be made in the side of the magnetic shields, which would be enough of a physical stress on the shields that they would have to be sent back to the manufacturer for re-annealing. However, the shields already had 2.5" diameter holes in the center of their endcaps, which is large enough to pass the outer cell beams. It was decided to leave the middle cell beams and detector optics as they were for HG3 (see Sec. 3.5), and that the outer beams would be sent down the shield axis. This

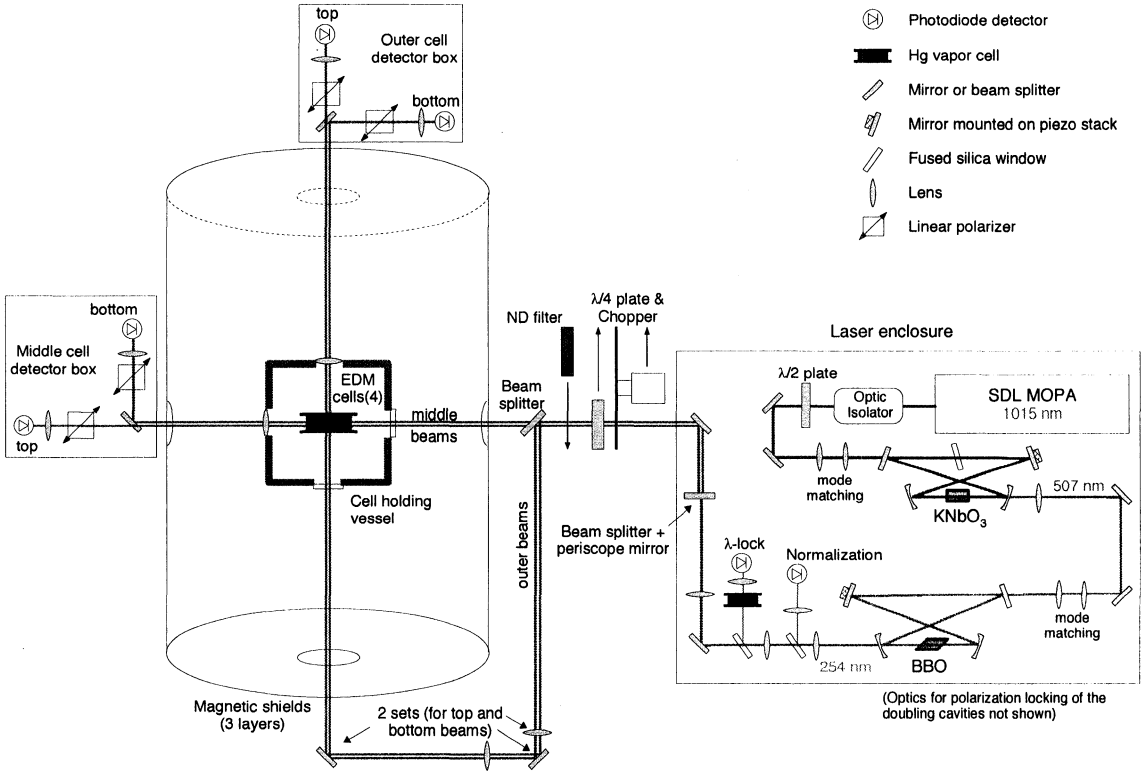

Figure 6.6: Top view of the optical setup for HG4.

meant that the outer beam path would have to be somewhat longer than the middle beam path (3 m compared to 1 m), and would require additional beam shaping lenses, and also the outer cell ^{199}Hg spins are oriented 90 degrees away from the middle cell spins as they precess. We do not believe that there are any intrinsic problems with orienting the outer light beams perpendicular to the middle beams, but if such a problem arises we can reasonably arrange to send all four beams along the shield axis.

Figure 6.6 shows an overview of the entire optical setup for the 4-cell apparatus. An approximately 50/50 beam splitter picks off the outer cell beams in between the pneumatic switch assembly and the magnetic shields. The beams are sent to the front end of the magnetic shields where two sets of steering mirrors are used to direct the beams into the cells. Before reaching the first steering mirror, each beam passes through an independently rotatable cylindrical lens (f = 200 mm), and then between the mirrors they pass through a common cylindrical lens (f = 50 mm). These lenses shape the beams so that when they reach the center of the magnetic shields they have the same

profile as the middle beams. After the second steering mirrors, the beams enter 0.5" diameter G10 light pipes that extend to the windows on the front face of the vessel. The light pipes keep the many cables and wires that also pass through the holes in the shield end caps from interrupting the light beams. After exiting the vessel and the back of the magnetic shields, the light enters a detector box that is essentially the same as the middle cell detector box.

6.4.2 Laser Upgrades

Besides the improvements made to the optics after the laser at the start of HG4, several upgrades were made to the frequency doubling cavities about a year and a half later. Maintaining the power output of the system had started to require frequent readjustment of the enhancement cavity optics. It was suspected that the two cavities had been walked away from optimal alignment over the course of many minor adjustments, and a major realignment would be required to improve the power stability. It was also decided that if a major realignment was performed, then it would also be an opportune time to replace the nonlinear crystals in both doubling cavities.

The first crystal ($KNbO_3$) had been "bought off the shelf," and was cut and AR coated for normal incidence phase matching at 1064 nm. It was also slightly cracked from being dropped at some point. A new crystal custom cut for use at 1015 nm was ordered from VLOC[4], with a dual band AR coating for 1015/507.5 nm. Unfortunately, the green light produced by this crystal would start out at a much improved level compared to the old crystal, but then would drop to a minuscule level after only an hour or so. The power could be recovered by translating the crystal a small amount, which indicated that the crystal surface coating was being damaged by the light. The crystal was returned to VLOC to have the dual band coating removed and replaced with a single band coating at 1015 nm, which is thinner than the dual band coating, so is less susceptible to damage. The recoated crystal (installed at Run 37240) has since performed quite reliably.

The second crystal (BBO) seemed to have acquired some surface damage, probably due to moisture, as the power output was quite dependent on the crystal translation. The crystal was sent back to the manufacturer[5] to have the surfaces repolished, which greatly improved its performance (installed at Run 41033). The combined improvements in the two doubling cavities allows the system to produce the light intensity required for the experiment with the semiconductor laser running at a 40% lower amplifier current (0.8 instead of 1.1 A) than before the crystals were replaced.

---

[4]New Port Richey, FL. http://www.vloc.com/

[5]Castech Crystals, Fujian, China. http://www.castech.com

We also installed a HEPA (high efficiency particulate air) filter above the laser system (at Run 39995). The filter is about one meter over the laser and gently blows highly filtered air down, greatly reducing the amount of dust that can drift into the laser area. Before installing the filter, dust could visually be seen drifting into the light beams circulating in the second doubling cavity, but with the filter on, this dust quickly vanishes. We now need to clean the second cavity mirrors on a monthly basis instead of every day.

6.5 Light Shift Compensation

If the light incident on the ^{199}Hg vapor is at all circularly polarized, then the Zeeman sublevels of the ground state will experience different energy shifts due to the light field, which can be treated as the effect of a virtual magnetic field in the light propagation direction. The virtual magnetic field's effect on the atomic spin direction can lead to apparent frequency noise that was observed in the HG4 dataset, and will be described more fully in Sec. 7.1.1. Here I will describe the changes implemented in the HG4 apparatus to combat this effect, which is minimized by ensuring that the spin precession frequency of the atoms matches exactly the modulation frequency of the circularly polarized pump light. The size of the light shift can also be set to zero by using a particular pump light wavelength. These changes were implemented and tested between Runs 27796 and 30690.

6.5.1 Gradient Coils

Since the pump light for the four cells is modulated by a single optical chopper wheel, the chopping frequency can match the spin precession frequency in all four cells only if the cells are subject to equal magnetic fields, leading to equal Larmor frequencies. We had found in HG3, that the middle two cells typically had a frequency difference of about 1 mHz. The magnetic field gradient in the vertical direction has a mainly quadratic dependence, though, so the outer cell frequencies tend to have a larger frequency offset from the middle cells of about 15 mHz. A typical frequency profile is shown in Figure 6.7.

In order to equalize the precession frequencies, we added three magnetic field coils to cancel the vertical magnetic field gradient. Each coil consists of a single wire horizontal loop attached to the inner surface of the main magnetic field coil form, running along the shield axis. Three independent controls are needed to cancel the gradient at four points, and from calculating the fields produced by three loops in various positions, compared with a wide sample of gradients that had been observed in the data so far, it was found that placing the loops at $+50°$, $-22.5°$, and $-45°$, measured from the horizon, would cancel all of the observed gradient conditions with the smallest amount of current

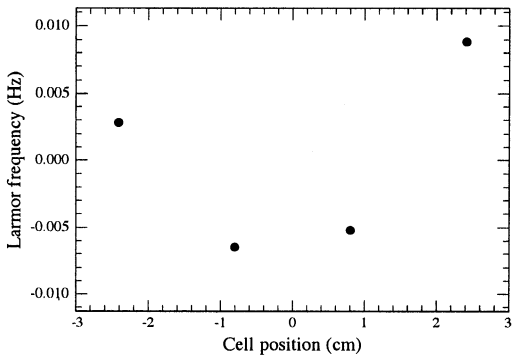

Figure 6.7: Larmor frequency profile measured in the four cell positions. The average frequency in the four cells of 16.44 Hz has been subtracted.

in the loops. The positions of the loops are shown in Figure 6.2. Typically, the gradient loops have between -10 and 10 mA applied to them, and they allow the Larmor frequencies to be easily matched to about 15 μHz.

6.5.2 Chopper Control

Once the four spin precession frequencies were equalized, the optical chopping frequency needed to be set to match the atoms. Previously the chopper frequency was set with the internal reference of the New Focus chopper wheel controller, which only allowed frequency steps of one part in 400 around the frequency we were using. The chopper controller also allows an external frequency source to provide the chopping frequency, though, so by using a digital function generator[6] we are able to set the chopper frequency to a resolution of a part in 10^9. The function generator also is computer controllable through GPIB, so we can have the computer fit the precession frequencies for the most recent scan, and then set the chopper frequency to the average frequency of the four cells.

6.5.3 Pump Wavelength Lock

The size of the virtual magnetic field caused by the Zeeman light shift crosses zero about 200 MHz below the absorption peak of the $F = 1/2$ line. Previously we attempted to tune the pump wavelength to the absorption peak at the beginning of a data run, and then the laser was allowed to run freely. The wavelength could slowly drift as much as 500 MHz in the course of a day, causing the

[6]Stanford Research Systems, DS345.

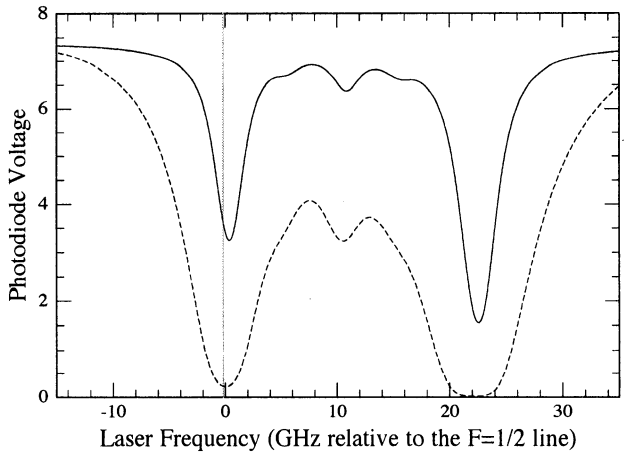

Figure 6.8: Transmission scan for the lock reference cell and an EDM cell. The solid line shows the lock cell, and the dashed line is the EDM vapor cell. The vertical line near 0 GHz marks the -200 MHz point that we wish to lock to.

noise from the vertical magnetization effect to get better or worse during the run. By installing a system to keep the pump wavelength constant at the zero light shift point throughout the run, we could further minimize the noise due to light shifts.

In order to lock the laser wavelength, we added a reference Hg vapor cell just after the output of the second doubling cavity. A simple feedback loop keeps the difference between the transmission signal through the reference cell as measured on a photodiode and the normalization photodiode signal locked to a constant value by adjusting the laser piezo voltage. To provide a decent error signal, the reference cell must have a large slope in its transmission around the desired wavelength, which is fairly close to the absorption peak. As shown in Figure 6.8, our current EDM vapor cells would not be able to provide a good lock signal very close to resonance. Instead, we use a cell with a smaller Hg density and buffer gas pressure ($\sim$ 300 Torr). The smaller pressure shift in the reference cell causes the $F = 1/2$ hyperfine line to be about 400 MHz higher than in the EDM cells. We are not exactly sure what the details of the origin of the lock cell are, but it was likely constructed sometime between the completion of HG2 and the construction of the cells used in HG3.

The wavelength lock from this system is not particularly robust at short time scales (< 1 s), and can be subject to wavelength changes if the steering of the beam out of the second doubling cavity causes a change in intensity at the lock photodiode, but its main purpose is to keep the pump wavelength from drifting over a timescale of many hours. The wavelength lock is only capable of

locking at one setpoint at a time, so the wavelength cannot be locked during both the pump and probe phases, so we lock only during the pump phase. For the probe wavelength, the lock is disabled and the laser piezo voltage is stepped by a constant value away from where the lock-point voltage ended up at the end of the pump phase. The probe wavelength then is allowed to freely drift until the start of the next pump cycle, when the piezo voltage is stepped back to what it had been the previous pump phase, and the lock is re-enabled.

Chapter 7

FOUR CELL DATA SO FAR. . .

After the construction of the basic 4-cell apparatus was completed in the spring of 2001, we began to acquire 4-cell EDM data. This chapter will describe the data taken with the HG4 apparatus from April 2001 through May of 2004. Data runs were first taken using essentially the same procedure and analysis used in HG3 that is described in Ch. 4, except with twice the number of precession signals. However, the procedure has evolved somewhat over time, and these changes will be described in Sections 7.1 and 7.2. We have taken about 200 24-hour days worth of data with the HG4 apparatus so far, which is significantly longer than the total HG3 dataset of 120 days, and although much of the HG4 data has had improved statistical sensitivity over the HG3 data (see Sec. 7.4.3), unfortunately we are not able to improve upon the HG3 limit (Eq. 4.30) on the ^{199}Hg EDM at this time. This is mainly due to the presence of persistent systematic effects that create HV correlated shifts in the spin precession frequencies and have contaminated much of the HG4 data. We currently do not fully understand the origin of these effects, but our attempts to diagnose the problems are described in Sections 7.4.1 and 7.5.

7.1 Probe Detuning Between the $F = 1/2$ and $3/2$ Lines

The most substantial change implemented in HG4 has been to use probe light wavelengths much closer to resonance, resulting in larger amplitude optical rotation signals. -20 GHz was the probe detuning used for most of the HG3 data, which results in an optical rotation angle of about 0.05 radians (see Fig. 2.9). If the probe light is tuned halfway between the $F = 1/2$ and $F = 3/2$ hyperfine lines (roughly $+10$ GHz), then the optical rotation angle increases to about 0.4 radians. Detuning closer to resonance also leads to an increase in the absorptivity of the vapor, and since the spin coherence times of the HG3 cells was degraded by exposure to resonant radiation, detunings smaller than 20 GHz were not explored. With the improved stability of the spin lifetimes of the new CO cells (see Sec. 6.1) we felt freer to use smaller probe detunings in HG4.

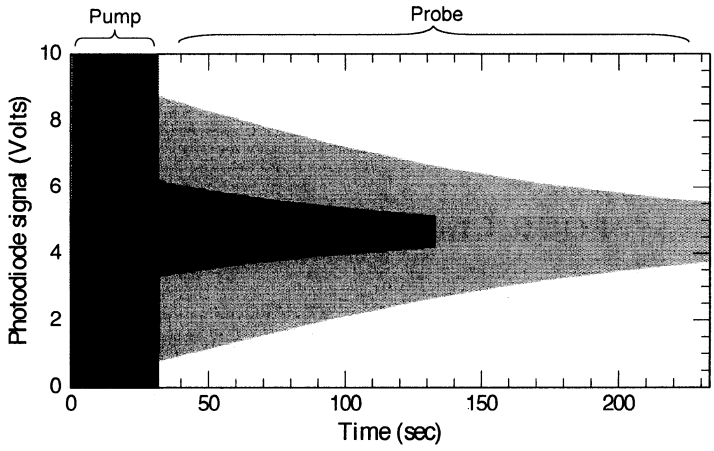

Figure 7.1: Precession signal size comparison between HG3 and HG4. The lighter signal is from the middle bottom cell in HG4 Scan 19750 with a probe time of 200 seconds, and the overlaid darker signal is from the top cell in HG3 Scan 44023 with a probe time of 100 seconds. In both cases the pump time is 30 seconds.

We also took advantage of the generally longer spin lifetimes in the CO cells by increasing the length of the probe phase from 100 to 200 seconds (starting in Run 11080). With the pump phase time of 30 seconds, and a transition time of 3 seconds, the total time of a single spin precession measurement increased from 133 to 233 seconds. Lengthening the period of the measurement cycle can lead to an increased sensitivity to $1/f$ noise, but the improved cancellation of magnetic field fluctuations possible with the 4-cell system mitigates this potential issue.

Figure 7.1 shows an example of the relatively larger amplitudes and spin coherence times obtained in HG4 compared to HG3. The improved signal amplitudes should lead to increased frequency sensitivity ($\delta\omega \propto 1/A$), but when the +10 GHz detuning point was first used (Run 19611) we found that the overall frequency sensitivity of the data runs at this detuning was no better than the sensitivity of smaller amplitude HG4 data runs taken at the -20 GHz detuning. Although fitting the larger amplitude precession signals gave a smaller frequency error for individual scans, there was also a relative increase in the amount of scatter between successive measurements, leading to no net increase in sensitivity.

After further investigation it was found that the frequency scatter was well correlated with fluctuations in the precession signal amplitude, and the fluctuations tended to change size over the course of a run leading to quieter and noisier periods. It was also found that if the 200 second precession signals were divided into two 100 second portions and fit separately, the fitted frequency

of the second half of the scans were almost always systematically shifted from the fitted frequency of the first half. The size of the shift was typically between 10^{-6} and 7×10^{-6} s^{-1}, depending on the particular cell and data run being looked at. We also reanalyzed some previous data runs taken at -20 GHz detuning and found that they also exhibited this shift, but with a generally smaller magnitude.

It seemed likely that the increased scatter in the data taken at $+10$ GHz detuning could be due to larger signal amplitude fluctuations affecting the frequency fits somehow, and this could easily create an apparent shift in frequency between the first and second half of the scans. Since the signal amplitude decreases over the course of a scan, then a coupling between the fitted frequency and the amplitude would lead to the fitted frequency changing over the course of the scan. Also, an effect associated with the magnitude of atomic magnetization in the vapor cell could lead to a physical change in the precession frequency that would be correlated with the signal amplitude. As will be described in the next two sections, both of these types of effects were found to be present.

7.1.1 Frequency Shifts due to Vertical Magnetization

The size of the frequency fluctuations tended to change during the course of a run, perhaps consistent with the noise changing as the laser wavelength freely drifted. This was especially evident in a couple of instances where the laser wavelength was manually adjusted in the middle of a run, leading to a definite shift in the character of the frequency fluctuations. The dependence on the laser wavelength (either the pump or probe wavelength) was suggestive of a light-shift related effect.

Circularly polarized light incident on ground state ^{199}Hg atoms shifts the two Zeeman levels differently, and so acts as an effective light shift induced magnetic field that can shift the spin precession frequency. As is discussed in Section 4.4.5, the direct effect of a probe light induced shift in the precession frequency is fairly small, since the probe light is nominally linearly polarized and directed perpendicular to the main magnetic field. The light shift effect is increased at $+10$ GHz relative to -20 GHz by the same factor that the optical rotation increases, though. Fluctuations in the probe detuning could cause correlated changes in the optical rotation amplitude and light shift strength, and the light induced frequency shift could drift during the course of the probe cycle if the laser systematically relaxes in one direction after the laser piezo voltage is changed. However, assuming that the probe beam circular polarization could be as much as 0.10, the light shift would cause a frequency shift of about 2×10^{-6} s^{-1} at $+10$ GHz, which indicates that the probe detuning would somehow have to change by at least 10 GHz during the course of the probe phase to account for the 5×10^{-6} s^{-1} frequency drifts we had seen.

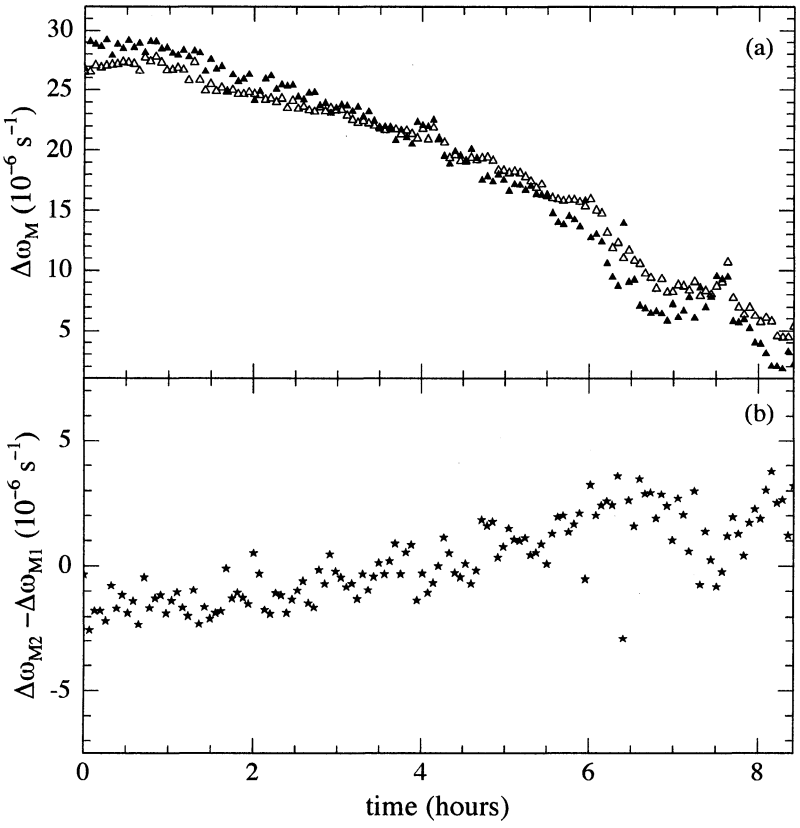

Figure 7.2: Bisected fitting of spin precession signals. The solid points in plot (a) show the frequency difference between the middle two cells fitted for the first 100 seconds of each probe phase, and the open points are from the last 100 seconds (the data is from Run 20089, and an offset of 0.018 rad/s has been added). Plot (b) shows the middle cell frequency difference of the second half ($\Delta\omega_{M2}$) minus the frequency difference from the first half ($\Delta\omega_{M1}$) of each scan. In this case the frequency shift changes sign over the course of the run.

The light shift magnetic field ($\boldsymbol{\delta B}_{LS}$) can have a substantial effect on the atomic polarization direction, though, if the frequency that the transverse optical pumping light is modulated does not match the Larmor precession frequency of the atoms. In the case of a perfectly matched chopper frequency, $\boldsymbol{\delta B}_{LS}$ is parallel with the average spin direction while the light is on, so $\boldsymbol{\delta B}_{LS}$ does not affect the spin direction, but if $\boldsymbol{\delta B}_{LS}$ is not parallel with the spin direction due to a mismatched chopper frequency, then the spins will precess a small amount into the vertical direction. Given the dominantly quadratic dependence of the (non-gradient compensated) magnetic field measured in the four cell positions (see Fig. 6.7), it was possible to match the chopper frequency well to either the middle two cells or the outer two cells, but not all four at once. This led to a typical chopper frequency mismatch of about 0.05 s^{-1} in some cells ($\omega_L \approx 100\ \mathrm{s}^{-1}$). From a numerical calculation (see Sec. A.4.1), this frequency mismatch would lead to a $\mu_z/\mu \simeq 0.04$ fractional polarization being tipped into the vertical direction at the end of 30 seconds of optical pumping.

Self field

The polarized ^{199}Hg spins generate a magnetic field, and if there is vertical polarization, then the magnetic field generated by the atoms directly modifies the main magnetic field that sets the Larmor frequency. This "self" field decreases as the spin polarization decays, leading to a systematic frequency drift during the probe phase. The magnetization (dipole moment per unit volume) generated by the ^{199}Hg spins is given by

$$\boldsymbol{M} = n\mu_{Hg}\boldsymbol{P}_A, \tag{7.1}$$

where $n \simeq 4 \times 10^{13}\ \mathrm{cm}^{-3}$ is the room temperature ^{199}Hg density, $\mu_{Hg} = 0.506\mu_N$, and $\boldsymbol{P}_A$ is the atomic polarization. If we assume the magnetization is constant in the volume of our cylindrical cell, then the magnetic field seen by a magnetic dipole (^{199}Hg atom) at point $\mathbf{r_0}$ is given by [Jac99, Ch. 5]

$$\boldsymbol{B}(\mathbf{r_0}) = \frac{\mu_0}{4\pi}\boldsymbol{\nabla} \times \int_V \frac{\boldsymbol{M} \times \hat{\boldsymbol{r}}'}{|\boldsymbol{r}'|^2}\mathrm{d}^3\mathrm{r} - \frac{2}{3}\mu_0\boldsymbol{M}, \tag{7.2}$$

where $\hat{\boldsymbol{r}}' = \mathbf{r} - \mathbf{r}_0$. The integral portion of Eq. 7.2 gives the vector potential due to the distribution of magnetic dipoles and for a constant magnetization, reduces to an integral over a surface current described by $\boldsymbol{M} \times \hat{\boldsymbol{n}}$. Subtracting $2/3\,\mu_0\boldsymbol{M}$ removes the $\hat{\boldsymbol{r}}' = 0$ contribution to the magnetic field, which is necessary because an individual ^{199}Hg dipole does not experience a magnetic field due to itself.

For the case of a spherical cell, the integral and $\hat{\boldsymbol{r}}' = 0$ contributions are exactly equal, so there is no self magnetic field experienced by the atoms. For a cylindrical cell with the magnetization along the cell axis, the vector potential is equivalent to a solenoid wound around the cell walls with

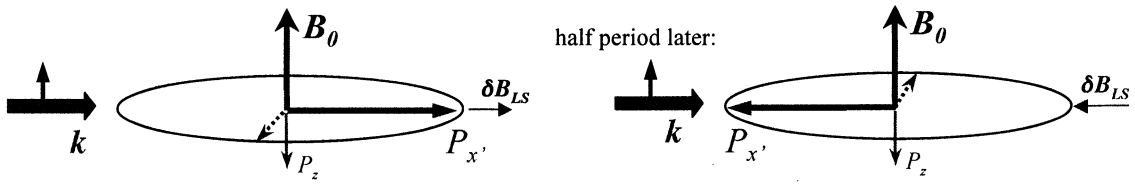

Figure 7.3: Effect of Zeeman light shifts during the probe phase. Linearly polarized probe light acquires a small degree of circularity due to absorption by the spin polarized vapor, leading to a virtual magnetic field $\propto \hat{k} \cdot \boldsymbol{P}$ that can coherently rotate P_z into the y' direction.

a current density per length of M_z. The field inside an infinitely long magnetized cylinder is then given by $\mu_0 M_z$. A numerical calculation for our non-infinite cells ($L = 1$ cm, $R = 1.2$ cm) gives an average field due to magnetization of about $0.5\mu_0 M_z$. Subtracting the $\hat{\boldsymbol{r}}' = 0$ contribution then gives

$$B_z \simeq -0.17\mu_0 M_z = 0.22 P_z \text{ nG}, \tag{7.3}$$

where P_z is the magnitude of the vertical atomic polarization component. For a realistic vertical polarization of 0.05, the self magnetic field would give a frequency shift of only 5×10^{-8} s^{-1}.

Probe light shift

Vertical atomic polarization can have a much larger effect on the precession frequency if light shifts during the probe phase are considered. While perfectly linearly polarized probe light would cause zero Zeeman light shift, the light seen by the atoms will generally have some amount of circular polarization due to birefringence of the cell walls and differential absorption of σ_+ and σ_- light by the spin polarized vapor. The dipolar absorption leads to a time dependent effective magnetic field along the light direction proportional to $\hat{k} \cdot \boldsymbol{P}_A$. In a frame rotating with the atomic spins at ω_L, this looks like a constant magnetic field along the spin direction (x'), and this field causes the vertical polarization to precess into the y'-direction in the rotating frame, developing a polarization component 90° out of phase with the main polarization component. The coherent growth of the orthogonal rotating polarization over the course of the probe phase leads to a phase change in the overall spin precession that looks like an apparent frequency drift during the probe phase.

Based on the calculations in App. A, at the -20 GHz detuning, a perfect linearly polarized probe beam would acquire a circularity of about $0.03\,P_x$ after passing through a cell filled with a vapor with polarization P_x along $\hat{k}$. Taking half this value as the average circularity seen by the atoms in

the cell, then the average precession frequency of the vertical magnetization in the $y'z$-plane is

$$\delta\omega = \gamma_{Hg}\delta B_{LS}\frac{0.03}{2}P_{x'}\langle\cos^2\omega_L t\rangle \simeq 1.6\times10^{-4}P_{x'}\ (\mathrm{s}^{-1}), \tag{7.4}$$

where δB_{LS} is evaluated from Eq. A.14 (at -20 GHz and $\mathrm{I}_0 = 10\ \mu\mathrm{W/cm}^2$), the average value of $\cos^2\omega_L t$ is $1/2$, and $M_{x'}/M$ gives the degree of atomic polarization in the rotating frame. If we disregard optical pumping effects of the light, then the time evolution of the atomic polarization in the rotating frame is

$$\frac{\mathrm{d}}{\mathrm{d}t}\boldsymbol{P} = -\Gamma_r\boldsymbol{P} - \delta\omega\boldsymbol{P}\times\hat{\boldsymbol{x}}', \tag{7.5}$$

which for an initial vertical polarization of $P_z(0)$ and initial rotating polarization component $P_{x'}(0)$ has solutions

$$\begin{aligned} P_{x'}(t) =& P_{x'}(0)e^{-\Gamma_r t}, \\ P_{y'}(t) =& P_z(0)e^{-\Gamma_r t}\sin\delta\omega t \simeq \delta\omega\, t\, P_z(0)e^{-\Gamma_r t} \\ P_z(t) =& P_z(0)e^{-\Gamma_r t}\cos\delta\omega t. \end{aligned} \tag{7.6}$$

The phase change of the rotating polarization vector due to precession of the vertical polarization is given by $\Delta\phi = P_{y'}/P_{x'}$, giving an apparent shift in the spin precession frequency of

$$\Delta\omega_L = \frac{\Delta\phi}{t} = \frac{P_z(0)}{P_{x'}(0)}\delta\omega \simeq 1.6\times10^{-4}P_z(0)e^{-\Gamma_r t}\ (\mathrm{s}^{-1}). \tag{7.7}$$

So for an initial vertical polarization of 0.04, the frequency shift due to the vertical magnetization is as large as $6.4\times10^{-6}\ \mathrm{s}^{-1}$. The effect decays with the spin polarization, giving a drift in the measured frequency of $5.5\times10^{-6}\ \mathrm{s}^{-1}$ over the course of the 200 second probe phase, which matches the frequency drifts we had observed.

Light shift zeroing

For a given sign of the light shift magnetic field, which is wavelength dependent, the direction that the frequency drifts depends on which direction the vertical magnetization accumulates during the pump phase, above or below the xy-plane, which in turn, depends on the sign of the chopper frequency mismatch, $\omega_c - \omega_L$. The buildup of vertical magnetization can be minimized by ensuring that the chopper frequency exactly matches ω_L, which we accomplished by installing gradient compensation coils (see Sec. 6.5.1) and improved control of the chopper frequency (Sec. 6.5.2). We also studied the light wavelength dependence of the frequency shift by deliberately setting the chopper frequency above and below the spin precession frequency in alternate scans (with the electric field off), and then analyzing the spin precession signal in the same way one analyzes for an EDM-like signal when the HV polarity is alternated.

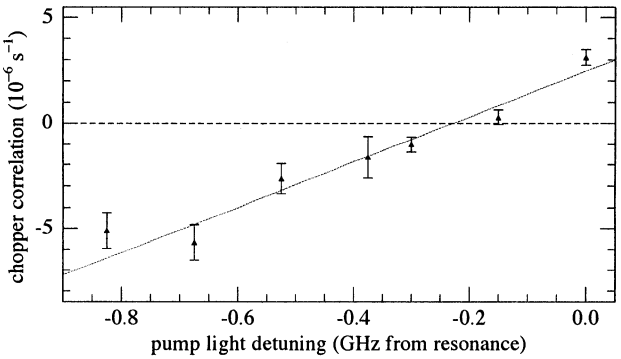

Figure 7.4: Frequency drift dependence on the pump light wavelength. The data is from the outer bottom cell with a probe detuning of +8 GHz. The solid line is a linear fit which crosses zero at -0.23 ± 0.03 GHz.

As is shown in Figure A.4, the Zeeman light shift responsible for generating vertical magnetization changes sign about 0.2 GHz below the $F = 1/2$ resonance. Figure 7.4 shows the chopper correlated ($\omega_c = \omega_L \pm 0.1$ s^{-1}) frequency shift in a single vapor cell as the pump wavelength is set at various points within 1 GHz of the $F = 1/2$ resonance. As expected, the shift crosses zero near -0.2 GHz. This also suggests that besides matching ω_c and ω_L, the vertical magnetization can be further minimized by setting the pump wavelength to the light shift zero point, which decreases the optical pumping rate by less than 1%. Since Run 30690, we have used a pump wavelength of -0.2 GHz, and the wavelength is kept from drifting from this point with a lock system described in Section 6.5.3.

The sign of the vertical magnetization induced frequency drift is also dependent on the probe light wavelength, which gives a different sign light shift field above and below the -0.2 GHz point, but we cannot use a probe wavelength of -0.2 GHz and set this shift to zero. However, there is an additional sign change due to the probe wavelength because the sense of circularity that the probe light acquires changes sign exactly halfway between the $F = 1/2$ and 3/2 lines, since the dipolar absorption crosses zero there (see Fig. A.3). When the dipolar absorption is zero, the probe light acquires no circular polarization from the atomic vapor, so there is no Zeeman light shift in this case. Figure 7.5 shows the chopper correlated frequency shift as the probe wavelength is set at several points in between the $F = 1/2$ and 3/2 lines, with the pump wavelength set to the $F = 1/2$ resonance. We can get an additional reduction of vertical magnetization frequency shifts by setting the probe detuning to about +11 GHz.

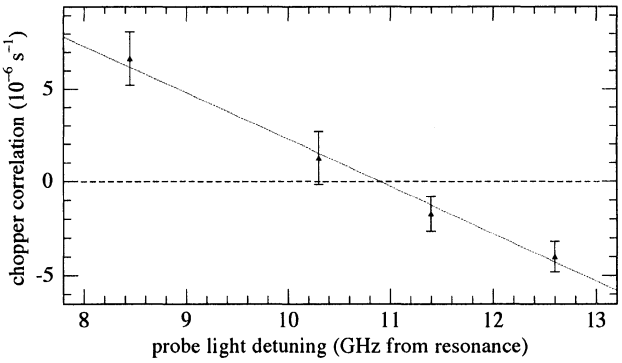

Figure 7.5: Frequency drift dependence on the probe light wavelength. The data is from the outer bottom cell with a pump detuning of zero. The solid line is a linear fit which crosses zero at 10.9 ± 2.4 GHz.

For the initial runs taken at the "+10" GHz probe detuning (19611 – 39699), the actual detuning used was closer to +8 GHz, which is the location of a local absorption minimum in the EDM cells (see Fig. 2.3), whereas the halfway point is a local absorption maximum due to trace amounts of even Hg isotopes in the enriched ^{199}Hg vapor. Since Run 39995, the data taken at "+10" GHz has used an actual detuning of +11.08 GHz to provide a third protection against vertical magnetization effects.

The installation of the light shift compensation measures led to improved sensitivity at the +10 GHz detuning by about a factor of two, but it was found that the systematic frequency shifts between the first and second 100 seconds of the probe phase, while reduced by 30–50%, were still definitely present.

7.1.2 Amplitude Dependent Shifts due to Signal Linearization

Upon further investigation, it was found that the size of the frequency drifts observed during the probe phase was smaller when a lower photodiode amplifier gain was used. This led us to suspect that phase shifts imparted on the signal by the detector electronics were causing the apparent frequency drifts, and ultimately this, along with our data analysis procedure, turned out to be the culprit.

Figure 7.6 shows the frequency response of our detector system (including the photodiode, photodiode amplifier, analog divider, and computer DAQ system) for our standard configuration. The response fits reasonably well to a system of two low-pass *RC* filters with poles at around 50 and

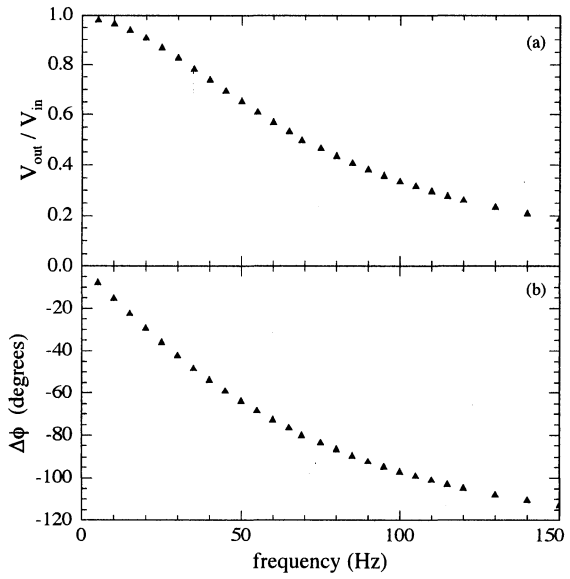

Figure 7.6: Frequency response of the detector system. Plot (a) shows the amplitude response and plot (b) shows the phase shift. The signal was generated by driving a LED in front of the photodiode with a sinusoidal current, and then the drive signal and computer acquired signals were compared.

100 Hz, which correspond to the bandpass of the photodiode amplifier and the 100 Hz filters on the DAQ analog inputs. The expected photodiode signal goes as

$$\mathrm{I}(t) = \mathrm{I}_0 \sin^2\big(\alpha + \varphi(t)\big), \tag{7.8}$$

where α is the analyzing linear polarizer angle and $\varphi(t) = \varphi_0 e^{-t/\tau}\sin(\omega t + \phi)$ is the optical rotation angle. As is described in Section 4.2.1, the fitting procedure begins by solving Eq. 7.8 for $\varphi(t)$, the result of which is then digitally filtered to keep only the first harmonic of the signal. However, since inverting Eq. 7.8 involves taking a square root, higher order harmonics with different instrumentation induced phase shifts (see Fig. 7.6) are mixed into the fundamental, leading to an apparent amplitude dependent frequency shift in the fitted signal.

As a simple example, we can work out the frequency shift due to the signal linearization in the small angle limit, $|\varphi_0| < \alpha < 1$, acted on by a single pole filter with width $\Gamma = 50$ Hz. In this limit the signal becomes proportional to

$$\begin{aligned}\sin^2(\alpha+\varphi) &= \alpha^2 + 2\alpha\varphi + \varphi^2 + \cdots \\ &\simeq \alpha^2 + \frac{\varphi_0^2}{2}e^{-2t/\tau} + 2\alpha\varphi_0 e^{-t/\tau}\sin(\omega t+\phi) - \frac{\varphi_0^2}{2}e^{-2t/\tau}\cos(2\omega t + 2\phi).\end{aligned} \tag{7.9}$$

When the filter is applied, the first harmonic is phase shifted by an angle $\theta_1 = \arctan(-\omega/\Gamma)$, and its amplitude is reduced by a factor of $1/\sqrt{1+\omega^2/\Gamma^2}$. Similarly, the second harmonic is phase shifted by $\theta_2 = \arctan(-2\omega/\Gamma)$ and its amplitude is reduced by $1/\sqrt{1+4\omega^2/\Gamma^2}$. If we divide Eq. 7.9 by α^2 and use the expansion, $\sqrt{1+x} = 1 + x/2 - x^2/8 + \cdots$, keeping only the first harmonic of the square root of Eq. 7.9 gives the terms

$$\frac{\varphi_0 e^{-t/\tau}}{\alpha\sqrt{1+\omega^2/\Gamma^2}}\left[\left(1-\frac{\varphi_0^2}{4\alpha^2}e^{-2t/\tau}\right)\sin(\omega t+\phi+\theta_1)\right.$$
$$\left.-\frac{\varphi_0^2}{8\alpha^2}\frac{e^{-2t/\tau}}{\sqrt{1+4\omega^2/\Gamma^2}}\sin(\omega t+\phi-\theta_1+\theta_2)\right]. \tag{7.10}$$

Equation 7.10 can be written as $A\sin(\omega t+\phi+\theta_1+\beta)$, where β is a phase shift introduced by the square root, which at lowest order in φ_0 is given by

$$\beta \simeq \frac{\varphi_0^2}{8\alpha^2}\frac{e^{-2t/\tau}}{\sqrt{1+4\omega^2/\Gamma^2}}\sin(2\theta_1-\theta_2). \tag{7.11}$$

The phase shift, β, leads to a frequency shift $\Delta\omega = \partial\beta/\partial t$ that varies in time as $e^{-2t/\tau}$. For $\varphi_0/\alpha = 0.25$, the size of the frequency shift is about $6\times10^{-6}e^{-2t/\tau}$ s^{-1}.

In order to avoid this type of frequency shift, we have simply removed the linearization step from the data analysis procedure. The signals are simply digitally filtered to keep only the first harmonic, and are then fit to the function $y(t) = Ae^{-t/\tau}\sin(\omega t+\phi)$. Without the linearization procedure, different frequency components are no longer mixed (by application of the square root), and we then no longer see any systematic frequency shift between the first and second half of the probe phase, or any correlations of the fitted precession frequency and the signal amplitude. However, since the signal envelope of the first harmonic is generally not a perfect exponential decay, removing the linearization procedure also leads to significantly larger amplitude deviations in the fit, as shown in Figure 7.7. The large amplitude deviation has relatively little effect on the fitted value of the precession frequency, though.

Data since Run 34658 have all been fit without linearization. We have not taken the time to refit all of the previous runs, but have fit several runs with and without linearization for comparison. The linearization procedure generally leads to a constant shift in the fitted frequencies of order 10^{-6} s^{-1}. As long as the signal amplitudes and spin relaxation times are the same in all the cells, this frequency shift tends to cancel when differences of frequencies are looked at, leading to a shift in a frequency difference of order 10^{-7} s^{-1}. When the string analysis is performed to extract the HV correlation, the linearization results for a run can be shifted by as much as a few times 10^{-9} s^{-1}, but generally the error estimate of the result is about the same whether or not linearization is used. So

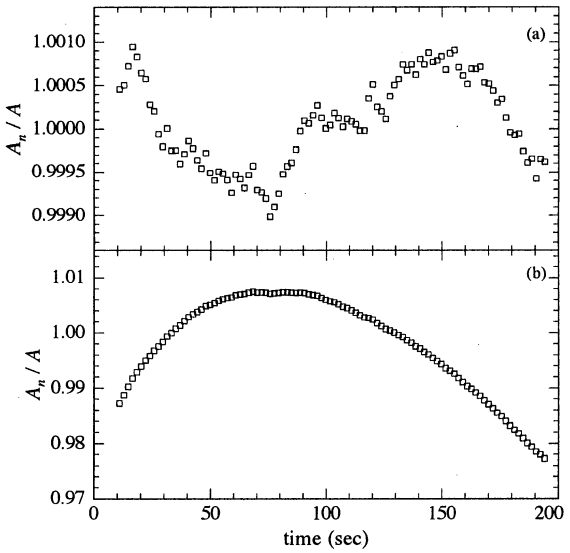

Figure 7.7: Amplitude deviations with and without linearization. Plot (a) shows the amplitude deviation for the middle bottom cell in Scan 19750 (see also Fig. 7.1) when the linearization procedure is performed using $\alpha = 45°$. Plot (b) shows the amplitude deviation when no linearization is used.

removing the systematic frequency drift during the probe phase has not led to a noticeable increase in sensitivity, but it is definitely good to remove a potential source of frequency noise.

7.2 Data Taking Procedure Changes

Besides using probe light detunings between the $F = 1/2$ and $3/2$ lines, two other changes that we have made in the data taking for HG4 are the details of the timing of the measurement cycle, and implementation of a parameter reversal sequence to evenly apply parameter settings.

7.2.1 HV Switch Time Offset

As is shown in Figure 4.19, the EDM signal in HG3 for different HV reversal times (HVS) looks like it has a possible correlation, but the correlation slope is not statistically significant. It would be easier to obtain a better limit on the possible correlation if a wider range of HVS times could be used, but if we want the HV ramp to finish by the end of the pump phase, we are limited to a maximum HVS time of 30 seconds. Instead, beginning with Run 37713 we have changed the time that the HV starts to ramp from the start of the pump phase, to 30 seconds before the start of the

pump phase, and use HVS times of 5, 10, 20, 30, 40, or 50 seconds. We have also increased the total data cycle time from 233 seconds to 263 seconds, which includes 30 sec. of optical pumping, 3 sec. to switch between pump and probe configuration, a 200 sec. probe phase at constant HV, and an additional 30 sec. in the probe configuration during which the HV might be ramping to its next value. The longer scan time decreases slightly the number of measurements we can perform in a given amount of time (by a factor of 0.89), but we can potentially gain much more knowledge about any HV ramp rate related systematic effects.

The first 200 seconds of the probe phase (with the HV constant) are fit to give the spin precession frequency of the scan, but we can also look for effects of the charging currents on the spin precession frequency by separately fitting the last 30 seconds of the probe phase. In HG3 we had only a very small amount of data where the HV was ramped outside of the pump phase, which showed no resolvable effect from the charging currents. We can now potentially obtain much better statistics on magnetic fields due to charging currents by having data for every scan we take.

7.2.2 Parameter Reversal Sequence

Since the application of parameter reversals was somewhat haphazard during HG3, we are attempting to follow a more stringent schedule of reversals for HG4. Table 7.1 shows the reversal plan, which consists of a total of 32 runs in four groups of eight run sequences, A, B, C, and D, where all possible combinations of five binary parameters are used. Each run is assumed to last approximately one day, and within each sequence, four additional runs to check for systematic effects are performed, giving a total of 12 days of data. At the end of each sequence the vessel is opened and the vapor cells are rearranged or replaced. Assuming that the cell replacement can be performed within two days, and there are no time consuming problems during the sequence, each sequence is expected to take about two weeks, and the entire schedule A–D would take about two months, after which the schedule would be repeated.

For the HV ramp time, + and − refer to a long and short ramp time used during a particular sequence. The planned long/short groupings are 30/5, 40/10, and 50/20 seconds. The middle and outer channel directions refer to the order in which signals from particular cell positions are input into the computer. For the middle cells, + designates that the middle top cell signal is on DAQ channel 1 and the middle bottom cell on channel 2, and − is the opposite configuration. For the outer cells, + designates that the outer top cell is on channel 3 and the outer bottom cell is on channel 4. We do not plan to mix the middle and outer channels with each other. For the magnetic field, + corresponds to the field pointing down and − is the field pointing up. For the probe detuning, the + and − correspond to the probe light being at about ±10 GHz from the $F = 1/2$ line.

Table 7.1: Data sequence parameter reversal plan.

	A	B	C	D
HV ramp time	+-+-+-+-	-+-+-+-+	+-+-+-+-	-+-+-+-+
middle channel direction	++--++--	--++--++	++--++--	--++--++
outer channel direction	+--++--+	-++--++-	+--++--+	-++--++-
$\boldsymbol{B}$ direction	++----++	++----++	--++++--	--++++--
probe detuning	++++----	----++++	++++----	----++++

This particular schedule was picked such that the parameter that is easiest to change, the HVS time, is changed the most frequently (7 times per sequence), and parameters that take more effort to change are reversed less frequently. Changing the magnetic field requires that the magnetic shields be degaussed, and the gradient compensation be readjusted, so it is changed twice per sequence. Changing the probe detuning requires that the probe light attenuation and the analyzing polarizer angles be adjusted, so it is changed just once per sequence.

The plan for the four systematic check runs are a run using an HV sequence of $+0-0$ to look for quadratic effects, two runs with the magnetic field tipped 10° from vertical (one run tipped NS and one run tipped EW) to monitor for $\boldsymbol{v} \times \boldsymbol{E}$ effects, and one run using probe light polarized 45° from vertical to check for light shift effects.

The plan shown in Table 7.1 is meant to be mainly a guideline to encourage even application of configurations rather than a strict schedule, and it is likely to evolve as it is applied. At this point, having taken over 200 days worth of data, we have only attempted to follow a schedule for three sequences. The parameter reversals employed in these runs are shown in Table 7.2.

7.3 Frequency Combinations

In a two cell experiment, there is only one significant linear combination of cell frequencies to consider: the difference between the two cells. With four cells, there are many more linear combinations of frequencies that can be of interest. Table 7.3 shows the relevant frequency combinations from four cells, where the precession frequencies from the cells are labeled from the topmost to bottommost cell as ω_{OT}, ω_{MT}, ω_{MB}, and ω_{OB}.

The six pairwise differences cancel common magnetic field fluctuations, and monitoring only the middle difference ($\Delta\omega_M$) would give essentially the same 2-cell measurement as in HG3. The outer

Table 7.2: HG4 data sequences. Parameter values are shown for HG4 data runs where some attempt was made to follow a parameter reversal schedule, however the reversals do not exactly conform to the schedule given in Table 7.1.

RUN	37713	37987	39447	39699	39995	41033	42061	42326	42963	43187	45638	45943	46515	47142	47799	48120	57005	57266	57847	58103	58399	58711	59308	59605
t_{HVS}	10	5	10	5	10	10	40	20	5	30	30	5	30	5	40	5	20	50	20	50	20	50	20	50
middle Ch	−	−	+	+	+	+	+	−	−	−	+	+	+	−	+	+	−	−	+	−	−	−	+	+
outer Ch	−	+	−	−	−	−	−	−	−	+	+	−	−	+	+	−	−	+	+	+	−	+	+	−
B	+	+	−	−	−	−	−	−	+	+	+	+	−	−	−	−	−	−	−	−	+	+	+	+
detuning	+	+	+	+	+	−	+	+	−	−	+	+	+	+	−	−	+	+	−	+	−	−	+	+

Table 7.3: Frequency combinations.

2-cell	3-cell	4-cell
$\Delta\omega_M = \omega_{MT} - \omega_{MB}$	$-\frac{1}{2}\omega_{OT} + \omega_{MT} - \frac{1}{2}\omega_{MB}$	$\Delta\omega_M - \frac{1}{3}\Delta\omega_O$
$\Delta\omega_O = \omega_{OT} - \omega_{OB}$	$-\frac{1}{2}\omega_{MT} + \omega_{MB} - \frac{1}{2}\omega_{OB}$	$\Delta\omega_T - \Delta\omega_B$
$\Delta\omega_T = \omega_{OT} - \omega_{MT}$	$-\frac{2}{3}\omega_{OT} + \omega_{MT} - \frac{1}{3}\omega_{OB}$	
$\Delta\omega_B = \omega_{MB} - \omega_{OB}$	$-\frac{1}{3}\omega_{OT} + \omega_{MB} - \frac{2}{3}\omega_{OB}$	
$\Delta\omega_{XT} = \omega_{OT} - \omega_{MB}$		
$\Delta\omega_{XB} = \omega_{MT} - \omega_{OB}$		

difference ($\Delta\omega_O$) is between two cells with no electric field, so it has no EDM sensitivity and can be used to screen for magnetic systematic effects. The other four differences have half the EDM sensitivity of $\Delta\omega_M$ (when oppositely directed electric fields are applied to the middle cells), but they can also be helpful in determining the location of magnetic effects. Due to magnetic gradient fluctuations, noise cancellation works better in adjacent cells than in differences between cells with one ($\Delta\omega_{XT}$, $\Delta\omega_{XB}$) or two ($\Delta\omega_O$) cells between them.

The 3-cell combinations listed in Table 7.3 are able to cancel common fluctuations and linear gradient fluctuations. Compared to $\Delta\omega_M$, the EDM sensitivities of the first two combinations are reduced by 1/4, and the second two are reduced by 1/2. We generally have not paid attention to the 3-cell combinations and have only monitored them in a few runs.

The first 4-cell combination listed in Table 7.3 has the same EDM sensitivity as $\Delta\omega_M$ and also cancels all magnetic fluctuations through second order gradient noise. This is the main EDM sensitive channel monitored in HG4, and we generally refer to this combination as the "Combo" channel. The factor of 1/3 comes from the fact that the outer cells are three times farther apart than the middle cells, and 1/3 precisely cancels a linear gradient. Depending on the strength of higher order gradients, though, a slightly different factor might give the best noise cancellation. The Combo factor can be determined from the linear correlation between $\Delta\omega_M$ and $\Delta\omega_O$, as is illustrated in Figures 7.8–7.10 for an individual run. We generally use the short term correlation factor as determined from the string analysis because it is the string points that are used to calculate the EDM signal. Figure 7.11 shows the short term linear correlation factor between $\Delta\omega_M$ and $\Delta\omega_O$ from a collection of about 100 different runs, which have an average value of 0.290(4). Using the fitted Combo factor for a run, instead of the expected value of 1/3 generally leads to a small increase in sensitivity in the Combo channel of a few percent.

The second 4-cell combination listed in Table 7.3 cancels up to a linear magnetic field gradient, similar to the 3-cell combinations, but it has no EDM sensitivity (for opposite electric fields applied to the middle cells), so it is our most sensitive monitor for magnetic systematic effects. We commonly refer to this channel as the LeakTest combination (or LeakT in cases of increased brevity), because this channel can help to test for leakage current magnetic fields.

7.4 Dataset

As of May 2004, we have taken a total of about 200 days worth of data with the 4-cell system in 327 data runs. The individual data runs are between 2 and 44 hours long, with an average run-time of 15.4 hours. Out of this dataset, electric fields were applied in one or both of the middle cells in

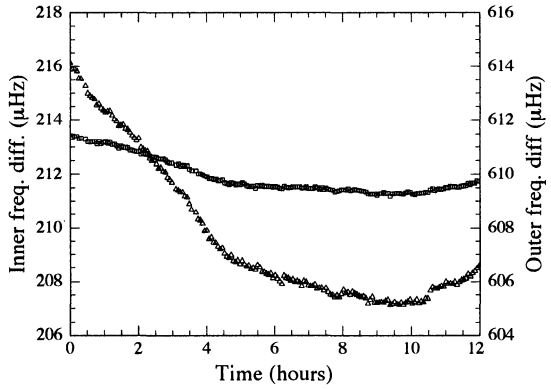

Figure 7.8: Frequency drift in the middle and outer frequency differences. The triangles are the outer difference and the squares are the middle difference.

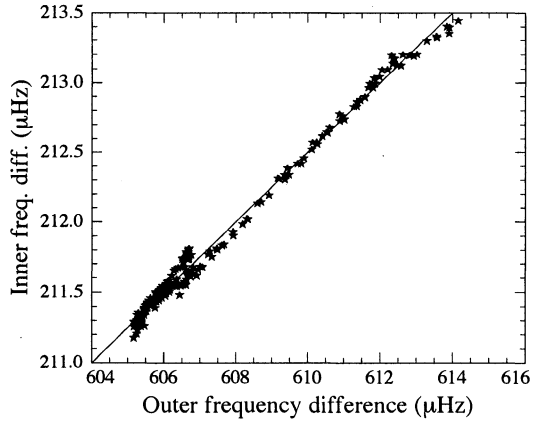

Figure 7.9: Long term correlation of the middle and outer frequency differences. The data in Fig. 7.8 has been plotted against each other. The solid line is a linear fit with a slope of 0.250(2), which gives the long term linear correlation.

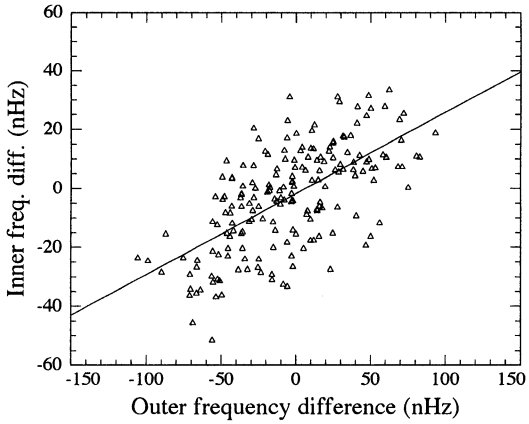

Figure 7.10: Short term correlation of the middle and outer frequency differences. This plot shows the correlation between string points (of length 3) calculated from the data in Fig. 7.8. A linear fit gives a correlation slope of 0.280(25).

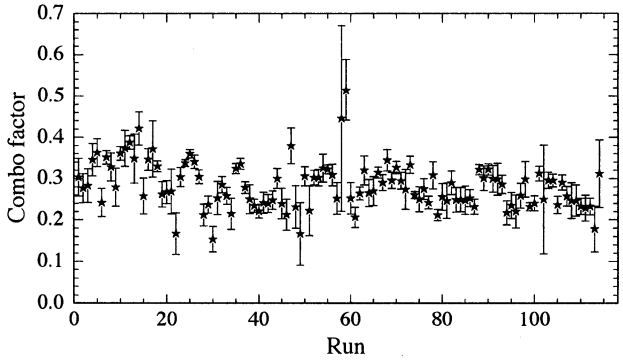

Figure 7.11: Short term correlation slopes from a collection of runs. These factors times the outer frequency difference should be subtracted from the middle difference to give the best noise cancellation.

160 days of data in 222 data runs. The EDM signal resulting from the electric field data runs as measured by the middle cell frequency difference is shown in Figure 7.12, and the signal as measured in the EDM sensitive 4-cell frequency combination is shown in Figure 7.13.

7.4.1 False Signals

The first thing one notices about the dataset shown in Figures 7.12 and 7.13 is that there are a large number of runs that resulted in significantly resolved non-zero signals, well outside even the bound set by the last lamp measurement, HG2, of $|d| < 8.7 \times 10^{-28}$ e cm [Jac95]. It can without question be assumed that these signals are not caused by a real ^{199}Hg EDM, for one thing, because of the definitely non-statistical fluctuations in the signal.

Furthermore, in many cases where there is a well resolved signal in $\Delta\omega_M$ or the Combo channel, there is also a well resolved signal in a non-EDM sensitive frequency combination, as indicated by the open circle points in Figures 7.12 and 7.13. The outer frequency difference should never give a signal from a real EDM. In addition, for runs where high voltage is applied to both of the middle cells (174 runs) the LeakTest channel also has no EDM sensitivity. In runs where the HV is applied only to the top middle cell (24 runs), $\Delta\omega_B$ and $\Delta\omega_{XT}$ give no EDM signal, and when the HV is applied to the bottom middle cell, $\Delta\omega_T$ and $\Delta\omega_{XB}$ give no EDM signal.

For the purposes of this chapter, a "false signal" is defined to be cases where the central value of that run's HV correlated string points is more than 3 standard deviations away from zero. The cutoff value of 3σ is somewhat arbitrary, although we might claim that through Chauvenet's criterion [Bev92], we can discard data if its distance from the mean is greater than the range outside of which we would expect less than half a data point, which for 222 points the cutoff is at 3.05σ. Comparing data points to an expected mean of zero is a safe assumption for non-EDM sensitive channels, but for the EDM sensitive channels such as $\Delta\omega_M$ and the Combo, we must be careful that in performing a non-blind measurement, we should not overly bias ourselves toward necessarily generating a null result. It would be slightly more correct to reference the data points to the mean of the dataset instead of zero, but this changes our classification of "false signals" in very few instances, because the typical error bar on an individual data run is much larger than the central value of the dataset.

By comparing Figures 7.12 and 7.13, it can be seen that the Combo channel has a smaller amount of scatter than $\Delta\omega_M$. While the middle frequency difference has 54 instances of $> 3\sigma$ resolved signals, the Combo channel has only 21, indicating that in many cases the frequency shift in $\Delta\omega_M$ is likely due to a magnetic field gradient that is canceled in the Combo. While the Combo channel might be less susceptible to the systematic effect polluting the middle frequency difference, the presence of

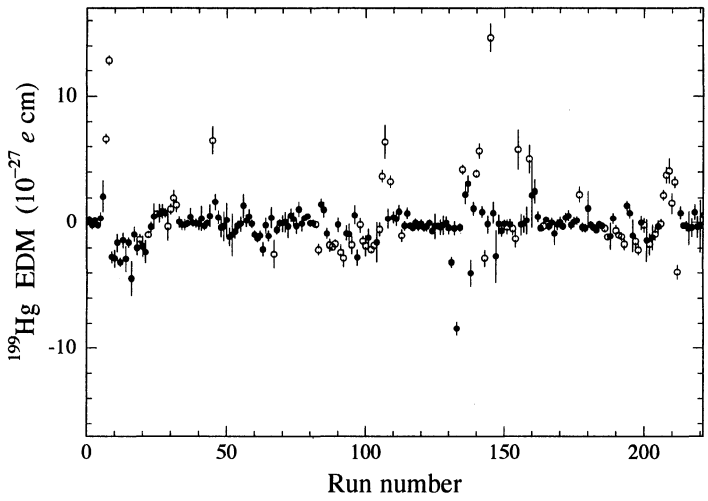

Figure 7.12: EDM signal measured by the middle frequency difference. The open points mark runs where a greater than 3σ resolved signal was found in any non-EDM sensitive frequency combination. A weighted average of the entire dataset gives a central value of $(-1.06 \pm 0.26) \times 10^{-28}$ e cm, χ^2/d.o.f. = 18.3, but this should in no way be interpreted as an actual measurement of the ^{199}Hg EDM.

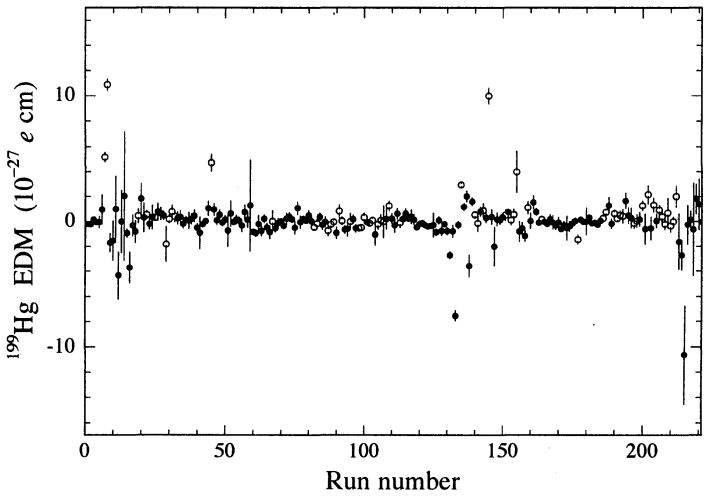

Figure 7.13: EDM signal measured by the Combo channel for the same dataset as in Fig. 7.12. A weighted average gives a central value of $(0.50 \pm 0.20) \times 10^{-28}$ e cm, χ^2/d.o.f. = 10.9.

a large HV correlated frequency difference in any frequency combination is an indicator that there is a problem with the apparatus, and the non-EDM HV correlation could very easily leak into the Combo channel at some level. Out of the 222 point HG4 dataset, about 100 runs have $> 3\sigma$ resolved signal in at least one frequency combination, making much of the dataset suspect of contamination.

In a small handful of cases we believe we understand the origin of the false signal. We have had false signals caused by anomalously large leakage currents, large currents flowing between the vessel and the magnetic field coil, and ferromagnetic orientation due to HV sparks in a broken cable/feedthrough. Unfortunately, we cannot satisfactorily explain the origin of a great majority of the false signals we have encountered.

The general pattern of data taking with the HG4 apparatus has been that we are able to take between several days and several weeks of good data, and then a resolved false signal would appear in multiple frequency channels, typically corresponding to a HV correlated magnetic field gradient of at least 10 pG/cm (a 5×10^{-8} s^{-1} frequency difference between adjacent cells), which is easily resolvable in any of the 2-cell differences in less than a day of data. The onset of problems usually occurred directly after the cell-holding vessel has been opened and cells have been rearranged, but occasionally the false signal would appear a week or two later. We would then spend several weeks or months attempting to find the source of the false signal by changing various experimental parameters, such as the HV reversal rate, the HV value, the side of the vessel to which the HV is connected, and the position of the electrodes and HV cables/feedthroughs.

The HV reversal rate never had any noticeable effect on a false signal, but there was generally a dependence on the HV value. We did not have the sensitivity to determine if the dependence on the electric field magnitude was linear or quadratic, but there was usually a threshold-type behavior, and sometimes the false signal would be present for one HV polarity and not the other. In almost all cases, the resolved signals could be isolated to one side of the vessel in that the signals would tend to appear at full strength when HV was applied to only one side of the vessel, and then the signal would not be present when the HV was applied only to the other side. Tests of this sort led us to believe that the false signals might be associated with a particular electrode or cable/feedthrough, after the false signal behavior seemed to follow the position of these components. However, it is difficult to trust this data because these tests require the vessel to be opened, and the cells removed, in order to exchange the electrodes or cables, and any time the vessel is opened there seems to be a good probability that the false signal character will change substantially.

The results of our efforts tended to be that while we might gain some knowledge about the general characteristics of a false signal after some time and effort and modifications to the vessel, at

Table 7.4: HG4 and HG3 false signal occurrence comparison. The "Runs" column gives the fraction of all HV runs where a 3σ signal was observed, and the "Sequences" column gives the fraction of times when any false signals occur in a sequence of runs between cell changes. In HG4 there are $N_R = 222$ total runs, and $N_S = 45$ sequences. HG3 has 127 total runs and 14 sequences.

		Runs: N	N/N_R	Sequences: N	N/N_S
HG4	all combinations	95	0.43	30	0.67
	$\Delta\omega_M$	54	0.24	26	0.58
	scaled $\Delta\omega_M$ (1.4)	35	0.158	19	0.42
	scaled $\Delta\omega_M$ (1.8)	21	0.095	12	0.27
HG3	$\Delta\omega$	6	0.047	3	0.21

some point the false signal would disappear without us being able to really say exactly why it had gone away. We could only shrug our shoulders and cautiously proceed to take data, but then several weeks later a new false signal would invariably appear. So after dealing with these types of issues fairly constantly over a couple year period of taking data with the 4-cell apparatus there are a few main questions one might ask...

Could these problems have existed during HG3 and we just didn't notice?

The total time we have spent dealing with false signals with the HG4 apparatus has seemingly been a much larger fraction of our efforts than it was during the HG3 dataset, but with the additional frequency combinations available to monitor and the improved HG4 sensitivity, it might be possible that false signals of the same size also occurred often during HG3 and they would not have been resolvable in the frequency difference, so they did not raise warning flags at the time.

In order to compare the false signal occurrence in HG3 versus HG4, one method is to take all of the data runs where HV was applied to the cells, and count the number of runs where there is at least a 3σ resolved frequency correlation. This count is shown in the "Runs" column of Table 7.4. For the HG4 section, the first row is the number of runs where there is a resolved signal in any frequency combination, and the second row considers only the middle difference to correspond with the only frequency difference available in HG3. Then, to account for the reduced sensitivity of HG3, in rows three and four the $\Delta\omega_M$ error estimate for each run is increased by a constant factor, which gives a reduced number of false signals. 1.4 is the ratio of the average sensitivity per unit time for HG3 and HG4 runs, and 1.8 is the ratio when the mode of the sensitivities per unit time are compared (see Sec. 7.4.3).

Since we believe that the onset of false signals is correlated with making changes to the cell holding vessel, strictly counting data runs might not be the best way to judge the false signal occurrence rate, because there were times when we took a large number of data runs without opening the vessel while attempting to study a false signal, and other times we opened the vessel after only a run or two which sometimes made the false signal disappear. If we define a "Sequence" of runs to start when the vessel is installed in the magnetic shields, and end the next time the vessel is removed, then we can count the number of sequences where any run during that sequence gives a resolved frequency difference signal. The result of this type of count is given in the "Sequences" column of Table 7.4.

Looking at the last three lines of Table 7.4, we can say that if we had the same sensitivity as in HG3, then we still would see between 1.3 and 3.4 times as many false signals during HG4 compared to HG3, depending on which comparison method is used. So while it is certainly possible that additional HV correlated frequency shifts were occurring unnoticed during HG3, it is fairly certain that HV correlated frequency shifts are occurring somewhat more often now than during HG3.

Do the additional false signals originate from a change made in the apparatus?

If we accept that false signals are occurring more often for HG4 than in HG3, then it is natural to wonder if a change made in the HG4 apparatus or procedure has led to the increase in false signals. Table 7.5 lists the differences between the HG3 and HG4 setups. It is of course easier to formulate plausible false signal generating scenarios involving some changes more than others, but with enough imagination one can probably figure out a way that any combination of changes might lead to an increase in unwanted HV correlations. To give a couple of examples, any change in the vessel/electrode/feedthrough construction might lead to a change in how rigidly the cells are held in place, making us more susceptible to HV induced movement of the cells. Also, the smaller diameter magnetic field coil, which was nested inside the larger coil, might have provided additional electromagnetic shielding (the coils were mounted on aluminum cylinders) of the effects of fast magnetic fields due to HV sparks on magnetic material outside the coils, such as the magnetic shields.

In late 2003 we began trying to test whether any of the changes listed in Table 7.5 had an effect on the false signals we were observing. We began by switching back to the (conductive polyethylene) 2-cell vessel from HG3, which also enabled us to test the feedthroughs, electrodes, and groundplane. We were still using the polyethylene shape adapter in the larger coil and the CO cells, though. In 9 runs, we encountered several well resolved false signals. Next we brought two of the N_2+CO cells back from retirement and installed them in the HG3 vessel, and we saw 3 instances of false signals

Table 7.5: Comparison of the HG3 and HG4 apparatus and procedure.

	HG3	HG4
vessel size	4×4×5"	5×5×6"
magnetic field coil	ID = 6"	7.5"
shape adapter	Teflon	polyethylene, has notches for gradient wires
HV feedthroughs	OD = 0.3"	0.5", substantially changed interface with vessel
electrodes	D = 2"	3", in 2 parts with nylon screws and conductive gasket
groundplane	2.8×2.8", suspended by screws	4×5", flush with vessel walls, thicker around the edge
vapor cells	90% N_2 + 10% CO	100% CO buffer gas
light shift compensation		3 grad. loops, funct. generator chopper control, pump λ-lock
magnetic field scan time probe detuning	17.5 mG 133 sec. -20 GHz	20 mG 233, and 263 sec. ± 10 GHz

in 23 runs. The final configuration change we implemented was to mount the vessel with the Teflon shape adapter in the smaller field coil, nested inside the larger coil (still with the N_2+CO cells). We did not go to the effort of changing the current source wiring to hook the smaller coil up, though, so the larger coil still provided the magnetic field. In this configuration we took 10 runs and saw 8 false signals. Throughout these runs, the light shift compensation measures were turned on and off, the scan time was shortened, and the probe detuning was varied, and we found that none of these parameters seemed to effect the false signals we were observing.

So, using the 2-cell vessel, we tested all of the configuration changes listed in Table 7.5 except for the magnetic field value, which was left at the larger value, and all of the tested configurations gave rise to false signals similar in size to what we have experienced with the HG4 setup. This seems to indicate that the false signals are not caused by any particular change made in implementing the 4-cell setup. We do not have enough runs with each individual configuration (i.e., older cells vs. new cells, after the smaller coil was installed) to do a comparison of the rate of false signal occurrence for each configuration, but considering all of the data runs taken during the 2-cell redux using the 2-cell vessel, we had resolved false signals in 14 out of 42 runs, giving a fractional occurrence of 0.29, and we had false signal runs occur in four out of four "sequences." The statistical sensitivity per unit time during these runs was comparable to the HG3 sensitivity, so there is no need to scale the results in doing a comparison to the HG3 results in Table 7.4. It seems that the incidence of false signals with the 2-cell vessel has increased significantly from when it was used during HG3.

So what's going on, really?

At this point, it is our belief that the large number of false signals, in the form of HV correlated spin precession frequency signals, that we have seen in the HG4 data are not the result of a particular change implemented in the 4-cell vessel. The source(s) of these false signals could easily have been present during the HG3 dataset and probably contributed to the couple of instances of unexplained false signals we encountered in HG3. The increased attention and effort we have had to devote toward these false signals is at least partially due to our improved statistical sensitivity and the additional frequency combinations available to monitor, but there is also evidence that suggests that the source of the false signals has somehow become more prolific than it was in 2000 when we took the HG3 data. We can at least take comfort that the 4-cell apparatus has performed well in that it has enabled us to much more quickly tell that there is a troublesome systematic effect present, but unfortunately, so far the 4-cell apparatus has not enabled us to figure out just what the source of the systematic effect is. An evaluation of the leading suspects for the source of our problems will be given in Section 7.5.

7.4.2 Statistical Sensitivity

Figure 7.14 displays the frequency sensitivity in nHz of the 2-cell and 4-cell frequency combinations that have been monitored during the HG4 dataset. The statistical error estimate for the entire 160 day dataset has been scaled to give the sensitivity for a 24 hour data run, assuming that the sensitivity scales as $1/\sqrt{t}$. For reference, if ± 10 kV is applied to both of the middle cells then a 1 nHz frequency sensitivity in $\Delta\omega_M$ is equivalent to 1.1×10^{-28} e cm in EDM units.

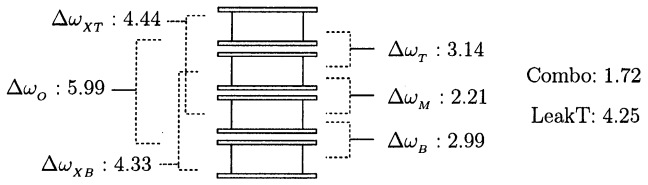

Figure 7.14: Frequency sensitivity in nHz of the HG4 dataset scaled to 24 hours.

The best sensitivity is given by the 4-cell combo, which gives a factor of 1.3 improvement over the 2-cell middle frequency difference due to gradient noise cancellation. The amount of noise cancellation in the Combo channel from run to run depends on the type of magnetic field noise present during the measurement and on the performance of the outer cells. Figure 7.15 shows a histogram of the amount of noise cancellation given in the Combo channel compared to $\Delta\omega_M$ for all of the HG4 data runs. In some cases the ratio is greater than one, indicating that no cancellation occurs, usually due to excessive noise in the outer frequency difference. At least some noise cancellation occurs in the Combo channel in over 75% of the HG4 data runs, and the maximum cancellation has been a factor of 5, and the most probable value of the Combo to $\Delta\omega_M$ sensitivity ratio is 0.875.

As expected, the 2-cell differences between adjacent cells have better sensitivity than differences between separated cells. What is not necessarily expected is that the sensitivities of the top ($\Delta\omega_T$) and bottom ($\Delta\omega_B$) differences are significantly worse than the middle difference, which indicates that the outer cell signals are noisier than the middle cells. To some degree this is because we have tended to put the cells with longer spin coherence times in the middle positions in order to optimize our EDM sensitivity. Over the entire dataset, the middle cell coherence times have ended up on average 30% longer than the outer cell coherence times, but this would not account for the factor of ~ 1.3 increase in noise observed in $\Delta\omega_T$ and $\Delta\omega_B$. The outer positions might be intrinsically noisier due to there being increased magnetic field noise farther from the center of the magnetic shields, there might be more mechanical vibration in the outer positions, or the longer light beam paths used for the outer cells might contribute extra noise compared to the middle beams.

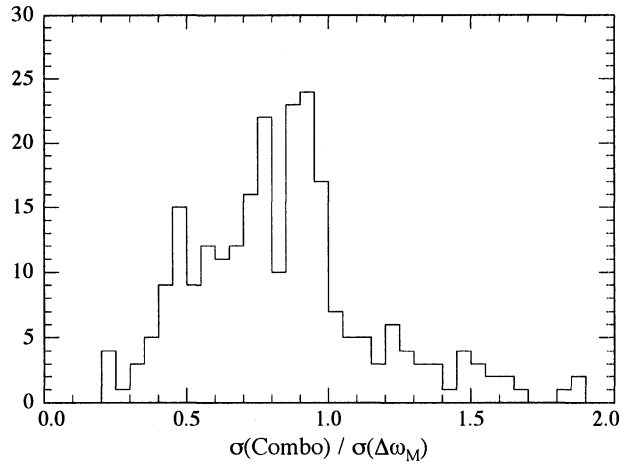

Figure 7.15: Noise cancellation by the 4-cell Combo channel. The plot shows a histogram of the ratio of the middle frequency difference and the Combo statistical sensitivities for each run.

The Leaktest 4-cell combination is also noisier than expected, and has about 2.5 times worse sensitivity than the Combo channel, and is also significantly worse than the adjacent cell differences. This could be due to 2nd order magnetic field gradient noise which is canceled in the Combo channel and not Leaktest, but also if the outer cell positions are intrinsically noisier than the middle positions, the effect on the Leaktest channel is much worse than the Combo because the factor of 1/3 reduction in the outer cells contribution to the Combo channel (see Table 7.3). It is important that we find the source of the extra noise in the outer positions, because if the Leaktest channel is to fully help in setting limits on systematic effects, then the sensitivity must be comparable to the EDM sensitivity. However, we have not been able to investigate this issue as of yet, because we have had to devote so much time into trying to understand the systematic effect that has been creating the large false signals that we have no trouble resolving even with somewhat reduced sensitivity in the outer cells.

7.4.3 Sensitivity Compared to HG3

The frequency difference sensitivity of the HG3 dataset scaled to 24 hours was 3.1 nHz, so in comparing HG4 to HG3 there is a modest improvement of a factor of 1.4 in the middle frequency difference, and the 4-cell Combo gives an additional factor of 1.3, for an overall improvement of a factor of 1.8. This perhaps does not do the HG4 apparatus justice, though, because we have not been able to focus fully on optimizing the 4-cell data signal to noise as we have been trying to deal

with the false signal problems, and many runs have been taken under non-ideal conditions. The best 4-cell run taken so far was Run 59308, which gave Combo sensitivity of 0.7 nHz (scaled to 24 hours), which is a factor of 4.3 improvement over the average HG3 sensitivity, and a factor of 2.8 better than the best 24-hour sensitivity achieved during HG3 of 2.0 nHz (Run 55182).

Figure 7.16 shows histograms (with a bin-width of 0.25 nHz) of the sensitivities of the HG3 and HG4 data runs scaled to 24 hours. From the modes of these distributions, the most probable HG3 sensitivity was 2.875 nHz, the HG4 middle frequency difference gives 1.625 nHz, a factor of 1.8 improvement, and the Combo channel distribution is peaked at 1.375 nHz, a factor of 2 improvement.

7.5 Possible Sources of False Signals

With the many instances of EDM-like false signals we have encountered, it is likely that they have arisen from different sources at different times, but it also seems likely that a predominant mechanism can probably account for a significant fraction of the false signals. The general characteristics of a false signal source candidate are that it must be able to generate HV polarity dependent frequency gradients between the cell positions of at least 10^{-7} s^{-1}/cm (corresponding to a magnetic field gradient of 20 pG/cm), is associated in some way with the vessel such that adjusting the vessel is likely to change the false signal characteristics, and the mechanism can be present for both the HG3 and HG4 configurations. The most easily understandable sources of EDM-like false signals are high voltage correlated magnetic fields.

7.5.1 Leakage Currents

In considering magnetic systematic effects in EDM experiments, the prime suspect is always leakage currents. In our case, any currents flowing near the vapor cells during the probe phase can generate magnetic fields that directly lead to HV correlated frequency shifts. The general false signals we have seen have not been correlated with abnormally large leakage currents, but the typical sizes of the leakage currents that we monitor are (averaged over probe phase):

- collected on the groundplane (Leak Cell) $\sim$ 1 pA
- collected on the vessel (Leak Vessel) $\sim$ 5 pA
- total currents collected at the vessel (top cell + bottom cell + Vessel) $<$ 10 pA
- measured current in the center conductor of the HV cable (Leak Cable) $\sim$ 0.1 nA

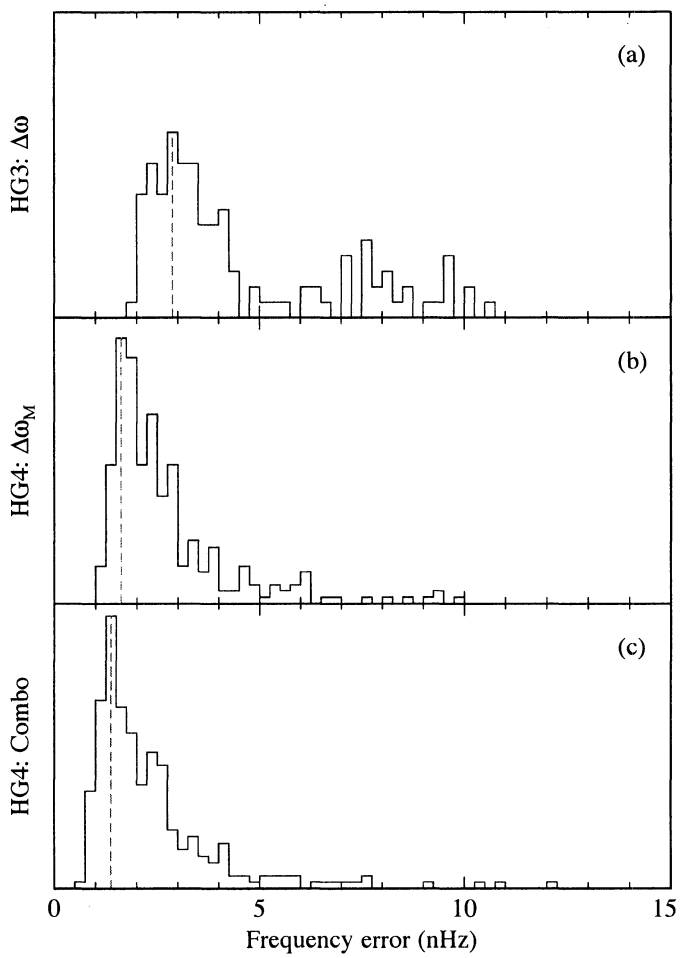

Figure 7.16: Comparison of the HG3 and HG4 data run sensitivities. Plots (a)–(c) show the distribution of 24-hour scaled statistical sensitivity obtained in all runs in the HG3 frequency difference, HG4 2-cell middle frequency difference, and 4-cell Combo channel. The dashed vertical lines mark the mode of the distribution.

The ^{199}Hg frequency shift that can be generated by these currents is dependent on the current's path. If a current happened to flow such that it made one complete loop around a cell, the magnetic field at the center of the cell would be

$$B = \frac{\mu_0 I}{2R}, \quad R = 0.5'' \rightarrow \Delta\omega = 2.4 \times 10^{-9}\ \mathrm{s}^{-1}/\mathrm{pA} \tag{7.12}$$

So if the entire cable current of 0.1 nA has this path, there would be a shift of 2.4×10^{-7} s^{-1}, but it is very unlikely that the majority of the cable current is flowing this close to the cell or it would show up in the cell or vessel current monitors.

We have one example of a run where a large leakage current definitely led to a well resolved EDM signal. In Run 72780 the top cell current began to increase rapidly and eventually it saturated the leakage monitor (> 200 pA), but the cable current monitor did not saturate and indicated that $\sim$ 15 nA was flowing in the cable. Before the Leak Cell 1 monitor saturated, the cable current reading scaled proportionally to the summation of the three leakage current monitors (the linear correlation slope gives $\sim$ 1.5 nA on the cable current per nA on the leakage monitors). Also, the bottom cell and vessel currents did not increase above 100 pA during this run, so it seems reasonable to assume that a large fraction of the 15 nA in the HV cable was flowing across the middle top cell onto the top half of the groundplane.

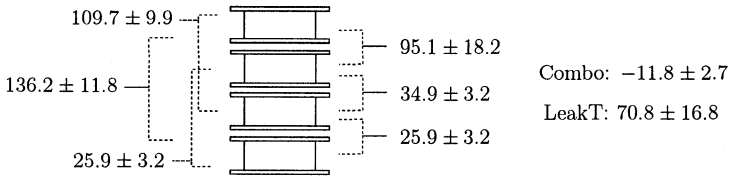

Figure 7.17: Frequency profile generated by large leakage currents in Run 72780. These signals occurred when about 10 nA of current flowed across the middle top cell to the groundplane.

The EDM profile for this leakage current generated signal is shown in Figure 7.5.1. The largest frequency differences involve the outer top cell, which indicate a leakage current EDM signal of about 10^{-7} s^{-1}/nA, an order of magnitude smaller than the simple complete loop estimate of 2.4×10^{-6} s^{-1}/nA.

So it seems that leakage currents are unable to generate a substantial EDM-like signal in individual runs unless there is enough current to saturate the leakage current monitors, which has only occurred in a few abnormal cases. It is still possible for steady state currents to generate a false signal if they are flowing in such a way that we do not detect them with our current monitors. This

has occurred in at least one instance (Runs 16733–17288), where the top HV cable shield was making intermittent contact with the magnetic field coil form, leading to ground loop currents. In this case there were very well resolved frequency shifts of $(3.0 \pm 0.5) \times 10^{-6}$ s^{-1} in the single cell frequencies (the largest frequency difference signal was $\Delta\omega_O = (25 \pm 5) \times 10^{-8}$ s^{-1}). We have eliminated this particular problem by providing additional electrical insulation around the HV cable/feedthrough interface.

7.5.2 Magnetic Imprint Effects

Although we don't believe that steady state currents during the probe phase are large enough to generate the false-EDMs, large magnetic field "events" during the HV ramp might leave a magnetic imprint on materials with ferromagnetic properties inside or near the vessel. This type of effect requires two ingredients, a fairly large magnetic field event occurring in opposite directions for opposite HV polarities, and a magnetically orientable source material that retains the effect of the magnetic field event for a timescale longer than 100 seconds.

Field generation

While the high voltage ramps to a new value, currents much larger than the leakage currents flow into the vessel, and the size of the currents is determined by the capacitance of the system:

$$C = \frac{Q}{V} = \frac{dQ/dt}{dV/dt} \quad \rightarrow \quad I = C\frac{dV}{dt} \tag{7.13}$$

The vessel (including the groundplane currents) has a capacitance of $\sim$ 20 pF and the coaxial HV cable has a capacitance of 30 pF/ft. The highest charging currents occur for the most rapid HV ramp rate of 4 kV/sec, which results in 100 nA flowing to the vessel, and perhaps 1 μA flowing in the HV cables entering the magnetic shields. The slowest ramp rate generally used is a factor of 10 slower.

It is hard to believe that magnetic fields generated by currents of this size would be large enough to orient a ferromagnetic material. Also, changing the HV ramp rate is the easiest experimental parameter to adjust, so almost all instances of false-EDMs have been checked for a dependence on the HV ramp rate, and there has never been any noticeable change in the signal size. Unless we have always been beyond a saturation point for this effect, it seems very unlikely that the charging currents are responsible for the false signals.

On the other hand, magnetic fields generated by fast time scale electric sparks could quite plausibly lead to ferromagnetic orientation which would cause HV polarity dependent frequency

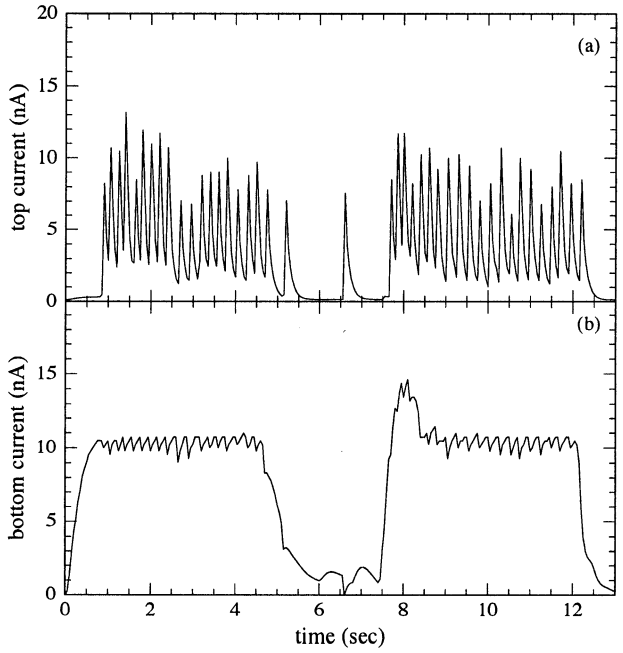

Figure 7.18: Charging current spikes in a broken HV feedthrough. Plot (a) shows the charging currents for the top side of the groundplane in Scan 43800 for which the cable inside the top feedthrough was broken, and plot (b) shows the charging currents on the bottom side of the groundplane in the same scan.

shifts. We have seen this type of effect with both the HG3 and HG4 apparatuses. In the HG3 occurrence, which is described in Section 3.2.2, occasional sparks in a broken HV feedthrough left permanent shifts of about 10^{-4} s^{-1} in the bottom cell precession frequency. The direction of the shift was dependent on the HV polarity at the time of the spark, but since there was usually a several hour delay between sparks, this did not lead to an EDM-like signal.

The HG4 occurrence was again caused by a broken HV feedthrough connection (in Runs 43724 and 44037), but this time the connection was more severely broken, leading to sparks across the broken connection every time the HV was ramped as shown in Figure 7.18. These sparks led to the frequency shift profile shown in Figure 7.19, and the shifts went away after the HV feedthrough was repaired.

We have also looked for magnetic fields created by HV sparks by mounting pickup coils on the outside of the vessel, as is described in Section 6.2.3. With a 20 turn, $R = 5$ cm coil mounted on the front of the vessel, we saw pickup events on the coil (400 mV) that were correlated with

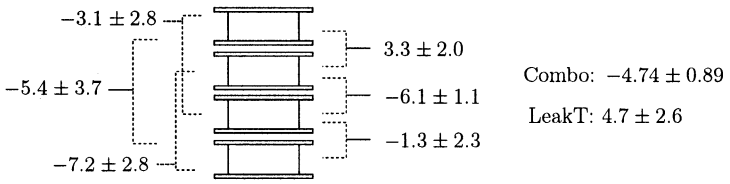

Figure 7.19: Frequency shift profile due to sparks in the top HV feedthrough, averaged from Runs 43724 and 44037.

spikes in the charging currents. The charging current spikes were removed by modifying the HV cable/feedthrough design and this also eliminated the pickup events in the coil, but we have no evidence that these spikes were causing any frequency shifts, and we have certainly continued to observe false signals since eliminating these spikes.

We later installed somewhat larger 100 turn, 4.5" square coils flush with the top and bottom faces of the vessel. With these coils we observed smaller pickup events (20 mV) that mainly occurred several seconds after the HV would finish a downward ramp ($+10 \rightarrow -10$, $+10 \rightarrow 0$, or $0 \rightarrow -10$ kV). The origin of these pickup events is not known, but once again they do not seem to correlate with the false EDM signals we were observing at that particular time. Depending on the HV ramp parameters (starting and final HV values, and the ramp rate) we sometimes saw a resolved false signal and no pickup events, and for some HV values we would see a large number of pickup events and no resolved false signal.

So it seems that with large enough spark events, EDM-like false signals can occur. It is probably impossible to guarantee that no electric discharge spark-like events will occur, but the particular details of the vessel and feedthrough design can help reduce sparking. Short spark magnetic fields can be observed with pickup coils, but we currently do not believe that pickup events we have observed in this manner are related to the false signals. It is always possible, though, that we are not detecting the "guilty" sparks due to their time scale or location.

Ferromagnetic source material

The fact that HV sparks can lead to permanent shifts in the magnetic field that the cells see is good evidence that there are ferromagnetic materials in or around the vessel. We have also applied "artificial sparks" where a capacitor is discharged over a small loop located inside the vessel to create a short magnetic field burst (see Sec. 3.2.2). The artificial sparks also create remnant magnetization, and by measuring the remnant magnetic field in the four cell positions, we can see

that the magnetization is consistent with a dipole source located at the loop position. We certainly try to avoid using magnetic materials in the vessel, but the ferromagnetic behavior could be due to local contaminants embedded in the materials, low levels of impurities throughout the bulk materials, or surface contamination.

The somewhat transient nature of many of the EDMs we have seen is suggestive of a "dirty" effect, such as a small (invisible to the naked eye) grain or speck of material that enters or leaves the vessel without our direct knowledge. In several instances of false signals, the onset of the problem, or a significant shift in the size of the signals, has occurred without our having modified anything internal to the magnetic shields, except by flowing the SF_6 gas through the vessel. A possible explanation for this behavior is that metal particles from the gas cylinder/regulator drift into the vessel through the SF_6 flow lines, become stuck somewhere in the vessel for a while, and eventually make their way out of the vessel. We have recently installed a Teflon membrane filter in the SF_6 line (with a 0.003 μm pore size) to guard against this possibility.

7.5.3 Force/Displacement due to High Voltage

Applying high voltage to the vessel can lead to a false signal if the HV causes the vapor cells to move in a magnetic field gradient, or if the HV causes a magnetized object near the cells to move. In most cases it would seem more likely that electric field induced motion would be HV polarity independent, but there is a possibility that some of the vessel materials might have piezoelectric properties.

Cells moving in a magnetic field gradient

Without compensation, the vertical stack of four cells is subject to a generally quadratic magnetic field gradient (see Fig. 6.7). Simply taking the difference between the Larmor frequency measured in an outer cell and a middle cell (~ 0.1 s^{-1}) gives an estimate of the linear gradient seen by an outer vapor cell to be 12.5 μG/cm. So to produce a false EDM of 10^{-7} s^{-1}, an outer cell only needs to move 16 nm.

However, the majority of 4-cell data (Scan number > 27000) has been taken with the vertical gradient compensation system, which equalizes the Larmor frequencies in the four positions to $\sim 10^{-4}$ s^{-1}, a factor of 1000 better than the "natural" gradient, and there has been no indication that turning the gradient compensation on or off has had any effect on the size of a false EDM signal.

Of course, the gradient compensation only applies to the gradient in the vertical direction, $\partial B_z/\partial z$, so it would not affect horizontal motion. It is also possible, that the gradient compensation might equalize the magnetic fields measured in all four positions, and vertical motion would

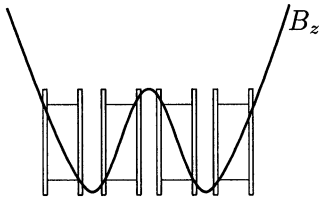

Figure 7.20: Hypothetical magnetic field that would elude gradient compensation. The four cells would measure equal precession frequencies, but vertical motion would still cause a frequency shift.

still cause frequency shifts as is shown in Figure 7.20. On two occasions (around runs 83378 and 87925) additional gradients were applied from loops configured to create linear gradients in B_z in the x, y, and z directions. The size of the additional gradient was estimated to be about 5× larger than normal, by measuring the decrease in T_2 due to the field gradient for several different currents. Applying the additional gradients had no observable effect on the false EDM signal that was present at that time, and we can also place a limit on HV induced relative cell motion to be less than ~ 10 nm.

The fact that significantly altering the magnetic gradient environment seen by the cells has not led to significant changes in the false-EDM's makes motion of the vapor cells as the main source of false signals seem very unlikely at this point. Given the possibility of different EDM-sources at different times, though, cell motion may not have been occurring during these gradient tests, but it might be involved in other instances.

Movement of nearby magnetic materials

We may be fairly confident that the cells do not move when the HV is applied, but some other component of the vessel could be moving, and this could generate false signals if that component is magnetized, perhaps due to an abnormally large HV spark, or if a magnetic contaminant has become attached to it. By moving various materials a few cm away from a flux gate magnetometer inside our magnetic shields, we can fairly easily check that none of the vessel parts generate magnetic field gradients larger than 10 μG/cm. At this level, though, HV induced motion of about 20 nm would produce a frequency shift of 10^{-7} s^{-1}.

We have attempted to make more precise measurements of the magnetization of materials with our ^{199}Hg magnetometers, by manually moving a test piece near the cells, making a 100 second spin precession measurement, and then repeating the measurement several more times each time

manually moving the test piece in or out. This is a somewhat tedious process, though, and to achieve good sensitivity (about 1 nG/cm) the test piece must be moved to the same position and orientation each time. At this point we have only tested electrodes T and E, and vapor cell #44. The cell had no magnetic signature to the nG level, but both electrodes tested gave measurable magnetic gradients of $\sim$ 10 nG/cm when moved near the magnetometer cells. A surface cleaning of electrode T did not cause an appreciable change to its magnetic signature. At this level, the electrode would have to move 20 μm to generate false signals of the proper size. Motion of the electrode would very likely also give corresponding motion of the cell inside, though, and the magnetic field gradient tests discussed in the previous section probably rule this out.

We have also looked for HV induced motion by attaching small current loops to vessel components, and looking for HV correlated signals associated with the extra gradient generated by the current loop. We have attached loops to the HV cable about an inch away from where it enters the vessel, on the ends of the HV feedthroughs outside the vessel, and on the outer feedthrough holding collars. We saw no resolved signals for these cases, and so can place limits on HV induced motion of these particular locations to be less than $\sim$ 10 nm.

At this point we have not fully tested for this effect. We definitely plan on making additional measurements of the magnetization of more vessel components, and also try to assess whether or not the magnetization can be reduced. It would be nice to test for motion of components inside the vessel, but we are somewhat wary of attaching current loops in places where there is exposed high voltage.

7.6 Summary and Outlook

After the publication of the HG3 2-cell result [Rom01a], it was hoped that we would be able to achieve a new limit with the 4-cell apparatus within one to two years, given that we were not making an especially radical change to the measurement technique. Four years later, we have not been able to publish a new limit due to the still unexplained outbreaks of false signals, and at this point it is entirely unclear how far away we are from an improved result.

On the bright side, though, the changes implemented in the 4-cell apparatus have led to a not insignificant improvement in our statistical sensitivity, between a factor of two and four, depending on how the HG3 and HG4 datasets are compared (see Sec. 7.4.3). If we were free from dealing with the false signal issues, then it seems reasonable to presume that we could fairly easily accumulate data that maintained a factor of three better sensitivity per unit time than the HG3 measurement. The HG3 dataset was taken over a period of six months and reached a statistical sensitivity of

4.9×10^{-29} e cm. Assuming the same duty cycle as the HG3 measurement, and a factor of three sensitivity per unit time improvement, it would take us less than one year to achieve an overall factor of four improvement in statistical sensitivity, and about 16 months to reach the 1×10^{-29} e cm level.

Most of the systematic error estimates that contributed to our HG3 systematic error budget were limited by statistics, so an improved statistical sensitivity would directly scale down all of the limits listed in Table 4.8 except for the one-loop leakage current contribution, which would only improve if the average leakage currents somehow became lower (so far the HG4 data have given about the same average cell leakage current as HG3 of 0.6 pA). If we assume the same one-loop leakage current contribution of 2.5×10^{-29} e cm, along with a factor of five reduction in all other error estimates, we would only achieve a factor of two improvement over the total HG3 uncertainty. However, the one-loop estimate can be considered quite a conservative evaluation of leakage current effects, and the additional magnetometer cells in HG4 can possibly increase our confidence such that we might take a slightly less conservative approach, such as using the correlation between the EDM signal and the leakage current fluctuations to set a limit on the leakage current contribution. The degree to which a signal is not resolved on the Leaktest 4-cell combination can also be used to estimate the leakage current contribution, but if the sensitivity obtained on this channel remains 2.5 times worse than the Combo channel, then if we assume that we can reach 1×10^{-29} e cm on the Combo channel, the Leaktest sensitivity would end up being 2.5×10^{-29} e cm, the same level as the one-loop estimate. Hopefully the Leaktest sensitivity can be improved somewhat, however, due to its sensitivity to second order magnetic gradient noise, it is probably unlikely that it can consistently match the Combo channel. There have been several runs where the Leaktest sensitivity has only been 5–10% worse than the Combo channel.

Of course, this prognosis is only valid if the large false signals that have plagued us with the 4-cell apparatus can be eliminated, or at least fixed such that they occur substantially less frequently. At this point it seems most likely that the problem is related to magnetic contaminants getting into the vessel that then lead to frequency shifts due to electric field induced motion or ferromagnetic orientation due to HV sparks. Some hope is left that the contaminants were entering through the SF_6 line, and that the installation of a filter in the gas line will solve our problems. We are also in the process of implementing a cleaner handling procedure for the cell holding vessel including the measures that the vessel will only be opened under a laminar flow hood, and the vessel will only be handled with nonmagnetic tools. It is planned that under clean conditions, the vessel will be entirely disassembled, thoroughly cleaned, and then put back together. If the false signals still persist, then we will likely seriously consider a major redesign of the vessel which would probably include (but not

be limited to) a different (more rigid) material for the bulk of the vessel, a more durable conductive layer on the groundplane, and a careful redesign of the HV feedthroughs, which are an especially likely problem spot for HV sparking and motion.

Assuming that the false signal occurrence rate can be greatly reduced, it is still an open question as to how we will decide that the problem has been "solved" to the level that we are confident that we can work on accumulating an unpolluted dataset. It will be especially difficult to be certain that the systematic issue is not present at a smaller level that we are not able to easily resolve in a day's worth of data. If that uncertainty remains, we can still use the Leaktest channel to place a limit on the systematic responsible for the false signals, since they seem to be magnetic effects measurable by the magnetometer cells. In that case, our overall uncertainty will likely be limited by the sensitivity we achieve on the Leaktest channel.

Although the persistent false signals have delayed a new 4-cell ^{199}Hg EDM result, we are aware of no fundamental reason why the experiment can not be made to work as reliably as it did during the HG3 dataset in 2000. Assuming that we can maintain uncontaminated operation for a reasonable amount of time ($\sim$ 1 year), we should be able to push our ^{199}Hg EDM sensitivity close to the 10^{-29} e cm level, but any increase in sensitivity is already probing an interesting region of CP violation beyond the Standard Model.

BIBLIOGRAPHY

[Abe01] S. Abel, S. Khalil, and O. Lebedev. EDM constraints in supersymmetric theories. *Nuclear Physics B*, 606:151–82, 2001.

[Bab01] Babar Collaboration, B. Aubert, *et al.* Observation of CP violation in the B_0 meson system. *Physical Review Letters*, 87:091801/1–8, 2001.

[Bar93] S. M. Barr. A review of CP violation in atoms. *International Journal of Modern Physics A*, 8:209–36, 1993.

[Bar04] V. G. Baryshevsky. Time-reversal-violating generation of static magnetic and electric fields and a problem of electric dipole moment measurement. *Physical Review Letters*, 93:043003/1–4, 2004.

[Bel61] William E. Bell and Arnold L. Bloom. Optically driven spin precession. *Physical Review Letters*, 6:280–1, 1961.

[Bel01] Belle Collaboration, K. Abe, *et al.* Observation of large CP violation in the neutral B meson system. *Physical Review Letters*, 87:091802/1–7, 2001.

[Bev92] Philip R. Bevington and D. Keith Robinson. *Data Reduction and Error Analysis for the Physical Sciences.* WCB/McGraw-Hill, Boston, 2nd edition, 1992.

[Blu04] Robert Bluhm. Lorentz and CPT tests in matter and antimatter. *Nuclear Instruments and Methods in Physics Research B*, 221:6–11, 2004.

[Brh99] M. Brhlik, L. Everett, G. L. Kane, and J. Lykken. Resolution to the supersymmetric CP problem with large soft phases via D-branes. *Physical Review Letters*, 83:2124–7, 1999.

[Bro52a] J. Brossel, A. Kastler, and J. Winter. Optical creation of an inequality of population between the Zeeman sub-levels of the ground state of atoms. *Journal de Physique et le Radium*, 13:668, January 1952.

[Bro52b] Jean Brossel and Francis Bitter. A new "double resonance" method for investigating atomic energy levels. Application to Hg $^3P_1$. *Physical Review*, 86:308–16, 1952.

[Bud02] D. Budker, W. Gawlik, D. F. Kimball, S. M. Rochester, V. V. Yashchuk, and A. Weis. Resonant nonlinear magneto-optical effects in atoms. *Reviews of Modern Physics*, 74:1153–201, 2002.

[Bur95] Eric A. Burt. *Demonstration of Trapped Single Laser Cooled Indium Ions.* PhD thesis, University of Washington, 1995.

[Cag58] B. Cagnac. Optical detection of the nuclear magnetic resonance of ^{201}Hg. *Journal de Physique et le Radium*, 19:863–5, 1958.

[Cag59] B. Cagnac and J. Brossel. Nuclear orientation by optical pumping of the isotopes ^{201}Hg and ^{199}Hg and measurement of their magnetic moments by nuclear magnetic resonance. *Comptes Rendus Hebdomadaires des Séances de l'Académie des Sciences*, 249:77–9, 1959.

[Cat88] G. D. Cates, S. R. Schaefer, and W. Happer. Relaxation of spins due to field inhomogeneities in gaseous samples at low magnetic fields and pressures. *Physical Review A*, 37:2877–85, 1988.

[Cho89] D. Cho, K. Sangster, and E. A. Hinds. Tenfold improvement of limits on T violation in thallium fluoride. *Physical Review Letters*, 63:2559–62, 1989.

[Chr64] J. H. Christenson, J. W. Cronin, V. L. Fitch, and R. Turlay. Evidence for the 2π decay of the $K_2{}^0$ meson. *Physical Review Letters*, 13:138–40, 1964.

[Cio98] Carmine Ciofi, Romano Giannetti, Vincenzino Dattilo, and Bruno Neri. Ultra low-noise current sources. *IEEE Transactions on Instrumentation and Measurement*, 47:78–81, 1998.

[Cog66] H. D. Coghill. Tin oxide: What can we do with it? In *Proceedings of the Eleventh Symposium on the Art of Glassblowing*, pages 128–37. The American Scientific Glassblower's Society, Wilmington Delaware, 1966.

[Cor77] Alan Corney. *Atomic and Laser Spectroscopy.* Oxford University Press, 1977.

[Cre79] R. J. Crewther, P. Di Vecchia, and G. Veneziano. Chiral estimate of the electric dipole moment of the neutron in quantum chromodynamics. *Physics Letters*, 88B:123–7, 1979. 91B:487(E), 1980.

[Cur01] L. J. Curtis, R. E. Irving, and M. Henderson. Measurements and predictions of the $6s6p^{1,3}P_1$ lifetimes in the Hg isoelectric sequence. *Physical Review A*, 63:042502/1–7, 2001.

[Deh57] H. G. Dehmelt. Modulation of a light beam by precessing absorbing atoms. *Physical Review*, 105:1924–5, 1957.

[DeM00] D. DeMille, F. Bay, S. Bickman, D. Kawall, D. Krause, Jr., S. E. Maxwell, and L. R. Hunter. Investigation of PbO as a system for measuring the electric dipole moment of the electron. *Physical Review A*, 61:052507/1–8, 2000.

[Dem04] Durmus Demir, Oleg Lebedev, Keith A. Olive, Maxim Pospelov, and Adam Ritz. Electric dipole moments in the MSSM at large $\tan\beta$. *Nuclear Physics B*, 680:339–74, 2004.

[Dil01] Angom Dilip, Bhanu Pratap Das, Warren F. Perger, M. K. Samal, and K. P. Geetha. Many-body theory of the electric dipole moment of atomic ytterbium. *Journal of Physics B*, 34:3089–106, 2001.

[Dmi03a] V. F. Dmitriev and R. A. Sen'kov. P- and T-violating Schiff moment of the mercury nucleus. *Yadernaya Fizika*, 66:1988–93, 2003. Translated in nucl-th/0304048 and *Physics of Atomic Nuclei*, 66:1940–5, 2003.

[Dmi03b] V. F. Dmitriev and R. A. Sen'kov. Schiff moment of the mercury nucleus and the proton dipole moment. *Physical Review Letters*, 91:212303/1–4, 2003.

[Dmi04a] V. F. Dmitriev and I. B. Khriplovich. P and T odd nuclear moments. *Physics Reports*, 391:243–60, 2004.

[Dmi04b] V. F. Dmitriev, R. A. Sen'kov, and N. Auerbach. Effects of core polarization on the nuclear Schiff moment. nucl-th/0408065, 2004.

[Dre77] W. B. Dress, P. D. Miler, J. M. Pendlebury, Paul Perrin, and Norman F. Ramsey. Search for an electric dipole moment of the neutron. *Physical Review D*, 15:9–21, 1977.

[Duh84] P. Duhamel and H. Hollmann. 'Split radix' FFT algorithm. *Electronics Letters*, 20:14–6, 1984.

[Dzu02] V. A. Dzuba, V. V. Flambaum, J. S. M. Ginges, and M. G. Kozlov. Electric dipole moments of Hg, Xe, Rn, Ra, Pu, and TlF induced by the nuclear Schiff moment and limits on time-reversal violating interactions. *Physical Review A*, 66:012111/1–7, 2002.

[Eid04] S. Eidelman *et al.* Review of particle physics. *Physics Letters B*, 592:1–1109, 2004.

[Eng03] J. Engel, M. Bender, J. Dobaczewski, J. H. de Jesus, and P. Olbratowski. Time-reversal violating Schiff moment of ^{225}Ra. *Physical Review C*, 68:025501/1–9, 2003.

[Ens67] E. S. Ensberg. Experimental upper limit for the permanent electric dipole moment of Rb^{85} by optical-pumping techniques. *Physical Review*, 153:36–43, 1967.

[Fal99] Toby Falk, Keith A. Olive, Maxim Pospelov, and Radu Roiban. MSSM predictions for the electric dipole moment of the ^{199}Hg atom. *Nuclear Physics B*, 560:3–22, 1999.

[Fla85a] V. V. Flambaum and I. B. Khriplovich. New bounds on the electric dipole moment of the electron-nucleon coupling. *Soviet Physics - JETP*, 62:872–5, 1985.

[Fla85b] V. V. Flambaum, I. B. Khriplovich, and O. P. Sushkov. Limit on the constant of T-nonconserving nucleon-nucleon interaction. *Physics Letters*, 162B:213–6, 1985.

[Fla86] V. V. Flambaum, I. B. Khriplovich, and O. P. Sushkov. On the P- and T-nonconserving nuclear moments. *Nuclear Physics A*, 449:750–60, 1986.

[Fla02] V. V. Flambaum and J. S. M. Ginges. Nuclear Schiff moment and time-invariance violation in atoms. *Physical Review A*, 65:032113/1–9, 2002.

[Fla03] V. V. Flambaum and V. G. Zelevinsky. Enhancement of nuclear Schiff moments and time-reversal violation in atoms due to soft nuclear octupole vibrations. *Physical Review C*, 68:035502/1–7, 2003.

[Gam65] Rodger L. Gamblin and Carver Thomas R. Polarization and relaxation processes in He^3 gas. *Physical Review*, 138:A946–60, 1965.

[Ger04] H. J. Gerber. Evidence for time-reversal violation? *European Physical Journal C*, 35:195–6, 2004.

[Gin04] J. S. M. Ginges and V. V. Flambaum. Violations of fundamental symmetries in atoms and tests of unification theories of elementary particles. *Physics Reports*, 397:63–154, 2004.

[Gol72] Leonard J. Goldwater. *Mercury: a History of Quicksilver.* York Press, Baltimore, Maryland, 1972.

[Gre74] R. W. Greaves, E. P. Fowler, A. Goodings, and D. R. Lamb. The direct piezoelectric effect in extruded polyethylene. *Journal of Materials Science*, 9:1602–8, 1974.

[Hän80] T. W. Hänsch and B. Couillaud. Laser frequency stabilization by polarization spectroscopy of a reflecting reference cavity. *Optics Communications*, 35:441–4, 1980.

[Hap67] W. Happer and B. S. Mathur. Effective operator formalism in optical pumping. *Physical Review*, 163:12–25, 1967.

[Hap72] William Happer. Optical pumping. *Reviews of Modern Physics*, 44:169–249, 1972.

[Hap87] W. Happer and W. A. Van Wijngaarden. An optical pumping primer. *Hyperfine Interactions*, 38:435–70, 1987.

[Har99] P. G. Harris, C. A. Baker, K. Green, P. Iaydjiev, S. Ivanov, D. J. R. May, J. M. Pendlebury, D. Shiers, K. F. Smith, and M. van der Grinten. New experimental limit on the electric dipole moment of the neutron. *Physical Review Letters*, 85:904–7, 1999.

[Har00] D. M. Harber and M. V. Romalis. Measurement of the scalar Stark shift of the $6^1S_0 \rightarrow 6^3P_1$ transition in Hg. *Physical Review A*, 63:013402/1–5, 2000.

[Hax94] W. C. Haxton. Limits on CP nonconserving interactions from electric dipole moments. *Chinese Journal of Physics*, 32:947–57, 1994.

[Hax04] Wick C. Haxton. private communication. 2004.

[Her88] Peter Herczeg. T-violation in nuclear interactions - an overview. *Hyperfine Interactions*, 43:77–93, 1988.

[Her95] Peter Herczeg. Time reversal violation in nuclear processes. In Wick C. Haxton and Ernest M. Henley, editors, *Symmetries and Fundamental Interactions in Nuclei*, pages 89–125. World Scientific, Singapore, 1995.

[HH87] Frank Rudolph Huang-Hellinger, Jr. *A Search for a Permanent Electric Dipole Moment in Rubidium.* PhD thesis, University of Washington, 1987.

[Hod91] J. Hodgdon, B. R. Heckel, and E. N. Fortson. Calculation of a linear-Stark effect in D-line absorption in rubidium. *Physical Review A*, 43:3343–7, 1991.

[Hol02] Roy J. Holt. Proposal to measure the electric dipole moment of radium-225. Talk presented at Univ. of Washington Institute for Nuclear Theory workshop (INT-02-3), http://www.int.washington.edu/talks/WorkShops/int_02_3/People/Holt_R/, 2002.

[Hud02] J. J. Hudson, M. R. Sauer, M. R. Tarbutt, and E. A. Hinds. Measurement of the electron electric dipole moment using YbF molecules. *Physical Review Letters*, 89:023003/1–4, 2002.

[Jac91] James Patrick Jacobs. *Search for a Permanent Electric Dipole Moment on Mercury 199 Atoms as a Test of Time Reversal Symmetry.* PhD thesis, University of Washington, 1991.

[Jac93] J. P. Jacobs, W. M. Klipstein, S. K. Lamoreaux, B. R. Heckel, and E. N. Fortson. Testing time-reversal symmetry using ^{199}Hg. *Physical Review Letters*, 71:3782–87, 1993.

[Jac95] J. P. Jacobs, W. M. Klipstein, S. K. Lamoreaux, B. R. Heckel, and E. N. Fortson. Limit on the electric-dipole moment of ^{199}Hg using synchronous optical pumping. *Physical Review A*, 52:3521–3540, 1995.

[Jac99] John David Jackson. *Classical Electrodynamics.* John Wiley & Sons, Inc., third edition, 1999.

[Jac03] James P. Jacobs and R. Bruce Warrington. Pressure shift and broadening of the 254-nm intercombination line of mercury by N_2. *Physical Review A*, 68:32722/1–6, 2003.

[Jun03] K. Jungmann *et al.* TRIμP - trapped radioactive isotopes: μicrolaboratories for fundamental physics. *Nuclear Physics B Proceedings Supplements*, 117(Supplement 1):939–41, April 2003.

[Kan98] G. L. Kane. *Perspectives on Supersymmetry.* World Scientific, Singapore, 1998.

[Kas50] A. J. Kastler. Some suggestions concerning the production and detection by optical means of inequalities in the populations of levels of spatial quantization in atoms. Application to the Stern and Gerlach and magnetic resonance experiments. *Le Journal de Physique et le Radium*, 11:255–65, 1950.

[Khr97] I. P. Khriplovich and S. K. Lamoreaux. *CP Violation Without Strangeness.* Springer, Berlin, 1997.

[Kli96] William M. Klipstein. *Constraints on Time Reversal Symmetry Violation from a New Limit on the Permanent Electric Dipole Moment of Mercury 199, and Observation of Spontaneous Atomic Spin Polarization in Cesium.* PhD thesis, University of Washington, 1996.

[Lam86a] S. K. Lamoreaux, J. P. Jacobs, B. R. Heckel, F. J. Raab, and E. N. Fortson. New limits on spatial anisotropy from optically pumped ^{201}Hg and ^{199}Hg. *Physical Review Letters*, 57:3125–8, 1986.

[Lam86b] Steve Keith Lamoreaux. *Searches for Spatial Anisotropy and a Permanent Atomic Electric Dipole Moment Using Optically-Pumped Mercury.* PhD thesis, University of Washington, 1986.

[Lam87] S. K. Lamoreaux, J. P. Jacobs, B. R. Heckel, F. J. Raab, and N. Fortson. New constraints on time-reversal asymmetry from a search for a permanent electric dipole moment of ^{199}Hg. *Physical Review Letters*, 59:2275–8, 1987.

[Lam92] S. K. Lamoreaux and E. N. Fortson. Calculation of a linear Stark effect on the 254-nm line of Hg. *Physical Review A*, 46:7053–9, 1992.

[Lam96] Steve K. Lamoreaux. Applications of optically pumped mercury to fundamental measurements. In James C. Berquist, editor, *Proceedings of the Fifth Symposium on Frequency Standards and Metrology*, pages 181–6, 1996.

[Lam99] S. K. Lamoreaux. Feeble magnetic fields generated by thermal charge fluctuations in extended metallic conductors: Implications for electric-dipole moment experiments. *Physical Review A*, 60:1717–20, 1999.

[Lam00] S. K. Lamoreaux and R. Golub. Remarks on "New experimental limit on the electric dipole moment of the neutron". *Physical Review D*, 61:051301(R)/1–3, 2000.

[Led02] M. P. Ledbetter and M. V. Romalis. Nonlinear effects from dipolar interactions in hyperpolarized liquid ^{129}Xe. *Physical Review Letters*, 89:287601/1–4, 2002.

[Lee94] Kar Yue Lee. *CP Violation, Schiff Moment and Hadronic Axions.* PhD thesis, University of Washington, 1994.

[Lid04] David R. Lide, editor. *CRC Handbook of Chemistry and Physics.* CRC Press, Boca Raton, FL, 84th edition, 2004.

[Liu92] Z. W. Liu and Hugh P. Kelly. Analysis of atomic electric dipole moment in thallium by all-order calculations in many-body perturbation theory. *Physical Review A*, 45:R4210–3, 1992.

[Mac01] R. Machleidt and I. Slaus. The nucleon-nucleon interaction. *Journal of Physics G: Nuclear and Particle Physics*, pages R69–108, 2001.

[Man63] Jean Manuel and Claude Cohen-Tannoudji. Optical detection of magnetic resonance via the modulation of the transverse paramagnetic Faraday effect at the Larmor frequency. *Comptes Rendus Hebdomadaires des Séances de l'Académie des Sciences*, 257:413–6, 1963.

[Man84] Aneesh Manohar and Howard Georgi. Chiral quarks and the non-relativistic quark model. *Nuclear Physics B*, 234:189–212, 1984.

[Mar03] Reina Maruyama. *Optical Trapping of Ytterbium Atoms.* PhD thesis, University of Washington, 2003.

[McG90] Douglas D. McGregor. Transverse relaxation of spin-polarized ^{3}He gas due to a magnetic field gradient. *Physical Review A*, 41:2631–5, 1990.

[Mil67] P. D. Miller, W. B. Dress, J. K. Baird, and N. F. Ramsey. Limit to the electric dipole moment of the neutron. *Physical Review Letters*, 19:381–4, 1967.

[MP86] Ann-Marie Mårtensson-Pendrill and Per Öster. Calculations of atomic electric dipole moments. *Physica Scripta*, 364:444–52, 1986.

[Mur89] S. A. Murthy, D. Krause, Jr., Z. L. Li, and L. R. Hunter. New limits on the electron electric dipole moment from cesium. *Physical Review Letters*, 63:965–8, 1989.

[Nag99] W. Nagourney, J. Torgerson, and H. Dehmelt. Optical frequency standard based upon single laser-cooled indium ion. *AIP Conference Proceedings*, 457:343–7, 1999.

[Pau55] W. Pauli. Exclusion principle, lorentz group and reflection of space-time and charge. In W. Pauli, Rosenfeld L., and V. Weisskopf, editors, *Niels Bohr and the Developments of Physics*, pages 30–51. Mcgraw-Hill, New York, 1955.

[Pec77] R. D. Peccei and Helen R. Quinn. CP conservation in the presence of pseudoparticles. *Physical Review Letters*, 38:1440–3, 1977.

[Phi77] Leon F. Phillips. Laser fluorescence study of $Hg(^3P_0)$ quenching rates. *Journal of the Chemical Society, Faraday Transactions II*, 73:97–100, 1977.

[Pit72] J. Pitre, K. Hammond, and L. Krause. 6^3P_1-6^3P_0 excitation transfer in mercury, induced in collisions with N_2 molecules. *Physical Review A*, 6:2101–6, 1972.

[Pos99] Maxim Pospelov and Adam Ritz. Theta-induced electric dipole moment of the neutron via QCD sum rules. *Physical Review Letters*, 83:2526–9, 1999.

[Pos01] Maxim Pospelov and Adam Ritz. Neutron electric dipole moment from electric and chromoelectric dipole moments of quarks. *Physical Review D*, 63:073015/1–5, 2001.

[Pos02] Maxim Pospelov. Best values for the CP-odd meson-nucleon couplings from supersymmetry. *Physics Letters B*, 530:123–8, 2002.

[Pre92] William H. Press, Saul A. Teukolsky, William T. Vetterling, and Brian P. Flannery. *Numerical Recipes in C: The Art of Scientific Computing.* Cambridge University Press, 2nd edition, 1992.

[Ram56] N. F. Ramsey. *Molecular Beams.* OUP, London, 1956.

[Reg02] B. C. Regan, Eugene D. Commins, Christian J. Schmidt, and David DeMille. New limit on the electron electric dipole moment. *Physical Review Letters*, 88:071805/1–4, 2002.

[Rom01a] M. V. Romalis, W. C. Griffith, J. P. Jacobs, and E. N. Fortson. New limit on the permanent electric dipole moment of ^{199}Hg. *Physical Review Letters*, 86:2505–8, 2001.

[Rom01b] M. V. Romalis and M. P. Ledbetter. Transverse spin relaxation in liquid ^{129}Xe in the presence of large dipolar fields. *Physical Review Letters*, 87:067601/1–4, 2001.

[Rom04] M. V. Romalis and L. Lin. Surface nuclear spin relaxation of ^{199}Hg. *Journal of Chemical Physics*, 120:1511–5, 2004.

[Ros72] F. Rosebury. *Handbook of Electron Tube and Vacuum Techniques.* Addison-Wesley, Reading, MA, 1972.

[Ros01] M. A. Rosenberry and T. E. Chupp. Atomic electric dipole moment measurement using spin exchange pumped masers of ^{129}Xe and ^{3}He. *Physical Review Letters*, 86:22–5, 2001.

[San64] P. G. H. Sandars and E. Lipworth. Electric dipole moment of the cesium atom. A new upper limit to the electric dipole moment of the free electron. *Physical Review Letters*, 13:718–20, 1964.

[San67] P. G. H. Sandars. Measurability of the proton electric dipole moment. *Physical Review Letters*, 19:1396–8, 1967.

[San93] Jon Carl Sandberg. *Research Toward Laser Spectroscopy of Trapped Atomic Hydrogen.* PhD thesis, Massachusetts Institute of Technology, 1993.

[Sat73] Takuzo Sato. Continuously tunable ultraviolet radiation at 2535 Å. *Journal of Applied Physics*, 44:2257–9, 1973.

[Sch63] L. I. Schiff. Measurability of nuclear electric dipole moments. *Physical Review*, 132:2194–200, 1963.

[Sch99] John H. Schwarz and Nathan Seiberg. String theory, supersymmetry, unification, and all that. *Reviews of Modern Physics*, 71:S112–20, 1999.

[Smi57] J. H. Smith, E. M. Purcell, and N. F. Ramsey. Experimental limit to the electric dipole moment of the neutron. *Physical Review*, 108:120–2, 1957.

[Smi90] K. F. Smith *et al.* A search for the electric dipole moment of the neutron. *Physics Letters B*, 234:191–6, 1990.

[Sus84] O. P. Sushkov, V. V. Flambaum, and Khriplovich I. B. Possibility of investigating P- and T-odd nuclear forces in atomic and molecular experiments. *Zhurnal Eksperimental'noi i Teoreticheskoi Fiziki*, 87:1521–40, 1984. Translated in *Sov. Phys. JETP*, 60:873–88, 1984.

[Swa05] M. D. Swallows, W. C. Griffith, L. K. Kogler, and E. N. Fortson. Measurement of a linear Stark effect on the 254 nm line of Hg. In preparation for submission to *Physical Review A*, 2005.

[Tro99] Mark Trodden. Electroweak baryogenesis. *Reviews of Modern Physics*, 71:1463–99, 1999.

[Var84] T. Varpula and T. Poutanen. Magnetic field fluctuations arising from thermal motion of electric charge in conductors. *Journal of Applied Physics*, 55:4015–21, 1984.

[Vik72] A. C. Vikis, G. Torrie, and D. J. Le Roy. Spin-orbit relaxation of $Hg(6^3P_1)$ by various gases. *Canadian Journal of Chemistry*, 50:176–82, 1972.

[Vol84] T. G. Vold, F. J. Raab, B. Heckel, and E. N. Fortson. Search for a permanent electric dipole moment on the ^{129}Xe atom. *Physical Review Letters*, 52:2229–32, 1984.

[Web80] C. R. Webster, L. Wöste, and R. N. Zare. Narrow-band UV radiation (250–260 nm) from intracavity doubling a single-mode dye laser. *Optics Communications*, 35:435–9, 1980.

[Wu57] C. S. Wu, E. Ambler, R. W. Hayward, D. D. Hoppes, and R. P. Hudson. Experimental tests of parity conservation in beta decay. *Physical Review*, 105:1413–5, 1957.

[Zem30] M. W. Zemansky. Absorption and collision broadening of the mercury resonance line. *Physical Review*, 36:219–38, 1930.

[Zim95] C. Zimmermann, V. Vuletic, A. Hemmerich, and T. W. Hänsch. All solid state laser source for tunable blue and ultraviolet radiation. *Applied Physics Letters*, 66:2318–20, 1995.

[Zoo72] J. D. Zook and S. T. Liu. Piezoelectric effect in Teflon cable. *Journal of Applied Physics*, 43:1304–6, 1972.

Appendix A

LIGHT INTERACTION CALCULATIONS

This appendix gives calculations of transition probabilities, optical rotation angles, and Zeeman light shifts for ^{199}Hg near the $6^1S_0 \rightarrow 6^3P_1$ resonance. These estimates use the derivation of Happer and Mathur [Hap67] which uses effective operators in a semiclassical formalism (the light field treated as classical electromagnetic waves and the atoms treated quantum mechanically).

The Schrödinger equation for the atomic ground state in the presence of the light field is

$$i\hbar\frac{\mathrm{d}\psi}{\mathrm{d}t} = (\mathcal{H}_0 + \delta\mathcal{H})\psi, \tag{A.1}$$

where $\mathcal{H}_0$ is the Hamiltonian of the atoms without the light field, and $\delta\mathcal{H}$ is the perturbation due to the light,

$$\delta\mathcal{H} = -(|E_0|^2/4)\mathbf{e}^* \cdot \alpha \cdot \mathbf{e} = \delta\mathcal{E} - i\hbar\frac{\delta\Gamma}{2}, \tag{A.2}$$

where $|E_0|$ and $\mathbf{e}$ are the magnitude and polarization direction of the electric field of the light wave, α is the atomic polarizability tensor operator, and in the second part of Eq. A.2 $\delta\mathcal{H}$ is written in terms of two Hermitian operators, where $\delta\mathcal{E}$ shifts the energy levels of the atom and $\delta\Gamma$ accounts for light absorption effects.

These operators can be further classified based on their effect on the magnetic sublevels of the atom. In the case of ^{199}Hg, which has a nuclear spin of 1/2 and no electronic spin in the ground state, the operator $\delta\mathcal{E}$ becomes

$$\delta\mathcal{E} = \delta\mathcal{E}_0 - \boldsymbol{\mu} \cdot \boldsymbol{\delta B}_{LS}, \tag{A.3}$$

where $\boldsymbol{\mu} = \hbar\gamma\boldsymbol{I}$ is the ^{199}Hg magnetic dipole moment, and $\delta\mathcal{E}_0$ and $\boldsymbol{\delta B}_{LS}$ are the scalar and vector light shift operators. The scalar light shift operator, $\delta\mathcal{E}_0$, gives a common shift to both m_F sublevels in the $F = 1/2$ ground state. The vector light shift operator gives different shifts to the m_F sublevels in the same manner as the low field magnetic Zeeman effect, and so can be treated as an effective magnetic field, $\boldsymbol{\delta B}_{LS}$. Similarly, the absorption operator can be split into a scalar and vector component to reflect the difference in absorption in the m_F sublevels,

$$\delta\Gamma = \delta\Gamma_0 + \boldsymbol{\mu} \cdot \boldsymbol{\delta\Gamma}_1. \tag{A.4}$$

A.1 Light Absorption

The excitation rate from the ^{199}Hg ground state to a given excited state F_e level for unpolarized atoms and light is given by the scalar absorption operator

$$\delta\Gamma_0(F_e) = \frac{\mathrm{I}_0\, G\, \mathrm{Im}Z'}{6\hbar}\frac{(2F_e+1)}{(2I+1)}, \tag{A.5}$$

where (non-script) I_0 is the intensity of the light and (script) I is the nuclear spin. The G factor is

$$G \equiv \frac{e^2}{4\pi\epsilon_0}\frac{\lambda^2 f_{ge}}{\pi m_e c^2 v_T}, \tag{A.6}$$

where $f_{ge} = 0.023$ is the oscillator strength of the transition, and $v_T \equiv \sqrt{2RT/M} = 158$ m/s is the room temperature thermal velocity of ^{199}Hg. Z' is a frequency dependent profile factor,

$$Z'(\omega-\omega_{eg}, \Delta_D, \Gamma) = Z\big(2(\omega-\omega_{eg})/\Delta_D + i\Gamma/\Delta_D\big), \tag{A.7}$$

where $\Delta_D \equiv 2(\omega_{eg}/c)\sqrt{2RT/M}$ is the Doppler width, Γ is the coherence lifetime of the excited state including the effects of dephasing collisions (pressure broadening) along with the natural linewidth of the transition, and Z is the plasma dispersion function defined by

$$Z(\zeta) = \frac{1}{\pi}\int_{-\infty}^{\infty}\frac{e^{-u^2}}{u-\zeta}\mathrm{d}u. \tag{A.8}$$

In our case, Δ_D is 1.2 GHz and Γ is about 4.2 GHz due to the 500 Torr buffer gas, compared to the natural linewidth of 1.3 MHz.

The imaginary part of Eq. A.7 is equivalent to a Voigt profile obtained from the convolution of a Gaussian profile with width Δ_D and a Lorentzian profile with a width of Γ. The Voigt profile must be evaluated numerically, but since in our case the Lorentzian width is significantly larger than the Doppler width, the profile can reasonably be approximated by a Lorentzian line-shape

$$\frac{2}{\pi\Delta_D}\mathrm{Im}Z' \simeq \frac{1}{2\pi}\frac{\Gamma}{(\omega-\omega_{eg})^2+\Gamma^2/4}, \tag{A.9}$$

as is shown in Figure A.1. In the limit where Eq. A.9 describes the profile factor for absorption effects ($\mathrm{Im}\,Z'$), the real part of Eq. A.7 can also be reasonably approximated by

$$-\frac{1}{\pi\Delta_D}\mathrm{Re}Z' \simeq \frac{1}{2\pi}\frac{\omega-\omega_{eg}}{(\omega-\omega_{eg})^2+\Gamma^2/4}. \tag{A.10}$$

To evaluate the absorption rate for the $6^1S_0 \rightarrow 6^3P_1$ transition, the contributions from Eq. A.5 for the $F_e = 1/2$ and $3/2$ hyperfine lines must be added. For a probe beam with an intensity of 10 μW/cm^2 (a 7 mm square beam profile with about 5 μW of power) and a -20 GHz detuning, the

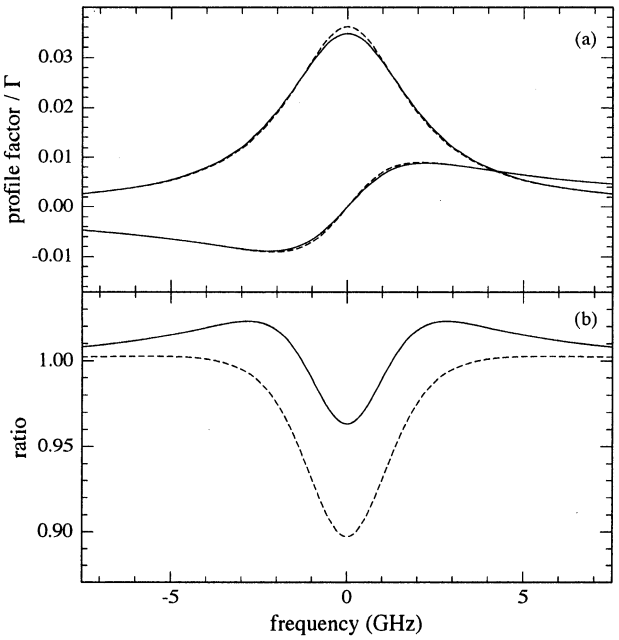

Figure A.1: Voigt and Lorentzian profile comparison. Plot (a) shows the profile factors given in equations A.9 and A.10 for $\Gamma = 4.2$ GHz and $\Delta_D = 1.2$ divided by the Lorentzian width. The solid lines give the profiles based on Z', and the barely visible dashed lines are the Lorentzian profiles. Plot (b) shows the ratio of the Z' profile divided by the Lorentzian. The solid line is Eq. A.9 and the dashed is from Eq. A.10.

calculated scalar pump rate would be 0.006 s^{-1}. The pump rate we observe with these parameters tended to be between 0.002 and 0.005 s^{-1}, as measured from the dependence on the dependence of the transverse relaxation rate on the incident intensity. The light intensity was measured before entering the magnetic shields.

From the absorption rate, $\delta\Gamma$, the absorption cross section can be obtained by dividing the rate of absorption by the number of photons incident per unit area per unit time

$$\sigma = \frac{\hbar\omega\delta\Gamma}{I_0} = \frac{2\pi\hbar c}{\lambda I_0}\delta\Gamma. \tag{A.11}$$

The transmitted intensity after passing a distance x through a vapor with number density ρ is then

$$I(x) = I_0 e^{-\sigma\rho x} \equiv I_0 e^{-\kappa x}, \tag{A.12}$$

where κL gives the optical depth of a vapor cell of length L. Figure A.2 shows the optical depth of a room temperature 1" diameter ^{199}Hg vapor cell calculated from Eqs. A.5, A.11, and A.12.

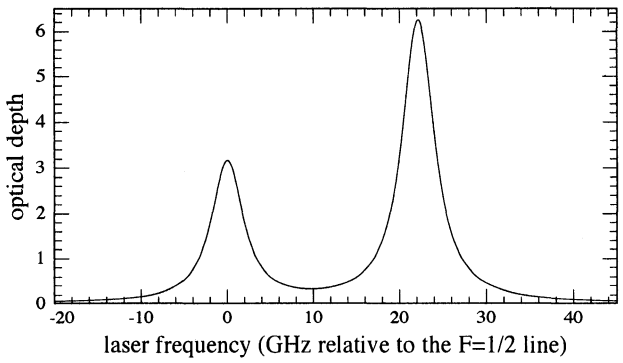

Figure A.2: Calculated optical depth for a ^{199}Hg vapor cell. The measured optical depth is displayed in Figure 2.3.

The polarization dependent absorption of light by ^{199}Hg is given by the dipolar absorption operator

$$\begin{aligned}\delta\Gamma_1(F_e) &= \boldsymbol{\mu}\cdot\boldsymbol{\delta\Gamma}_1 \\ &= -\boldsymbol{P}_A\cdot\boldsymbol{P}_L\frac{\mathrm{I}_0 G\,\mathrm{Im}Z'(2F_e+1)}{8\hbar(I+1)(2I+1)}\big(2+I(I+1)-F_e(F_e+1)\big),\end{aligned} \tag{A.13}$$

where $\boldsymbol{P}_A = \langle I\rangle/I$ is the atomic polarization and $\boldsymbol{P}_L = i\mathbf{e}^*\times\mathbf{e}$ is the circular polarization of the light ($\boldsymbol{P}_L = \hat{x}$ for fully circularly polarized light propagating in the x-direction). Figure A.3 shows a plot of Eqs. A.5 and A.13 for light circularly polarization parallel to the atomic spin polarization. The full absorption rate is obtained by adding the scalar and dipolar absorption contributions.

A.2 Light Shifts

The only light induced energy shifts that concern us are shifts that affect the ^{199}Hg spin precession frequency, which are generated when the m_F sublevels are shifted unequally. The scalar light shift does not lead to shifts in the Larmor frequency, so I will not reproduce it here. The effective magnetic field produced by the dipolar light shift operator is

$$\boldsymbol{\delta B}_{LS} = -\frac{\mathrm{I}_0 G\,\mathrm{Im}Z'(2F_e+1)}{16\hbar\gamma I(I+1)(2I+1)}\big(2+I(I+1)-F_e(F_e+1)\big)\boldsymbol{P}_L. \tag{A.14}$$

Figure A.4 shows the calculated size of the effective magnetic field due to the light shift for a fully circularly polarized light beam with an intensity of 10 μW/cm^2. For an isolated line, the profile factor, ImZ', would cross zero at exactly $\omega = \omega_{eg}$, but due to the influence of the $F = 3/2$ line, the

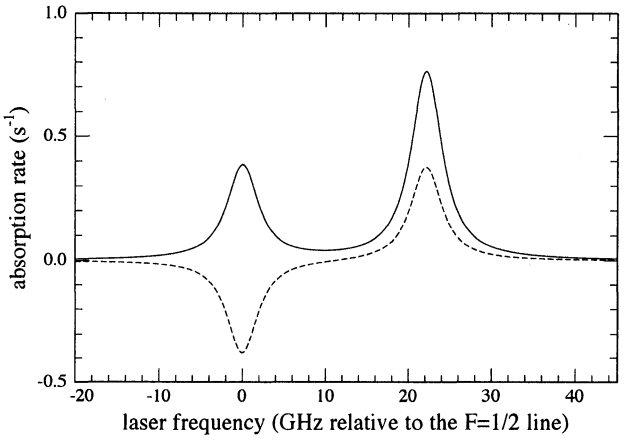

Figure A.3: Calculated absorption rate frequency dependence for a light intensity of 10 μW/cm^2. The solid line is the scalar absorption rate and the dashed line is the dipolar absorption rate for light circularly polarized parallel to the atomic spin polarization.

light shift field goes to zero about 200 MHz to the red of the $F = 1/2$ resonance. The exact location of the zero-crossing is dependent on the linewidth of the transitions.

A.3 Optical Rotation

The dielectric susceptibility χ, is related to the polarizability tensor operator in Eq. A.2 by multiplying by the number density, $\chi = \rho\alpha$. With $\epsilon = \epsilon_0(1+\chi)$, the susceptibility can be used to calculate the complex index of refraction

$$n = \sqrt{\frac{\epsilon\mu}{\epsilon_0\mu_0}} = \sqrt{1+\chi} \simeq 1 + \chi/2, \tag{A.15}$$

where we have assumed that χ is small for our experimental parameters. Rotation of the polarization direction of linearly polarized light occurs if the indexes of refraction for σ_+ and σ_- circularly polarized light are not the same. The rotation angle after traversing a distance L is given by

$$\varphi = \frac{\omega L}{c}(n_+ - n_-), \tag{A.16}$$

where n_+ and n_- are the real parts of the indexes of refraction for σ_+ and σ_- circularly polarized light. The difference, $n_+ - n_-$, can be obtained from the real part of the dipolar susceptibility operator, which gives

$$n_+ - n_- = -\frac{\rho c G \,\mathrm{Im}Z'(2F_e+1)}{8(I+1)(2I+1)}\big(2 + I(I+1) - F_e(F_e+1)\big)\hat{k}\cdot\boldsymbol{P}_A. \tag{A.17}$$

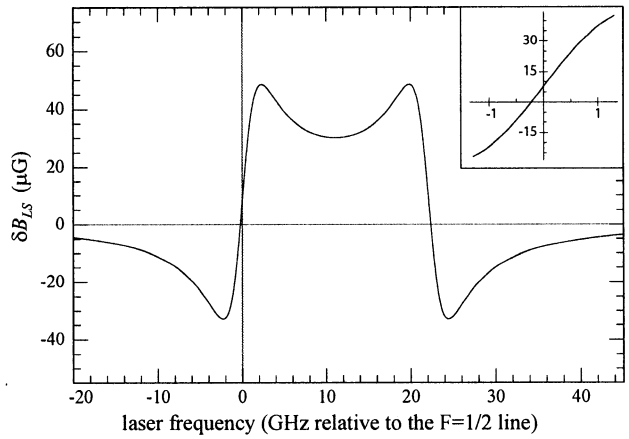

Figure A.4: Virtual Magnetic field due to the Zeeman light shift for fully circularly polarized light with intensity of 10 μW/cm^2. The inset plot zooms in on the zero crossing near the $F = 1/2$ line.

Combining equations A.16 and A.17 gives the optical rotation angle, and a plot of the detuning dependence of the rotation angle for a fully polarized room temperature ^{199}Hg vapor in a 1" diameter cell is shown in Fig. 2.9.

A.4 Transverse Optical Pumping

The evolution of the atomic spin polarization exposed to a magnetic field and a light beam can be described classically with the vector equation

$$\frac{\mathrm{d}}{\mathrm{d}t}\boldsymbol{P}_A = \Gamma_p(\boldsymbol{P}_L - \boldsymbol{P}_A) - \Gamma_r \boldsymbol{P}_A - \gamma \boldsymbol{P}_A \times \boldsymbol{B}, \tag{A.18}$$

where Γ_r describes the total spin relaxation rate, $\boldsymbol{P}_L = i\mathbf{e}^* \times \mathbf{e}$ describes the circular polarization of the light, and Γ_p is the rate that the light can cause a spin to be pumped into the spin state parallel to $\boldsymbol{P}_L$. If the magnetic field is in the z direction and the pump light is turned off, then the spins precess in the xy-plane with frequency $\omega = \gamma B$, and the spin polarization magnitude decays as $P_A(t) = P_A(0)e^{-\Gamma_r t}$.

If a circularly polarized light beam along the $\hat{x}$ direction is turned on, then the atomic spins will tend to be oriented along the light beam, but since the spins then precess due to the magnetic field, there is no significant buildup of polarization. Instead, the light is modulated with a chopper wheel at about the Larmor frequency of the atoms, so that optical pumping only occurs when the aligned

spins are parallel with $\hat{k}$. The effect of the chopper can be inserted into Eq. A.18 by multiplying Γ_p by a periodic function

$$C(t) = u(\cos(\omega_c t) - \cos(\Delta\theta/2)), \quad u(x) = \begin{cases} 0, & x < 0 \\ 1, & x > 0, \end{cases} \tag{A.19}$$

where ω_c is the chopper frequency, and $\Delta\theta$ is the angle of the open portion of the chopper wheel such that the light would be on 50% of the time if $\Delta\theta = \pi$.

Starting from an initial polarization of zero, and for specific values of $\Delta\theta$ and Γ_p, Eq. A.18 can be numerically integrated (by Mathematica with `NDSolve` for example), to find the magnitude of the atomic polarization after 30 seconds of pumping. Generally the polarization evolves as

$$P_A(t) = A\left(1 - \exp\left[-\frac{\Gamma_p \Delta\theta}{2\pi} t\right]\right). \tag{A.20}$$

The effective pump rate is reduced by a factor of $\Delta\theta/2\pi$, reflecting the amount of time the light is on out of a precession period. With an on resonance incident pump intensity of 100 μW/cm^2, and a chopper wheel angle of $\Delta\theta = \pi/2$, we measure an effective pump rate of 1/15 s^{-1}. The pump rate can also be obtained from equations A.5 and A.13, $\Gamma_p = (\delta\Gamma_0 + \delta\Gamma_1)/2$. There is a factor of 1/2 because the absorption rate formulas give the rate for making transitions out of the ground state, and once in the excited state the atom is quenched by buffer collisions and has a 50% probability of returning to either ground state spin sublevels. The calculated effective pump rate for 100 μW/cm^2 intensity is then 0.48 s^{-1}, significantly larger than $1/15 \simeq 0.07$ s^{-1} . However, since there are about 3 optical depths of Hg on resonance, the full power of the light beam is only seen by atoms at the very front of the cell, lowering the average pump rate in the cell.

Using the measured pump rate of $1/15 \simeq 0.07$ s^{-1}, Figure A.5 shows the magnitude of the calculated atomic polarization achieved after 30 seconds of pumping for a range of chopper wheel opening angles. The polarization has a broad maximum peaked near 110°, giving a polarization of about 70%. We generally use a chopper wheel opening between 90° and 120°, so that the light is unblocked 25–33% of the time.

The optical pumping efficiency is maximized only if the chopper frequency matches the spin precession frequency exactly. Figure A.6 shows the calculated polarization after 30 seconds of pumping for the chopper frequency ω_c mistuned from the precession frequency ω_L ($\omega_L = 100$ s^{-1} in the calculation). For a mistuning of 0.01 s^{-1} the polarization is still within 0.3% of its maximum value, but for a mistuning of 0.1 s^{-1}, the polarization is decreased by 25%.

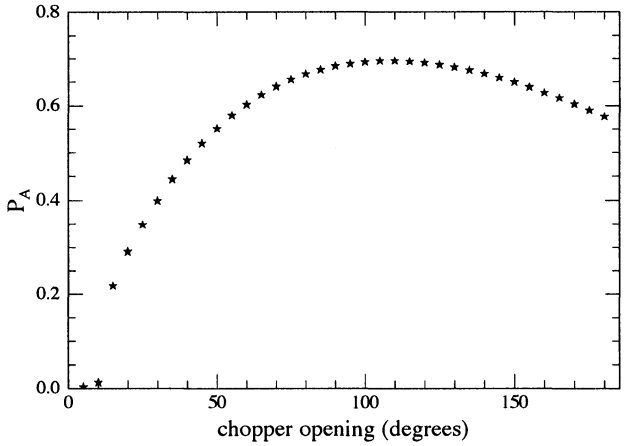

Figure A.5: Effect of the chopper wheel opening angle on P_A.

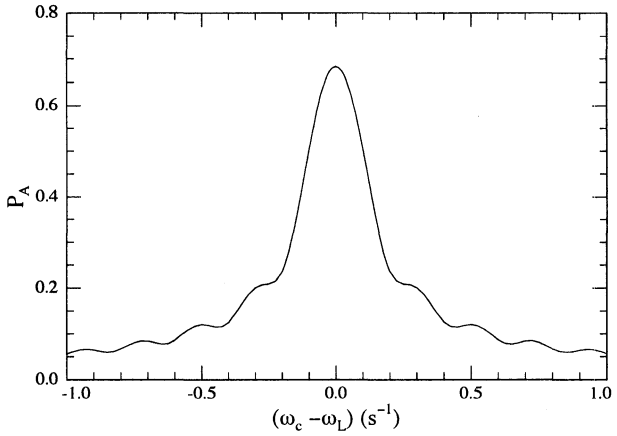

Figure A.6: Effect of the chopper frequency on P_A.

A.4.1 Vertical Magnetization

If the only magnetic field seen by the atoms is the main field in the z direction, then $\boldsymbol{P}_A$ will be confined to precess in the xy-plane. However, the Zeeman light shift from the circularly polarized pump light generates a modulating magnetic field in the x direction that can cause spins to precess into the z direction. The effect of this light shift can be added to Eq. A.18 by setting $B_x = C(t)\delta B_{LS}$, where C(t) is the chopper modulation function from Eq. A.19. For a pump rate of $1/15$ s^{-1} the light shift field from Eq. A.14 is $0.05/\gamma$.

If the chopper frequency matches the spin precession frequency, then the light shift field will be parallel to the average atomic spin direction while the light is on, so the spins will generally stay in the xy-plane. If the chopper frequency is mistuned, then besides having a decrease in the pumping efficiency, the light shift can tip the spins into the vertical (z) direction. Numerical calculations from Eq. A.18 estimate that the relative amount of vertical magnetization built up after 30 seconds of pumping goes as

$$\frac{M_z}{\sqrt{M_x^2 + M_y^2}} \simeq 0.85(\omega_c - \omega_L). \tag{A.21}$$

Appendix B

HG4 DATA RUN SUMMARY

This appendix gives details on the experimental parameter values used in data runs taken since the end of the HG3 dataset in a similar manner to Table 4.1 in Section 4.1.2. Shortly after the completion of HG3 (January 2001), several runs were taken using the first batch of 100% CO buffer gas cells (see Sec. 6.1) in the 2-cell conductive polyethylene vessel. These runs are listed in Table B.1 using the same conventions as in Table 4.1. Data files for these runs all use the filename prefix "`Series2`."

Data runs taken after the implementation of the 4-cell apparatus are listed in Table B.3, which covers from April of 2001 through May of 2004. Data files for these runs all use the filename prefix "`Series3`." The columns in Table B.3 have the same meaning as in Table 4.1 with the following exceptions: two values are listed under the Ch column, the first corresponds to the middle cell DAQ channel direction (for '+' the middle top cell signal is on the first DAQ channel and the middle bottom cell signal is on the second DAQ channel, and '–' indicates the opposite configuration), the second value gives the outer cell DAQ channel direction (for '+' the outer top cell signal is on the third DAQ channel and the outer cell signal is on the fourth DAQ channel, and '–' indicates the opposite configuration). In the case of "dipole" runs, the HV column is one half the difference between the two HV values used in the run. For example, if the run switches between +10 and −10 kV, then $(+10 - (-10))/2 = 10$ is the value given. If the two HV values are not symmetric

Table B.1: Data runs taken with CO buffer gas cells after the end of HG3 but before the 4-cell apparatus was implemented.

RUN	L	C	B	Ch	t_{pump}	t_{probe}	det.	HV	t_{HVS}	cells	misc
10001	496	D	–	–	30	100	−4	0.0	0	35,36	
10505	487	D	–	–	30	100	−5	10.0	10	35,37	FS
10993	283	D	–	–	30	100	−5	10.0	10	35,37	FS
11705	172	D	–	–	30	100	−5	5.0	10	37,35	

about zero then the upper and lower HV values are given in the "misc" column. In the case of "quadrupole" runs, the HV column gives the higher magnitude HV value used (HV= 10 corresponds to a +10, 0, −10, 0 sequence), and all of the quadrupole runs use a lower value of zero or 1 kV. The cells column gives the cells used in the vessel positions ordered from top to bottom (outer top, middle top, middle bottom, outer bottom). Runs where the outer cell positions are listed as zero used the 2-cell conductive polyethylene vessel (89127–105551). Descriptions for the codes in the "misc" column are given in Table B.2.

Table B.2: Code descriptions for "misc" parameters used in Table B.3.

Code	Description
AC	Chopper frequency during pump phase is alternated each scan by ± 0.02 Hz
AlT	Aluminum tube added around HV cables as they enter the magnetic shields
API	Pump light intensity alternated by $\pm 20\%$ each scan
APλ	Pump light wavelength alternated by ± 1.5 GHz each scan
ChS	DAQ channels usually used for middle cells swapped with outer channels
IV	Vessel installed upside down compared to normal operation
FS	A frequency parameter showed an anomalously large HV correlation
HB	Main magnetic field oriented horizontally along shield axis
HVB	HV connected to bottom cell only, top was grounded
HVT	HV connected to top cell only, bottom was grounded
HV$*$	Multiple HV configurations (value, HVT, or HVB) used during the run
MS	HV ramped midway through the probe phase
NHV	Excessive frequency scatter correlated with HV application
OB	Horizontal offset magnetic field applied (tips $\boldsymbol{B}$ by 5–45° from vertical)
Pθ	Probe light polarization oriented θ degrees from vertical
SBI	Probe light intensity stepped through several values during the run
SBλ	Probe light wavelength stepped through several values during the run
SPλ	Pump light wavelength stepped through several values during the run
XA	Extra attenuation in probe beam
XG	Additional magnetic field gradient applied
XM	Steel washer or current loop attached to a vessel component
$++--$	HV sequence that ramps to a new value every other scan

Table B.3: HG4 data run summary.

RUN	L	C	B	Ch	t_{pump}	t_{probe}	det.	HV	t_{HVS}	cells	misc
10016	395	D	+	++	30	100	−5.00	0.00	0	26,37,35,23	
10436	301	D	+	++	30	100	−5.00	0.00	0	35,36,34,37	
10745	273	D	+	++	30	100	−4.00	0.00	0	35,36,34,37	
11080	300	D	+	++	30	200	−5.00	10.00	10	35,36,34,37	
11381	300	D	+	++	30	200	−5.00	10.00	10	35,36,34,37	
11688	324	D	+	++	30	200	−5.00	10.00	15	35,36,34,37	
12014	336	D	+	++	30	200	−5.00	10.00	10	35,36,34,37	
12351	231	D	+	++	30	200	−5.00	10.00	10	35,36,34,37	
12590	109	D	−	++	30	200	−5.00	10.00	10	35,36,33,34	HV∗, NHV
12700	58	D	−	++	30	200	−5.00	10.00	10	35,36,33,34	NHV
12761	144	D	−	++	30	100	−5.00	2.75	10	35,36,33,34	HV∗, NHV
12916	232	D	−	−+	30	200	−5.00	10.00	10	35,36,33,34	
13149	128	D	−	−+	30	100	−5.00	10.00	10	35,36,33,34	
13280	327	D	−	−+	30	200	−5.00	10.00	10	37,35,36,32	FS
13795	274	D	−	−+	30	200	−5.00	10.00	10	37,35,36,32	FS
14132	67	D	−	−+	30	200	−5.00	10.00	10	37,36,35,32	FS
14210	153	D	−	−+	30	200	−5.00	10.00	10	37,36,35,32	HVT, FS
14364	91	D	−	−+	30	200	−5.00	10.00	10	37,36,35,32	HVB
14456	73	Q	−	−+	30	200	−5.00	10.00	10	37,36,35,32	
14530	170	D	−	−+	30	200	−5.00	10.00	10	37,36,35,32	FS
14701	147	D	−	−+	30	200	−5.00	5.00	10	37,36,35,32	+10+0, FS
14849	65	D	−	−+	30	200	−5.00	5.00	10	37,36,35,32	+0−10, FS
14915	37	D	−	−+	30	200	5.00	10.00	10	37,36,35,32	FS, MS
14959	147	D	−	−+	30	200	5.00	10.00	100	37,36,35,32	FS
15107	363	Q	−	−+	30	200	−5.00	10.00	10	37,36,35,32	
15474	319	D	−	−+	30	200	−4.50	10.00	10	37,36,35,33	FS
15795	163	Q	−	−+	30	200	−4.50	10.00	10	37,36,35,33	
15999	200	D	−	−+	30	200	−4.50	10.00	10	37,36,35,33	++−−, FS
16273	93	D	+	−+	30	200	−4.50	10.00	10	37,36,35,33	FS
16368	130	D	+	−+	30	200	−4.50	10.00	10	37,36,35,33	
16531	83	D	+	−+	30	200	−4.50	10.00	10	37,36,35,33	
16733	202	D	+	−+	30	200	−4.00	10.00	10	34,35,36,37	FS
16936	101	D	+	−+	30	200	−4.50	10.00	10	34,35,36,37	FS
17038	244	D	+	−+	30	200	−4.50	5.00	5	34,35,36,37	FS

Table B.3 continued.

RUN	L	C	B	Ch	t_{pump}	t_{probe}	det.	HV	t_{HVS}	cells	misc
17288	317	D	+	−+	30	200	−4.50	10.00	5	34,35,36,37	FS
17610	183	D	+	−+	30	200	−4.50	10.00	10	34,35,36,37	
17827	164	D	+	−+	33	200	5.00	10.00	10	34,35,36,37	
18015	579	D	+	−+	30	200	−5.00	10.00	10	34,35,36,37	FS
18595	489	D	+	−+	30	200	−5.00	10.00	10	34,35,36,37	HVT
19086	507	D	+	−+	30	200	−5.00	10.00	10	34,35,36,37	HVB
19611	478	D	+	−+	30	200	1.85	10.00	10	34,35,36,37	FS
20089	174	D	+	−+	30	200	1.85	0.00	10	34,35,36,37	
20289	154	D	+	−+	30	200	1.85	0.00	0	34,35,36,37	
20446	273	D	+	−+	30	200	−1.25	0.00	0	34,35,36,37	
20722	48	D	+	−+	30	200	−1.25	0.00	0	34,35,36,37	
20771	74	D	+	−+	17	213	2.50	0.00	0	34,35,36,37	
20846	163	D	+	−+	30	200	−2.00	0.00	0	34,35,36,37	
21059	144	D	+	−+	30	200	−2.00	0.00	0	34,35,36,37	API
21208	55	D	+	−+	30	200	−4.00	10.00	10	34,36,35,37	FS?
21264	290	D	+	−+	30	200	−4.00	10.00	10	34,36,35,37	FS
21556	277	D	+	−+	30	200	−4.50	10.00	10	34,36,35,37	FS
21834	287	D	+	−+	30	200	−4.00	10.00	10	34,36,35,37	FS
22123	331	D	+	−+	30	200	−4.00	10.00	10	34,35,36,37	
22477	339	D	+	−+	30	200	−4.00	10.00	10	34,35,36,37	
22819	272	D	+	−+	30	200	−4.00	10.00	10	34,35,36,37	
23092	299	D	+	−+	30	200	−4.00	10.00	10	34,35,36,37	
23392	345	D	−	−+	30	200	−4.00	10.00	10	34,35,36,37	
23738	312	D	−	−+	30	200	−5.00	0.00	0	34,35,36,37	SBλ
24051	414	D	−	−+	30	200	−4.00	10.00	10	34,35,36,37	SPλ
24466	171	D	−	−+	30	200	−4.00	10.00	10	34,35,36,37	APλ
24639	157	D	−	−+	30	200	−4.80	10.00	10	34,35,36,37	OB, APλ
24797	184	D	−	−+	30	200	−4.00	10.00	10	34,35,36,37	OB, APλ
25028	176	D	−	−+	30	200	−4.00	0.00	0	34,35,36,37	API
25339	234	D	+	−+	30	200	−4.00	0.00	0	34,35,36,37	APλ
25580	342	D	+	−+	30	200	−4.00	0.00	0	34,35,36,37	OB, APλ
25931	301	D	+	−+	30	200	−4.00	0.00	0	34,35,36,37	OB, APλ
26233	209	D	+	−+	30	200	3.60	0.00	0	34,35,36,37	OB, APλ
26443	177	D	+	−+	30	200	−4.00	0.00	0	34,35,36,37	OB, APλ

Table B.3 continued.

RUN	L	C	B	Ch	t_{pump}	t_{probe}	det.	HV	t_{HVS}	cells	misc
26720	101	D	+	−+	30	200	−4.00	0.00	0	34,35,36,37	APλ, AC
26851	382	D	+	−+	30	200	4.00	10.00	10	34,35,36,37	
27236	265	D	+	−+	30	200	1.85	10.00	10	34,35,36,37	
27527	268	D	+	++	30	200	1.85	0.00	0	38,35,36,40	
27796	325	D	+	++	30	200	1.85	0.00	0	38,35,36,40	
28122	660	D	+	++	30	200	1.85	0.00	0	38,35,36,40	
28789	96	D	+	++	30	200	1.85	0.00	0	38,35,36,40	SPλ, AC
28898	152	D	+	++	30	200	1.85	0.00	0	38,35,36,40	
29052	56	D	+	++	30	200	1.85	0.00	0	38,35,36,40	
29119	308	D	+	++	30	200	1.85	0.00	0	38,35,36,40	
29483	253	D	+	++	30	200	1.85	0.00	0	38,35,36,40	SPλ, AC
29737	84	D	+	++	30	200	1.85	0.00	0	38,35,36,40	SPλ, AC
29823	330	D	+	++	30	200	1.85	0.00	0	38,35,36,40	SPλ, AC
30155	177	D	+	++	30	200	1.85	0.00	0	38,35,36,40	SPλ, AC
30334	352	D	+	++	30	200	1.85	0.00	0	38,35,36,40	SPλ, AC
30690	136	D	+	++	30	200	1.85	0.00	0	38,35,36,40	
30828	139	D	+	++	30	200	1.85	0.00	0	38,35,36,40	
30972	156	D	+	++	30	200	1.85	0.00	0	38,35,36,40	
31135	182	D	+	++	30	200	1.85	0.00	0	38,35,36,40	
31322	163	D	+	++	30	200	1.85	0.00	0	38,35,36,40	
31487	143	D	+	++	30	200	1.85	0.00	0	38,35,36,40	
31644	131	D	+	++	30	200	−4.00	0.00	0	38,35,36,40	
31779	270	D	+	++	30	200	−4.00	0.00	0	38,35,36,40	
32051	144	D	+	++	30	200	−4.00	0.00	0	38,35,36,40	
32203	57	D	+	++	30	200	1.85	0.00	0	38,35,36,40	
32312	265	D	+	++	30	200	1.85	0.00	0	38,35,36,40	
32598	54	D	+	++	30	200	1.85	0.00	0	38,35,36,40	
32654	158	D	+	++	30	200	1.85	0.00	0	38,35,36,40	
32816	90	D	+	++	30	200	−1.85	0.00	0	38,35,36,40	
32908	63	D	+	++	30	200	−1.85	0.00	0	38,35,36,40	
32978	42	D	+	++	30	200	1.85	0.00	0	38,35,36,40	SBλ, AC
33036	122	D	+	++	30	200	1.85	0.00	0	38,35,36,40	SBλ, AC
33159	94	D	+	++	30	200	2.75	0.00	0	38,35,36,40	SBλ
33254	186	D	+	++	30	200	2.00	0.00	0	38,35,36,40	SBλ

Table B.3 continued.

RUN	L	C	B	Ch	t_{pump}	t_{probe}	det.	HV	t_{HVS}	cells	misc
33443	156	D	+	++	30	200	1.85	0.00	0	38,35,36,40	SBI
33634	70	D	+	++	30	200	1.85	0.00	0	38,35,36,40	XA
33708	111	D	+	++	30	200	1.85	0.00	0	38,35,36,40	
34034	49	D	+	++	5	200	1.85	0.00	0	38,35,36,40	
34089	74	D	+	++	5	200	1.85	0.00	0	38,35,36,40	
34164	124	D	+	++	30	200	1.85	0.00	0	38,35,36,40	P90
34296	158	D	−	++	30	200	1.85	0.00	0	38,35,36,40	
34658	293	D	−	++	30	200	1.85	10.00	10	38,35,36,40	
34965	249	D	−	+−	30	200	1.85	0.00	0	38,35,36,40	HB
35222	270	D	−	+−	30	200	1.85	10.00	10	38,35,36,40	HB
35499	262	D	+	++	30	200	1.85	0.00	0	38,35,36,40	OB
35803	235	D	+	+−	30	200	1.85	0.00	0	38,35,36,40	OB
36054	230	D	+	+−	30	200	1.85	0.00	0	38,35,36,40	
36288	103	D	+	+−	30	200	1.85	0.00	0	38,35,36,40	OB
36567	77	D	+	+−	30	200	1.85	0.00	0	38,35,36,40	
36658	141	D	+	+−	30	200	1.85	0.00	0	38,35,36,40	
36807	127	D	+	+−	30	200	1.85	0.00	0	38,35,36,40	
37078	60	D	+	+−	30	200	1.85	0.00	0	38,35,36,40	OB
37192	44	D	+	+−	30	195	1.85	10.00	10	43,37,42,47	
37248	176	D	+	−−	30	200	1.85	0.00	0	43,37,42,47	
37426	107	D	+	−−	30	200	1.85	0.00	0	43,37,42,47	
37713	272	D	+	−−	30	230	1.85	10.00	10	43,37,42,47	
37987	296	D	+	−+	30	230	1.85	10.00	5	43,37,42,47	
38333	312	D	−	++	30	200	1.85	10.00	10	43,37,42,47	FS
38647	170	D	−	+−	30	200	1.85	10.00	5	43,37,42,47	FS
38818	128	D	−	+−	30	200	1.85	10.00	10	43,37,42,47	FS?
38947	175	Q	−	+−	30	200	1.85	10.00	10	43,37,42,47	
39123	317	D	−	+−	30	200	1.85	10.00	10	43,37,42,47	HV*
39447	251	D	−	+−	30	200	1.85	10.00	10	47,42,37,43	
39699	293	D	−	+−	30	200	1.85	10.00	5	47,42,37,43	
39995	335	D	−	+−	30	200	2.40	10.00	10	47,42,37,43	
40331	84	D	−	+−	30	200	2.40	0.00	0	47,42,37,43	AC
40417	219	D	−	+−	30	200	2.40	10.00	10	47,42,37,43	P45
40648	169	D	−	+−	30	200	−2.40	10.00	10	47,42,37,43	

Table B.3 continued.

RUN	L	C	B	Ch	t_{pump}	t_{probe}	det.	HV	t_{HVS}	cells	misc
40824	205	D	−	+−	30	200	−3.00	10.00	10	47,42,37,43	
41033	597	D	−	+−	30	200	−2.40	10.00	10	47,42,37,43	
41632	421	Q	−	+−	30	200	2.40	10.00	10	47,42,37,43	
42061	264	D	−	+−	30	200	2.40	10.00	40	47,42,37,43	
42326	337	D	−	−−	30	200	2.40	10.00	20	47,42,37,43	
42671	275	D	+	−−	30	200	2.40	10.00	20	47,42,37,43	OB
42963	222	D	+	−−	30	200	−2.40	10.00	5	47,42,37,43	
43187	257	D	+	−+	30	200	−2.40	10.00	30	47,42,37,43	
43458	246	D	+	++	30	200	2.40	10.00	30	47,40,42,35	
43724	310	D	+	++	30	200	2.40	10.00	10	47,40,42,38	FS
44037	386	D	+	+−	30	200	2.40	10.00	40	47,40,42,38	FS
44431	184	D	+	++	30	200	2.40	10.00	30	47,40,42,38	
44616	109	D	+	+−	30	200	2.40	10.00	5	47,40,42,38	
44727	188	D	+	+−	30	200	2.40	10.00	5	47,40,42,38	
44916	260	D	+	+−	30	200	2.40	10.00	5	47,40,42,38	HV*
45177	140	D	+	+−	30	200	2.40	10.00	5	47,40,42,38	
45318	234	D	+	+−	30	200	2.40	10.00	5	47,40,42,38	HVT
45553	69	D	+	+−	30	200	2.40	10.00	10	47,40,42,38	HVB
45638	304	D	+	++	30	200	2.40	10.00	30	47,40,42,38	
45943	313	D	+	+−	30	200	2.40	10.00	5	47,40,42,38	
46262	252	Q	−	+−	30	200	2.40	10.00	30	47,40,42,38	
46515	318	D	−	+−	30	200	2.40	10.00	30	47,40,42,38	
47142	339	D	−	−+	30	200	2.40	10.00	5	47,40,42,38	
47489	307	D	−	++	30	200	2.40	10.00	10	47,40,42,38	P45
47799	320	D	−	++	30	200	−2.40	10.00	40	47,40,42,38	
48120	308	D	−	+−	30	200	−2.40	10.00	5	47,40,42,38	
48435	258	D	−	+−	30	200	−2.40	10.00	5	47,40,42,38	OB
48696	218	D	+	−−	30	200	−2.40	10.00	30	47,40,42,38	OB, FS
48958	257	D	+	−−	30	200	−2.40	10.00	30	47,40,42,38	OB, FS?
49221	229	D	+	−−	30	200	−2.40	10.00	30	47,40,42,38	
49460	287	D	+	−+	30	200	−2.40	10.00	5	47,40,42,38	FS?
49778	247	D	+	−+	30	200	−2.40	10.00	5	47,40,42,38	OB
50027	229	D	+	−+	30	200	2.40	10.00	30	47,40,42,38	OB
50333	278	D	−	−−	30	200	2.40	10.00	50	40,37,39,42	FS

Table B.3 continued.

RUN	L	C	B	Ch	t_{pump}	t_{probe}	det.	HV	t_{HVS}	cells	misc
50612	225	D	−	−+	30	200	2.40	10.00	20	40,37,39,42	HVT, FS
50838	321	D	−	−+	30	200	2.40	10.00	20	40,37,39,42	HVB, FS
51160	302	D	−	−+	30	200	2.40	10.00	50	40,37,39,42	HVB
51465	356	D	−	−+	30	200	2.40	5.00	50	40,37,39,42	+10+0
51822	198	D	−	−+	30	200	2.40	10.00	5	40,37,39,42	HVT, FS
52025	263	D	+	−+	30	200	2.40	10.00	50	40,37,39,42	FS
52290	165	D	+	−+	30	200	2.40	10.00	50	40,37,39,42	FS
52456	157	D	+	−+	30	200	2.40	10.00	50	40,37,39,42	HVT, FS
52614	90	D	+	−+	30	200	2.40	10.00	50	40,37,39,42	HVB, FS
52705	61	D	+	−+	30	200	2.40	10.00	50	40,37,39,42	FS
52767	163	D	+	−+	30	200	2.40	5.00	50	40,37,39,42	+0–10
52931	106	D	+	−+	30	200	2.40	5.00	50	40,37,39,42	+10+0
53047	32	D	+	−+	30	200	2.40	10.00	50	40,37,39,42	FS
53080	181	D	+	−+	30	200	2.40	10.00	50	40,37,39,42	++−−
53263	306	D	+	−+	30	200	2.40	5.00	50	40,37,39,42	
53570	42	D	+	−+	30	200	2.40	10.00	20	40,37,39,42	FS
53619	262	D	+	−+	30	200	2.40	7.50	50	40,37,39,42	FS
53882	278	D	+	−+	30	200	2.40	7.50	50	40,37,39,42	+10–5, FS
54161	116	D	+	−+	30	200	2.40	7.50	50	40,37,39,42	+5–10, FS
54280	226	D	−	−+	30	200	2.40	10.00	50	40,37,39,42	FS
54510	191	D	−	−+	30	200	2.40	10.00	50	40,37,39,42	FS, IV
54705	197	D	−	−+	30	200	2.40	10.00	50	40,37,39,42	FS
54903	35	D	−	−+	30	200	2.40	10.00	50	40,37,39,42	
54943	219	D	−	−+	30	200	2.40	10.00	50	40,37,39,42	FS
55170	158	D	−	−+	30	200	2.40	10.00	50	40,37,39,42	FS
55329	74	D	−	−+	30	200	2.40	10.00	50	40,37,39,42	HVT, FS
55404	196	D	−	−+	30	200	2.40	10.00	50	40,37,39,42	HVB
55604	237	D	−	−+	30	170	2.40	10.00	50	40,37,39,42	FS
55844	199	D	−	−+	30	200	2.40	10.00	50	40,37,39,42	
56044	69	D	−	−+	30	200	2.40	10.00	5	40,37,39,42	
56116	179	D	−	−+	30	200	2.40	10.00	50	40,37,39,42	
56300	163	D	−	−+	30	200	2.40	10.00	50	40,37,39,42	FS
56466	260	D	−	−+	30	200	2.40	10.00	50	40,37,39,42	
56729	268	D	−	−+	30	200	2.40	10.00	50	40,37,39,42	

Table B.3 continued.

RUN	L	C	B	Ch	t_{pump}	t_{probe}	det.	HV	t_{HVS}	cells	misc
57005	260	D	−	−−	30	200	2.40	10.00	20	42,38,39,40	
57266	324	D	−	−+	30	200	2.40	10.00	50	42,38,39,40	
57591	229	Q	−	−+	30	200	2.40	10.00	50	42,38,39,40	HVT
57847	255	D	−	++	30	200	−2.40	10.00	20	42,38,39,40	
58103	291	D	−	−+	30	200	2.40	10.00	50	42,38,39,40	
58399	311	D	+	−−	30	200	−2.00	10.00	20	42,38,39,40	
58711	323	D	+	−+	30	200	−2.00	10.00	50	42,38,39,40	
59036	271	D	+	−+	30	200	−2.00	10.00	50	42,38,39,40	P45
59308	296	D	+	++	30	200	2.40	10.00	20	42,38,39,40	FS?
59605	295	D	+	+−	30	200	2.40	10.00	50	42,38,39,40	
59906	236	D	+	+−	30	200	2.40	10.00	20	42,38,39,40	OB
60150	282	D	+	+−	30	200	2.40	10.00	50	42,38,39,40	OB
60438	281	D	+	+−	30	200	2.40	10.00	20	42,38,39,40	HVT
60720	280	D	+	+−	30	200	2.40	10.00	20	42,38,39,40	HVB
61001	300	D	+	+−	30	200	2.40	10.00	50	42,38,39,40	HVT
61302	307	D	+	+−	30	200	2.40	10.00	50	42,38,39,40	HVB
61612	138	D	+	+−	30	200	2.40	10.00	20	40,39,38,42	FS
61751	148	D	+	+−	30	200	2.40	10.00	20	40,39,38,42	HVB
61900	177	D	+	+−	30	200	2.40	10.00	20	40,39,38,42	HVT, FS
62083	359	Q	+	+−	30	200	2.40	10.00	20	40,39,38,42	FS
62444	346	D	+	+−	30	200	2.40	10.00	20	40,39,38,42	HVB
62793	281	D	+	+−	30	200	2.40	10.00	20	43,36,38,42	FS
63078	188	D	+	+−	30	200	2.40	10.00	20	42,36,38,43	FS
63267	151	D	+	+−	30	200	2.40	10.00	20	42,36,38,43	HVB, FS
63419	255	D	+	+−	30	200	2.40	10.00	20	42,36,38,43	HVT, FS
63703	249	D	−	+−	30	200	2.40	10.00	20	42,36,38,43	HVB, FS
63962	180	D	−	+−	30	200	2.40	10.00	20	42,36,38,43	FS
64143	77	D	−	+−	30	200	2.40	10.00	20	42,36,38,43	HVB, FS
64221	263	D	−	+−	30	200	2.40	10.00	20	42,36,38,43	HVT
64491	197	D	−	+−	30	200	2.40	10.00	20	42,36,38,43	HVB, FS
64689	300	D	−	+−	30	200	2.40	10.00	20	42,36,38,43	HVT
64993	93	D	−	+−	30	200	2.40	10.00	20	43,36,38,42	HVT, FS
65087	246	D	−	+−	30	200	2.40	10.00	20	43,36,38,42	HVB
65338	195	D	−	+−	30	200	2.40	10.00	20	43,36,38,42	HVT

Table B.3 continued.

RUN	L	C	B	Ch	t_{pump}	t_{probe}	det.	HV	t_{HVS}	cells	misc
65534	176	D	−	+−	30	200	2.40	10.00	20	43,36,38,42	HVT
65711	150	D	−	+−	30	200	2.40	10.00	20	43,36,38,42	
65862	346	D	−	+−	30	200	2.40	10.00	50	43,36,38,42	
66209	204	D	−	+−	30	200	2.40	10.00	20	43,36,38,42	HVB
66447	215	D	−	+−	30	200	2.40	10.00	20	43,36,38,42	XG
66667	216	D	−	+−	30	200	2.40	10.00	20	43,36,38,42	XG
66888	309	D	−	+−	30	200	2.40	10.00	20	42,36,38,43	HVT
67220	120	D	−	+−	30	200	2.40	10.00	20	42,36,38,43	HVT
67341	158	D	−	+−	30	200	2.40	10.00	20	42,36,38,43	HVB
67500	327	D	−	+−	30	200	2.40	10.00	20	42,36,38,43	HVB
67835	368	D	−	+−	30	200	2.40	10.00	20	42,36,38,43	HVT
68222	110	D	−	+−	30	200	2.40	10.00	20	36,39,40,43	FS
68333	170	D	−	+−	30	200	2.40	10.00	20	36,39,40,43	HVB
68504	170	D	−	+−	30	200	2.40	10.00	20	36,39,40,43	HVT
68675	134	D	−	+−	30	200	2.40	10.00	20	36,39,40,43	
68818	489	D	−	+−	30	200	2.40	10.00	20	36,39,40,43	FS?
69308	254	D	−	+−	30	200	2.40	10.00	5	36,39,40,43	FS
69585	270	D	−	+−	30	200	2.40	10.00	50	36,39,40,43	
69856	277	D	−	+−	30	200	2.40	10.00	5	36,39,40,43	
70137	253	D	−	+−	30	200	2.40	10.00	5	36,39,40,43	HVB
70391	236	D	−	+−	30	200	2.40	10.00	5	36,39,40,43	HVT
70628	296	D	−	+−	30	200	2.40	10.00	5	36,39,40,43	HVT
70925	298	D	−	+−	30	200	2.40	10.00	5	36,39,40,43	HVB
71224	270	D	−	+−	30	200	2.40	10.00	5	36,39,40,43	
71495	305	D	−	++	30	200	2.40	10.00	5	36,39,40,43	ChS
71802	200	D	−	++	30	200	2.40	10.00	5	36,39,40,43	ChS
72003	295	D	−	++	30	200	2.40	10.00	5	36,39,40,43	ChS
72303	264	D	+	++	30	200	2.40	10.00	5	36,39,40,43	ChS
72579	192	D	+	++	30	200	2.40	8.00	5	36,39,40,43	ChS
72780	249	D	+	++	30	200	2.40	8.00	5	40,42,38,39	ChS
73033	203	D	+	++	30	200	2.40	10.00	5	40,42,38,39	ChS
73241	282	D	+	++	30	200	2.40	10.00	5	40,42,38,39	ChS
73524	213	D	+	++	30	200	2.40	10.00	5	40,42,38,39	ChS
73738	312	D	+	++	30	200	2.40	0.00	5	40,42,38,39	ChS

Table B.3 continued.

RUN	L	C	B	Ch	t_{pump}	t_{probe}	det.	HV	t_{HVS}	cells	misc
74051	320	D	+	+−	30	200	2.40	10.00	50	40,42,38,39	ChS
74372	312	D	+	−−	30	200	2.40	10.00	50	40,42,38,39	ChS
74689	374	D	−	−−	30	200	2.40	10.00	5	40,42,38,39	ChS
75064	272	D	−	−−	30	200	2.40	10.00	50	40,42,38,39	ChS
75337	284	D	−	−−	30	200	2.40	10.00	5	40,42,38,39	
75622	283	D	−	+−	30	200	2.40	10.00	50	40,42,38,39	FS
75916	244	D	+	+−	30	200	2.40	10.00	50	40,42,38,39	FS
76161	88	D	+	+−	30	200	2.40	10.00	50	40,42,38,39	HVT, FS
76250	229	D	+	+−	30	200	2.40	10.00	50	40,42,38,39	HVB
76480	140	D	+	+−	30	200	2.40	10.00	50	40,42,38,39	FS
76621	180	D	+	+−	30	200	2.40	10.00	5	40,42,38,39	FS
76803	76	D	+	−−	30	200	2.40	10.00	5	40,42,38,39	FS
76880	213	Q	+	−−	30	200	2.40	10.00	5	40,42,38,39	
77094	193	D	+	−−	30	200	2.40	5.00	5	40,42,38,39	+10+0, FS
77288	219	D	+	−−	30	200	2.40	5.00	5	40,42,38,39	+0–10
77508	308	D	+	−−	30	200	2.40	4.50	5	40,42,38,39	–1-10
77817	247	D	+	−−	30	200	2.40	4.50	5	40,42,38,39	+10+1
78067	262	D	+	−−	30	200	2.40	5.50	5	40,42,38,39	$+10-1$, FS
78330	300	D	+	−−	30	200	2.40	4.50	5	40,42,38,39	+10+1, FS
78631	149	D	+	−−	30	200	2.40	5.50	5	40,42,38,39	+1–10
78780	174	D	+	−−	30	200	2.40	7.50	5	40,42,38,39	+5–10, FS
78955	314	D	+	−−	30	200	2.40	5.00	8	40,42,38,39	
79271	105	D	+	−−	30	200	2.40	5.00	5	40,42,38,39	FS
79377	237	D	+	−−	30	200	2.40	3.25	5	40,42,38,39	+7.5+1
79615	319	D	+	−−	30	200	2.40	4.50	5	40,42,38,39	+10+1, FS
82774	200	D	+	−−	30	200	2.40	5.50	5	40,42,38,39	+1–10
82983	203	D	+	−+	30	200	2.40	7.50	5	37,36,42,35	+5–10, FS
83195	179	D	+	−+	30	200	2.40	7.50	5	37,36,42,39	+5–10, FS
83378	57	D	+	−+	30	200	2.40	7.50	5	37,36,42,39	+5–10, XG, FS
83436	23	D	+	−+	30	200	2.40	7.50	5	37,36,42,39	+5–10, XG, FS
83472	37	D	+	−+	30	200	2.40	7.50	5	37,36,42,39	+5–10, XG, FS
83510	121	D	+	−+	30	200	2.40	7.50	5	37,36,42,39	+5–10, XG, FS
85021	215	D	+	−+	30	200	2.40	10.00	5	37,42,36,39	MS, FS
85237	173	D	+	−+	30	200	2.40	4.50	5	37,42,36,39	+10+1, FS

Table B.3 continued.

RUN	L	C	B	Ch	t_{pump}	t_{probe}	det.	HV	t_{HVS}	cells	misc
85416	163	D	+	−+	30	200	2.40	10.00	5	37,42,36,39	HVT
85580	190	D	+	−+	30	200	2.40	10.00	5	37,42,36,39	
85771	299	D	+	−+	30	200	2.40	5.00	9	37,42,36,39	
86072	168	D	+	−+	30	200	2.40	10.00	5	37,42,36,39	
86241	85	D	+	−+	30	200	2.40	5.50	5	37,42,36,39	+1–10, HVB
86328	252	D	+	−+	30	200	2.40	5.50	50	37,42,36,39	+10–1, HVB, FS
86585	184	D	−	−+	30	200	2.40	5.50	50	37,42,36,39	+10–1, HVB, FS
86772	514	D	−	−+	30	200	2.40	4.25	50	37,42,36,39	+7.5–1, HVB
87287	273	D	−	−+	30	200	2.40	3.00	50	37,42,36,39	+5–1, HVB
87568	331	Q	−	−+	30	200	2.40	10.00	50	37,42,36,39	XG
87925	244	Q	−	−+	30	200	2.40	10.00	50	37,42,36,39	XG
88173	160	Q	−	+−	30	200	2.40	10.00	50	37,42,36,39	XG
88355	273	Q	−	−+	30	200	2.40	10.00	50	35,42,36,39	HVB
88645	234	Q	−	−+	30	200	2.40	10.00	50	35,42,36,39	HVT
88880	229	Q	−	−+	30	200	2.40	0.00	0	35,42,36,39	
89127	178	Q	−	−+	30	200	2.40	10.00	5	0,41,36,0	
89310	694	Q	−	−+	30	200	2.40	10.00	5	0,41,36,0	
90008	363	Q	−	−+	30	200	2.40	10.00	4	0,41,36,0	
90425	203	D	−	−−	30	200	2.40	10.00	50	0,39,41,0	
90640	537	D	−	−−	30	200	2.40	10.00	50	0,39,41,0	FS?
91178	133	D	−	−−	30	200	2.40	10.00	5	0,39,41,0	FS
91312	210	Q	−	−−	30	200	2.40	10.00	5	0,39,41,0	
91534	235	D	+	−−	30	200	2.40	10.00	5	0,39,41,0	
91772	294	D	+	−−	30	200	2.40	10.00	5	0,39,41,0	FS?
92067	432	D	+	−−	30	200	2.40	10.00	50	0,39,41,0	FS
92500	237	D	+	−−	30	200	2.40	10.00	5	0,39,41,0	HVT
92738	316	D	+	−−	30	200	2.40	10.00	5	0,39,41,0	HVB, FS
93055	276	D	+	−−	30	200	2.40	10.00	5	0,39,41,0	HVT
93348	628	D	+	−+	30	200	2.40	10.00	5	0,23,26,0	
93978	651	D	+	−+	30	200	2.40	10.00	50	0,23,26,0	
94631	496	D	+	−+	30	150	2.40	10.00	4	0,23,26,0	
95129	373	D	−	−+	30	150	2.40	10.00	5	0,23,26,0	FS?
95506	244	D	−	−+	30	150	2.40	10.00	50	0,23,26,0	FS?
95751	164	D	−	−+	30	150	2.40	10.00	5	0,23,26,0	HVT

Table B.3 continued.

RUN	L	C	B	Ch	t_{pump}	t_{probe}	det.	HV	t_{HVS}	cells	misc
95916	363	D	−	−+	30	150	2.40	10.00	5	0,23,26,0	HVB
96283	350	D	−	−+	30	150	−4.00	10.00	5	0,23,26,0	
96634	262	D	−	−+	30	150	−4.00	10.00	5	0,23,26,0	
96897	518	D	−	−+	30	150	−4.00	10.00	50	0,23,26,0	
97416	652	D	−	−+	30	150	−4.00	10.00	5	0,23,26,0	
98069	425	D	−	−+	30	150	2.40	10.00	5	0,23,26,0	FS
98496	359	D	−	−+	30	150	−4.00	10.00	5	0,23,26,0	
98857	276	D	−	−+	30	150	−2.40	10.00	5	0,23,26,0	FS
99136	316	D	+	−+	30	200	−4.00	10.00	5	0,23,26,0	
99469	221	D	+	−+	30	200	−4.00	10.00	5	0,23,26,0	
99693	191	D	+	−+	30	200	2.40	10.00	5	0,23,26,0	
99887	155	D	+	−+	30	200	2.40	10.00	5	0,23,26,0	
100045	300	D	+	−+	30	150	2.40	10.00	5	0,23,26,0	
100349	175	D	+	−+	30	150	2.40	10.00	5	0,23,26,0	
100526	254	Q	+	−+	30	150	2.40	0.00	0	0,23,26,0	
100781	559	D	+	−+	30	200	2.40	10.00	10	0,23,26,0	FS
101348	367	D	+	−+	30	175	2.40	10.00	5	0,23,26,0	
101721	259	D	+	−+	30	175	2.40	10.00	5	0,23,26,0	
101989	268	D	+	−+	30	165	2.40	10.00	5	0,23,26,0	
102272	276	D	+	−+	27	165	2.40	10.00	5	0,23,26,0	FS
102550	389	D	+	−+	30	165	4.00	10.00	5	0,23,26,0	FS
102940	393	D	+	−+	27	165	4.00	10.00	20	0,23,26,0	FS
103335	384	D	+	−+	30	165	2.40	10.00	20	0,23,26,0	FS
103720	320	D	+	−+	27	165	−4.00	10.00	5	0,23,26,0	FS
104042	458	D	+	−+	30	165	2.40	10.00	5	0,23,26,0	FS
104504	311	D	+	−+	30	162	2.40	10.00	5	0,23,26,0	AlT
104816	390	D	+	−+	30	162	2.40	10.00	20	0,23,26,0	FS:AlT
105207	318	D	+	−+	30	162	−4.00	10.00	5	0,23,26,0	FS, AlT
105551	436	Q	+	−+	30	162	2.40	10.00	20	0,23,26,0	FS, AlT
105989	184	D	+	−+	30	200	2.40	10.00	5	44,43,37,45	HVB
106202	208	D	+	−+	30	200	2.40	10.00	5	39,43,37,48	
106421	209	D	+	−+	30	200	2.40	10.00	5	39,43,37,48	XM
106637	287	D	−	−+	30	200	2.40	10.00	5	39,43,37,48	XM
106929	215	D	+	−+	30	200	2.40	10.00	5	39,43,37,48	XM

Table B.3 continued.

RUN	L	C	B	Ch	t_{pump}	t_{probe}	det.	HV	t_{HVS}	cells	misc
107152	579	D	+	−+	30	200	2.40	10.00	5	39,43,37,48	XM
107746	201	D	+	−+	30	200	2.40	10.00	5	39,43,47,48	XM
107949	112	D	+	−+	30	200	2.40	10.00	5	39,43,47,48	XM
108063	205	Q	+	−+	30	200	2.40	10.00	5	39,43,47,48	XM
108275	333	Q	+	−+	30	200	2.40	10.00	5	39,43,47,48	XM
108612	253	D	+	−+	30	200	2.40	10.00	5	39,43,47,48	
108872	199	Q	+	−+	30	200	2.40	10.00	20	39,43,37,48	HVB, XM
109075	308	Q	+	−+	30	200	2.40	10.00	20	39,43,47,48	XM
109391	344	Q	+	−+	30	100	2.40	10.00	10	39,43,47,48	XM
109738	265	Q	+	−+	30	200	2.40	10.00	10	39,43,47,48	XM
110006	391	Q	+	−+	30	155	2.40	10.00	30	39,43,47,48	XM
110400	396	Q	+	−+	30	150	2.40	10.00	10	39,43,47,48	XM
110797	404	D	+	−+	30	150	2.40	10.00	30	39,43,47,48	XM
111203	423	D	+	−+	30	150	2.40	10.00	10	39,43,47,48	
111627	346	Q	+	−+	30	150	2.40	10.00	10	39,43,47,48	
111975	367	D	+	−+	30	150	2.40	10.00	30	39,43,47,48	XM
112344	282	D	+	−+	30	150	2.40	10.00	10	39,43,47,48	XM
112628	293	Q	+	−+	30	150	2.40	10.00	10	39,43,47,48	XM
112923	475	Q	+	−+	30	150	2.40	10.00	30	39,43,47,48	
113403	203	Q	+	−+	30	150	2.40	10.00	10	39,43,47,48	XM
113610	334	Q	+	−+	30	150	2.40	10.00	10	39,43,47,48	XM
113947	367	D	+	−+	30	150	2.40	10.00	10	39,43,47,48	
114315	872	D	+	−+	30	150	2.40	10.00	10	39,43,47,48	

Appendix C

FALSE SIGNAL HISTORY

This appendix relates the history of all of the "false signals" that have been encountered during the HG3 and HG4 datasets. A false signal is considered to have occurred any time an HV correlated shift in a spin precession frequency channel was resolved by more than three sigma in a data run (usually 6–24 hours of data). For the purposes of this section, these false signals will be referred to as EDMs, although this is in no way meant to imply that they have any relation to an actual electric dipole moment, and in most cases it seems likely that they are the result of HV correlated magnetic fields. As was discussed in Section 7.4.1, these EDMs tend to appear after the cell holding vessel is opened and closed for cell adjustment, and then the EDM usually persists until the cells are adjusted again, although it sometimes takes several iterations of vessel perturbations for the EDM to disappear. This appendix treats each EDM occurrence of this type as a separate "episode," and for each episode gives a description of our attempts to diagnose the source of the EDM, and any speculative conclusions that were made at the time. Significant apparatus changes made during the interim periods between episodes are also given.

Unless explicitly noted otherwise, the sizes of EDMs (false signals) are all given in units of 10^{-8} s^{-1}, and for runs taken with the magnetic field in the $B-$ direction, the frequency shifts have been multiplied by -1. The descriptions for EDMs that occurred with the 4-cell apparatus include a frequency profile of the EDM for all the pairwise frequency differences and the Combo and LeakTest four cell combinations (see Table 7.3 for definitions). In some cases the profile is calculated by averaging two or more nearby runs that resulted in a similar frequency profile.

C.1 HG3 False Signals

Experimental parameter descriptions for runs in this section are given in Table 4.1.

EDM3.1: 2/14/2000, Run 22308

A large EDM appeared in Run 22308, the third run to be taken after the start of the HG3 dataset, just after remelted cells were installed in the vessel:

$$\omega_T - \omega_B = -28 \pm 3.7.$$

This run used an HVS time of 10 seconds, and we tried to look for a dependence on the HV ramp rate by changing HVS to 20 seconds in the next run, but then the effect disappeared, and returning to HVS = 10 did not cause the EDM to come back.

Conclusions: It is hard to say anything about this EDM since it did not stick around very long. There was only half an hour of time separation between the end of run 22308 and the start of the next run with HVS = 20 in which there was no EDM. Probably it had something to do with the installation of the remelted cells, or perhaps there was some unknown periodic fluctuation with the same frequency as the HV reversals, as we were not inserting skips in the HV sequence yet.

Interim: Random skips in the HV reversal sequence were added after run 23697. All of the data up to run 30471 were taken with the magnetic field pointed down (forward). We started doing more regular reversals of the magnetic field direction after run 31342.

EDM3.2: 3/26/2000, Runs 36803 → 38764

Occasional spikes in the HV caused the frequency difference to semipermanently shift by $\sim 10^{-5}$ s^{-1}. The shift direction was dependent on the HV polarity when the spikes occurred. No EDM was generated because the spikes occurred infrequently (about once per hour). When the vessel was next opened it was found that the bottom electrode did not have good electrical contact with the HV cable, which was probably the origin of the HV disturbances.

Conclusions: The HV spikes seemed to be causing magnetization of ferromagnetic impurities in the Teflon electrode cups, vessel walls, or the polyethylene feedthroughs. This led to a long study of the effect of current surges sent through loops wrapped around the HV feedthroughs (see Sec. 3.2.2). The general conclusions of this study were that almost all materials can be

magnetized to some degree, but our Teflon pieces had worse properties than some polyethylene samples we looked at, which led us to eventually change all of the vessel/electrode materials from aluminum coated Teflon to carbon filled polyethylene.

Interim: The first polyethylene electrode was installed before run 55182, and the entire vessel was switched to the conductive polyethylene version before run 59717.

EDM3.3: 8/2/2000 → 8/14/2000, Runs 68357 → 69342

$$\omega_T - \omega_B \simeq 40.$$

After installing new HV cables and feedthroughs (the first use of a conductive PE pellet as the contact between cable and cup), an EDM appeared that persisted for several runs and seemed to only be associated with HVB runs. However, data were mostly taken with HVB because we were having trouble getting the top portion of the vessel to hold high voltage. A single run (69342) taken with HVT did not show an EDM (except when the leakage currents were saturating). The signal did not get significantly smaller at HV = ±5 kV ($\Delta\omega \simeq 30$) and changed sign with the magnetic field, although it appeared to be smaller ($\Delta\omega \simeq 15$) for $B-$. The cable leakage current was found to be saturating after run 69271, and it is possible that it was saturating during much of the other HVB data. It was also found that the resistance between the vessel and the HV ground was a little low (6 GΩ). The HV cables were then replaced with cable with a thicker multistranded wire and thicker insulation, and the strain relief system for the leakage collection wires was changed from pieces of PCB to polyethylene. The EDM was no longer present upon reinstallation of the vessel after making these changes.

Conclusions: It is quite possible that the appearance and disappearance of the EDM was associated with the installation of the new feedthroughs/cables. There might have been a bad connection within the bottom feedthrough that was fixed upon reassembly of the cable/feedthrough when the thicker cable was installed. It is difficult to associate the problem with any particular part of the cable/feedthrough assembly since we have used both versions without having false signals prior to and after this effect showed up (thin/thick cables, solder blob/polyethylene pellet at the end of the feedthrough). It is also possible that the EDM was somehow associated with the saturated cable current, and addressing this problem caused the EDM to go away.

Interim: The main two-cell data set (HG3) was completed at the end of August, 2000, and a few more B misalignment runs were taken in October. New cells with 100% CO buffer gas were

filled in December and were tested in several runs in the two-cell polyethylene vessel. These runs are described in Table B.1.

EDM3.4: 1/25/2001 CO Cell Runs 10505 and 10993

$$\omega_T - \omega_B = 9.4 \pm 1.1.$$

This "interim" data set between the completion of the HG3 measurement and the installation of the 4-cell apparatus consisted of only 1900 scans that were mainly taken to test the spin lifetime behavior of the new CO buffer gas cells under UV exposure. However, the first run (10505) where HV was applied resolved an EDM. After this effect appeared, the electrodes were cleaned with methanol and the cell walls were recleaned, but after reassembling the vessel, large leakage currents prevented taking data at 10 kV. There was possible evidence that the leakage current problems were associated with one of the electrodes. We took one more run at ± 5 kV, where the leakage currents were under control, and this run (11705) showed no signal to the level of 3×10^{-8} s^{-1}. This problem was not investigated further, though, due to the switchover to the 4-cell vessel.

Conclusions: After having relatively few false signals occur (2 instances) during the entire HG3 data set, a problem occurred immediately upon installation of the new CO cells. Since there has been no shortage of problems with false signals since this point, this might be an indication that there is something associated with the different buffer gas, or something else about the construction of the new cells, that has led to there being more EDMs than before. However, data taken later on with the older N_2+CO cells (see Sec. C.3) seemed to show an increased instance of EDMs compared to the HG3 dataset, indicating that the false signals are not related to the cells. We have also generally not found the EDM behavior to follow specific cells. Probably, the EDM seen in this case was related to another unknown issue that appeared upon insertion of cells in the vessel, or it could have been related to deterioration of the groundplane in the 2-cell vessel.

Interim: The apparatus was prepared for 4-cell operation. Precession signals in all four cells were established on 4/3/2001 (HG4 Run 10016), and the first high voltage data run was taken on 4/18/2001 (HG4 Run 11080).

C.2 HG4 False Signals

Experimental parameter descriptions for runs in this section are given in Table B.3.

EDM4.1: 4/30/2001 → 5/2/2001, Runs 12590 → 12761

Large frequency jumps began occurring for ±10 kV in only the sixth electric field HG4 data run, although the shifts were not well enough correlated with the HV polarity to generate an EDM. This run was taken immediately after the vessel was opened to switch out the MB cell. Also prior to this run, a relay was added to the leakage current box to enable a digitally controlled change of gain in order to measure charging currents (see Sec. 6.3.1). The shifts were as large as 10^{-4} s^{-1} in the bottommost cell, but only occurred for HVB, and became significantly smaller in the upper cells. The HVS setting had no noticeable effect on this behavior, and the HV magnitude did not affect the size of the shifts but did affect their rate of occurrence. We were initially suspicious that this behavior appeared due to adding the charging current relay, but enabling and disabling this feature did not affect the behavior. The vessel surfaces near the bottom electrode were swabbed with trichloroethylene/acetone/methanol, and the HV cables were exchanged. The cable, which had been on the bottom, came apart during an attempt at cleaning the feedthrough in an acetone/methanol ultrasonic bath and so had to be reassembled. The HV induced noise disappeared on the next data run.

Conclusions: Possibly a magnetic contaminant was removed upon cleaning the bottom end of the vessel. There also seemed to be a lot of sparking in the leakage currents, especially for HVB at −10 kV. This might have been due to a bad connection in the bottom HV cable that was improved after reassembling the feedthrough, although there seem to have also been similar current spikes before and after these runs.

EDM4.2: 5/11/2001 → 7/15/2001, Runs 13280 → 19611

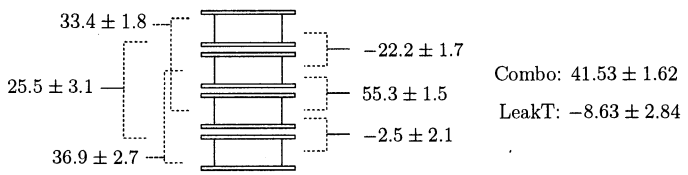

Figure C.1: Initial frequency profile of EDM4.2. Signal is averaged from Runs 13280 and 13795.

A large effect appeared, especially in the middle frequency difference ($\Delta\omega_M$) after installing new cells (see Fig. C.1). Initial tests showed that it seemed to scale linearly with HV and not depend on the HVS rate. Very small data sets, with middle cell data only, indicated that the EDM was present for both HVT and HVB. Subsequently the middle cells were cleaned, repainted and swapped, and we ended up with a smaller and opposite sign EDM:

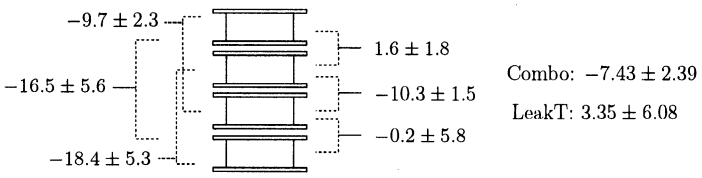

Figure C.2: EDM4.2 frequency profile after an adjustment of the middle cells. The signals are averaged from Runs 14132, 14456, 16273, 16368 and 16531.

During this period, the OB cell Hg density was dropping to minuscule levels, so some channels were not very sensitive, but the signal still seemed to be present for both HVT and HVB (at $\sim 50\%$ the size compared to when both sides were connected), and persisted through a change of only the OB cell. Several non-standard voltage sequences were introduced (+0+0, 0−0−, ++−−++−−) which possibly showed that there was a larger signal for the negative polarity. The ++−− run gave about equal signals for analyzing only the scans immediately after HV ramps, or only scans without HV ramps before them. It had been noticed that there were patches of the aluminum coating on the top side of the groundplane that had very low conductivity, mainly on the corner "plateaus." We painted over these low conductivity patches with silver paint, the electrodes and middle cells were reversed, and the outer cells were remelted. After combating a large single cell signal (see EDM4.3), there was still an EDM at a reduced level.

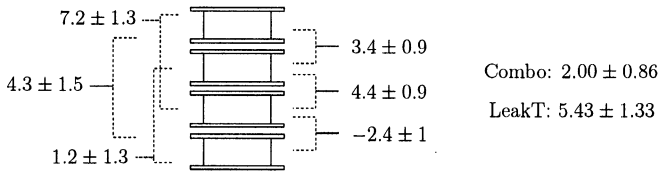

Figure C.3: EDM4.2 frequency profile after painting over parts of the groundplane, reversal of the electrodes and middle cells, and remelting of the outer cells. The signal is averaged from Runs 18015 and 19611.

Conclusions: This was a long-standing problem that went through several phases of behavior, so it's very possible that we were subject to several different effects. Our main suspicion ended

up on the groundplane, which definitely had isolated patches and areas of poor conductivity that seemed to be getting worse over time. This might have led to trickle currents between regions of the groundplane that would not register on the leakage current monitors. There did seem to be a direct change in the EDM signal after painting over patches of the groundplane, but we continued to have EDM problems after installing a new groundplane.

EDM4.3: 6/28/2001 → 7/2/2001, Runs 16733 → 17288

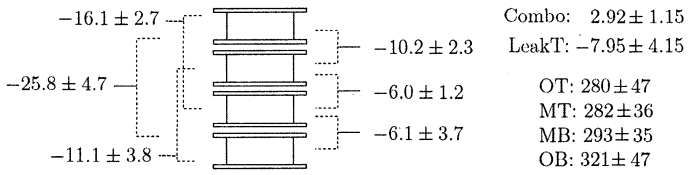

Figure C.4: EDM4.3 frequency profile. Signals are averaged from Runs 16733 and 17288. Single cell signals are given below the 4-cell combinations.

During the course of EDM4.2, a very resolvable single cell EDM showed up after swapping out cells and an attempt at repairing the Al coated groundplane. The HV value and HVS rate had little or no affect on this single cell signal. However, it was found that the top HV cable shield was tending to short to the magnetic field coil form (12 Ω–2 MΩ depending on the cable position when jostled from outside the magnetic shields). A single run (17610) was taken with the coil form connected directly to the HV cable shield, which gave no resolved single cell or frequency difference signals. The shields were then opened, the outer cells were remelted, and better isolation of the HV cable shields and the coil form was established.

Conclusions: This signal was definitely related to the HV cable shield shorting to the magnetic field coil form, resulting in magnetic fields generated by a large current flowing between the coil and cable shield. On subsequent runs the frequency difference channels again gave resolved EDMs, but this was thought to be due to the groundplane (see EDM4.2).

Interim: Since it was believed that the groundplane was causing our problems, several runs were taken with no applied HV while a new groundplane was being machined and coated. We started investigating using a probe detuning halfway between the F=1/2 and 3/2 lines to get larger rotation amplitudes (see Sec. 7.1).

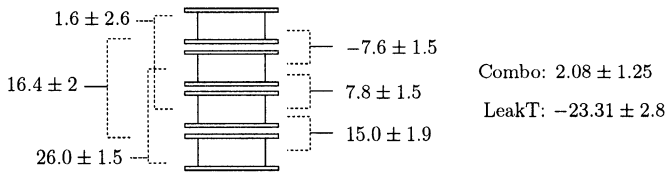

Figure C.5: EDM4.4 frequency profile. Signals are averaged from Runs 21264–21834.

EDM4.4: 8/20/2001 → 8/25/2001, Runs 21264 → 21834

An EDM as shown in Figure C.5 appeared immediately after installing a new gold coated groundplane. The leakage currents tended to start high (Leak Cell 1 and 2: 30 pA, vessel: saturated) and decayed slowly (over about 40 seconds) to reasonable levels. After Run 21834, the vessel was opened and the HV cable to cell disk electrode resistance was measured to be > 5 MΩ. After adding silver paint to the cable/electrode and electrode/cell interface, this was improved to several hundred kΩ, but after this point it became impossible for the top cell to hold HV above 8 kV. This was thought to have been due to the cell indentation in the groundplane being larger than the previous version (the plastic had expanded during the gold coating process). Enlarging the cell disk, which interfaced with the groundplane, with silver paint enabled 10 kV to be applied to the top cell with reasonable leakage currents. As soon as this was done, though, the bottom cell began to break down for HV above 7 kV. This was also improved by enlarging the bottom cell disk with silver paint. In several subsequent runs there were no false EDMs.

Conclusions: It seems likely that the breakdown in cell leakages was related to the larger gap between the cell disk and groundplane since it went away after enlarging the cell disks. It's not entirely clear that this behavior caused the EDMs seen initially after installing the gold groundplane. The long decay time of the large cell leakage currents was certainly unusual behavior and could have been related to the larger cell indentation issue, or could have been due to something else entirely that might have been causing the EDMs. It is not clear what caused the long decay cell leakage current behavior to disappear either, but even after this EDM went away the vessel leakage tended to be large and have a long decay. It is hard to say how stable (to false EDMs) this situation (this groundplane with painted cell disks) would have been under extensive operation because only three HV runs were taken at this point. At the time, it was felt that using the cells with painted cell disks would generally work, but since this situation would impede the changing of cell orientation and position, we planned on replacing the groundplane before starting intensive data taking.

Interim: In the next year, very little HV data runs were taken. During this time, the light shift/vertical magnetization suppression elements were installed (see Sec. 6.5 and 7.1.1), and we waited out a period of extra large magnetic noise due to electric buses outside the building during the summer of 2002. The second gold groundplane was installed on 8/30/2002, after which there was still a two month delay before an HV data run was taken because of problems with the new KNbO3 crystal AR coating (see Sec. 6.4.2).

EDM4.5: 11/16/2002 → 11/18/2002, Runs 38333 → 38818

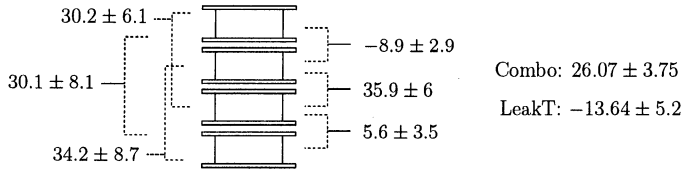

Figure C.6: EDM4.5 frequency profile (Run 38647).

We began taking data with HV again with Run 37713, attempting to follow an eight run parameter reversal sequence (see Sec. 7.2.2). After the first two runs without any problems, the magnetic field direction was reversed, and then the next run (38333) had strongly resolved signals as large as 150 in the middle and outer differences, but the size and also the sign of the EDM changed during the course of this run. This behavior repeated for the most part in run 38647, and possibly at a much lower level in run 38818, after which the effect did not seem to reappear. When the vessel was opened several runs later, the only thing that seemed slightly unusual was that one of the leakage collection wires attached to the groundplane was oriented such that it was not unthinkable that it could have at times made contact with the vessel wall.

Conclusions: It is possible that the leakage collection wire could have been making intermittent contact with the vessel wall, and this could have led to unusual "erratic" behavior, but the leakage current signals showed no sign of strange behavior and did not appear to change characteristics when the EDM signal changes. This type of "erratic" behavior was seen again several months later (EDM4.10), and at that point the behavior was thought to be perhaps associated with the deterioration of the gold coating on the groundplane. In this case, the gold coating was fairly new and should not have had any bare spots.

Interim: The rest of the eight run data sequence was completed without incident. A repolished BBO crystal was installed in the second cavity and a laminar flow system was installed over the laser (see Sec. 6.4.2).

EDM4.6: 1/1/2003, Runs 43724 and 44037

While changing out cells, the top HV cable conductor pulled out of its feedthrough. Rather than performing a full disassembly of the feedthrough, the cable was merely reinserted and superglued, which at the time seemed to give a decent resistance from the cable to the cell face. The connection was not reliable, though, and this led to very large current spikes in the top cell charging current (see Fig. 7.18), and resolved EDMs in several frequency differences in Runs 43724 and 44037:

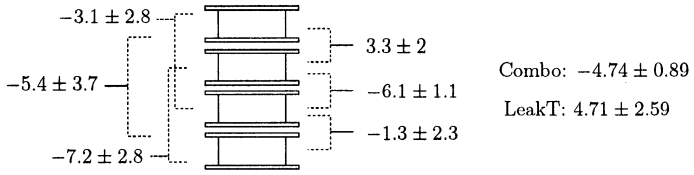

Figure C.7: EDM4.6 frequency profile due to sparking in the HV feedthrough. The signals are averaged from Runs 43724 and 44037.

Subsequent runs showed no EDMs, but were subject to occasional jumps in the main magnetic field current source that were definitely correlated with spark events in the high voltage. The sparks were between the bottom HV cable/feedthrough interface (which was coming apart) and the leakage current collection wires on the outside of the vessel, and possibly the coil form.

Conclusions: EDM4.6 was almost definitely due to the sparking occurring inside the broken HV feedthrough during HV ramps. These current spikes likely were orienting ferromagnetic impurities in the feedthrough or electrode. The occasional sparking that occurred after this did not lead to EDM like signals, but did show that the main current source can be affected by voltages applied to the coil form, which could possibly lead to false EDMS if there were periodic perturbations to the coil form (from the vessel or through the grounding wire).

EDM4.7: 1/31/2003, 48696 → 49460

We were taking tilted magnetic field data near the end of a "sequence" when we encountered a resolved single cell EDM. The field was tilted at 10 deg. in the z-direction (shield axis). The single cell EDM was -400 ± 110 in all four cells and there were no significant signals in the frequency differences. The next run was taken with the field tilted along the x-direction (axial: horizontal) and showed a less significant (2.5σ) single cell signal of $+150 \pm 60$. After turning off the offset field we no longer saw resolvable single cell signals, but there were some significant (3σ) EDMs in frequency difference channels in runs 49221 and 49460 (see Fig. C.8).

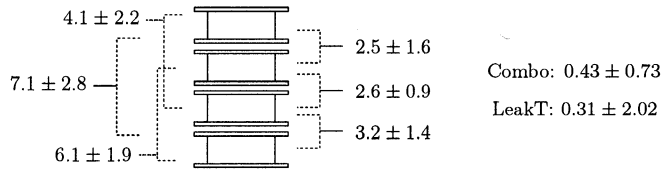

Figure C.8: EDM4.7 frequency profile. Signals are averaged from Runs 49221 and 49460.

Two additional runs were taken with the magnetic field tilted in the z-direction, but the single cell EDM did not return and there were no resolved frequency difference signals. The vessel was then opened and examined. A leakage current collection wire had to be repaired on the outside of the vessel, but it's possible that the wire broke after the vessel was removed from the shields. Remelted cells were put into the middle positions and the vessel was reinserted into the shields. The single cell EDM did not reappear after this point, but resolved signals in the frequency differences became a persistent problem in subsequent runs (EDM4.8).

Conclusions: The onset of the single cell signal occurred right after switching to the tilted magnetic field, which was suggestive that perhaps the EDM was related somehow to the misaligned field, but returning to the same configuration a couple of runs later did not show the same effect. It is remotely possible that some subtle differences in the degaussing or gradient adjustment played a role. The broken leakage current wire could also have led to problems, especially if it was making intermittent contact with the vessel. It is also unknown if the resolved single cell signal and the frequency difference signals were at all related.

Interim: A new field switching box was installed to more easily handle tilted magnetic field runs, electrical tape was put in between the HV cables and the vessel to improve the HV shield to vessel resistance (improved from about 1 TΩ to greater than 10 TΩ), and new cells were swapped into the vessel.

EDM4.8: 2/12/2003 → 3/16/2003, Runs 50333 → 55604

After opening the vessel, and not finding anything to satisfactorily explain the coming and going of the EDM4.7, we put remelted cells in the middle positions, closed the vessel, and hoped that we could resume taking data. Instead, the next run gave a slightly larger EDM in the frequency difference channels than we had been seeing previously. At first there seemed to be comparable sized signals from HVT and HVB (a little larger for HVT). The HV ramp rate had little or no effect, and

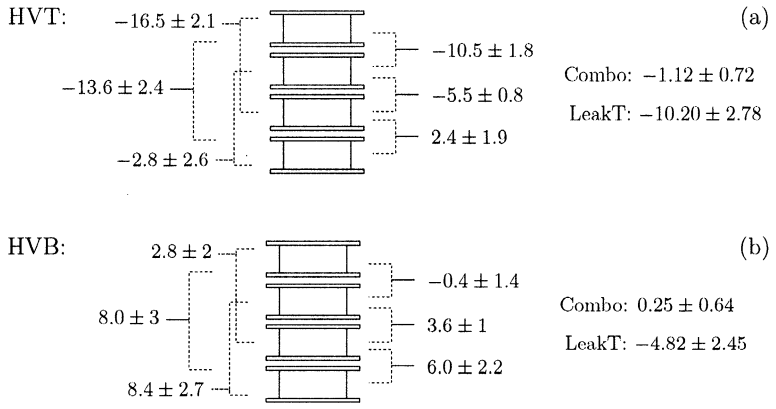

Figure C.9: Frequency profile of EDM4.8 for HVT and HVB. Part (a) shows the signal for HVT Runs 50612 and 51882. Part (b) shows the signal for HVB Runs 50838 and 51160.

a run with a 0,+10,0,+10 HV sequence did not show well resolved signals, but was consistent with being half the size of the ±10 kV signal.

Cell 37 (MT) was giving very low transmission, so it was removed and its walls were scrubbed with trichloroethylene/acetone/methanol. This did not seem to improve the transmission, but it was found that rotating the cell stem forward by ∼ 20 degrees gave a slightly better transmission. Small blobs of conductive epoxy were added around the window holders on the outside of the vessel (entrance windows for middle and outer beams) to give a conductive path to all conductive plastic parts on the vessel. After reinstalling the vessel in the shields, the next run showed a slightly larger EDM:

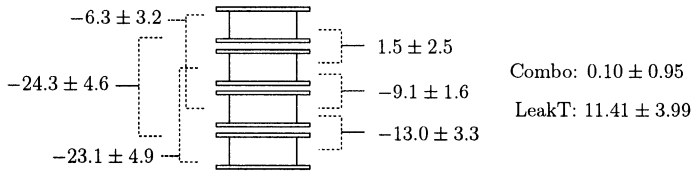

Figure C.10: EDM4.8 frequency profile after adjustments were made to the MT cell (Run 52290).

The larger signal was entirely due to an effect present only for HVB. A single run taken with HVT showed a resolved signal not inconsistent with the previous behavior, but at a slightly smaller level. We then began examining different HV sequences. It was found that 0,+10,0,+10 kV and 0,−10,0,−10 kV did not give any signal. A ++−− run indicated that there was no difference in the signal for dwells immediately after a ramp versus dwells with no ramp. A ±5 kV run gave no

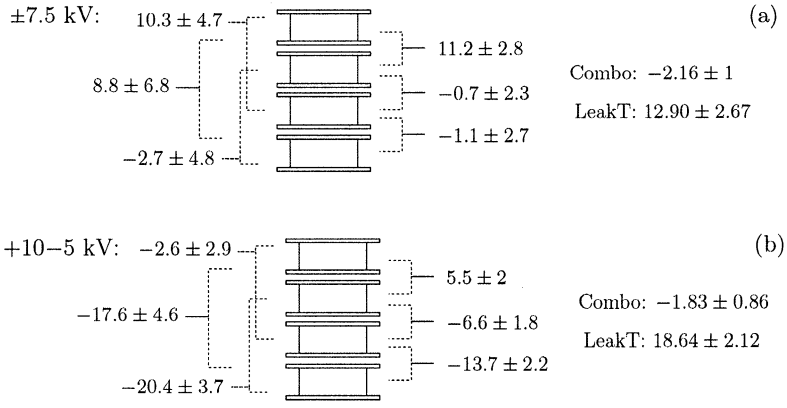

Figure C.11: EDM4.8 frequency profile for different HV sequences. Part (a) shows the signal for HV= ±7.5 kV (Run 53619). Part (b) shows the signal for a +10−5 kV sequence (Run 53882).

signal, and a ±7.5 kV run gave some resolved signals but with a different profile than had been seen at ±10 kV. Runs with +10−5 and −10+5 sequences gave essentially the same signal as ±10 kV.

A run taken with the vessel inverted about the shield axis (Run 54510) showed signals consistent with the source of the EDM being within the vessel or HV cables. Next the HV cables and feedthroughs were swapped, which gave EDMs of the same sign as before, but now the largest signals were associated with the topmost cell instead of the bottommost. Suspicion rested on something associated with the HV cable or feedthrough currently connected to the top. It was thought that there might be large currents flowing to the HV cable shield. This was investigated by stripping back the shield on the top cable past the front face of the vessel, but this led to no change in the signal (Run 54943). Both the HV cables were then replaced while keeping the same feedthroughs, which seemed to lead to a signal that had changed sign and gotten twice as large, and was still only present for HVT (see Fig. C.12).

This led us to then replace the top cable feedthrough. The new feedthrough used a solder blob to make contact between the cable and the electrode instead of a conductive plastic pellet. A new

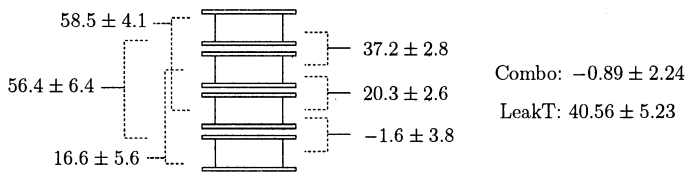

Figure C.12: EDM4.8 frequency profile after replacement of the HV cables. The signal is from Run 55170 (HVT).

collar (round conductive plastic part that presses down on the feedthrough) was also made. It was noticed at this point that the resistance to the thinnest part of both sides of the groundplane was getting a bit large (> 150 MΩ). Data taken with the new feedthrough still showed a large EDM coming mainly from the top, but smaller than the signal from the runs taken before changing the feedthrough:

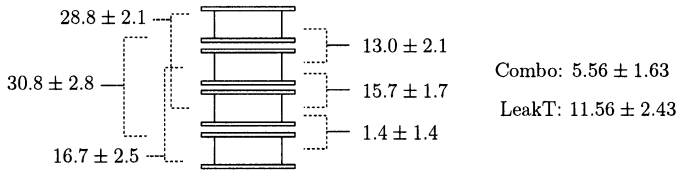

Figure C.13: EDM4.8 frequency profile after replacing the top HV feedthrough (Run 55604).

The HV cables (and feedthroughs) were then swapped again, to try to verify that the EDM would change position with the cable/feedthrough, but after doing so, the EDM seemed to disappear. Several efforts were made to return to the conditions where the false signals had been occurring, but the EDM stubbornly remained absent for several weeks.

Conclusions: This was again a very long-standing problem that exhibited several changes in behavior. The run taken with the vessel inverted gave very good evidence that the problem originated in the vessel or HV cables, and after the signal seemed to move with the HV cable/feedthrough, it seemed very likely to us that we had a problem with one of the cable/feedthrough assemblies. However, replacing all parts of that cable/feedthrough did not immediately cause the EDM to disappear. When we swapped the cable/feedthroughs the second time, we were expecting the EDM to change position, not disappear, but it's possible that a subtle change in the way the feedthrough was inserted into the vessel was responsible for the disappearance.

After the EDM went away, we noticed that spikes in the vessel charging current after the HV changed polarity (see Fig. 6.5) were leading to magnetic fields that could be picked up on a coil outside the vessel ($B \simeq 0.25$ mG). The spikes had apparently been occurring throughout our entire data set, or at least ever since we had the ability to observe the charging currents (after HG4 Run 12590). It was thought that ferromagnetic orientation associated with these spikes might have been causing some of our EDM troubles, and the disappearance of EDM4.8 might have been due to the inadvertent removal of a ferromagnetic contaminant. However, purposely adding some ferromagnetic "contaminants" (screwdriver shavings or a mu-metal speck) on the outside of the vessel did not make the EDM come back, but perhaps the added materials were

not placed close enough to the sparks or the cells to create a measurable effect. We did find that feedthroughs that interfaced with the thinner coaxial cable that had been used for the first half of the HG3 data set showed no evidence of sparking during the HV ramp. Eliminating this source of HV sparking would hopefully lead to it being less likely that ferromagnetic contaminants would create false signals, so we replaced the HV cable/feedthroughs with the thinner cable design.

Some other definite problems were found during the course of this EDM investigation. The first time the shields were opened after the EDM disappeared it was discovered that the stop that would normally fix the position of the vessel in the coil-form had come unglued. This probably occurred several "vessel insertions" before it was noticed because it had been previously observed that the vessel had been sitting further back in the coil by several mm. This could have led to additional motion of the vessel along and about the shield axis. We also found that the groundplane was starting to deteriorate, and it is possible that changes in the way cells were sitting on the groundplane might have led to changes in the false signal behavior. We attempted to make the EDM return through these potential problems by letting the vessel sit looser in the coil, and by rotating the MT cell to a position it was believed to have been in when the EDM was observed, but these tests did not make the EDM return.

Interim: Silver paint traces were added to the top groundplane to ensure a conductive path to the bottom of the cell indentations. The vessel stop was reglued in the coil.

EDM4.9: 4/14/2003 → 4/23/2003, Runs 59308 → 61302

After becoming satisfied that the EDM4.8 signal had disappeared, we tried again to start a data sequence (with Run 57005). We had completed most of the 8 run sequence, when we achieved the best sensitivity in the Combo channel per unit time (Run 59308: 0.67×10^{-8} s^{-1} in 12 hours), but this run also showed a 4σ resolved signal. Taking the combined average including the previous 8 runs also showed resolved signals in the middle difference and possibly the cross top ($\Delta\omega_{XT}$) difference:

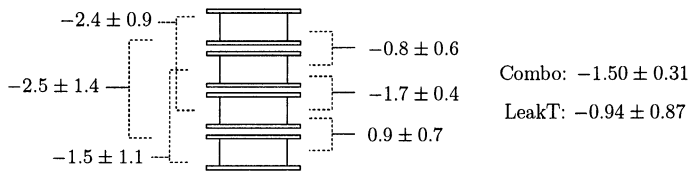

Figure C.14: EDM4.9 frequency profile. The signal is averaged from Runs 57005–59605.

This signal was small enough that we weren't initially sure that we were dealing with a false signal necessarily, but after taking data with HVT and HVB (2 runs each), it seemed that the EDM was present only for HVB, which convinced us that we were definitely dealing with a false signal once again. We hoped to discover if the EDM was associated with any of the cells, electrodes or HV cables by swapping all of these elements top/bottom, but after doing so, the EDM became larger by a factor of 10 (see EDM4.10).

Conclusions: This false signal was only noticed because of the extremely good sensitivity in the Combo channel. The effect was possibly also present in runs prior to 57005, but was not resolved well enough, so it is hard to pinpoint the onset of this effect.

EDM4.10: 4/23/2003 → 6/27/2003, Runs 61612 → 68675

After seeing the fairly small EDM4.9, the vessel was opened and the cells, electrodes, and HV cables were all swapped top/bottom. Immediately after doing so, the EDM became larger by a factor of ten:

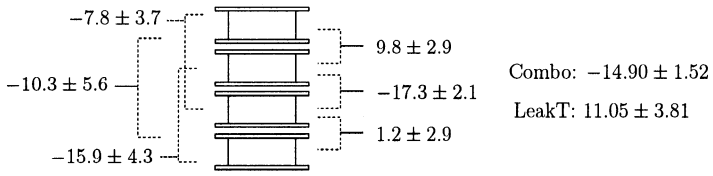

Figure C.15: Initial frequency profile of EDM4.10.

The larger signal was only associated with HVT, but data taken with HVB at this time was not sensitive enough to tell if the previous smaller signal was still present. The vessel was opened again and the top two cells were removed and replaced, while leaving the bottom cells untouched. This led to a somewhat larger and opposite sign signal:

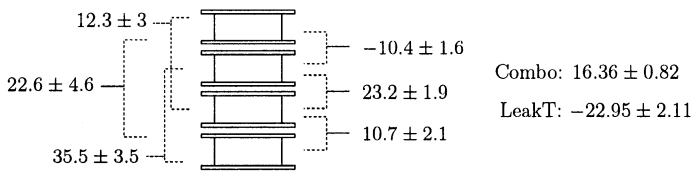

Figure C.16: EDM4.10 frequency profile after MT and OT cell replacement.

Only one run was taken with this configuration before the vessel was opened and the electrodes (and outer cells) were swapped top/bottom. We were attempting to leave in place cells or electrodes when possible, in case the groundplane/cell disk interface was affecting the signal. In this case, the MT cell remained in place, while the MB cell had to be moved when the electrodes were removed. The resulting behavior was that HVT gave somewhat "erratic behavior: for short periods of time there would be an extremely large EDM ($> 10^{-6}$ s^{-1}), then the signal might change sign, and for a fairly long period the large EDM might disappear. One change of behavior seemed to occur close to a SF6 gas refresh, but many other times the signal changed without a gas refresh. For HVB on the other hand, there was a fairly stable and resolved EDM:

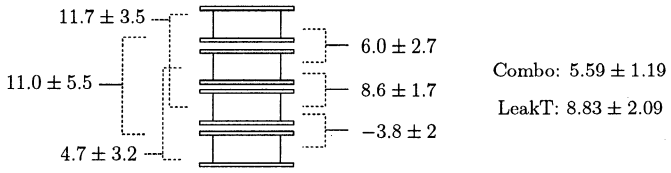

Figure C.17: HVB frequency profile of EDM4.10 (Run 63267) after the electrodes were swapped.

Our interpretation was that the EDM seen before this change had moved from the top to the bottom, and that the large and erratic EDM seen in the top was a new effect, perhaps caused by the top cell not being held firmly enough, although upon examination the next time the vessel was opened, the top cell did not seem any looser than normal. At this point, we began to believe that the EDM was associated with one of the electrodes 'P,' which was on the bottom at this point. We attempted to clean the bottom electrode with methanol, the screws were cleaned, and a new conductive gasket was made. On the top, the solder blob on the end of the HV feedthrough was enlarged to make it possible to hold the top cells more firmly. This resulted in no EDM or erratic signals for a run taken with HVT (64221), and the signal for HVB had become larger:

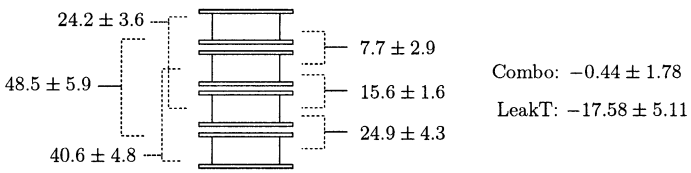

Figure C.18: HVB freq. profile of EDM4.10 (Run 64143) after the bottom electrode (P) was cleaned and given a new conductive gasket.

The vessel was opened again, and some modifications were made to the bottom (we attempted to leave the top untouched). Silver paint was added around the entire rim of the cell indentation on the groundplane to cover all of the bare spots, and the electrode screws were backed off a little (the OB cell had been affecting the light polarization strangely — but this did not help). After reinstalling, there was still no signal for HVT, and the EDM from HVB had changed sign and been reduced by about one half:

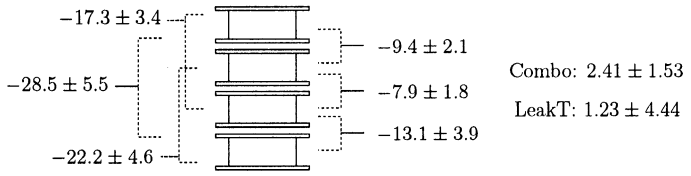

Figure C.19: HVB frequency profile of EDM4.10 (Run 64491) after modifying the bottom groundplane by adding silver paint around the cell indentation.

We then swapped the electrodes top/bottom again (top: P, bottom: C), and this seemed to give no EDM signal for HVB (Run 65087), but a large EDM for HVT:

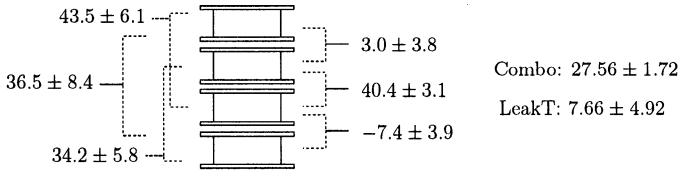

Figure C.20: HVT frequency profile of EDM4.10 (Run 64993) with electrode P on top.

This seemed like fairly good evidence that the EDM was associated with electrode P. We machined a new electrode (T) that was essentially the same design as C and P, except for adding a lip on the bottom portion for the conductive gasket to press down against. Electrode P was removed and the cell inside was installed in the electrode T and put in the top position in the vessel. The installation of the new electrode at least seemed to cause the large false signals coming from the top to go away, but there now seemed to be a fairly consistent EDM coming from the bottom (see Fig. C.21). Two runs were taken with enhanced magnetic gradients along the shield axis (2.8 mA and 4.5 mA applied to the gradient coil), but this did not seem to lead to a larger false signal. We attempted to make the larger EDM (see Fig. C.20) come back by reinstalling electrode P in the top position. Also,

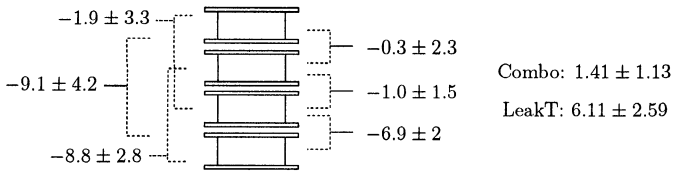

Figure C.21: HVB frequency profile of EDM4.10 (Run 66209) with electrodes T and C.

electrode C was removed and electrode T was moved to the bottom. The first run was taken with HVT, and showed a return of "erratic" behavior. A large signal mainly in the MT cell started at about 10^{-6} s^{-1} and then abruptly shifted to -3×10^{-7} s^{-1}. The change in signal happened several runs after a change in the charging currents (the charging currents started changing by 10% a quarter of the way into the HV ramp), which occurred right after a HV reversal skip. This behavior was perhaps related to problems with the groundplane, because when the vessel was opened later it was found that there was not a good conductive path to the top cell indentation. For HVB, there were possibly signals of the same size as from 66209 (see Fig C.21), but there was not anything very well resolved. Due to the problems with the top groundplane, the top cells and electrode were removed (the bottom was untouched) and silver paint was added around the cell indentation (the bottom side had been repaired previously before Run 64491). A single run was taken with HVT, in which the strange behavior in the charging currents had gone away, and there were no especially large EDMs:

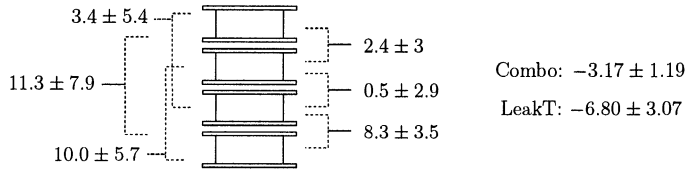

Figure C.22: HVT frequency profile of EDM4.10 (Run 67835) after modifying the top groundplane by adding silver paint around the cell indentation.

There was still suspicion that if electrode P had been causing problems and replacing it with a new electrode had improved the situation, then the other original electrode (C) might also have gone "bad," so we had a new electrode (E) machined. New electrodes were then installed in both positions (top: E, bottom: T). Initial data taken with HV on both sides started off showing a strong EDM ($\sim 10^{-6}$ s^{-1}), but once again, the signal shifted by a large amount in the middle of the run, several dwells after a SF6 refresh. The several runs taken after this did not show large EDMs but did have some slightly resolved signals (see Fig. C.23).

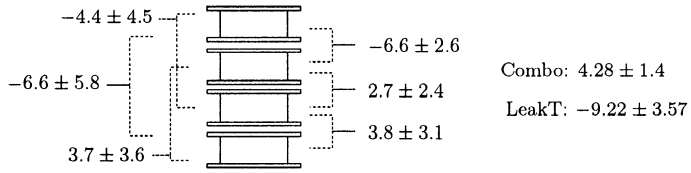

Figure C.23: EDM4.10 frequency profile (Run 68675) with electrodes E and T.

The new electrodes had not, apparently, solved all of our problems, and the somewhat "erratic" nature of the false signals was making the problem harder to diagnose through making systematic changes to the vessel. There was some suspicion that shifts in the false signals might be related to small shifts in position of a cell relative to the bare spots on the groundplane, and since we had a freshly gold-coated groundplane on hand, we decided to install it at this point. After installing the new groundplane we continued to occasionally resolve EDMs, but at least there has not been a return of the "erratic" behavior so far.

Conclusions: It was fairly convincing to us that the EDM had something to do with electrode P after the effect seemed to change location consistently following the electrode position. The large EDM also disappeared after electrode P was replaced by T. We became a little less convinced when we put electrode P back in the vessel and the large EDM did not return, and we have continued to have false signals since switching out both of the old electrodes. It's possible that the "erratic" false signals, and not taking more than a single run for some configurations, might have led us to make the wrong conclusion about the electrode. We also were suspicious about the deteriorating gold coating on the groundplane. If the groundplane was responsible for the "erratic" signal behavior, then it could also be responsible for the more "stable" EDMs.

EDM4.11: 7/8/2003 → 8/10/2003, Runs 68818 → 75337

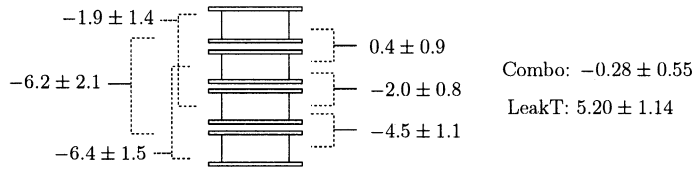

Figure C.24: Initial EDM4.11 frequency profile after installation of the third gold groundplane. The signal is averaged from Runs 68818(HVS=20), 69308(5), and 69856(5).

After a new groundplane (the third gold groundplane) was installed, the initial runs seemed to often show signals resolved at the 2.5–3.0 sigma level, mostly from signals involving the OB cell (see Fig. C.24). A single run taken with HVS=50 seconds (69585) seemed to not have a similar signal, though. We expected that we should see a similar EDM to Figure C.24 at HVS=5 for HVB, and no signal for HVT, but data taken with the HV on one side showed no signals for either side. Returning to having the HV on both sides, it seemed like there were no longer false signals coming from the OB cell, and we started getting resolved signals from signals involving the OT cell:

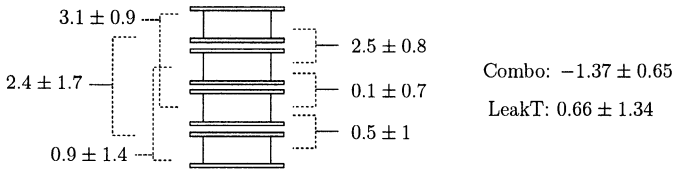

Figure C.25: EDM4.11 frequency profile. The signal is averaged from Runs 71495–72579.

We had changed the signal cabling before Run 71802 so that the analog dividers and DAQ channels usually used for the middle cells now were monitoring the outer cells, and vice versa. It was initially thought that the change in the electronics setup might have corresponded to the change in the EDM profile, but later changes in the electronics setup did not seem to affect the false signals. The vessel was then opened and remelted cells were put in the middle positions and the old middle cells were moved to the outer positions. Since the size of the EDM we were seeing at this point was small enough that we did not always resolve them within a single day, our approach was to take data stepping through some standard reversals: B direction, channel direction, and HVS. We generally continued to get various false signals at the 2-3 sigma level in various channels:

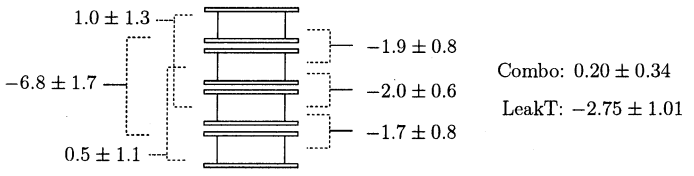

Figure C.26: EDM4.11 frequency profile after changing cells. The signals are averaged from Runs 73241, 74051, 74372, and 75337.

It was difficult to say if any of the reversals we were applying had any effect. It did seem that runs taken with HVS=50 seconds were showing some false signals, compared to Run 69585 which

had earlier given some indication that longer ramp times might not have given false signals. A larger EDM ($> 10^{-7}$ s^{-1}) appeared in the middle of run 75622, seemingly coinciding with a SF6 refresh, and this larger signal remained fairly stable and persistent for many runs (see EDM4.12).

Conclusions: Apparently the new groundplane did not solve all our problems, although the EDM in this case was somewhat smaller than other instances, which made it more difficult to diagnose. Probably, the EDM did not depend on the HVS rate as was initially indicated by run 69585, and if we had taken more data at that point we would have seen resolved signals for HVS = 50. It is probably also safe to conclude that the changes made to the signal monitoring setup did not actually have any effect on the EDM.

EDM4.12: 8/10/2003 → 9/1/2003, Runs 75622 → 83510

After dealing with the smallish EDM4.11 for many runs, the signal shifted in the middle of run 75622 and remained stable at a larger value:

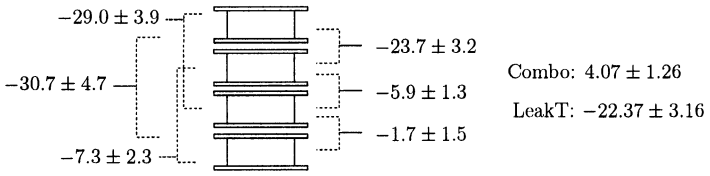

Figure C.27: EDM4.12 frequency profile (Run 75916).

The large signal seemed to be present only for HVT. We proceeded to explore a wide variety of different HV sequences. We generally found that when a HV sequence gave an EDM, it was about the same size as the signal from ±10 kV. It seemed that while +10+1, −10+5, and ±5 kV sequences created EDMs, −10+1 and +7.5+1 kV sequences did not. While performing the non-symmetric HV sequences, we found that we were resolving signals on the four-quadrant detector monitoring the beam from the outer top cell, indicating possible motion of the OT cell. The 4-quadrant signal seemed to be E^2 dependent, though, so had not shown up in the standard ±10 kV runs. We expected that if cell motion in a magnetic field gradient was responsible for the EDM, then increasing the gradient should increase the size of the EDM. We then applied gradients about five times larger than usual, but saw no large change in the EDM with the applied gradient or when the gradient was reversed. This seemed to rule out motion as a cause of the current EDM.

Conclusions: EDM4.12 marked somewhat of a turning point in our general approach in dealing with the false signals. Up until this point, when we encountered an EDM, our approach was to then change various parameters to try to find an association of the EDM with a particular parameter or part of the apparatus. However, it had become increasingly apparent in our dealings with the previous several EDMs that it was difficult to tell whether or not changes in the EDM behavior had anything to do with the deliberate changes that we implemented. We decided that instead of spending our time trying to find the characteristics of the EDM du jour, we would try to address various plausible mechanisms that might lead to EDM-like shifts.

In the case of EDM4.12, the resolved beam position monitor signal made vapor cell motion an obvious candidate, but the enhanced gradient tests, seemed to rule cell motion out as the cause of this EDM. We next started looking into the possibility that the EDMs were due to HV spark induced ferromagnetic orientation by looking at the effects of artificial sparks, similar to the tests described in Section 3.2.2.

Interim: HV was not applied to the vessel for several weeks while artificial spark testing was performed with 5 turn, 1 cm diameter loops around the feedthroughs inside and just outside vessel, and inside the electrodes. Loops inside the vessel caused frequency shifts about 10 times larger than the loops outside the vessel. 10 μF at 1 V discharged over an inside loop could create an EDM signal of about 10^{-7} s^{-1}, and also created a signal (20 mV initial spike) in a pickup coil (4.5 square, 100 turns) mounted on the outside face (top or bottom) of the vessel. The cells were removed and reinstalled a couple of times while these tests were carried out.

EDM4.13: 9/25/2003 → 11/5/2003, Runs 85021 → 88173

Having found that artificial sparks that generated a frequency shift of 10^{-7} s^{-1} created detectable pickup events on coils mounted on the outside of the vessel, we next looked to see if similar pickup events were observable under actual HV operation. We indeed found signals in the pickup coils when the HV was ramped, and we also had well resolved HV correlated frequency shifts. Data for this EDM was somewhat hampered because the OT cell amplitude decreased very quickly such that frequency combinations involving this cell were extremely noisy. An EDM was persistently resolved in the middle, bottom, and cross-bottom 2-cell differences, though. The signal seemed to be present for HVB and not for HVT connections, and was also probably the most "quadrupole" resolved signal we have encountered, in that the signals from the bottom three cells were very symmetric and of opposite sign for positive and negative HV (see Fig. C.28), and there was not a very well

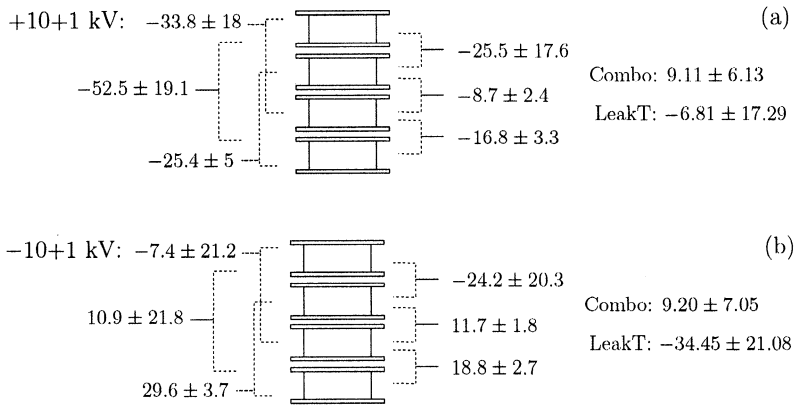

Figure C.28: Frequency profile of EDM4.13 for +10+1 (a) and −10+1 (b) HV sequences.

resolved signals for ±10 kV sequences. While the false signal was now quadratic in character, the quadratic beam position signal that had been resolved during EDM4.12 was no longer present. We also repeated the enhanced magnetic gradient test to check for cell motion, but did not see a change in the signal.

The spark events we were seeing during the HV ramp were much more prevalent for downward ramps than upward, and the pickup events indicated a magnetic field in the same direction independent of the HV polarity or ramp direction. The pickup events became less frequent when the HV value was lowered, as did the size of the frequency shifts. There were also more sparks with HVB than HVT, which was consistent with the current false signal being mainly on the bottom, but there were also more sparks for $0 \longrightarrow -10$ ramps than $+10 \longrightarrow 0$ ramps, which was inconsistent with the false signal behavior. The pickup events were also reduced for a longer HVS time, which had no effect on the frequency shifts.

Conclusions: While this is the only seemingly E^2 frequency effect we have encountered, we did not test every EDM occurrence with HV sequences that would have revealed an E^2 effect, so there could have been other instances we did not notice. This effect did not appear to be due to cell motion, and we also concluded that it seemed unlikely that the pickup coil events were related to the frequency shifts since their behavior was somewhat uncorrelated as different HV conditions were applied. If the pickup events were being caused by sparks, then these sparks have probably been present throughout much of the previous data as well, but their characteristics do not match well with other EDM instances either, given their HVS dependence and unidirectionality.

Interim: After changing out cells it became impossible for the top side of the vessel to hold 10 kV. This problem seemed to be associated with the groundplane as inverting the groundplane caused the HV breakdown problem to move to the bottom side of the vessel. This may have had something to do with the groundplane becoming a bit warped from unequal pressure on the groundplane when the vessel was tested without cells on one side, but attempts to reflatten the groundplane in place did not seem to solve the problem. Enlarging the cell disk with silver paint also did not seem to work in this case. It was decided that a new groundplane was needed, and while this was under preparation, EDM tests continued with the old 2-cell polyethylene vessel.

C.3 Two Cell Vessel Revisited

In an effort to examine if any changes made in implementing the 4-cell vessel setup had caused the increase in EDM occurrence, we reinstalled the vessel that had been used at the end of the HG3 dataset. 2-cell data runs were taken from 12/17/2003 to 3/23/2004 and are designated with HG4 run numbers 89127–105551. During these runs our goal was mainly to see how often false signals occurred relative to vessel openings and we did not expend much effort trying to diagnose the sources of the false signals that appeared.

EDM4-2.1: 1/10/2004 → 1/19/2004, Runs 90640 → 93055

Initially, HG4 CO vapor cells (#41 and 36) were installed in the HG3 vessel, and the smaller vessel was installed in the larger 7.5" ID magnetic field coil by using polyethylene shims around inside edge of the 4-cell vessel shape adapter. The first three runs taken in this configuration (Runs 89127, 89310 and 90008, all three were taken with a +10,−1, −10,+1 HV sequence) did not show evidence of a large false signal. The vessel was opened between the second and third runs to see if moving the cells around might cause an EDM to appear. The spin coherence times in Run 90008 were much lower than in Run 89310, though, so the vessel was removed again to investigate this. The drop in spin lifetimes was traced to larger than usual magnetic field gradients that seemed to be caused by problems with the degaussing system.

Starting again with cells #39 and 41, a somewhat resolved 2.7σ signal of $\Delta\omega_M = 6.7 \pm 2.5 \times 10^{-8}$ s^{-1} was found in Run 90640, and then a larger signal (-15.5 ± 3.0) was seen in the very next run (91178). This was the largest signal seen during this EDM, and in subsequent runs the signal seemed more stable around the 6×10^{-8} level. It was also found that the EDM was only present for HVB.

Conclusions: This was a relatively small EDM except for Run 91178. There were still several major differences between the configuration used in this period versus the HG3 configuration, including that the CO vapor cells were used, all the runs were taken at the +10 GHz detuning, and the 4-cell vessel polyethylene shape adapter was used.

EDM4-2.2: 1/20/2004 → 2/6/2004, Runs 99348 → 99136

We next installed N_2+CO cells that had been used during the HG3 measurement (#23 and 26). The first several runs (93348, 93978, 94631) did not show any especially large signals, although each individual run gave a frequency shift of $4 \pm 2 \times 10^{-8}$ s^{-1}, and combining the three runs gave a resolved signal of 3.9 ± 1.1. Subsequent runs continued to show signals in the 4–7 range, similar in size to EDM4-2.1, but in this case it seemed that the EDM was associated with HVT. There was only one run (98069) during this period that individually resolved a greater than 3σ signal: 6.8 ± 2.0.

About half of the runs during this period were taken at the +10 GHz probe detuning and the other half were at −20 GHz. As we were taking the data, it seemed that the −20 GHz data runs usually gave a smaller signal than the +10 detuning. The average signal at the −20 detuning was 2.3 ± 0.9, and the average signal at +10 was 4.9 ± 0.8, giving a 2.1σ difference between the two results.

Conclusions: This was a similar size signal to EDM4-2.1, although it did seem that the source of the EDM had moved from the bottom to the top side of the vessel when the cells were changed. Since the first use of the CO cells resulted in EDM3.4, it had been a long standing suspicion that the new cells were somehow related to increased occurrence of EDMs, but this EDM seemed to indicate that the old cells were now just as likely to give false signals as the CO cells. While taking this data there was a fair amount of concern regarding the difference between the +10 and −20 GHz detuning signal size. We have occasionally checked other EDM occurrences for a detuning dependence and not found one, although a light shift effect might have been enhanced in this case if the alignment of $\boldsymbol{B}$ relative to $\boldsymbol{E}$ was worse than at other times. The utmost maximum size of the Stark interference effect discussed in Section 4.4.5 would be about 5×10^{-8} s^{-1} at +10 GHz, but this would require an extremely severe misalignment of 45°.

Interim: A 10 μF capacitor was added across the leads for the main magnetic field coil which stopped the current source from being perturbed when different voltages were applied to the coil form. Previously, the current would be shifted by about 20 μA (always in the same direction) when the grounding of the coil form was disturbed (also see EDM4.6).

EDM4-2.3: 2/26/2004, Run 100781

Cells 23 and 26 were remelted and installed back in the vessel before Run 99469. We saw only one significantly resolved signal between this point and the next time the vessel was removed from the shields. This was from Run 100781, which gave a signal of $-4.9 \pm 1.3 \times 10^{-8}$ s^{-1}, the opposite sign from EDM4-2.2. The other six runs during this period gave an average signal of -1.7 ± 1.0, which is 2.4σ away from the Run 100781 signal.

Conclusions: Several of the runs during this period had somewhat low sensitivity, so it is hard to tell if the apparent effect in Run 100781 was present in other runs. The removal and reinstallation of the cells seemed to have an effect on the sign of the EDM. The cells were installed in the same positions as before, but we did not keep track of their orientation.

Interim: Some artificial spark testing was performed with drive coils located in between the innermost magnetic shield layer and the magnetic field coil form, Shifts generated by "sparks" in this location were about 100 times larger in the single cell frequencies than in their difference.

EDM4-2.4: 3/10/2004 → 3/22/2004, Runs 102272 → 105551

We next reinstalled the smaller diameter (6") magnetic field coil that had been used during HG3, although we still used the larger 7.5" coil to generate the magnetic field. This also enabled the use of the HG3 Teflon shape adapters. An initial run (101989) in this configuration did not resolve a signal ($\Delta\omega = 0.01 \pm 2.7$). The shields were opened after this run, though, so that polyethylene fittings could be installed on the front face of the vessel, replacing two brass hose barbs that had been used to connect to the SF_6 inlet and outlet lines. It should be noted that all HG3 data runs with this vessel had used short Teflon tubes that slip fit into the front face of the vessel, to attach the gas lines. These Teflon pieces had been incorporated into the HG4 vessel, and the brass hose barbs were installed in the 2-cell vessel during HG4 data taking so that it could be used as a test setup to check leakage currents of cells under HV outside of the main apparatus. For this installation, the front vessel face was removed and to drill and tap new holes, but the cells were not touched.

The next data run showed a large EDM ($\Delta\omega = 31.3 \pm 2.1$), and over the next several runs the EDM remained very well resolvable, but its magnitude seemed to grow smaller (see Fig. C.29). We also tried to revert the optical setup closer to the HG3 configuration by removing the beam splitter for the outer light beams and disabling all aspects of the light shift compensation setup (see Sec. 6.5). These changes, along with the -20 GHz probe detuning, did not seem to affect the false signal, which seemed to be steadily drifting independent of any conditions we applied.

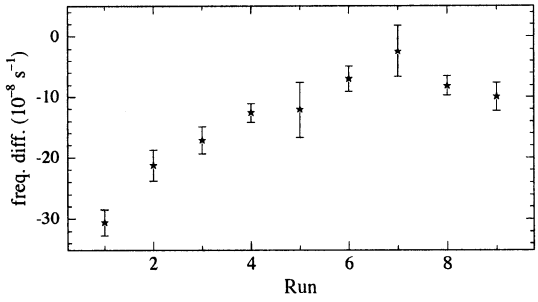

Figure C.29: EDM signal for EDM4-2.4 versus run (102272–105207).

Before Run 104504, an aluminum tube (1 mm wall thickness) was installed around all of the cabling going through the holes in the magnetic shield endcaps. The tube interfaced with an aluminum plate over the end of the magnetic field coil form with a hole the same diameter as the tube. The tube and plate were meant to completely isolate the magnetic shields from the effects of fast spark magnetic fields originating in the HV cables. This did not appear to significantly affect the size of the false signal.

Conclusions: It seems fairly certain that this EDM was associated with the vessel modifications to install the polyethylene hose barbs. Either an impurity entered the vessel when it was opened, or an impurity might have been embedded in the front vessel face when it was modified. This was not particularly unusual, though, that an EDM would appear or disappear after opening and closing the vessel. This particular effect probably originated from inside the vessel, so it is unlikely that the additional shielding around the HV cables would have affected this EDM.

Epilogue

After EDM4-2.4, it was decided that our tests with the 2-cell vessel had sufficiently demonstrated that it was more susceptible to false signals than it had been during the HG3 dataset. A new groundplane had been prepared and installed in the 4-cell vessel so we returned to 4-cell operation. We next took data (Runs 106421–113610) to test for HV induced motion by attaching current loops to external vessel components and looking for an enhanced HV correlated signals (see Sec. 7.5.3). No motion was found at the 10 nm level, and we also saw no large false signals during this period. Directly EDM related measurements were put on hold in mid June of 2004 as the apparatus was switched to a configuration to measure the Stark interference effect [Swa05]. Further EDM work will likely begin in March of 2005 after the completion of the Stark interference measurement.

VITA

William Clark Griffith was born in Portland, Oregon in 1976, and spent his formative years in Forest Grove, Oregon. He graduated from Forest Grove High School in 1994 and received a Bachelor of Arts degree in physics from Whitman College in 1998. He began graduate studies in physics at the University of Washington in the fall of 1998, where he earned a Master of Science degree in 2000, and completed his physics Ph.D. in 2005.